Physical conditions of the interstellar medium in high-redshift submillimetre bright galaxies

Chentao Yang

Physical conditions of the interstellar medium in high-redshift submillimetre bright galaxies

Thèse de doctorat de University of the Chinese Academy of Sciences et de l'Université Paris-Saclay, préparée à l'Université Paris-Sud

École doctorale n°127 Astronomie et Astrophysique d'Île-de-France :
Institut d'Astrophysique Spatiale (IAS),
Purple Mountain Observatory (PMO)
Spécialité de doctorat : Astronomie et astrophysique

Thèse présentée et soutenue à Nanjing, le 22 Septembre 2017

Chentao YANG

Composition du Jury :

M. Guillaume PINEAU DES FORETS PREM, Université Paris-Sud	Directeur de thèse
M. Yu GAO Astronome, Purple Mountain Observatory, CAS	Co-Directeur de thèse
M. Marian DOUSPIS Astronome, Université Paris-Sud	Président
M. Yong SHI Professeur, Nanjing University	Examinateur
M. Hongchi WANG Astronome, Purple Mountain Observatory, CAS	Examinateur
M. Johan RICHARD Astronome, Observatoire de Lyon	Rapporteur
M. Qiusheng GU Professeur, Nanjing University	Rapporteur
M. Alexandre BEELEN Astronome, Université Paris-Sud	Invité
M. Alain OMONT Directeur de Recherche, Institut d'Astrophysique de Paris	Invité

Acknowledgements

Without the unconditionally support of my parents and friends, I would never have the chance to treat astronomy as a career to pursue.

It is my supervisors: Alain Omont, Yu Gao and Alexandre Beelen who guide me through the mist. Yu helped me entering the world of submm/mm astronomy. Alexandre is always happy to answer all of my questions and gives me new insights into data reduction and analysis. I would like to give my special thanks to Alain who helped me a lot not only in my daily life during my stay in France, but also being a model of a hardworking astronomer with an incredible amount of energy and enthusiasm in astrophysics. I always feel grateful that he pays attention to my every each idea, and gives me helpful advice. It's a great honour for me to pursue astronomical research with such a legendary figure.

My friends at Purple Mountain Observatory are great treasures to me. They are the people who support me and help me even with trivial matters. They include Hongjun Ma, Zhiyu Zhang, Daizhong Liu, Fangxia An, Yuxiang Gao, Kexin Guo, Qinghua Tan, Ao Zhao, Xuejian Jiang, Yinghe Zhao, Cong Ma, Zhangzheng Wen, Xiaolong Wang, Lijie Liu, Qian Jiao, En Chen, Qianru He, and many others. Zhiyu's passion in astronomy inspires me as always. I have also learned a lot from them, such as Daizhong's circumspection and Fangxia's diligence. The "star formation in galaxies" group is like a big happy family. And I treasure the time spent with it.

I also enjoy the two years that I spent at IAS in Orsay a lot. The people are friendly there and treated me very well, and I had a great time with all the other PhD students and postdoc there, including Jean-Baptiste, Raoul, Lapo, Clara, Guillaume, Cristiano, Gururaj, Samantha, Amine, Benjamin, Lucie, David and many others. I miss the movie nights with pizzas, and the sushi weekends. I would also like to thank the staff/professors in the MIC group: Mathieu, Nabila, Bruno, Hervé, Nicole and Marian. The administrative members at IAS: Véronique and Patricia also helped me a lot during the two years. I had a great time in Paris with friends from the CNRS French course, especially Yusuke Tanimura, Jerry Yang and Rasa Lk, with whom I was enjoying Paris. I would also like to thank them for sharing the memories.

As last, I also thank my collaborators who have enlightened discussions with me and help me to finish the scientific projects that I worked on: Roberto Neri, Pierre Cox, Eduardo González-Alfonso, Matthew Lehnert, Raphaël Gavazzi, Melanie Krips, Iván, Rob Ivison and many others in the *Herschel*-ATLAS team. I would like to give my special thank to Roberto who shared his great knowledge of millimetre interferometry with me, to Eduardo with his great expertise in molecular astronomy, and to Raphaël who shared his expertise in gravitational lensing.

Résumé

La découverte à l'aide de caméras submillimétriques, d'une population de galaxies submillimétriques (SMGs) obscurcies par la poussière à grand décalage spectral redshift (z), a révolutionné notre connaissance de l'évolution des galaxies et de la formation stellaire dans les conditions physiques extrêmes. Ces galaxies ultra-lumineuses infrarouges (ULIRGs) renferment les flambées de formation stellaire ('starburst') les plus intenses dans l'Univers, avec des taux de formation stellaire dépassant 1000 $M_\odot$/an, approchant donc la limite de stabilité par pression de radiation d'Eddington. La particularité du domaine millimétrique /submillimétrique et de leur distribution spectrale d'énergie (SED) dans l'infrarouge lointain permet de les étudier avec une bonne sensibilité pour toute la gamme de décalages spectraux de 1 à 6. Elles sont considérées comme les progéniteurs des galaxies actuelles les plus massives. Les modèles théoriques d'évolution de galaxies ont été remis en question par la très grande densité observée de ces SMGs à très grand décalage spectral. Les grands relevés extra-galactigues récemment effectués, tels que *Herschel*-ATLAS et *Her*MES, en ont découvert des centaines de milliers, ouvrant de nouvelles opportunités pour observer ces objets, leurs groupements et leurs connections avec les grandes structures de l'Univers.

La taille de ces échantillons permet d'y trouver des objets singuliers très rares. C'est le cas de celles de ces SMGs très lointaines (environ une sur mille) qui sont fortement lentillées gravitationnellement par un objet massif (déflecteur) à distance intermédiaire. Dans la grande majorité des cas ces déflecteurs sont des galaxies massives elliptiques assez lointaines à décalage spectral compris entre environ 0.2 et 1.2. L'intérêt de telles lentilles gravitationnelles est de produire à la fois une amplification substantielle de la luminosité apparente de la SMG lointaine, par un facteur typique $\mu \sim 5$–15, et une dilatation de ses dimensions par un facteur $\sim \sqrt{\mu}$. L'accroissement substantiel de sensibilité et de résolution angulaire effectives qui en résulte est un énorme atout pour l'étude de ces objets et spécialement de leur milieu interstellaire et de leurs flambées de formation stellaire. Mais la complexité des effets de lentille gravitationnelle impose la construction de modèles élaborés pour reconstruire l'image réelle de la source lointaine à partir de l'image lentillée observée.

Nous avons utilisé cette puissance des lentilles gravitationnelles pour une étude systématique du milieu interstellaire des flambées de formation stellaire des SMGs, basée principalement sur un nouveau critère, l'intensité des raies d'émission submillimétrique de la vapeur d'eau. Nos études antérieures avaient en effet montré d'une part que ces raies submillimétriques pouvaient être les plus intenses après celles de CO dans les SMGs à grand décalage spectral z, et d'autre part qu'elles constituaient un puissant diagnostic des conditions dans les ULIRGs locales, dont on pense qu'elles sont le meilleur modèle (réduit) local des SMGs à grand z. Cette étude est centrée sur l'observation des raies de H_2O dans un échantillon substantiel de SMGs effectuée à l'Institut de radioastronomie millimétrique (IRAM) avec l'interféromètre millimétrique NOEMA. Nous lui avons adjoint une étude systématique des raies de CO dans les mêmes sources à l'IRAM/30m pour un diagnostic complémentaire, ainsi que celle de H_2O^+, clé de la chimie de H_2O dans quelques sources, et l'observation multi-raies de deux sources à haute résolution angulaire avec

ALMA ou NOEMA pour sonder la structure du gaz moléculaire et de la flambée de formation stellaire dont il est le siège.

Nous avons donc sélectionné un échantillon de 16 SMGs fortement lentillées, extrêmement brillantes, en choisissant celles dont les densités de flux submillimétrique sont les plus élevées dans les 300 deg2 des champs Nord et équatoriaux du relevé *Herschel*-ATLAS. Leur observation à l'aide de l'interféromètre millimétrique NOEMA nous a permis de détecter dans chacune au moins une raie submillimétrique de H_2O, déplacée dans une fenêtre atmosphérique millimétrique. Leur forte intensité confirme que ces raies sont les raies submillimétriques les plus brillantes dans ces objets après celles de CO. Nous avons trouvé une corrélation linéaire forte entre la luminosité de H_2O et la luminosité infrarouge totale. Cela indique le rôle important du pompage infrarouge lointain dans l'excitation des raies de l'eau. En utilisant un modèle de pompage infrarouge, nous avons obtenu les propriétés physiques du gaz et de la poussière interstellaires ainsi que l'abondance de H_2O. Nous avons montré que les raies de H_2O tracent un gaz chaud et dense, baignant dans un champ de rayonnement infrarouge lointain intense, émis par les flambées extrêmes de formation stellaire.

Plusieurs raies de H_2O^+ ont également été détectées dans trois de ces SMGs dans la bande de fréquence des observations de NOEMA. Elles montrent qu'il existe une corrélation étroite entre les luminosités des raies de H_2O et H_2O^+, qui s'étend des ULIRGs locales aux SMGs à très grand z. Le rapport élevé de flux H_2O^+/H_2O suggère que des rayons cosmiques très intenses, produits dans les fortes flambées de formation stellaire, sont probablement à l'origine de la chimie de l'oxygène dans ce milieu en y formant abondamment les molécules H_2O et H_2O^+.

Nous avons observé en complément de multiples transitions rotationnelles de la molécule CO dans chacune de cette quinzaine de SMGs, avec le spectromètre millimétrique multi-bande EMIR du télescope de 30m de l'IRAM. Nous avons ainsi établi la distribution spectrale de l'émission dans les raies de CO de ces galaxies. Elle semble présenter une certaine similitude avec celle des ULIRGs locales. Nous avons mis en évidence un effet significatif de lentillage différentiel qui pourrait entraîner une sous-estimation de la largeur de raie d'un facteur allant jusqu'à 2. A l'aide d'une modélisation de type LVG et en utilisant une approche bayésienne, nous avons estimé la densité et la température du gaz, ainsi que sa densité de colonne dans la molécule CO. Nous avons ensuite mis en évidence une corrélation entre la pression thermique du gaz et l'efficacité de la formation stellaire. Nous avons également étudié les propriétés globales du gaz moléculaire et sa relation avec la formation d'étoiles ainsi que le rapport masse de gaz sur poussière et le temps d'épuisement du gaz. La détection de raies du carbone atomique neutre [CI] dans ces SMGs à grand décalage spectral y a étendu la corrélation linéaire, connue pour les galaxies locales, entre luminosité des raies de CO et de [CI]. Enfin, nous avons comparé les largeurs de raie de CO et H_2O et constaté qu'elles étaient en bon accord. Cela suggère que les régions émettrices soient co-spatiales.

Afin de comprendre les propriétés des émissions moléculaires dans ces sources, et plus généralement, leur structure et leurs propriétés dynamiques, il est crucial d'en acquérir des images à haute résolution angulaire. Nous avons donc observé deux de ces sources avec les interféromètres ALMA ou NOEMA en configuration étendue des antennes. Grâce à une modélisation du lentillage de ces sources, ces données nous ont permis de reconstituer la morphologie intrinsèque de la source. Nous avons ainsi mis en évidence que la région de l'émission de la poussière relativement froide qui évacue l'énergie considérable de la flambée stellaire, a une plus petite taille en comparaison de celle du gaz CO et H_2O, tandis que les régions d'émission de ces deux dernières molécules sont de taille similaire. En ajustant le modèle dynamique de la galaxie aux données CO, nous avons montré qu'elle peut être modélisée par un disque en rotation, duquel nous avons pu déduire la masse dynamique projetée et le rayon effectif. Ces études nous ont également

permis de confirmer la détection à grand z de l'isotopologue rare $H_2^{18}O$ dans ces deux sources, montrant que de futures études de cette molécule avec ALMA dans de telles galaxies lentillées devraient apporter des informations intéressantes sur la nucléosynthèse de ^{18}O à grand z.

Avec ALMA et la future extension de NOEMA, nous pourrons étendre ce genre d'observations, spécialement à haute résolution angulaire, à un plus grand nombre de SMGs à grand décalage spectral fortement amplifiées (et même à des SMGs non lentillées grâce à la sensibilité d'ALMA), afin d'étudier divers traceurs du gaz moléculaire et de comprendre les conditions physiques et chimiques du milieu interstellaire et leur relation avec la formation des étoiles.

Table of contents

Chapter 1

Introduction

That destructive monster of a hundred heads, impetuous Typhon. He withstood all the gods, hissing out terror with horrid jaws, while from his eyes lightened a hideous glare.

Prometheus Bound by Aeschylus

1.1 Discoveries of the submillimetre-bright galaxies at high-redshift

Deep submillimetre (submm) imaging using SCUBA/JCMT (Holland et al., 1999) of the Hubble deep and blank field has revealed a new population of galaxies releasing massive amount of energy through the Rayleigh-Jeans side of the blackbody emission of the dust (Barger et al., 1998; Hughes et al., 1998; Smail et al., 1997). This discovery as a major breakthrough in the late 1990s expanded our understanding of the big picture of galaxy formation and evolution and opened a new observation window in submm bands.

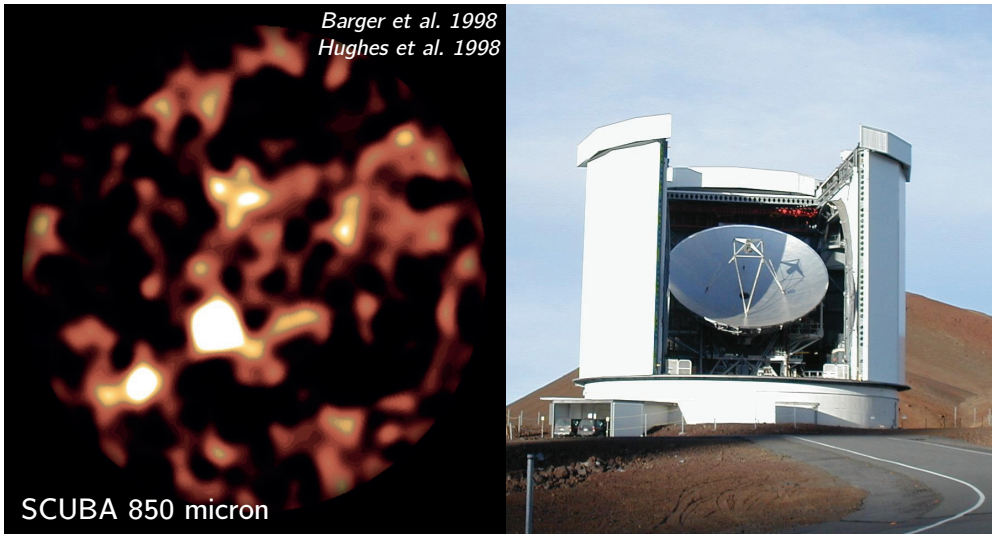

Fig. 1.1 *Left:* First image of SMGs detected by SCUBA-850 μm imaging reported by Barger et al. (1998); Hughes et al. (1998); Smail et al. (1997). *Right:* The James Clerk Maxwell Telescope (Credit: www.roe.ac.uk) on which the SCUBA instrument is mounted.

Since the initial discovery of SMGs at 850 μm with SCUBA at the end of last century, a large number of studies have been conducted, and mostly with the help of interferometric observation in order to pinpoint the number counts and the positions of the SMGs (Blain et al., 2002; Casey et al., 2014; Smolčić et al., 2012). The success of SMG observations is also partially due to the negative K-correction, especially for the studies conducted at ~ 1 mm bands. As illustrated in Fig. 1.2, with increasing redshift, spectral energy distributions (SED) of Arp 220 shifts towards longer wavelength while its total flux decreases and the emission peak also shifts in the same direction. As a result, the flux density at ~ 1 mm bands practically does not vary with redshifts. Chapman et al. (2005) carefully studied the properties of this 850 μm-selected SMG population and concluded that those with $S_{850\,\mu\mathrm{m}} > 1$ mJy contribute a significant fraction to the cosmic star formation around $z = 2$–3, i.e. $\gtrsim$10%. Fig 1.3 shows the evolution of the contribution of different types (defined by their far-IR luminosity) of galaxies to the cosmic star formation along different redshifts. The importance of the most luminous galaxies in the far-IR is clearly increasing with redshift. Several other works have also confirmed that SMGs play a key role in the cosmic star formation at high-z (e.g. Michałowski et al., 2017; Murphy et al., 2011; Swinbank et al., 2014). For the ULIRGs studied with a median redshift of 2.2, it can be > 65% according to Le Floc'h et al. 2005 and Dunlop et al. 2017 (see also ALMA works by Aravena et al. 2016a; Dunlop et al. 2017; Karim et al. 2013; Oteo et al. 2016; and Casey et al. 2014 for redshift distributions of SMGs selected at 850–870 μm by SCUBA/LABOCA and at 1.1 mm by AzTEC). In the redshift range around $z = 1$ to $z = 3$, also known as the epoch of galaxy assembly, the cosmic star formation rate density reaches its peak (as shown in the left panel of Fig. 1.3, Lilly et al. 1996; Madau et al. 1996, see also Madau & Dickinson 2014 for a review). Around half the stars in the present-day Universe have formed around this period (Shapley, 2011, and the references within).

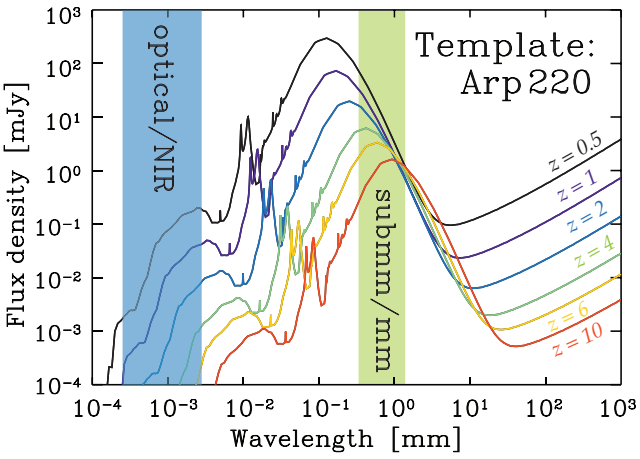

Fig. 1.2 The observed spectral energy distributions (SED) of Arp 220 from the optical to the radio wavelengths as seen at different redshifts. The optical/NIR band is shown in blue while the submm/mm band is shown in green.

This new population of dusty starbursts are the strongest starbursts throughout the star formation history of our Universe. The most luminous ones with infrared luminosities integrated over 8–1000 μm $L_{\mathrm{IR}} \sim 10^{13}\,L_{\odot}$, and star formation rate (SFR) around 1000 $M_{\odot}\,\mathrm{yr}^{-1}$, approach the limit of maximum starbursts (Barger et al., 2014). These submm bright galaxies (SMGs, see reviews by Blain et al., 2002; Casey et al., 2014) are the veritable "monsters" in our universe just like the Typhon in ancient Greek myth. Even comparing with the local ultra-luminous infrared galaxies (ULIRGs, whose L_{IR} equals a few $10^{12}\,L_{\odot}$), they are somewhat more luminous (Tacconi et al., 2010). Their extremely intense star-forming activity indicates that these "Typhon"-like galaxies generating enormous energy at far-infrared (far-IR) are in the critical phase of rapid stellar mass assembly as mentioned above. Although there are pieces of evidence of a diverse population of the SMGs (e.g. Banerji et al., 2011), they are believed to be the progenitors of the most massive galaxies today (e.g Lonsdale et al., 2006; Simpson et al., 2014).

To understand such a cosmic star formation history shown in Fig. 1.3, compatibility with the galaxy formation models in the context of ΛCDM (the hierarchical cold dark matter halo model) is needed. Therefore, under the big picture of galaxy formation and evolution, it is important to understand the

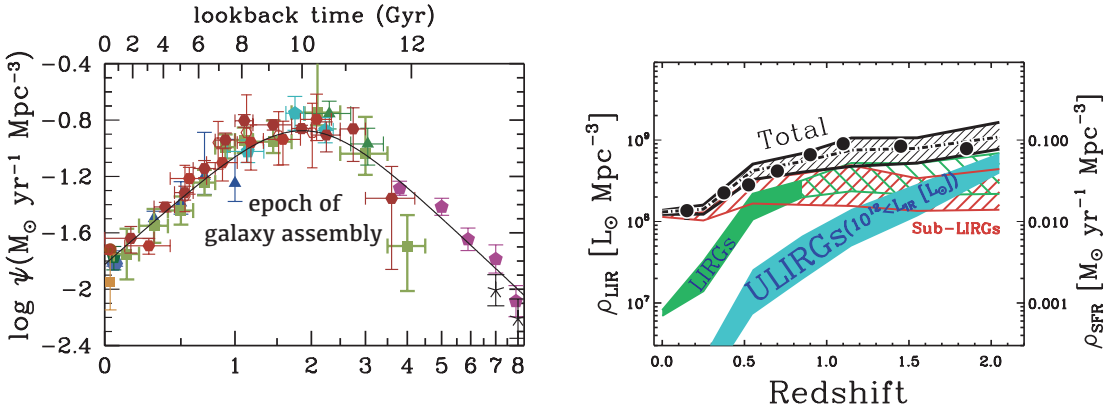

Fig. 1.3 The history of cosmic star formation and the contribution from various types of galaxies. *Left:* the evolution of cosmic star formation density, defined by the mass of stars formed per year per comoving volume in cubic Mega-parsec, along the lookback time (redshifts), adapted from Madau & Dickinson (2014). *Right:* the evolution of the contribution from different types of galaxies to the cosmic infrared luminosity, which serves as a proxy of star formation rate. This figure is adapted from Magnelli et al. (2013).

extreme star-forming activity within SMGs through studying their molecular gas content which serves as the raw ingredient for star formation, especially those at the peak of the star formation history (i.e. $z \sim 2$–3, Madau & Dickinson, 2014). Moreover, theoretical models of galaxy evolution have been challenged by the observed large number counts of high-z SMGs (e.g., Casey et al., 2014). Nevertheless, due to their great distances, the number of well studied high-z SMGs is limited (see reviews by Carilli & Walter 2013; Solomon & Vanden Bout 2005) and the observations were mostly achieved through a few cases of strong gravitation lensing, including IRAS F10214+4724 (Ao et al., 2008), APM 08279+5455 (Weiß et al., 2007), Cloverleaf (Bradford et al., 2009), SMM J2135-0102 (Danielson et al., 2011) and in the weakly lensed SMG, HFLS3 at $z = 6.34$ (Cooray et al., 2014; Riechers et al., 2013). Therefore, studies of the star formation properties of such a population of galaxies based on a fairly large sample is needed.

1.2 Studying the high-redshift SMGs with various molecular gas tracers

1.2.1 Molecular gas in galaxies

Although, the interstellar medium (ISM), that is, the gas and dust between stars, makes only a small fraction of the total baryonic content (its mass is ~ 10% of the total mass of a galaxy), it plays an essential role in shaping a galaxy that we can observe, by circling the fuel and ashes of the death and birth of stars and transferring energies into different phases within a galaxy as shown in Fig. 1.4. It serves as the key framework of star formation (e.g. Omont, 2007). For the gas phase ISM, it is mostly made of ions, atoms and molecules. In the Milky Way, the ionised gas mostly consists of ionised hydrogen (H II) that contributes to 23% of the total gas mass, while the neutral gas, mostly neutral hydrogen (H I) makes a fraction of 50% and the molecular gas, mostly H_2 gas, makes a fraction of 16% (e.g. Draine, 2011). The fraction of the molecular gas can be much higher than that of the Milky Way in high-z star forming galaxies (e.g. Tacconi et al., 2013). The physical conditions of the ISM itself exhibit a large range of kinematic temperature (T_k) and volume density (n), so that the ISM is presented in different phases. The hot ionised gas, with $n < 0.01\,\mathrm{cm^{-3}}$ and $T_k > 10^5$ K, fills approximately half of the ISM volume in our Galaxy. The warm ionised H II gas has $n \sim 0.3$–$10^4\,\mathrm{cm^{-3}}$ and $T_k \sim 10^4$ K. The warm neutral gas shows $n \sim 0.6\,\mathrm{cm^{-3}}$ and $T_k \sim 5000$ K

while the cool neutral atomic gas has $n \sim 30\,\mathrm{cm}^{-3}$ and $T_\mathrm{k} \sim 100\,\mathrm{K}$. For the molecular gas, it usually resides in two environments: the diffuse molecular gas with $n \sim 100\,\mathrm{cm}^{-3}$ and $T_\mathrm{k} \sim 10$–$50\,\mathrm{K}$ and the dense molecular gas with $n \sim 10^3$–$10^6\,\mathrm{cm}^{-3}$ and $T_\mathrm{k} \sim 10$–$50\,\mathrm{K}$ (e.g. Draine, 2011; Tielens, 2005). Not only the ISM shows a large variety of its physical conditions, but it also has a complicated dynamics, which can transfer matter and energy between the different phases. These various processes are thus tightly linked with the ecosystem of the galaxy (Fig. 1.4).

Among the different phases of the ISM, the dense molecular gas is usually in form of gravitationally bound clouds that can eventually proceed to star formation. Thus, it serves as a key for us to understand star formation in galaxies. According to the solar element abundances, hydrogen is above $\gtrsim 10^3$ times more abundant comparing with heavy elements (except for helium which is about 10 times less abundant than H). This makes the abundance of H_2 to be orders of magnitude larger than that of the other molecules. Nevertheless, the direct observation of H_2 is difficult in the molecular gas phase ISM because H_2 has no dipole moment[1] and therefore very weak rotational transitions. Thus, the observation of the molecular phase of the ISM much relies on molecular species with non-zero dipolar moments, especially the $^{12}C^{16}O$ (we use CO if not otherwise specified in this thesis) molecule. We will further explain the basics of the molecule species and describe their energy levels in the next section.

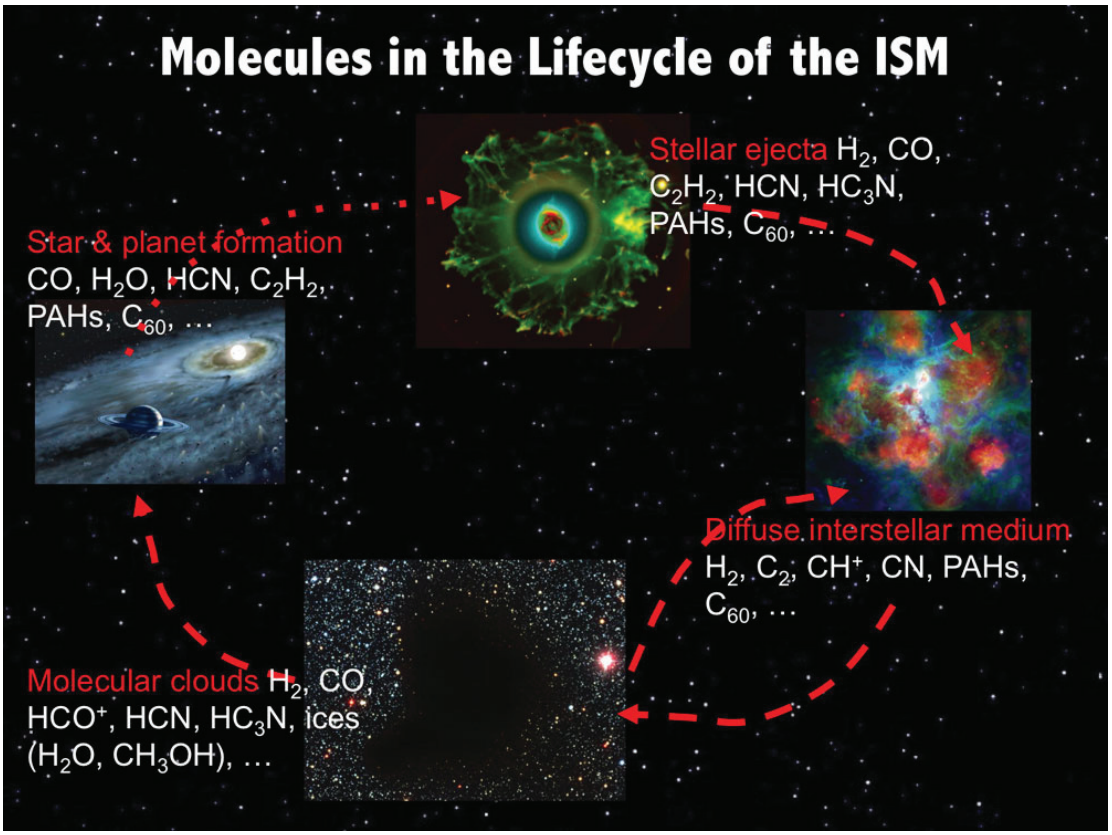

Fig. 1.4 The life cycle of the ISM (figure adapted from Tielens 2013): gas and dust are ejected by dying starts into the diffuse ISM (stellar ejecta), and by cooling, the neutral gas forms molecular clouds which then proceed to star and planet formation when being gravitationally unstable. Legends show some common gas tracers of different stages of the life-cycle.

[1] If the positive and negative charges of neutral molecule do not completely overlap, the electric dipole moment can be defined as a vector pointing from the negative to the positive charge, whose length equals the strength of each charge times the charge separation. As all molecules with a centre of symmetry, H_2 has no dipole moment because it has no separation of the charges.

1.2.1.1 Energy levels of molecules

Molecular spectra are unlike atomic ones that can be determined simply by transitions between individual electronic states. They show a complexity because of the extra degrees of freedom coming from vibration and rotation. The electronic transitions of molecules generally emit in the ultraviolet wavelength. For a molecule that transits between specific rotational levels of certain vibration states, the transition is called a ro-vibrational transition. It emits photons in the infrared bands (e.g. Williams & Viti, 2014). The most commonly observed transitions belong to the pure rotational transitions that happen between two rotational energy levels within one vibrational state (usually the ground state in the molecular gas phase). Fig. 1.5 shows the pure rotation energy levels (in the ground vibrational state and the ground electronic state) of the CO and H_2O molecules together with their dipole moments. CO is a typical diatomic molecule while H_2O is a non-linear polyatomic molecule. For the latter, the two protons of H_2O can either have antiparallel ("para") or parallel ("ortho") nuclear spins, which makes the transition between para and ortho-H_2O impossible. Thus, H_2O can be treated as two molecules, e.g. para-H_2O and ortho-H_2O, as shown in Fig. 1.5.

For diatomic molecule like CO (see Fig. 1.5 for a sketch of the CO molecule structure), and in the ground vibrational state and the ground electronic state, the rotational energy level is decided by the rotational angular momentum J (energy levels are shown in Fig. 1.5). The rotational selection rules for the heteronuclear diatomic molecules are $\Delta J = \pm 1$ (not counting net spin or orbital angular momentum), while the homonuclear diatomic quadrupole selection rules $\Delta J = \pm 2$. As for the case of CO, the $J = 1 \rightarrow 0$ transition, i.e. CO(1–0), is at 115.271 GHz (see a list of transitions in Table 1.1).

For the polyatomic molecules that include more than two atoms, the situation can be classified into four categories: 1) linear molecules such as HCN, CO_2 and HCO^+; 2) symmetric top molecules such as NH_3 and H_3^+; 3) spherical tops such as CH_4; 4) asymmetric tops such as H_2O and H_2CO. Using three mutually orthogonal moments of inertia, $I_{\boldsymbol{a}}$, $I_{\boldsymbol{b}}$ and $I_{\boldsymbol{c}}$ ($\boldsymbol{a}$, $\boldsymbol{b}$ and $\boldsymbol{c}$ are three mutually orthogonal axes), one can describe the state of a polyatomic molecule. Generally, the moment of inertia is defined by $\sum_i m_i r_i^2$, where m_i is the mass of the $i^{\rm th}$ atom at a distance of r_i from the centre of mass.

This can be further simplified for many linear molecules, where the energy levels can be given by

$$E(J) = \frac{\hbar}{2I} J(J+1), \tag{1.1}$$

in which I is the moment of inertia and J is the rotational level of the molecule. This means that the heavier molecules (whose values of I are large) will have closer energy levels. Selection rules for this kind of molecule is also $\Delta J = \pm 1$. Taking HCN for example, the $J = 1$ to ground level $J = 0$ transition is allowed and can be written as HCN(1–0).

For the case of symmetric top molecules, two of the moments are the same. Thus, either $I_{\boldsymbol{a}} < I_{\boldsymbol{b}} = I_{\boldsymbol{c}}$ (prolate) or $I_{\boldsymbol{a}} = I_{\boldsymbol{b}} < I_{\boldsymbol{c}}$ (oblate) can describe the state of a molecule. The energy level can thus be written as

$$E(J,K) = \frac{\hbar}{2I_{\boldsymbol{a}}} J(J+1) + \frac{\hbar}{2}\left(\frac{1}{I_{\boldsymbol{a}}} - \frac{1}{I_{\boldsymbol{b}}}\right) K^2, \tag{1.2}$$

which is characterised by the angular momentum J and its projection on the symmetry axis, i.e. K. The corresponding selections rules are $\Delta K = \pm 0$ and $\Delta J = \pm 0, \pm 1$.

As for spherical top molecules like CH_4, three moments of inertia, $I_{\boldsymbol{a}}$, $I_{\boldsymbol{b}}$ and $I_{\boldsymbol{c}}$, are equal but have no dipole moments, resulting the transitions between two rotational levels to be weak.

Another category of molecules, asymmetric tops are nonlinear rotors. The value of I_a, I_b and I_c are all different, thus the energy levels are computed using numerical methods. To describe the energy level of such a molecule, one needs the angular momentum J and its projection on the a and c principal axes (see the sketch of H_2O molecule in Fig. 1.5), K_a and K_c. Accordingly, the energy can be expressed as $E(J, K_a, K_c)$, and the quantum numbers can be written as $J_{K_a K_c}$. The election rules depend on the components of the permanent dipole moment μ along the principal axes a, b and c: when $\mu_a \neq 0$, the selection rules are $\Delta K_a = \pm 0, \pm 2, \pm 4, ...$, $\Delta K_c = \pm 1, \pm 3, \pm 5, ...$; when $\mu_b \neq 0$, the selection rules are $\Delta K_a = \pm 1, \pm 3, \pm 5, ...$, $\Delta K_c = \pm 1, \pm 3, \pm 5, ...$; when $\mu_c \neq 0$, the selections rules are $\Delta K_a = \pm 1, \pm 3, \pm 5, ...$, $\Delta K_c = \pm 0, \pm 2, \pm 4, ...$ For all the three cases, $\Delta J = \pm 0, 1$. Take the most important asymmetric top molecule, H_2O, for example. The transition of ortho-H_2O from energy level 5_{23} to 5_{14} is allowed, which is written as $H_2O(5_{23}–5_{14})$, corresponding to a frequency of 1410.618 GHz. As we mentioned previously, ortho-H_2O and para-H_2O can be treated as two molecules. For ortho-H_2O, the value of $K_a + K_c$ is odd, while for the para-H_2O, $K_a + K_c$ is even.

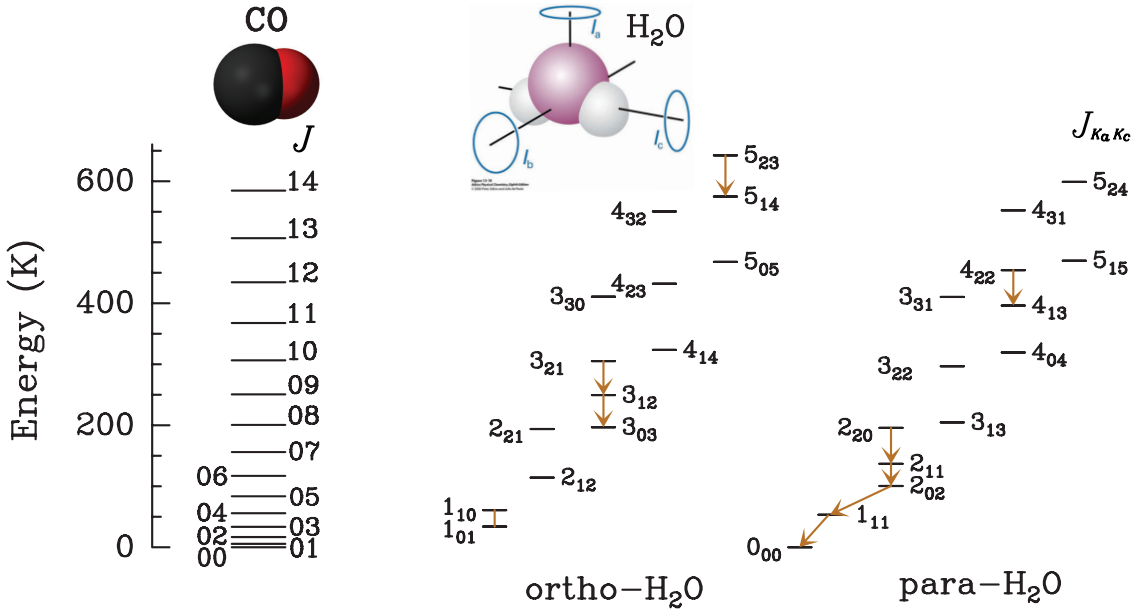

Fig. 1.5 The energy levels of CO and H_2O molecules, together with their quantum numbers J and $J_{K_a K_c}$. The upper sketches show the structure of the CO and H_2O molecules. The three axes of the H_2O molecule are also indicated. Yellow arrows show the eight brightest H_2O rotational lines that are detected in local galaxies (Yang et al., 2013).

1.2.1.2 Line radiative transfer

The transition between different rotational energy levels of molecules can happen with several processes: mainly interactions with photons and collisions with other atoms, molecules and electrons. In short, the excitation can be either radiative or collisional. Fig. 1.6 shows a cartoon comparing collisional excitation with radiative excitation. The molecule can jump from a lower rotational energy to a higher one by colliding with another gas particle (mainly H in the atomic gas and H_2 in the molecular gas) or by a photon with an energy equal to the energy difference between the two rotational energy levels. Then the molecule can jump back to the lower energy levels by emitting photons. This radiative de-excitation is determined by the Einstein A-coefficient. Take CO molecule for example, the excitation through collisions with H_2 and

the following de-excitation can be expressed as:

$$\begin{aligned} \mathrm{CO}(J{=}0,\ {}_1) + \mathrm{H_2} &\longrightarrow \mathrm{CO}(J{=}2) + \mathrm{H_2}, \\ \mathrm{CO}(J{=}2) &\longrightarrow \mathrm{CO}(J{=}1) + h\nu, \end{aligned} \tag{1.3}$$

for the collisional processes, and

$$\begin{aligned} \mathrm{CO}(J{=}1) + h\nu &\longrightarrow \mathrm{CO}(J{=}2), \\ \mathrm{CO}(J{=}2) &\longrightarrow \mathrm{CO}(J{=}1) + h\nu, \end{aligned} \tag{1.4}$$

for the radiative excitation. The corresponding CO line for Eqs.1.3 and 1.4 is CO(2–1).

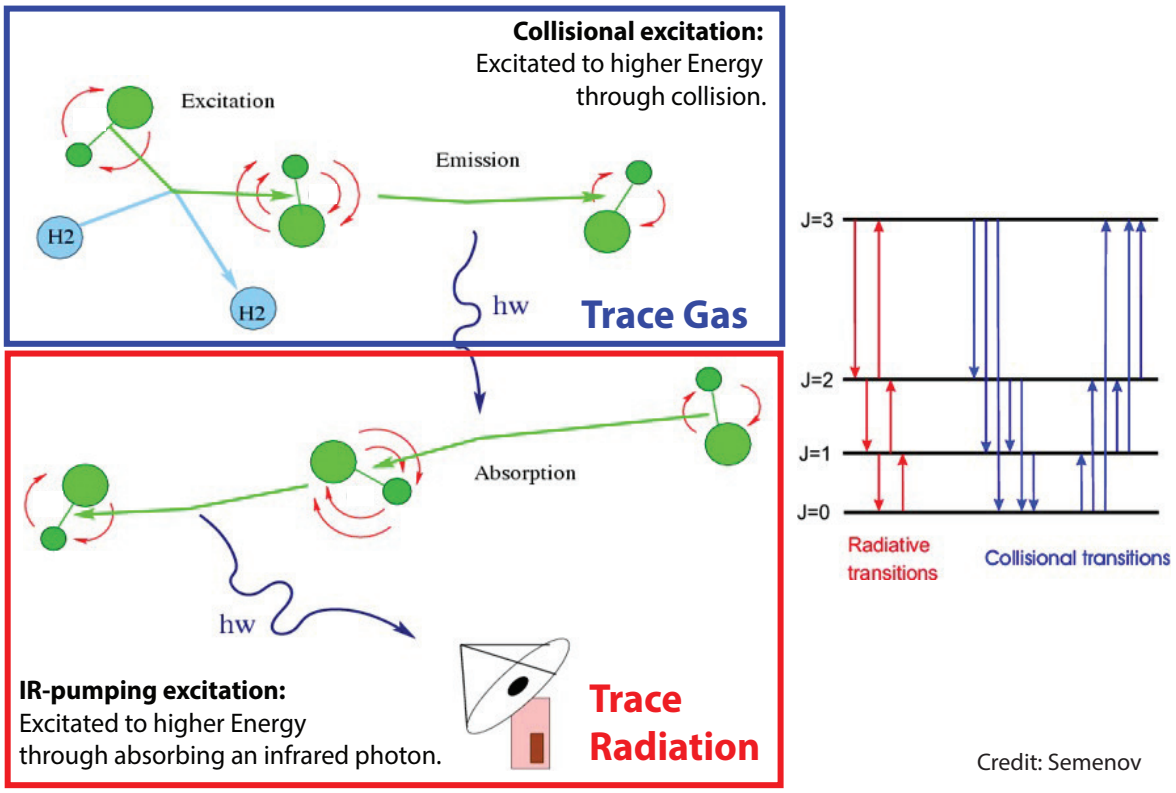

Fig. 1.6 A cartoon showing a comparison between collisional excitation and radiative excitation of a diatomic molecule. The left panel shows the process of excitation and de-excitation while the right panel shows the energy level diagram and the transitions shown in the left panel.

To further quantify the permitted transition between different energy levels, one needs the Einstein coefficients. Taking a two-level system as an example, as shown in Fig. 1.7, the upper and lower level energies are E_{U} and E_{L}, respectively. For an atom/molecule transitioning from an upper (U) to a lower (L) energy state, the spontaneous emission coefficient A_{UL} describes the photon spontaneous emission rate per second, while the absorption coefficient B_{LU} and the stimulated emission coefficient B_{UL} quantify the processes of absorption and stimulated emission.

Considering a system with a large number of atoms/molecules, the number of particles per unit volume in the upper energy state U is n_{U} and n_{L} is the number for the particles in the lower state L. Then,

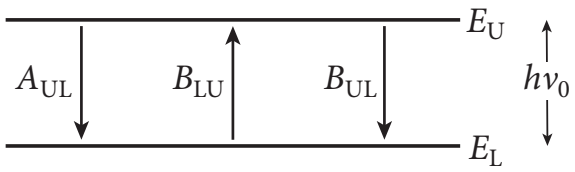

Fig. 1.7 Figure adapted from (Condon & Ransom, 2016) showing a sketch of a two-level system (upper level U and lower level L). The three Einstein coefficients are A_{UL} for spontaneous emission, B_{LU} for absorption, and B_{UL} for stimulated emission. E_U and E_L are the upper and lower level energies. $h\nu_0$ is the photon energy that equals to $E_U - E_L$.

because of the balance between emission and absorption, in the absence of collisions we can have

$$n_U A_{UL} + n_U B_{UL} \bar{u} = n_L B_{LU} \bar{u}, \tag{1.5}$$

in which $\bar{u}$ is the profile-weighted mean radiation energy density because of the finite width of the spectral line profile (so that $B_{UL}\bar{u}$ and $B_{LU}\bar{u}$ equal the average rate per second at which the photons are emitted/absorbed by a single particle). If we consider now the collisional excitation/de-excitation, using the C_{UL} and C_{LU} to describe the possibilities of the collisional excitation transition, Eq. 1.5 becomes

$$n_U A_{UL} + n_U B_{UL} \bar{u} + n_U C_{UL} = n_L B_{LU} \bar{u} + n_L C_{LU}. \tag{1.6}$$

For a system that has a well-defined temperature on a scale much greater then the free mean path of a photon, it is said to be in local thermodynamic equilibrium (LTE). That well-defined temperature is the kinetic temperature T_k related to the Maxwellian speed distribution of the particles. Nevertheless, in general, the energy levels will not be in LTE (non-LTE). It is thus instructive to quantify T_{ex} by

$$\frac{n_U}{n_L} \equiv \frac{g_U}{g_L} \exp\left(-\frac{h\nu_0}{kT_{ex}}\right), \tag{1.7}$$

where g_U and g_L are the statistical weights of the energy states E_U and E_L, respectively. k is the Boltzmann constant. T_{ex} quantify the ratio of n_U to n_L. Observationally, whether the molecular line appears in absorption or emission depends on the value of the excitation temperature, T_{ex} comparing with the background temperature T_{bg}: if $T_{ex} > T_{bg}$, the line will be seen in emission and the line appears in absorption if $T_{ex} < T_{bg}$. For collisional excitation, this excitation temperature can depend on the critical density, at which the excitation balances spontaneous de-excitation, of a particular transition. The critical density can be written as

$$n_{crit,UL} \equiv \frac{A_{UL}}{\Sigma_{i \neq U} \gamma_{Ui}}, \tag{1.8}$$

where γ_{Ui} is the collision rate coefficient from level U to level i (e.g. Tielens, 2005). Table 1.1 shows the critical densities (n_{crit}) of CO lines calculated by assuming a gas temperature $T_k = 100$ K, an ortho to para ratio of H_2 of 3 and an optically thin regime.

A special case of the transition happens when the upper energy level is overpopulated as,

$$\frac{n_U}{n_L} > \frac{g_U}{g_L}, \tag{1.9}$$

then from Eq.1.7, we can then derive that $T_{ex} < 0$. This gives a negative net line opacity, namely that the brightness will gain instead of decrease. This phenomenon is called maser (microwave amplification by

stimulated emission of radiation) at radio wavelengths (see reviews by e.g. Elitzur, 1992; Lo, 2005; Reid & Moran, 1981). The most commonly detected astrophysical masers include OH masers and H_2O masers.

Table 1.1 Basic information about the CO rotational lines.

Molecule	Transition $J_U \rightarrow J_L$	ν_{rest} (GHz)	E_{up}/k (K)	A_{UL} (s^{-1})	n_{crit} (cm^{-3})
CO	$1 \rightarrow 0$	115.271	5.5	7.20×10^{-8}	2.4×10^{2}
	$2 \rightarrow 1$	230.538	16.6	6.91×10^{-7}	2.1×10^{3}
	$3 \rightarrow 2$	345.796	33.2	2.50×10^{-6}	7.6×10^{3}
	$4 \rightarrow 3$	461.041	55.3	6.12×10^{-6}	1.8×10^{4}
	$5 \rightarrow 4$	576.268	83.0	1.22×10^{-5}	3.6×10^{4}
	$6 \rightarrow 5$	691.473	116.2	2.14×10^{-5}	6.3×10^{4}
	$7 \rightarrow 6$	806.652	154.9	3.42×10^{-5}	1.0×10^{5}
	$8 \rightarrow 7$	921.800	199.1	5.13×10^{-5}	1.5×10^{5}
	$9 \rightarrow 8$	1036.912	248.9	7.33×10^{-5}	2.1×10^{5}
	$10 \rightarrow 9$	1151.985	304.2	1.00×10^{-4}	2.9×10^{5}
	$11 \rightarrow 10$	1267.014	365.0	1.34×10^{-4}	3.9×10^{5}

Note: The frequencies (ν_{rest}), upper level energies (E_{up}/k) and Einstein A coefficients are taken from the LAMDA database (Schöier et al., 2005). The collision rate coefficients are from Yang et al. (2010). We assume the gas temperature $T_k = 100$ K, and an ortho-H_2 to para-H_2 ratio of 3 and an optically thin regime for calculating the critical densities here.

To summarise, through observing the multiple transitions of the molecular gas tracers such as CO, one can in principle derive a rich information about the physical conditions of the ISM such as the density and temperature of the molecular gas, if the molecules are collisionally excited. If radiative excitation is involved, one can also infer information about the surrounding radiation fields, by observing the lines. We will further discuss the implications of such kind in high-z SMGs in the next section.

1.2.2 Probing the physical properties of the ISM in high-z SMGs

Because high-z SMGs are highly dust-obscured, it is difficult or impossible in most situations to observe them with optical/near-infrared (NIR) telescopes that probe their stellar content. On the other hand, thanks to the magical power of the negative K-correction (see Section 1.1) at submm/mm, the dust continuum emission at submm and molecular lines are the most efficient way to study star formation in high-z SMGs.

Molecular gas serves as the direct fuel of star formation (Leroy et al., 2008; Schruba et al., 2011). The linear correlation found between the dense molecular gas and the star formation rate from the dense cores of galactic clouds (Wu et al., 2005) to ULIRGs (Gao et al., 2007; Gao & Solomon, 2004) has shown that the dense molecular phase traced by HCN is directly linked to star formation. Therefore, investigating the molecular gas and dust content in those high-z SMGs is the key to understand the conditions of star formation, the nature of SMGs and how they fit into the big picture of galaxy evolution. Such high-sensitivity observations at submm/mm bands are now technically feasible thanks to the Atacama Large Millimetre/submillimetre Array (ALMA) and IRAM's northern extended millimetre array (NOEMA) (Fig. 1.8). ALMA, currently contains fifty 12 m dishes in the 12-m array and twelve 7 m dishes plus four 12 m dishes in the compact array, provides continuum and spectral line capabilities from ~ 0.3 mm to 3.6 mm, with

angular resolutions from ~ 0.02" to 3.4". NOEMA, currently contains 9 15 m dishes, equipped with state-of-the-art high-sensitivity receivers, provides continuum and spectral line capabilities from ~ 0.8 mm to 3.6 mm, with angular resolutions from ~ 0.4" to 3.6".

Fig. 1.8 Photos of ALMA and NOEMA (credit: ESO and IRAM).

Molecular gas tracers are among the most important means through which we understand the nature of these high-z SMGs. The observations of the cool molecular gas traced by low energy levels and low critical density gas tracers, such as low-J lines and the two [CI] fine-structure lines (CI $^3P_1 \rightarrow {}^3P_0$ at 492.2 GHz and CI $^3P_2 \rightarrow {}^3P_1$ at 809.3 GHz, [CI](1–0) and [CI](2–1) hereafter, respectively) are able to provide a rich set of information about the galaxies where they reside. Because those molecular gas lines trace the bulk of the total molecular gas of the SMGs, from the emission/absorption line profiles, one can have insights into the dynamics of the galaxies. One can even be able to reveal the kinematical structure of the SMGs given enough spatial resolution (achievable with submm/mm interferometers), e.g. a rotating disk (e.g. Dye et al., 2015) or a dissipative merger system (e.g. Tacconi et al., 2008). With only unresolved single-dish observations, those linewidths can provide estimates of the dynamical masses (Bothwell et al., 2013b, however one needs to assume whether the source is a major merger or a rotating disk, which can lead to very different results).

The flux of the CO(1–0) line is also a powerful/standard tool to derive the total mass of molecular gas in galaxies by assuming that the molecular gas mass is proportional to the luminosity of the CO(1–0) line, $L'_{\rm CO(1-0)}$ (in unit of K km s^{-1} pc^2) which can be derived following Solomon & Vanden Bout (2005)

$$L'_{\rm CO(1-0)} = 3.25\times10^7 S_{\rm CO}\Delta v \nu_{\rm obs}^{-2} D_{\rm L}^2 (1+z)^{-3} \tag{1.10}$$

where $S_{\rm CO}\Delta v$ is the velocity-integrated flux in Jy km s^{-1}, $\nu_{\rm obs}$ is the observed frequency in GHz, $D_{\rm L}$ is the luminosity distance in Mpc and z is the redshift. The molecular gas mass can then be derived through a conversion factor $\alpha_{\rm CO}$ such as $M_{\rm H_2} = \alpha_{\rm CO} L'_{\rm CO(1-0)}$, where $M_{\rm H_2}$ is the mass of molecular hydrogen and

α_{CO} is the conversion factor to convert observed CO line luminosity to the molecular gas mass without helium correction (this factor may also be written as X_{CO} depending on the units, see Bolatto et al. 2013 for a review). This method is commonly used in extragalactic studies. Nevertheless, the value of the CO to H_2 conversion factor α_{CO} appears to be different in various systems. The determination of α_{CO} is usually achieved by constraining the dynamical mass from the virial mass, or from the measurement of the H_2 gas mass by γ-ray observation or by using a gas to dust mass ratio. For normal local galaxies, the value of this conversion factor measured appears to be within a narrow range (e.g. Donovan Meyer et al., 2013; Leroy et al., 2011; Solomon et al., 1987), $\alpha_{CO} \sim 3$–$6\,M_\odot\,(\mathrm{K\,km\,s^{-1}\,pc^2})^{-1}$. On the other hand, for local ULIRGs (Downes et al., 1993, , $\alpha_{CO} \sim 0.8\,M_\odot\,(\mathrm{K\,km\,s^{-1}\,pc^2})^{-1}$) and high-$z$ SMGs (Tacconi et al., 2008, , $\alpha_{CO} \sim 1\,M_\odot\,(\mathrm{K\,km\,s^{-1}\,pc^2})^{-1}$), the conversion factor appears several times smaller. More recent results for SMGs using the dust to gas mass ratio method and/or the virial mass method found a range of $\alpha_{CO} \sim 0.4$–$2.5\,M_\odot\,(\mathrm{K\,km\,s^{-1}\,pc^2})^{-1}$ (e.g. Bothwell et al., 2017; Hodge et al., 2012; Magdis et al., 2011; Magnelli et al., 2012). Moreover, both observational results (e.g. Genzel et al., 2012; Leroy et al., 2011; Magdis et al., 2011; Wilson, 1995) and theoretical works (e.g. Narayanan et al., 2012) show that the value of α_{CO} depends on the metallicity, which could be a primary source of the variability.

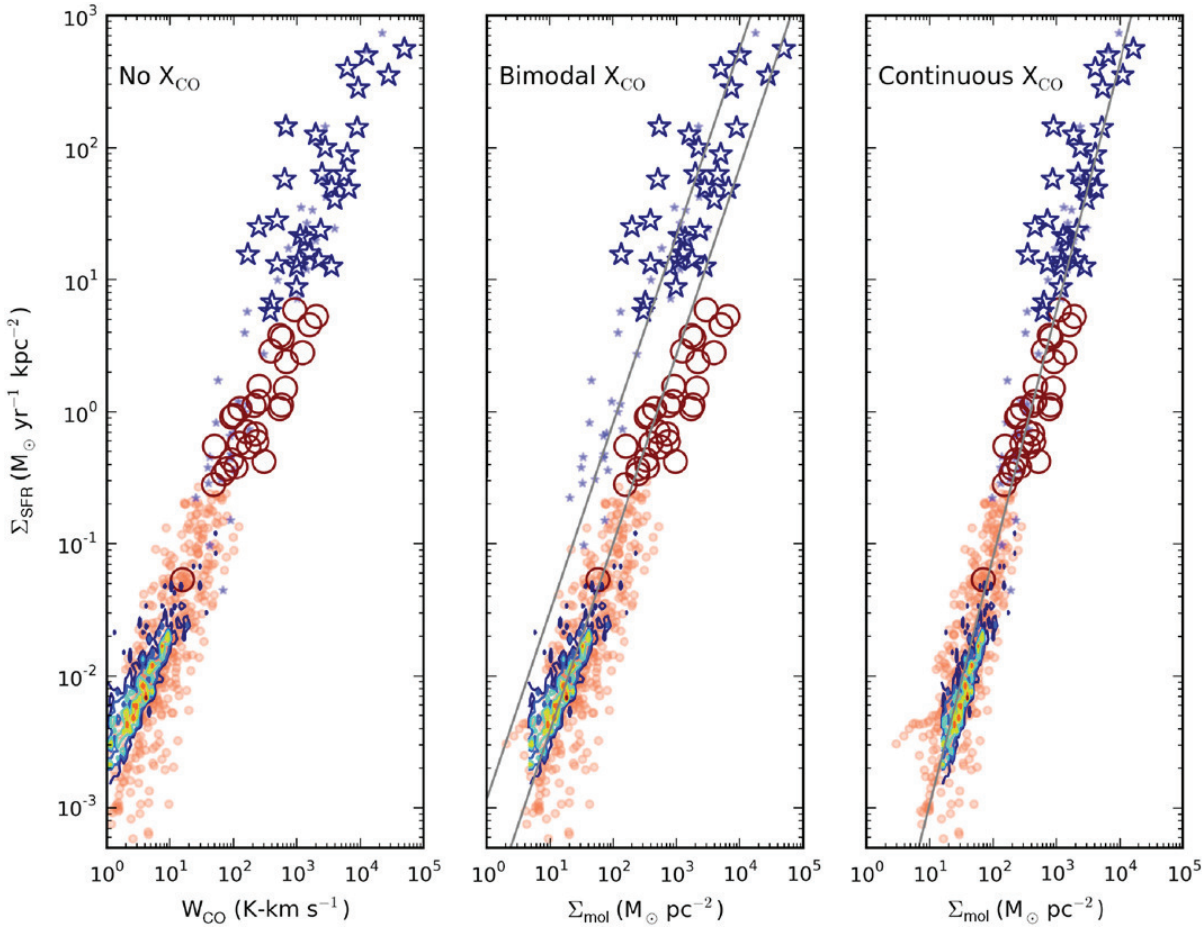

Fig. 1.9 Figure adapted from Casey et al. (2014) showing the Kennicutt–Schmidt (KS) law from local galaxies (orange open circles and small blue stars) to high-z galaxies (red open circles and big blue stars). The colour density contours show the resolved observations from Bigiel et al. (2008). *Left:* Integrated CO line flux plotted against SFR surface density. *Middle:* Molecular gas surface density (converted using a bimodal conversion factor) plotted against SFR surface density. *Right:* Molecular gas surface density (converted using a continuous conversion factor) plotted against SFR surface density.

After deriving the molecular gas mass, the close relation between the surface molecular gas mass and the surface star formation rate (one form of the "Kennicutt–Schmidt (KS) law" for star formation, discovered by Schmidt 1959 and Kennicutt 1998) is again found for the high-z SMGs, as shown by the big blue stars in Fig.1.9. This law is not only an essential input for the theoretical models of galaxy formation and evolution but also an important tool to study the relation between star formation and its fuel. Nevertheless, as mentioned above, by using different values for the conversion factor $\alpha_{\rm CO}$, different conclusions can be drawn from the KS law: by adopting a bimodal $\alpha_{\rm CO}$ (e.g. Daddi et al., 2005), a break in the KS law can be found between the luminous systems and other normal star-forming galaxies, while the relation stays tight if using a single conversion factor. In fact, as mentioned previously, the value $\alpha_{\rm CO}$ of the high-z SMGs can be quite uncertain and is still under debate, though the common adopted values are around $\alpha_{\rm CO} \sim 1$–$0.8\,M_\odot\,(\mathrm{K\,km\,s^{-1}\,pc^2})^{-1}$.

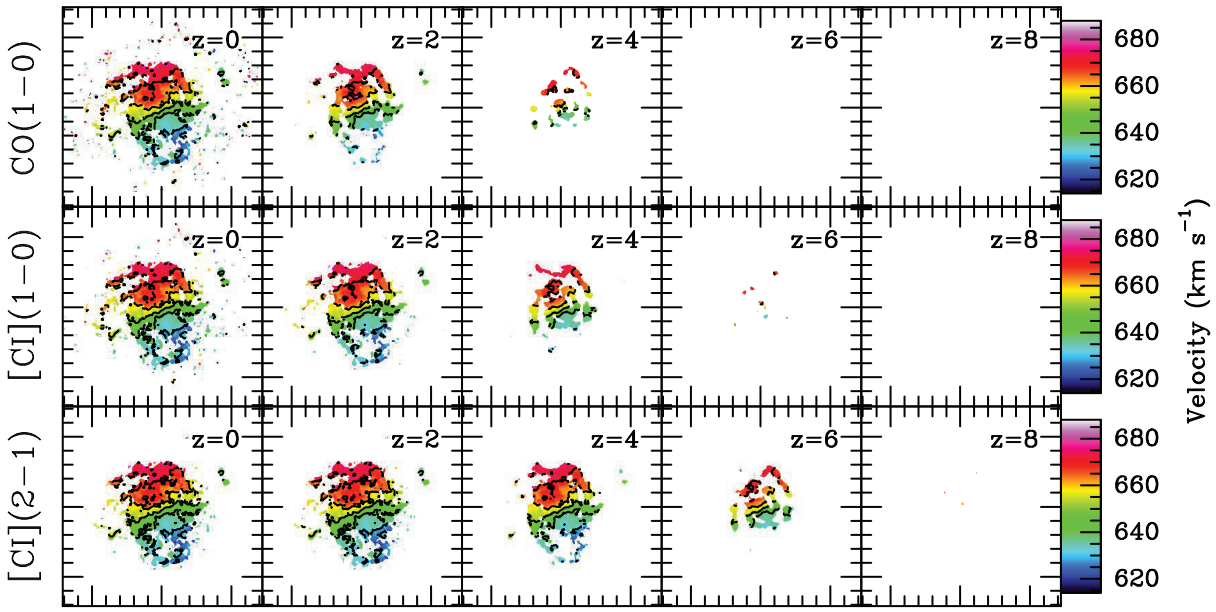

Fig. 1.10 Figure adapted from Zhang et al. (2016) showing the simulated observation results of different gas tracers of a galaxy at different redshifts. It is clear that the CO(1–0) line suffers much more from the CMB comparing to the [CI] lines.

Besides CO(1–0), the ^{3}P fine structure [CI] lines of atomic carbon are also found to be good tracers of the total molecular gas mass. The atomic carbon gas is found to be well-mixed with the bulk of the H_2 gas (e.g. Papadopoulos & Greve, 2004). The [CI] lines likely trace H_2 even more robustly than the low-J CO lines in extreme conditions on galactic scales (e.g. Zhang et al., 2014b). High-redshift observations (e.g. Alaghband-Zadeh et al., 2013; Weiß et al., 2003) also support such an agreement, although Bothwell et al. (2017) recently found that either a larger $\alpha_{\rm CO}$ or a high [CI] abundance is needed to balance the gas mass derived from CO and from [CI] lines. Papadopoulos & Greve (2004) find a good agreement between the total molecular gas mass derived from [CI] and CO lines and dust continuum in local ULIRGs. Since the observations of CO(1–0) lines at high-z become observationally difficult, acquiring the intensities of the [CI] lines, which are usually brighter than the CO(1–0) line and residing in favourable bands for observation, could help us to better determine the total molecular mass in high-z SMGs. Zhang et al. (2016) show that at high-z the CO(1–0) line will also suffer observing against the CMB, making the line to be more difficult to be observed (Fig. 1.10). Moreover, it is also found that CO can be destroyed by the

cosmic rays coming from the intense star-forming activities, leaving the [CI] lines a better tracer of the total molecular gas mass in such environments (Bisbas et al., 2015).

Most importantly, using the integrated fluxes of the molecular lines, we can derive the physical conditions of the molecular gas. As mentioned in Section 1.2.1, the most common excitation mechanism for the CO line ($J_{\rm up} \lesssim 11$) is through collisions with molecular hydrogen. Thus, for high-z SMGs, people usually use the non-local thermodynamic equilibrium (non-LTE) radiative transfer calculations to model the observed CO spectral line energy distributions (SLEDs). Such models take the advantages of a large velocity gradient (LVG, e.g. Goldreich & Kwan, 1974; Scoville & Solomon, 1974; Sobolev, 1960) statistical equilibrium method. One of the most popular radiative transfer code of such kind is `RADEX` that calculates the fluxes of atomic and molecular lines produced in homogeneous clouds (van der Tak et al., 2007). From such models, the physical conditions of the molecular gas, such as gas density, gas temperature and the column density of the gas tracer, can be derived. Fig. 1.11 shows examples of different CO SLEDs generated by different conditions of the molecular gas.

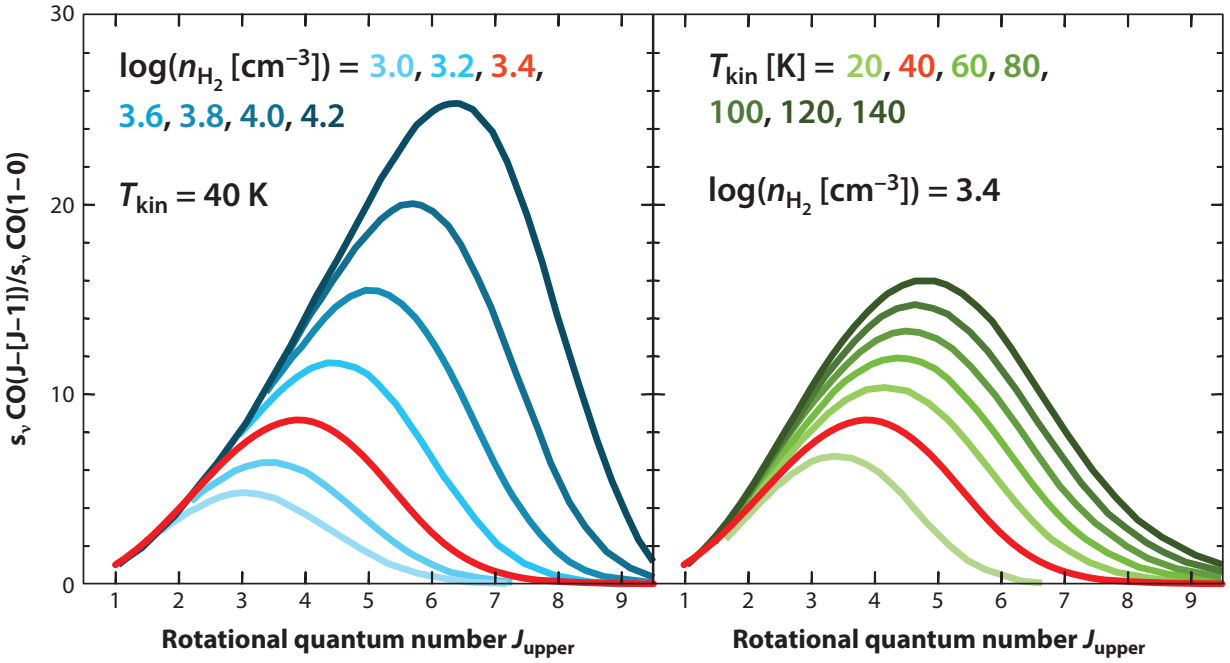

Fig. 1.11 Figure adapted from Carilli & Walter (2013) showing the CO SLEDs derived from different physical conditions shown in the legends. *Left:* The CO SLEDs based on a fixed gas temperature of 40 K and a varying gas density from $10^{3.0}$ cm^{-3} to $10^{4.2}$ cm^{-3}. *Right:* The CO SLEDs based on a fixed gas density of $10^{3.4}$ cm^{-3} and a varying gas temperature from 20 K to 140 K.

The CO SLED for high-z SMGs shows a variety of shapes, with the peak mostly located above $J_{\rm up} \gtrsim 4$ as shown in Fig. 1.12, with thermalised level populations being up to $J_{\rm up} \sim 6$. Comparing to the CO SLED of the SMGs, those of the local starbursts (M 82 and NGC 253) show much weaker excitation. This indicates that the excitation conditions in SMGs are quite extreme. Nevertheless, the CO SLEDs of local ULIRGs also share similarities with those of the SMGs. For the most striking case of HFLS 3 (Riechers et al., 2013), the CO SLED is even comparable to that of the lensed QSO Cloverleaf (Solomon et al., 2003).

Thermal collisional excitation is commonly seen in the ISM, but there are also other excitation mechanisms that influence the molecular line emission/absorption, especially in the extreme ISM environments

like SMGs. Shocks[2] can be a significant way to excite the molecular gas as found in NGC 6240 through analysis of the CO SLEDs (Meijerink et al., 2013). Strong radiation from active galactic nuclei (AGN) can also excite CO SLEDs, and the signature is usually seen in very high excitation levels ($J_{\rm up} \gtrsim 10$) of the CO lines. Such a signature usually presents a rather flat CO SLED at the high-J end, being different from the SLED generated from other excitation mechanisms. van der Werf et al. (2010) show a good example of a local AGN-dominated ULIRG, Mrk 231, where the $J_{\rm up} \gtrsim 10$ part of the CO SLED is dominated by and X-ray dominated region related to the central AGN. As mentioned in Section 1.2.1, gas tracers, such as the submm H_2O lines, can be dominated by far-IR pumping, especially for the $E_{\rm up} \gtrsim 200$ K lines (e.g. González-Alfonso et al., 2014, 2010; Omont et al., 2013; Yang et al., 2013, 2016). Because the excitation of the H_2O lines comes from both collisional (dominating the lines with $E_{\rm up} \lesssim 150$ K), and also from far-IR, the H_2O SLED will thus help us to understand not only the physical properties of the molecular gas but also the far-IR radiation field, namely the properties of dust emission. Thus, the H_2O lines become a unique probe for studying the ISM in high-z SMGs.

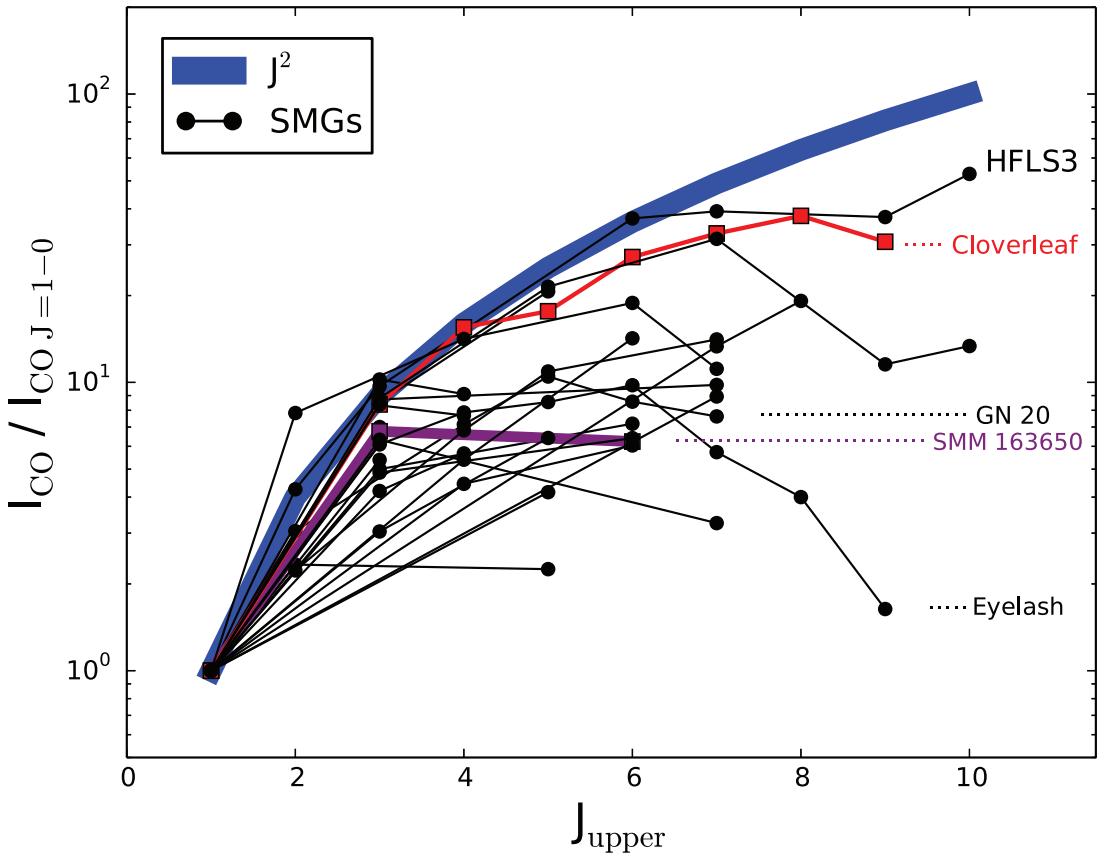

Fig. 1.12 Figure adapted from Narayanan & Krumholz (2014) showing the CO SLEDs from different SMGs as indicated by the black dots. Red data points show the lensed QSO, Cloverleaf, while the violet line shows SMM 163650. The blue stripe shows the Rayleigh–Jeans limit assuming local thermodynamic equilibrium (LTE). See Narayanan & Krumholz (2014) for references.

[2]Shock wave is defined by a pressure-driven disturbance propagating faster than the sound velocity. In such cases, the upstream material cannot dynamically respond to the upcoming material, resulting in an irreversible change. The two main types of shocks happen in the gas phase ISM are J-shock and C-shock. For the former, the properties of the ISM appear as a jump from the preshock front to the postshock front. While for the latter, the shock front is much thicker than the cooling length scale, the jump condition is no longer available.

1.2.3 Important chemical processes revealed by the molecular lines

Chemistry is another important prospective for the ISM, that describes the formation, destruction and excitation of molecules in astronomical environments. The subject not only includes the chemical aspects of molecules, but also influences the diagnostics of the physical conditions, since the chemical reactions, especially those happening in the gas-phase ISM, are closely related to the radiation field and/or the ionization states.

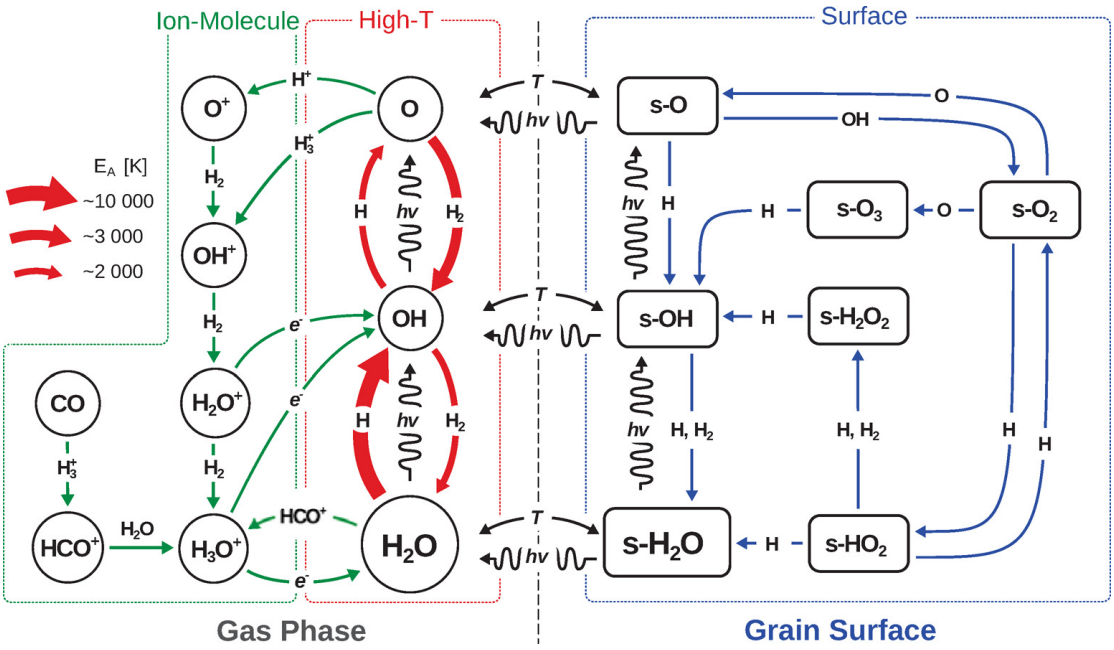

Fig. 1.13 The formation routes and related chemical reactions of H_2O molecules as described in the text. Figure adapted from van Dishoeck et al. (2013).

Take H_2O for example, as shown in Fig. 1.13, H_2O can be formed through both solid-state and gas-phase chemical reactions (van Dishoeck et al., 2013). On dust-grain mantles (shown in blue colour in the figure), surface chemistry dominates the formation of H_2O molecules. Then they can be released into the gas phase ISM through sublimation. While in the gas phase, H_2O can be produced through two routes: the neutral-neutral reaction (shown in red colour in the figure), usually related to shocks, creates H_2O via $O + H_2 \longrightarrow OH + H$; $OH + H_2 \longrightarrow H_2O + H$ at high gas temperature. At lower gas temperature, the ion-neutral reactions (shown in green colour) in photon-dominated regions (PDRs), cosmic-ray-dominated regions and X-ray-dominated regions (e.g. Meijerink & Spaans, 2005) generate H_2O from O, H^+, H_3^+ and H_2, with intermediates such as O^+, OH^+, H_2O^+ and H_3O^+, and finally $H_3O^+ + e \longrightarrow H_2O + H$. Thus, the H_2O^+ lines can be among the most direct tracers of the cosmic-ray or/and X-ray ionization rate (e.g. Gérin et al., 2010; González-Alfonso et al., 2013; Neufeld et al., 2010) of the ISM. Recent detections of H_2O^+ lines in extragalactic environments (van der Tak et al., 2016; Yang et al., 2016) show rich information about the dominating chemical process and also the ionisation states.

1.3 Studying the SMGs through the cosmic telescope: gravitational lensing

1.3.1 Basic principles of gravitational lensing

The physical phenomenon called gravitational lensing was first raised by Einstein (1936), showing that the travelling path of the photons from distant objects can be perturbed by the inhomogeneously distributed matter along their trajectories, being much like photons passing through lenses, but from the effect of gravity (gravitational lensing). In the real cases, such an effect is usually minor, and it slightly distorts the appearance of the source. This mild effect is called weak gravitational lensing (e.g. Bartelmann & Schneider, 2001). In rare cases, the foreground gravity potential (usually formed by massive galaxies or galaxy clusters) is strong enough to produce multiple images, arcs, or even Einstein rings (see Fig. 1.14 for an illustration). This is called strong gravitational lensing. We will briefly describe some basic principles of lensing in the following paragraphs.

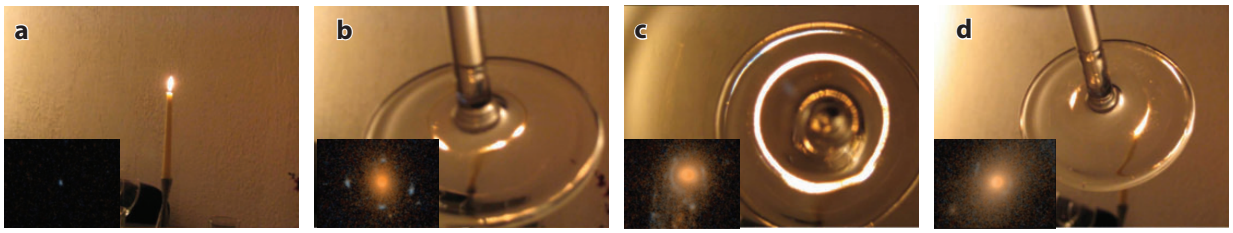

Fig. 1.14 Figure adapted from Treu (2010) (image courtesy of P. Marshall) displaying an optical analogy of the gravitational lensing phenomenon. The optical properties stem of a wineglass share similarities with the galaxy-type deflectors. The analogies are: a) viewing a distant object directly; b) multiple images in observed in the image plane; c) an Einstein ring; d) two arcs in the image plane. The corresponding astrophysical real images (Moustakas et al., 2007) are also shown in the lower left corner of each insets.

A typical gravitational lens system is shown in Fig. 1.15. The mass over-density (deflector) resides at redshift $z_{\rm d}$, corresponding to an angular diameter distance of $D_{\rm d}$. The background lensed object emits photons at redshift $z_{\rm s}$, corresponding to a distance of $D_{\rm s}$. The distance between the source and the deflector is $D_{\rm ds}$ (note that because the distance is not additive, $D_{\rm ds} \neq D_{\rm s} - D_{\rm d}$). After defining the observation axis indicated by the dashed line in the figure, we find two planes perpendicular to our observation axis: the source plane where the background source emission can be described and the lens plane that characterises the mass distribution of the deflector. Then, we can write the position of a source at the angular position $\vec{\beta}$ as $\vec{\eta} = \vec{\beta} D_{\rm s}$. The deflection angle is $\vec{\alpha}$ while the angle of the source in the image plane is $\vec{\theta}$. Due to the deflection of the light emitted by the background object, the observer receives the light coming from the source from $\vec{\beta}$ as if it was emitted at the angular position $\vec{\theta}$ (corresponding to an impact parameter $\vec{\xi} = \vec{\theta} D_{\rm d}$). If $\vec{\alpha}$, $\vec{\beta}$ and $\vec{\theta}$ are small, we can describe the relation of these three angles using the angular diameter distance as,

$$\vec{\theta} D_{\rm s} = \vec{\beta} D_{\rm s} + \vec{\alpha} D_{\rm ds}. \tag{1.11}$$

By defining the angular diameter distance between the deflector and source as $\vec{\alpha}(\vec{\theta}) = (D_{\rm ds}/D_{\rm s})\vec{\alpha}(\vec{\theta})$, we can further rewrite Eq. 1.11 into

$$\vec{\beta} = \vec{\theta} - \vec{\alpha}(\vec{\theta}), \tag{1.12}$$

which is usually called *lens equation*. When this equation has multiple solutions corresponding to multiple images, strong lensing occurs. The most common configurations of such kind of strong lensing are shown

in Fig. 1.14. In such systems, the strong-lensing cross section is defined by the solid angle in the source plane that produces multiple images. If we define ψ as the two-dimensional lensing potential, the *Jacobian* of the transformation from image to the source plane can be written as

$$A = \frac{\partial \vec{\beta}}{\partial \vec{\theta}} = \delta_{ij} - \frac{\partial^2 \psi}{\partial \vec{\theta}_i \partial \vec{\theta}_j} = \begin{pmatrix} 1-\kappa-\gamma_1 & -\gamma_2 \\ -\gamma_2 & 1-\kappa+\gamma_1 \end{pmatrix} = (1-\kappa)\begin{pmatrix} 1 & 0 \\ 0 & 1 \end{pmatrix} - \gamma \begin{pmatrix} \cos 2\phi & \sin 2\phi \\ \sin 2\phi & -\cos 2\phi \end{pmatrix}, \tag{1.13}$$

where κ describe the convergence of the image (Fig. 1.14), which is also called dimensionless surface mass density

$$\kappa(\vec{\theta}) \equiv \frac{\Sigma(D_d \vec{\theta})}{\Sigma_{\rm cr}} \quad \text{with} \quad \Sigma_{\rm cr} = \frac{c^2}{4\pi G} \frac{D_{\rm s}}{D_{\rm d} D_{\rm ds}}, \tag{1.14}$$

where is the critical surface mass density that defines the chacteristic scale for the occurrence of strong lensing features likes arcs and multiple images. While γ describes the shear, which has two shear components γ_1 and γ_2 that

$$\gamma \equiv \gamma_1 + \mathrm{i}\gamma_2 = |\gamma| \, \mathrm{e}^{2\mathrm{i}\phi}, \tag{1.15}$$

which have

$$\begin{pmatrix} \gamma_1 & \gamma_2 \\ \gamma_2 & \gamma_1 \end{pmatrix} = \gamma \begin{pmatrix} \cos 2\phi & \sin 2\phi \\ \sin 2\phi & \cos 2\phi \end{pmatrix}. \tag{1.16}$$

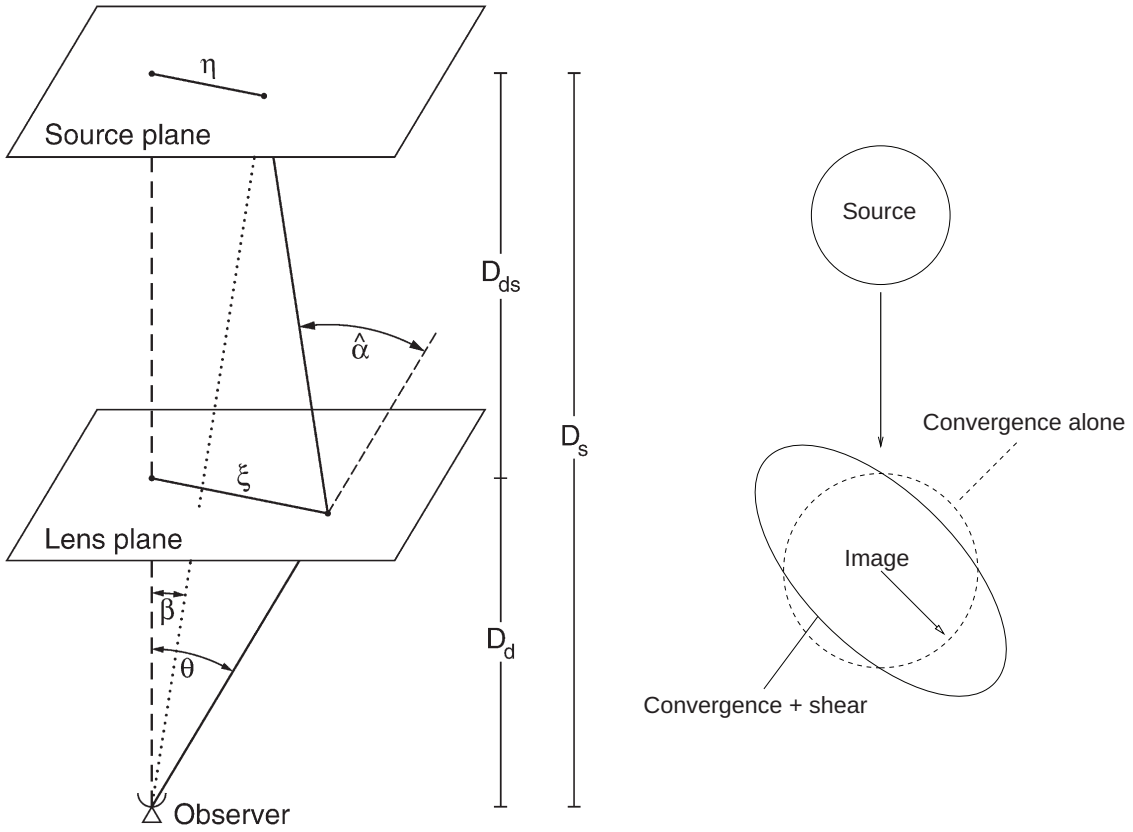

Fig. 1.15 *Left:* Figure adapted from Bartelmann & Schneider (2001) displaying a sketch of a typical gravitational lensing system (see text for descriptions). *Right:* Sketch showing the effect of convergence and shear adapted from Umetsu (2010).

The inverse of the determinant of the *Jacobian* matrix gives the magnification, as

$$\mu = \frac{1}{\det A} = \frac{1}{(1-\kappa)^2 - |\gamma|^2} \tag{1.17}$$

In the cases of extended sources, the magnification also depends on the distribution of the surface brightness of the background source. The magnification μ reflects the increase of total emission area, corresponding to the total amplification of its integrated flux.

In Eq. 1.17, the locations (satisfying $1-\kappa = \pm\gamma$) for which $\det A = 0$ have infinite magnification. The corresponding source plane positions are the *caustics*, while these locations are called *critical curves* in the image plane. However, in the real astronomical practice, the finite object size keeps its observed magnification finite, which is usually a few up to more than one hundred for a typical galaxy-galaxy lensing system (e.g. Meylan et al., 2006).

Strong gravitational lensing is a powerful tool for not only studying the mass structure of the foreground deflector, the geometry of the Universe, but also offering precious opportunities to observe the weak background source, by magnifying its flux by up to more than an order of magnitude, and its size by a smaller factor. This offers a cosmic telescope that helps us to detect emission from the background source that is beyond our observation limits. It can also help us to understand the mass structure of the foreground source and to test models of the Universe's geometry. Our work thus takes advantage of strong gravitational lensing to focus on the emission from the background source, by first searching for a sample of lensed candidates using large survey data and then performing follow-up observations of the molecular gas and dust in the SMGs. The related description of the survey and the source selection are given in Sections 2.1 and 2.2.

1.3.2 Studies of the high-redshifted strongly-lensed SMGs

Although strong gravitational lensing offers a powerful tool for studying the high-redshift universe, the surface density of such kind of sources is very low. Depending on the observation depth, current telescopes can usually achieve detection of strong lensing at a rate of ~ 1 out of 1000 galaxies (Marshall et al., 2005). The observations of the ISM of such strongly lensed galaxies at high-redshift therefore limited, and usually in those brightest systems. Such systems include the famous gravitationally lensed quasar/AGN-dominated sources, Cloverleaf (e.g. Barvainis et al., 1994; Bradford et al., 2009; Weiß et al., 2003), APM 08279+5455 (e.g. Downes et al., 1999; Lewis et al., 1998; Riechers et al., 2009; Weiß et al., 2007) and IRAS F10214+4724 (e.g. Broadhurst & Lehar, 1995; Downes et al., 1992; Rowan-Robinson et al., 1991).

A detailed study of a lensed submm bright galaxy at $z = 2.8$, SMM 02399-0136, was presented by Ivison et al. (1998). Frayer et al. (1998) report the CO detection in a $z = 2.8$ submm-selected bright galaxy SMM 02399-0136, with an SFR $\sim 10^3\ M_\odot$. Later, the same team has discovered another similar galaxy, SMM J14011+0252, having a similar total molecular gas mass and SFR (Frayer et al., 1999). All the three sources were selected in a submm survey using SCUBA through lensing clusters (Smail et al., 1998). The massive molecular gas reservoirs indicate the link of these galaxies to the present day massive elliptical galaxies. One of the most remarkable cases of the strongly lensed sources discovered in the field of such massive galaxy clusters is SMM J2135-0102 (Swinbank et al., 2010). The $z = 2.3$ source has been magnified by a factor of 32, which offers a unique opportunity for a detailed study of the physical properties of the source. The source thus has been observed intensively using the ground-based telescopes like GBT, NOEMA, APEX, and SMA (Danielson et al., 2011). Fig. 1.16 shows the observed spectra of the CO, [C I], and

HCN lines. By analysing the CO line excitation of the source, Danielson et al. (2011) show that the source share similarity in the CO excitation condition as in local starburst galaxies. The CO ladder includes at least two phases with different gas densities and temperatures. Combing the lensing magnification, the work shows that the Kennicutt–Schmidt relation breaks down on scales of < 100 pc.

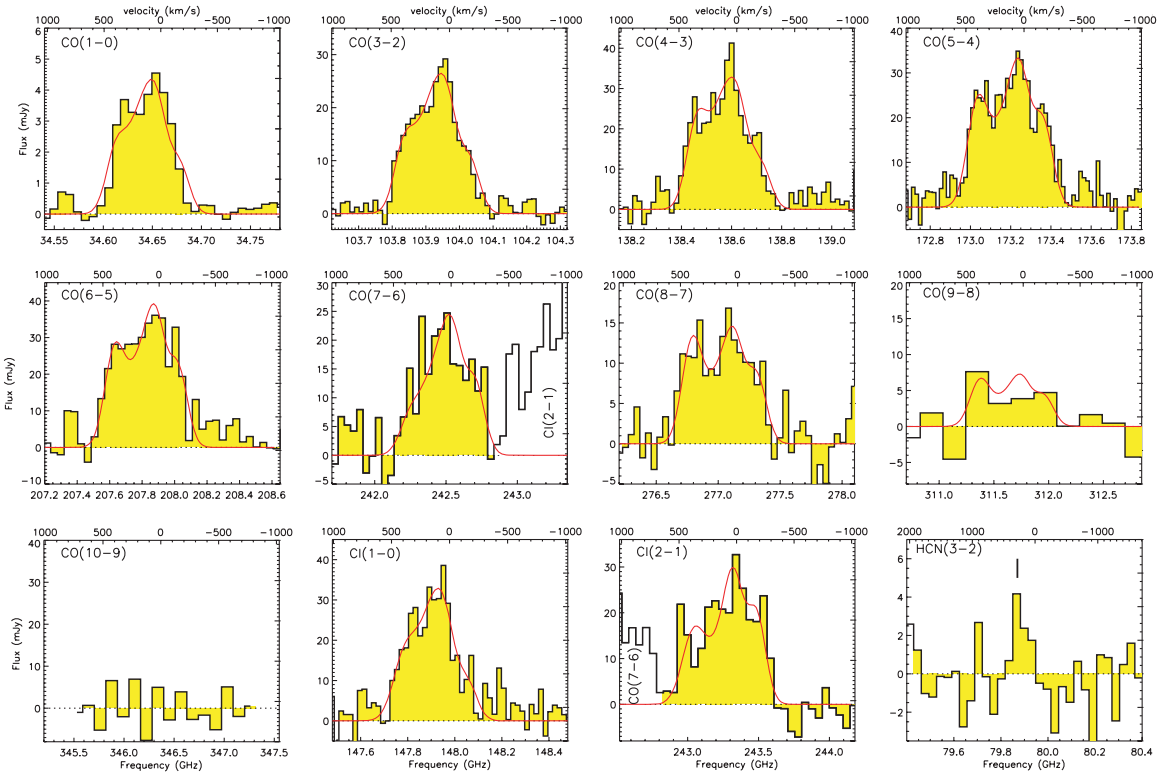

Fig. 1.16 Figure adapted from Danielson et al. (2011) showing the CO, [CI], and HCN line spectral of the source SMM J2135-0102 by GBT, NOEMA, APEX, and SMA.

With the development of efficient selecting the strongly lensed candidates using large area submm surveys (Negrello et al. 2010, 2007, as described in Section 2.1), a large number of lensed candidates were identified. This technique offers new opportunity to study the submm-bright sources, usually with an intrinsic surface SFR around several hundred $M_\odot$ yr^{-1} kpc^{-2}.

One of the examples of such studies include the lensed source discovered by the *Herschel* Astrophysical Terahertz Large Area Survey (*H*-ATLAS, Eales et al., 2010), *H*-ATLAS J114637.9-001132 (Fu et al. 2012, see also other examples by e.g. Conley et al. 2011; Cox et al. 2011; Gavazzi et al. 2011). Through high-resolution observations of the dust continuum using SMA, KECK K-band imaging and JVLA observation of the CO(1–0) tracing the total molecular gas, the work reveals that the system is a gas-rich starburst galaxy similar local ULIRGs and other unlensed SMGs. The total molecular gas mass contributes ~ 68% visible baryonic mass. There is also a ~ 4 kpc separation between the spatial location of the stellar component and that of the dust and molecular gas. Such an offset has also been found in other high-redshift lensed SMGs (e.g. Dye et al., 2015).

The most stunning example is shown by the high-resolution ALMA images of the source SDP 81 (*H*-ATLAS J090311.6+003906) as further described in Chapter 5. With the help of boosted brightness and spatial resolution, these images allow us to study the high-redshift galaxy in unprecedented detail.

1.4 Thesis outline

In this thesis, I will present a series of works focused on the molecular gas, from the observational perspectives, in a sample of strongly gravitationally lensed SMGs. By studying mostly H_2O and CO lines, we learn the physical conditions of the star-forming molecular gas content and also the thermal dust emission properties. Through the analysis of these properties, we have gained a better view of the star formation conditions/processes within these SMGs.

In Chapter 2, I will briefly describe our sample selection. Then I will present the work on H_2O line observations in the SMGs in Chapter 3. Chapter 4 shows our multiple-J CO and [CI] line observations, from which we study the properties of the bulk of molecular gas properties. The high angular-resolution study of two SMGs via ALMA and NOEMA extended configurations is presented in Chapter 5. In the end, the thesis work is summarised in Chapter 6 together with prospectives.

Chapter 2

Source selection

You behold Atlas supporting the whole of heaven.

Propertius, Elegies

2.1 Identifying the strongly lensed candidates

The key to study the SMGs through strong gravitational lensing is to find an efficient way to identify such systems from large survey data. However, the strong gravitational lensing at submm bands is rare (less than

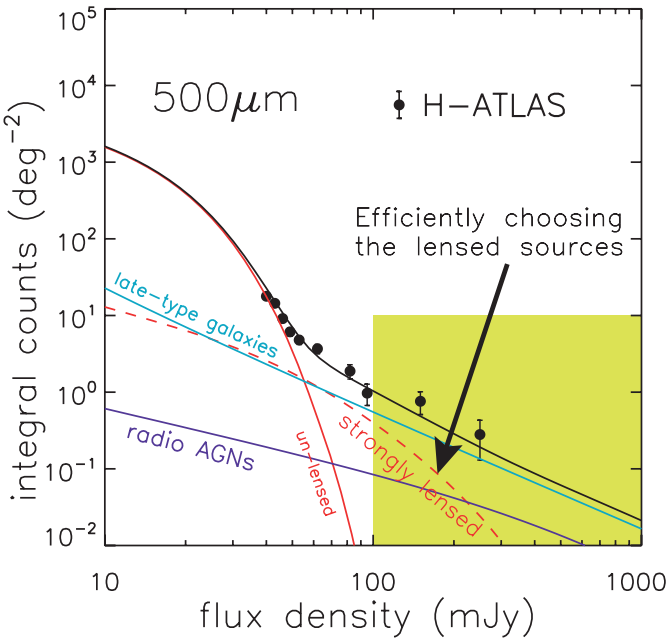

Fig. 2.1 The 500 μm number counts of different types of galaxies. The solid violet line shows the number counts from radio active galactic nuclei (blazars), while the green one shows that of nearby late-type galaxies. Solid red line shows the number counts of SMGs without lensing, while the dashed red line show the results considering the lensing. The black curve shows the total number counts predicted while the observation data points are derived from the *H*-ATLAS maps. The yellow square shows the region from where lensed candidates can be most efficiently selected. (Figure adapted from Negrello et al. 2010).

0.5 deg^{-2} at 500 μm, e.g. Negrello et al. 2007). Note that the density of lensed SMGs with $S_{500\mu m} > 100$ mJy in this 14 deg^2 *H*-ATLAS SDP field (Negrello et al., 2010) is anomalously high, ~ 0.35 deg^{-2}, while the average density of lens candidates in the 550 deg^2 of the *H*-ATLAS survey is only 0.13 deg^{-2} (Negrello et al., 2017). The measured number counts of a submillimeter map can be compared with predictions from models for SMGs. It is found that the gravitationally lensed SMGs make up a significant fraction around the bright-end of the number counts at submm bands. As shown in Fig. 2.2, without strong lensing, the number counts of SMGs have a steep decrease towards ~ 90 mJy with a surface density of $\sim 10^{-2}$ deg^{-2}, one can place a cut-off of the number counts around 100 mJy, namely nearly no SMGs can be found above this flux level. Then the lensing effect will boost the number of bright sources, as shown in the dashed red line in Fig. 2.2. Nevertheless, there can also be contaminations from other galaxies species, although their numbers are not dominating at fainter-end. Thanks to the negative *K*-correction, the SMGs appear to be the dominating kind of galaxies submm-detected in the high-z universe. Once using a flux cut at 500 μm of $\sim$ 90–100 mJy, one can simply select lensed candidates. For detected sources from 500 μm maps, contamination from

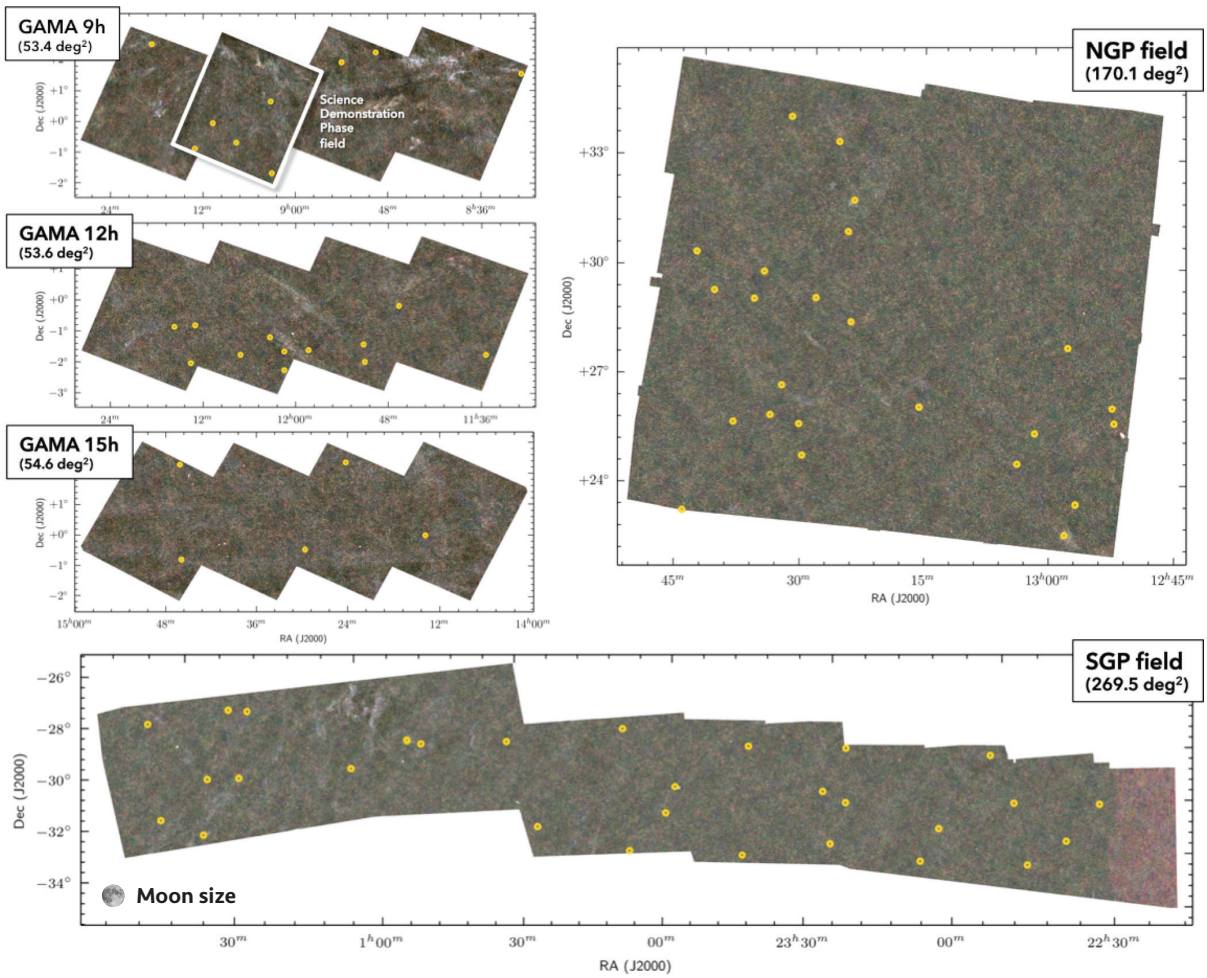

Fig. 2.2 Figure adapted from Negrello et al. (2017) displaying the lens candidates with $S_{500\mu m} > 100$ mJy in the whole regions of the *H*-ATLAS survey. The real size of the Moon is also indicated in the bottom figure.

radio AGN (mostly blazars) and late-type galaxies is easy to be identified. Therefore, such observations at submm bands are extremely efficient to discover lensed candidates. Previous follow-up observations have demonstrated that such a simple method can be used to identify gravitationally lensed SMGs with an efficiency better than 90% at 500 μm (e.g. Negrello et al., 2017, 2010; Wardlow et al., 2013).

Thanks to the extra-galactic surveys at submm and far-IR (corresponding to rest-frame far-IR wavelengths) bands like the *H*-ATLAS (sky area shown in Fig. 2.2, Eales et al., 2010), the *Herschel* Multi-tiered Extragalactic Survey (*Her*MES, Oliver et al., 2012) and the South Pole Telescope (SPT) survey (Vieira et al., 2013), large and statistically significant samples of strongly lensed SMGs have been built. Our work is mainly based on the sample selected from *H*-ATLAS maps (see Valiante et al. 2016 for a description of the catalogue).

2.2 *H*-ATLAS survey and the source selection

The *H*-ATLAS is the largest key astronomical project awarded on *ESA*'s *Herschel* Space Observatory as an Open Time survey. A 600 hr observation time was awarded for surveying the submm sky area with $\sim 600\,\mathrm{deg}^{-2}$ (Fig. 2.2, Eales et al., 2010; Valiante et al., 2016). The survey covers 5 bands with PACS and SPIRE from 100 μm to 500 μm in fast parallel mode. The resolution at 250 μm reaches around 18".

In order to find the strongly lensed SMGs, all of our targets were selected from the phase-I *H*-ATLAS catalogue (Valiante et al., 2016) with a criterion of $S_{500\,\mu\mathrm{m}} > 100$ mJy based on theoretical models of the submm source number counts (e.g. Negrello et al., 2017, 2010). Then, a Submillimeter Array (SMA) subsample as shown in Fig. 2.3 was selected based on the availability of previously spectroscopically confirmed redshifts obtained by CO observations (Bussmann et al., 2013, hereafter Bu13). It includes all high-z *H*-ATLAS sources with $F_{500\,\mu\mathrm{m}} > 200$ mJy in the GAMA and NGP fields ($\sim 300\,\mathrm{deg}^2$). From SMA 880 μm images and the identification of the lens deflectors and their redshifts, Bu13 have built lensing models for most of them.

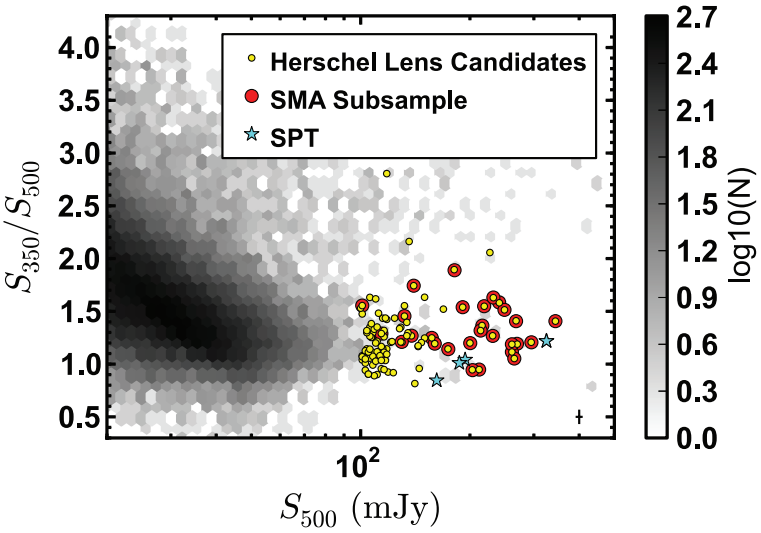

Fig. 2.3 The photometric flux-density ratio versus flux-density of the *H*-ATLAS catalog. Yellow points show the sources selected with the flux-cut criteria mentioned above. The dots with red circle show the SMA subsample studied by Bussmann et al. (2013). And the cyan stars show a comparison of a few lensed SPT-discovered SMGs. Figure adapted from Bussmann et al. (2013).

Our sample of 17 SMGs from $z \sim 1.6$ to $z \sim 4.2$ was thus extracted from Bussmann et al. 2013's *H*-ATLAS-SMA sources with the initial goal of studying their H_2O emission lines. The sources were selected primarily based on flux-cut and also on their H_2O-line observational availability. We list the *H*-ATLAS coordinates and measured far-IR, submm and radio flux densities of the sample in Table 2.2 (see also Tables 1 and 2 of Omont et al. 2013 and Yang et al. 2016). All the sources in our sample have a 500 μm flux density above 170 mJy, and the sample is practically complete above 200 mJy in the $\sim 300\,\mathrm{deg}^2$ of the *H*-ATLAS GAMA and NGP fields. The 880 μm magnification range from 2 up to 15. The previous measured CO redshifts (see Table 2.2) allowed us to perform follow-up observations of various gas tracers from the SMGs.

Table 2.1 Basic properties of the SMG sample in this work.

Source	IAU-name	RA (deg)	DEC (deg)	$z_{\rm spec}$	ref	S_{250} (mJy)	S_{350} (mJy)	S_{500} (mJy)	S_{880} (mJy)	$S_{1.4\rm GHz}$ (mJy)
G09v1.97	H-ATLAS J083051.0+013224	08:30:51.02	+01:32:24.88	3.634	R-p	260 ± 7	321 ± 8	269 ± 9	85.5 ± 4.0	<0.45
G09v1.40	H-ATLAS J085358.9+015537	08:53:58.9	+01:55:37.0	2.0923	R-p	389 ± 7	381 ± 8	241 ± 9	61.4 ± 2.9	0.75 ± 0.15
SDP17b	H-ATLAS J090302.9-014127	09:03:03.02	−01:41:26.9	2.3051	L12	347 ± 7	339 ± 8	219 ± 9	54.7 ± 3.1	<0.51
SDP81	H-ATLAS J090311.6+003906	09:03:11.61	+00:39:06.7	3.042	F11	138 ± 7	199 ± 8	174 ± 9	78.4 ± 8.2	0.61 ± 0.16
SDP9	H-ATLAS J090740.0-004200	09:10:43.061	−00:03:22.76	1.577	L12	471 ± 7	343 ± 8	181 ± 9	24.8 ± 3.3	1.07 ± 0.14
SDP11	H-ATLAS J091043.1-000321	09:07:40.05	−00:41:59.5	1.786	L12	417 ± 6	378 ± 7	232 ± 8	30.6 ± 2.4	<0.51
G12v2.43	H-ATLAS J113526.3-014605	11:35:26.36	−01:46:05.56	3.1276	H12	290 ± 7	295 ± 8	216 ± 9	48.6 ± 2.3	<0.45
G12v2.30	H-ATLAS J114637.9-001132	11:46:37.99	−00:11:32.0	3.2592	H12	290 ± 6	356 ± 7	295 ± 8	86.0 ± 4.9	<0.42
NCv1.268	H-ATLAS J125135.4+261457	12:51:35.46	+26:14:57.52	3.675	K-p	145 ± 7	201 ± 8	212 ± 9	78.9 ± 4.4	1.10 ± 0.15
NCv1.143	H-ATLAS J125632.7+233625	12:56:32.70	+23:36:24.86	3.565	R-p	214 ± 7	291 ± 8	261 ± 9	97.2 ± 6.5	0.61 ± 0.16
NAv1.195	H-ATLAS J132630.1+334410	13:26:30.12	+33:44:09.90	2.951	H-p	179 ± 7	279 ± 8	265 ± 9	65.2 ± 2.3	<0.42
NAv1.177	H-ATLAS J132859.3+292327	13:28:59.29	+29:23:27.07	2.778	K-p	264 ± 9	310 ± 10	261 ± 10	50.1 ± 2.1	<0.45
NBv1.78	H-ATLAS J133008.4+245900	13:30:08.56	+24:58:58.3	3.1112	R-p	273 ± 7	282 ± 8	214 ± 9	59.2 ± 4.3	0.67 ± 0.20
NAv1.144	H-ATLAS J133649.9+291801	13:36:50.00	+29:17:59.6	2.2024	H12	295 ± 8	294 ± 9	191 ± 10	36.8 ± 2.9	<0.42
NAv1.56	H-ATLAS J134429.4+303036	13:44:29.518	+30:30:34.05	2.3010	H12	481 ± 9	484 ± 13	344 ± 11	73.1 ± 2.4	1.12 ± 0.27
G15v2.235	H-ATLAS J141351.9-000026	14:13:52.092	−00:00:24.43	2.4782	H12	190 ± 7	240 ± 8	200 ± 9	33.3 ± 2.6	<0.59
G15v2.779	H-ATLAS J142413.9+022303	14:24:13.90	+02:23:04.0	4.243	C11	115 ± 19	308 ± 47	220 ± 34	90.0 ± 5.0	<0.46

Note: RA and DEC are the J2000 coordinates from *Herschel*/SPIRE image coordinates in Valiante et al. 2016, i.e. the *Herschel*-ATLAS survey results. $z_{\rm spec}$ is the redshift inferred from previous CO detection as reported by C11: Cox et al. (2011), F11: Fu et al. (2012), H12: Harris et al. (2012), L12: Lupu et al. (2012), H-p: Harris et al. (in prep.), K-p: Krips et al. (in prep.), R-p: Riechers et al. (in prep.). F_{250}, F_{350} and F_{500} are the *Herschel* SPIRE flux densities at 250, 350 and 500 μm, respectively (Valiante et al., 2016); F_{880} is the 880 μm SMA flux density (Bu13); $f_{1.4\rm GHz}$ is the 1.4 GHz band flux density from the VLA FIRST survey (Becker et al., 1995), and we use 3 σ as upper limits for non-detections.

Chapter 3

H_2O and its related ionic and isotope molecules in the high-redshift SMGs

Water is the driver of nature.

Leonardo da Vinci

3.1 Introduction and Background

3.1.1 H_2O observations in the Milky Way and nearby galaxies

As described in Chapter 1, water is one of the most important molecules in the Universe. In the standard Λ-CDM cosmology picture (Planck Collaboration et al., 2014), hydrogen and oxygen are the first and third most abundant elements in our present universe. In the gas phase ISM, after H_2, H_2O is the most abundant molecule together with CO in the ISM of galaxies. While it remains mostly locked up in icy grains (in solid phase) in the cold molecular ISM, it can be desorbed into gas phase in certain conditions (see e.g. van Dishoeck et al., 2013).

Comparing with other gas tracers like CO, HCN, CH, CN, OH, CS, etc., the observations of H_2O lines was much limited due to mostly the earth atmosphere (see e.g. Omont, 2007; Williams & Viti, 2013). The water vapour within the earth atmosphere is generating rich emission and absorption features that block our sight of observing the H_2O lines in our Milky Way and nearby galaxies. However, There are a few atmospheric windows which allow us to observe some of the H_2O lines in the local universe using ground-based telescopes, like the first detection of $H_2O(6_{16}–5_{23})$ ($E_{up}/k \sim 700$ K) maser line at 22 GHz in the Galaxy by Cheung et al. (1969). This maser line was identified to be a good tracer of star-forming regions and the highly excited post-main sequence circumstellar gas. Since that, several H_2O maser lines were studied: $H_2O(3_{13}–2_{20})$ at 183 GHz (Gonzalez-Alfonso et al., 1995), $H_2O(4_{14}–3_{21})$ at 380 GHz (Phillips et al., 1980), $H_2O(10_{29}\text{-}9_{36})$ at 321 GHz (Menten et al., 1990a) and $H_2O(5_{15}–4_{22})$ at 325 GHz (Menten et al., 1990b). However, these maser lines only trace small scales of several tens of AU. Until recent years, we still lacked knowledge of the non-maser emitting H_2O gas at larger scales.

To observe the bulk of H_2O gas in the universe, we could either use space telescopes that operate above the atmosphere, or observe the H_2O lines at high-z so that the lines could be redshifted within certain atmospheric windows to be observed on the ground. For the former kind of studies, people started around

1995, after the launch of the *Infrared Space Observatory* (ISO, Kessler et al., 1996). ISO was working on the bands from 2 μm to 200 μm. It could detect not only the rovibrational H_2O lines at 2.5 μm to 45 μm using its Short Wavelength Spectrometer (SWS) but also rotational absorption lines at longer wavelength using its Long Wavelength Spectrometer (LWS). Using the LWS instrument on ISO, Harwit et al. (1998) detected eight H_2O lines in the Orion BN-KL region, and they argue that those H_2O lines are generated mostly by C-shocks. Using the shock model, they find a H_2O abundance to be 5×10^{-4}. Besides, Ceccarelli et al. (2002) also detected a rich set of far-IR H_2O absorption lines in Sgr B2 that offer information on the physical properties of the molecular gas. Later, other space projects targeted especially on the H_2O lines were also launched, such as the Submillimeter Wave Astronomy Satellite (SWAS, Melnick et al., 2000) and Odin (Hjalmarson et al., 2003), due to higher spatial resolution comparing with ISO, these two space telescopes have a better view of the submm H_2O lines in our Galaxy. Nevertheless, due to technical limitations, the bandwidth and spectral resolution were limited, which made the study of H_2O lines very difficult, especially for the objects at greater distances and even more extragalactic environments.

The situation was dramatically changed with the launch of the *Herschel* Space Observatory (*Herschel* hereafter) in 2009. Unlike its precursors, both the spatial and spectral resolution and the sensitivity were much improved (Pilbratt et al., 2010). Thus, *Herschel* offered us a great opportunity to study not only the H_2O lines in the Milky Way, but also in the nearby extragalactic sources. There were three instruments mounted on *Herschel*: Photodetecting Array Camera and Spectrometer (PACS) working at 55 μm–210 μm that mainly performs far-infrared imaging and acquires low spectral resolution spectra (Poglitsch et al., 2010); Spectral and Photometric Imaging Receiver (SPIRE) that works from 194 μm to 627 μm, not only performing imaging at 250, 350 and 500 μm but also gathering spectral data (Griffin et al., 2010); the last instrument is Heterodyne Instrument for the Far-Infrared (HIFI) that acquires high spectral resolution data from 157 μm to 212 μm, and and from 240 to 625 μm.

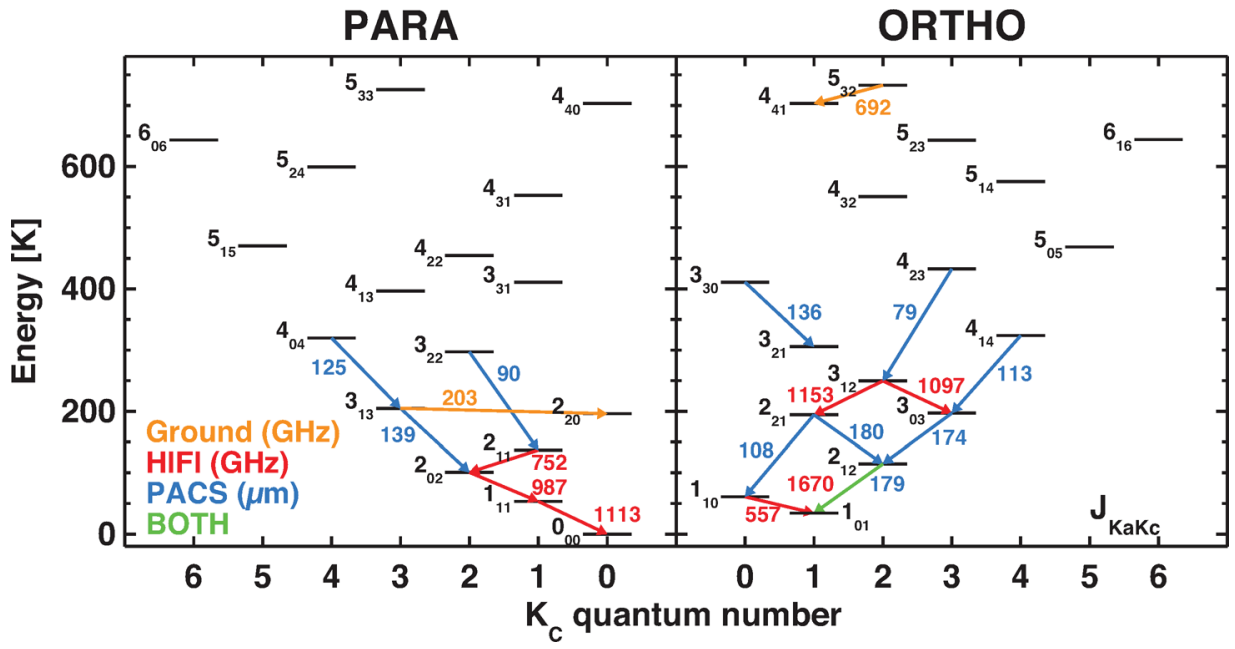

Fig. 3.1 The energy level diagram of the main para- and ortho-H_2O transitions for observations. Figure is adapted from van Dishoeck et al. (2013). See Section 1.2.1.1 for the details of the H_2O quantum number $J_{K_aK_c}$.

There is a rich set of submm molecular lines which are detected by *Herschel*, mostly by SPIRE/FTS, in nearby infrared galaxies ($L_{IR} > 10^{10}\ L_\odot$): e.g. in NGC 4418 (González-Alfonso et al., 2012), NGC 1068

(Spinoglio et al., 2012), NGC 6240 (Meijerink et al., 2013) and M 82 (Kamenetzky et al., 2012). Although those submm H_2O lines are found faint in archetype molecular sources such as Orion PDR or M 82, they can reach an intensity comparable to CO in Milky Way hot cores and in local ULIRGs. The latter, such as Mrk 231 and Arp 220, display a rich spectrum of submm H_2O emission lines up to upper level energies of $E_{up}/k = 642$ K (e.g. Rangwala et al., 2011; van der Werf et al., 2010). Our Herschel archive survey (Yang et al., 2013) shows that most local ULIRGs emit such luminous high-excitation H_2O lines. Indeed, *Herschel* opens a new window for us to study the H_2O in unprecedented details. Besides SPIRE, PACS and HIFI can also covers some H_2O lines, especially absorption lines at higher frequencies. Fig. 3.1 shows the main lines covered by the *Herschel* PACS and HIFI, and also some aforementioned ground maser lines.

Using the *Herschel* SPIRE spectra, González-Alfonso et al. (2010) studied eight submm H_2O emission lines in Mrk 231. They found that the excitation of the H_2O lines with $E_{up}/k > 150$ K are likely dominated by far-IR pumping. As we also discuss in Section 3.3, there are likely two excitation components that are related to the H_2O line excitation. One is an extended relatively cool component that dominates the H_2O lines mostly with $E_{up}/k < 150$ K, and the excitation is collisional, as shown in green colour in Fig. 3.2. Another dominant feature is the warm component that is more compact than the cool component as shown in red colour in Fig. 3.2. The excitation of this component is dominated by far-IR pumping as mentioned in Section 1.2.1. These submm H_2O lines with $E_{up}/k > 150$ K are directly tracing the far-IR radiation field in the star-forming nuclear regions (see also González-Alfonso et al., 2014). Unlike the CO usual lines that are mostly collisionally excited, the H_2O lines provide therefore a unique diagnostic of the dust emission properties of the warm dense gas it resides.

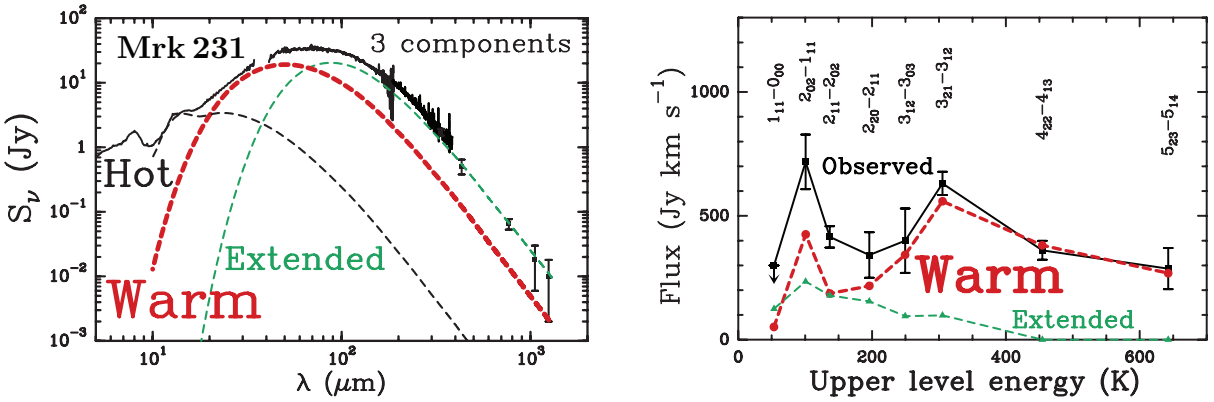

Fig. 3.2 Figures are adapted from González-Alfonso et al. (2010). *Left panel*: dust SEDs generated from the far-IR pumping model for the compact warm (red dashed line), extended cool (green dashed line) and hot core components (black dashed line). The observed dust SED and photometric data are shown in the black solid line and black data points. *Right panel*: The H_2O SLED modelling results for the warm (red) and cool extended (green) component. The observed H_2O fluxes are shown in black data points.

In the work of the first systematic study of submm H_2O lines in local infrared galaxies by Yang et al. (2013), we found that among the 176 galaxies with publicly available FTS data, 45 have at least one H_2O emission line detected. In addition, we also found emission lines of H_2O^+ and $H_2^{18}O$ in the sample. We discovered that H_2O, for most galaxies, is the strongest molecular emitter after CO in the submm domain; the luminosity of the five brightest H_2O lines we observed is near-linearly correlated with L_{IR}, regardless of whether or not strong active galactic nucleus signature is present (Fig. 3.3); although the slope turns out to be slightly steeper when $z \sim 2$–4 ULIRGs are included (greed dots), the correlation is still closely linear. We noticed that the luminosity ratios between H_2O and IR decreases with increasing f_{25}/f_{60} (flux

ratio between 25 μm and 60 μm), but saw no dependence on f_{60}/f_{100}, possibly indicating that very warm dust contributes little to the excitation of the submillimeter H_2O lines. We found the average spectral line energy distribution (SLED) of the entire sample is consistent with individual SLEDs and the IR pumping plus collisional excitation model, showing that the strongest lines are $H_2O(2_{02}–1_{11})$ and $H_2O(3_{21}–3_{12})$.

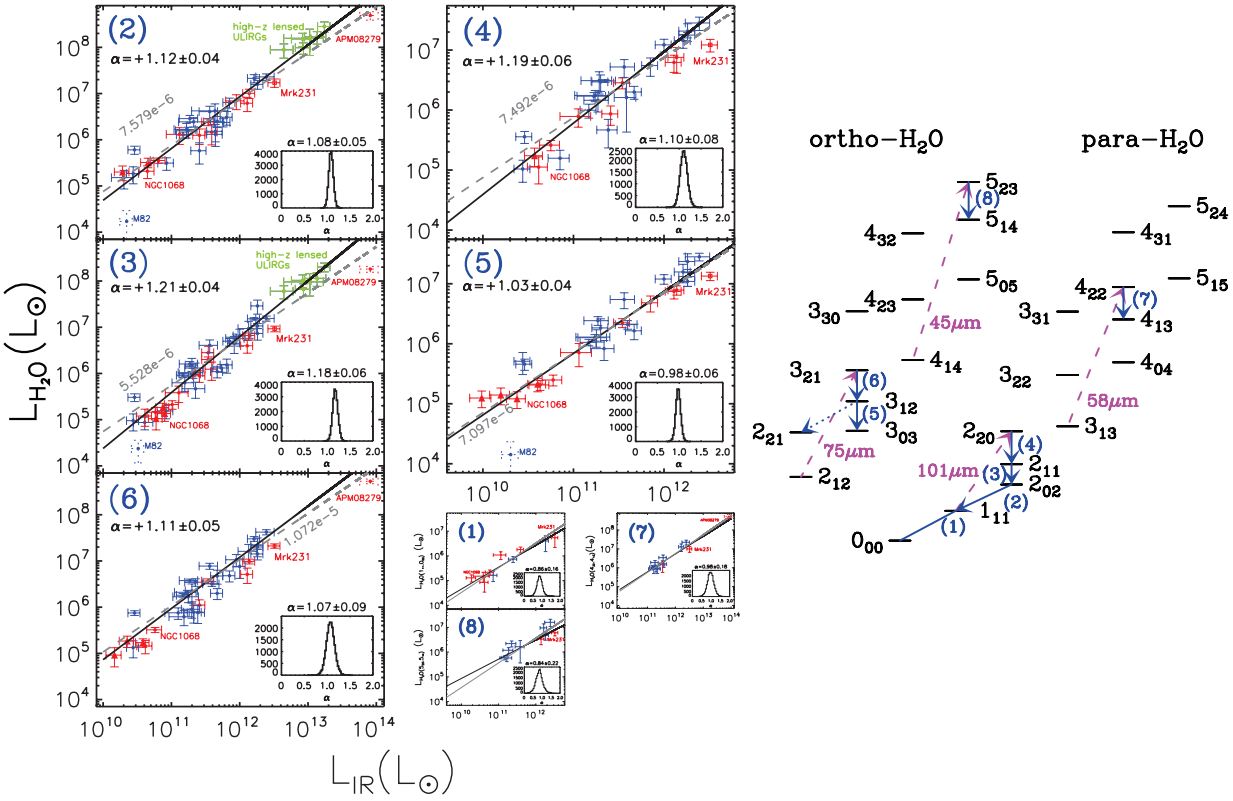

Fig. 3.3 *Left panel*: Figure adapted from Yang et al. (2013). Correlation between L_{H_2O} and the corresponding L_{IR} for local infrared galaxies. The grey lines are the linear fitting with a fixed slope ($\alpha = 1$). The red, blue, green, and black dots represent strong-AGN, H II+mild-AGN-dominated galaxies, high-z ULIRGs, and the upper limits for non-detections, respectively. The solid triangles are the mapping mode data of NGC 1068. Mrk 231 is marked in red squares. M 82 and APM 08279+5255, marked with dashed error bars, are excluded from the fitting. *Right panel*: The energy level diagram (see Section 1.2.1) indicating the eight transitions we observed. Pink dashed lines show the FIR-pumping paths and the blue arrows show the observed transitions.

3.1.2 High-z studies of the H_2O lines

As mentioned in the previous Chapter 3.1, another way to observe the rest-frame submm H_2O lines is to go to the Universe at high-z. At redshift higher than ~ 2, the H_2O lines will be redshifted into mm atmospheric windows so that they can even be observable using the ground-based telescopes. Nevertheless, due to the great distances, normally such detections can be only achieved in the most luminous systems, e.g. QSOs and high-z (Hy)ULIRGs. Since submm H_2O lines are strong in local ULIRGs, similar processes must be present in high-z ULIRGs, which are much more numerous and often more luminous than local ones.

Indeed, efforts have been put to observe H_2O lines in most luminous systems at high-z. Since our first detection of submm H_2O in a lensed *Herschel* source, SDP17b, at $z = 2.3$ (Omont et al., 2011) using the IRAM NOrthern Extended Millimeter Array (NOEMA), several individual detections at high-z have

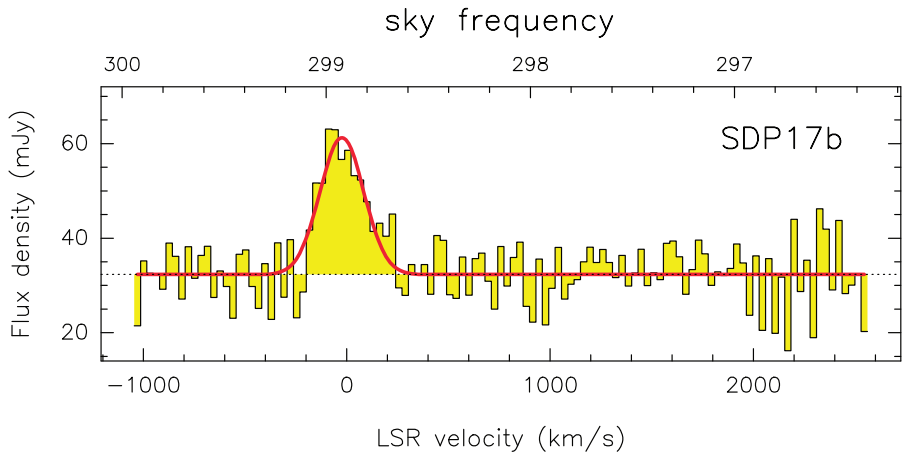

Fig. 3.4 The first detection of submm H_2O ($H_2O(2_{02}–1_{11})$ emission line) line in a lensed SMG at high-z reported by Omont et al. (2011). The detection shows an integrated line flux of ~ 7.8 Jy km s^{-1}.

also been reported (ALMA Partnership, Vlahakis et al., 2015; Bothwell et al., 2013a; Bradford et al., 2011; Combes et al., 2012; Lis et al., 2011; Lupu et al., 2012; Omont et al., 2013; Rawle et al., 2014; Riechers et al., 2013; van der Werf et al., 2011; Vieira et al., 2013; Weiß et al., 2013). Most of the detections were achieved in galaxy-galaxy strongly gravitational lensed systems, in which the flux has been boosted and also the spatial resolution has been magnified. These individual detections of H_2O lines in high-z lensed ULIRGs show that the H_2O lines are the strongest submm molecular lines after CO and a unique tool for studying the ISM of these galaxies.

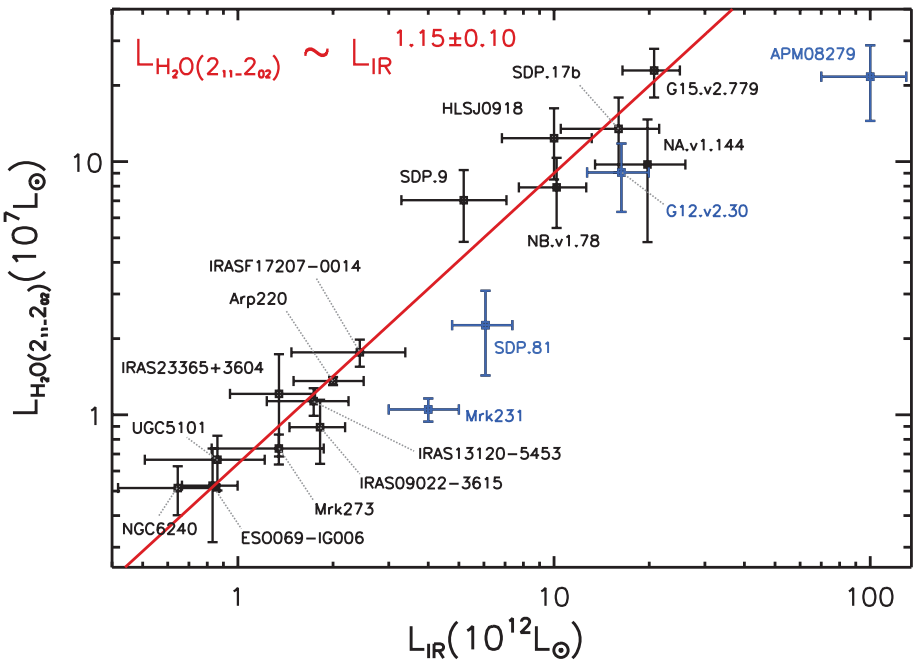

Fig. 3.5 The super-linear correlation between L_{IR} and L_{H_2O} as reported in Omont et al. (2013). The red line shows the fit of the correlation from local ULIRGs to the high-z SMGs. L_{H_2O} increasing very fast following $L_{H_2O} \sim L_{IR}^{1.2}$, which indicates that importance of far-IR pumping to the H_2O line excitation.

After the detection of H_2O in SDP17b, our team proposed a larger survey for the submm H_2O lines in high-z strongly lensed SMGs selected by *Herschel*-ATLAS surveys using mostly NOEMA telescopes. Later,

in Omont et al. (2013), we reported the detection of H_2O lines in six other lensed SMGs. As the first step of our survey, we started from the low frequency lines, e.g. $H_2O(2_{02}–1_{11})$ and $H_2O(2_{11}–2_{02})$. The detected H_2O lines are strong, with integrated line fluxes ranging from 1.8 to 14 Jy km s^{-1}. This work confirms that the submm H_2O lines are among the strongest molecular lines in high-z SMGs, with intensities almost comparable to those of the high-J CO lines. Most striking is the similarity between the linewidth of CO and H_2O. We also found that L_{H_2O} is is strongly depending on L_{IR} as $L_{H_2O} \propto {L_{IR}}^{1.2}$ (Fig. 3.5). This relation is consistent with the local finding that far-IR pumping is playing a key role in the excitation of the H_2O lines, and implies that high-z SMGs with $L_{IR} \gtrapprox 10^{13}\ L_\odot$ are probably the strongest H_2O emitters in the Universe.

Nevertheless, as shown in the modelling work of the submm H_2O lines (González-Alfonso et al., 2014), the $J \geq 3$ H_2O lines are critical for probing the physical properties of the far-IR field that powers the H_2O lines. And the excitation of higher levels remains to be confirmed at high-z by direct observation of those high excitation lines. We therefore proposed a further observation plan for: 1). Expanding our number of detections of $J = 2$ H_2O lines in the lensed SMGs sample; 2). detecting higher energy level of H_2O lines at higher frequencies. For these two reasons, we have conducted a series of sample selections and following-up observations. The resulted sample is 11 $z \sim 2$–4 SMGs. Using NOEMA, we observed 16 H_2O emission lines. In the end, we have efficiently detected 14 of them, including five $H_2O(3_{21}–3_{12})$ lines and nine $J = 2$ para-H_2O lines, either $H_2O(2_{02}–1_{11})$ or $H_2O(2_{11}–2_{02})$. Besides, 4 H_2O^+ lines have also been detected along with the $H_2O(2_{11}–2_{01})$. Their velocity-integrated fluxes are ranging from 2 to 15 Jy km s^{-1}. The similarities in linewidths and fluxes between CO and H_2O indicate that they likely arise from similar regions within the SMGs. With a larger sample size, we confirm again the strong correlations between luminosities of H_2O lines and that of the total infrared, $L_{H_2O} \sim {L_{IR}}^{1.1–1.2}$. This strong correlation suggests a dominant role of far-IR pumping in the H_2O line excitation at high-z, following our findings in local starburst galaxies. We derived the warm dust temperature and H_2O column density using the far-IR pumping model developed by González-Alfonso et al. (2014). We have also found a very tight correlation between the luminosities of the H_2O and H_2O^+line, from local ULIRGs to our high-z SMGs. The line flux ratio indicates that intense cosmic rays generated by strong star formation are possibly driving the oxygen chemistry in the gas-phase ISM.

The detailed work is described in the following Section 3.2. In this work, we have carefully studied a sample of 11 SMGs at redshift ~ 2–4. Together with the submm H_2O-detected sources reported in Omont et al. (2013), we have built a rich H_2O-line-detected (in $J = 2$ and/or $J = 3$ H_2O lines) sample of 16 SMGs. We show that the detection of submm H_2O line is efficient with NOEMA within a reasonable observing time. The H_2O line profile are close to that of the CO, suggesting they are spatially co-located. We also find tight close-to-linear correlation between L_{H_2O} and L_{IR} from local ULIRGs to these high-z SMGs. This indicates the importance of far-IR pumping to the excitation of the H_2O lines. Using the far-IR pumping model, we find that the far-IR radiation fields have warm dust temperature ~ 45–75 K, H_2O column density per unit velocity interval $\sim 10^{15}$ cm^{-2} km^{-1} s and 100 μm continuum opacity $\tau_{100} > 1$ (optically thick). This shows that H_2O lines trace the warm dense gas that may be closely related to the active star formation. Along with the H_2O lines, several H_2O^+ lines have also been detected in three of our high-z SMGs. After including local infrared galaxies that have H_2O^+ detections (Yang et al., 2013), we find a tight correlation between L_{H_2O} and $L_{H_2O^+}$. The flux ratio between H_2O^+ and H_2O suggests that cosmic rays from strong star forming activities are possibly driving the related oxygen chemistry.

3.2 Publication (Published in A&A)

A&A 595, A80 (2016)
DOI: 10.1051/0004-6361/201628160

Astronomy & Astrophysics

Submillimeter H_2O and H_2O^+ emission in lensed ultra- and hyper-luminous infrared galaxies at $z \sim 2$–4★,★★

C. Yang (杨辰涛)[1,2,3,4,5], A. Omont[4,5], A. Beelen[2], E. González-Alfonso[6], R. Neri[7], Y. Gao (高煜)[1], P. van der Werf[8], A. Weiß[9], R. Gavazzi[4,5], N. Falstad[10], A. J. Baker[11], R. S. Bussmann[12], A. Cooray[13], P. Cox[14], H. Dannerbauer[15], S. Dye[16], M. Guélin[7], R. Ivison[17,18], M. Krips[7], M. Lehnert[4,5], M. J. Michałowski[17], D. A. Riechers[12], M. Spaans[19], and E. Valiante[20]

(Affiliations can be found after the references)

Received 19 January 2016 / Accepted 20 July 2016

ABSTRACT

We report rest-frame submillimeter H_2O emission line observations of 11 ultra- or hyper-luminous infrared galaxies (ULIRGs or HyLIRGs) at $z \sim 2$–4 selected among the brightest lensed galaxies discovered in the *Herschel*-Astrophysical Terahertz Large Area Survey (*H*-ATLAS). Using the IRAM NOrthern Extended Millimeter Array (NOEMA), we have detected 14 new H_2O emission lines. These include five 3_{21}–3_{12} ortho-H_2O lines (E_{up}/k = 305 K) and nine $J = 2$ para-H_2O lines, either 2_{02}–1_{11} (E_{up}/k = 101 K) or 2_{11}–2_{02} (E_{up}/k = 137 K). The apparent luminosities of the H_2O emission lines are $\mu L_{H_2O} \sim 6$–$21 \times 10^8\ L_\odot$ ($3 < \mu < 15$, where μ is the lens magnification factor), with velocity-integrated line fluxes ranging from 4–15 Jy km s^{-1}. We have also observed CO emission lines using EMIR on the IRAM 30 m telescope in seven sources (most of those have not yet had their CO emission lines observed). The velocity widths for CO and H_2O lines are found to be similar, generally within 1σ errors in the same source. With almost comparable integrated flux densities to those of the high-J CO line (ratios range from 0.4 to 1.1), H_2O is found to be among the strongest molecular emitters in high-redshift Hy/ULIRGs. We also confirm our previously found correlation between luminosity of H_2O (L_{H_2O}) and infrared (L_{IR}) that $L_{H_2O} \sim L_{IR}^{1.1-1.2}$, with our new detections. This correlation could be explained by a dominant role of far-infrared pumping in the H_2O excitation. Modelling reveals that the far-infrared radiation fields have warm dust temperature $T_{warm} \sim 45$–75 K, H_2O column density per unit velocity interval $N_{H_2O}/\Delta V \gtrsim 0.3 \times 10^{15}$ cm^{-2} km^{-1} s and 100 μm continuum opacity $\tau_{100} > 1$ (optically thick), indicating that H_2O is likely to trace highly obscured warm dense gas. However, further observations of $J \geq 4$ H_2O lines are needed to better constrain the continuum optical depth and other physical conditions of the molecular gas and dust. We have also detected H_2O^+ emission in three sources. A tight correlation between L_{H_2O} and $L_{H_2O^+}$ has been found in galaxies from low to high redshift. The velocity-integrated flux density ratio between H_2O^+ and H_2O suggests that cosmic rays generated by strong star formation are possibly driving the H_2O^+ formation.

Key words. galaxies: high-redshift – galaxies: ISM – infrared: galaxies – submillimeter: galaxies – radio lines: ISM – ISM: molecules

1. Introduction

After molecular hydrogen (H_2) and carbon monoxide (CO), the water molecule (H_2O) can be one of the most abundant molecules in the interstellar medium (ISM) in galaxies. It provides some important diagnostic tools for various physical and chemical processes in the ISM (e.g. van Dishoeck et al. 2013, and references therein). Prior to the *Herschel* Space Observatory (Pilbratt et al. 2010), in extragalactic sources, non-maser H_2O rotational transitions were only detected by the Infrared Space Observatory (ISO, Kessler et al. 1996) in the form of far-infrared absorption lines (González-Alfonso et al. 2004, 2008). Observations of local infrared bright galaxies by *Herschel* have revealed a rich spectrum of submillimeter (submm) H_2O emission lines (submm H_2O refers to rest-frame submillimeter H_2O emission throughout this paper if not otherwise specified). Many of these lines are emitted from high-excitation rotational levels with upper-level energies up to E_{up}/k = 642 K (e.g. van der Werf et al. 2010; González-Alfonso et al. 2010, 2012, 2013; Rangwala et al. 2011; Kamenetzky et al. 2012; Spinoglio et al. 2012; Meijerink et al. 2013; Pellegrini et al. 2013; Pereira-Santaella et al. 2013). Excitation analysis of these lines has revealed that they are probably excited through absorption of far-infrared photons from thermal dust emission in warm dense regions of the ISM (e.g. González-Alfonso et al. 2010). Therefore, unlike the canonical CO lines that trace collisional excitation of the molecular gas, these H_2O lines represent a powerful diagnostic of the far-infrared radiation field.

Using the *Herschel* archive data, Yang et al. (2013, hereafter Y13) have undertaken a first systematic study of submm H_2O emission in local infrared galaxies. H_2O was found to be the strongest molecular emitter after CO within the submm band in those infrared-bright galaxies, even with higher flux density than that of CO in some local ULIRGs (velocity-integrated flux density of $H_2O(3_{21}$–$3_{12})$ is larger than that of CO(5–4) in four galaxies out of 45 in the Y13 sample). The luminosities of the submm H_2O lines (L_{H_2O}) are near-linearly correlated with total infrared luminosity (L_{IR}, integrated over 8–1000 μm) over three orders of magnitude. The correlation is revealed to be a straightforward result of far-infrared pumping: H_2O molecules are excited to higher energy levels through absorbing far-infrared photons, then the upper level molecules cascade toward the lines we

★ *Herschel* is an ESA space observatory with science instruments provided by European-led Principal Investigator consortia and with important participation from NASA.
★★ The reduced spectra as FITS files are only available at the CDS via anonymous ftp to cdsarc.u-strasbg.fr (130.79.128.5) or via http://cdsarc.u-strasbg.fr/viz-bin/qcat?J/A+A/595/A80

observed in an almost constant fraction (Fig. 1). Although the galaxies dominated by active galactic nuclei (AGN) have somewhat lower ratios of L_{H_2O}/L_{IR}, there does not appear to be a link between the presence of an AGN and the submm H_2O emission (Y13). The H_2O emission is likely to trace the far-infrared radiation field generated in star-forming nuclear regions in galaxies, explaining its tight correlation with far-infrared luminosity.

Besides detections of the H_2O lines in local galaxies from space telescopes, redshifted submm H_2O lines in high-redshift lensed Ultra- and Hyper-Luminous InfraRed Galaxies (ULIRGs, $10^{13}\,L_\odot > L_{IR} \geq 10^{12}\,L_\odot$; HyLIRGs, $L_{IR} \geq 10^{13}\,L_\odot$) can also be detected by ground-based telescopes in atmospheric windows with high transmission. Strong gravitational lensing boosts the flux and allows one to detect the H_2O emission lines easily. Since our first detection of submm H_2O in a lensed *Herschel* source at $z = 2.3$ (Omont et al. 2011) using the IRAM NOrthern Extended Millimeter Array (NOEMA), several individual detections at high-redshift have also been reported (Lis et al. 2011; van der Werf et al. 2011; Bradford et al. 2011; Combes et al. 2012; Lupu et al. 2012; Bothwell et al. 2013; Omont et al. 2013; Vieira et al. 2013; Weiß et al. 2013; Rawle et al. 2014). These numerous and easy detections of H_2O in high-redshift lensed ULIRGs show that its lines are the strongest submm molecular lines after CO and may be an important tool for studying these galaxies.

We have carried out a series of studies focussing on submm H_2O emission in high-redshift lensed galaxies since our first detection. Through the detection of $J = 2$ H_2O lines in seven high-redshift lensed Hy/ULIRGs reported by Omont et al. (2013, hereafter O13), a slightly super-linear correlation between L_{H_2O} and L_{IR} ($L_{H_2O} \propto {L_{IR}}^{1.2}$) from local ULIRGs and high-redshift lensed Hy/ULIRGs has been found. This result may imply again that far-infrared pumping is important for H_2O excitation in high-redshift extreme starbursts. The average ratios of L_{H_2O} to L_{IR} for the $J = 2$ H_2O lines in the high-redshift sources tend to be 1.8 ± 0.9 times higher than those seen locally (Y13). This shows that the same physics with infrared pumping should dominate H_2O excitation in ULIRGs at low and high redshift, with some specificity at high-redshift probably linked to the higher luminosities.

Modelling provides additional information about the H_2O excitation. For example, through LVG modelling, Riechers et al. (2013) argue that the excitation of the submm H_2O emission in the $z \sim 6.3$ submm galaxy is far-infrared pumping dominated. Modelling of the local *Herschel* galaxies of Y13 has been carried out by González-Alfonso et al. (2014, hereafter G14). They confirm that far-infrared pumping is the dominant mechanism responsible for the submm H_2O emission (except for the ground-state emission transitions, such as para-H_2O transition 1_{11}–0_{00}) in the extragalactic sources. Moreover, collisional excitation of the low-lying ($J \leq 2$) H_2O lines could also enhance the radiative pumping of the ($J \geq 3$) high-lying lines. The ratio between low-lying and high-lying H_2O lines is sensitive to the dust temperature (T_d) and H_2O column density (N_{H_2O}). From modelling the average of local star-forming- and mild-AGN-dominated galaxies, G14 show that the submm H_2O emission comes from regions with $N_{H_2O} \sim (0.5\text{–}2) \times 10^{17}$ cm^{-2} and a 100 μm continuum opacity of $\tau_{100} \sim 0.05$–0.2, where H_2O is mainly excited by warm dust with a temperature range of 45–75 K. H_2O lines thus provide key information about the properties of the dense cores of ULIRGs, that is, their H_2O content, the infrared radiation field and the corresponding temperature of dust that is warmer than the core outer layers and dominates the far-infrared emission.

Observations of the submm H_2O emission, together with appropriate modelling and analysis, therefore allows us to study the properties of the far-infrared radiation sources in great detail. So far, the excitation analysis combining both low- and high-lying H_2O emission has only been done in a few case studies. Using H_2O excitation modelling considering both collision and far-infrared pumping, González-Alfonso et al. (2010) and van der Werf et al. (2011) estimate the sizes of the far-infrared radiation fields in Mrk 231 and APM 08279+5255 (APM 08279 hereafter), which are not resolved by the observations directly, and suggest their AGN dominance based on their total enclosed energies. This again demonstrates that submm H_2O emission is a powerful diagnostic tool which can even transcend the angular resolution of the telescopes.

The detection of submm H_2O emission in the *Herschel*-ATLAS[1] (Eales et al. 2010, *H*-ATLAS hereafter) sources through gravitational lensing allows us to characterise the far-infrared radiation field generated by intense star-forming activity, and possibly AGN, and learn the physical conditions in the warm dense gas phase in extreme starbursts in the early Universe. Unlike standard dense gas tracers such as HCN, which is weaker at high-redshift compared to that of local ULIRGs (Gao et al. 2007), submm H_2O lines are strong and even comparable to high-J CO lines in some galaxies (Y13; O13). Therefore, H_2O is an efficient tracer of the warm dense gas phase that makes up a major fraction of the total molecular gas mass in high-redshift Hy/ULIRGs (Casey et al. 2014). The successful detections of submm H_2O lines in both local (Y13) and the high-redshift universe (O13) show the great potential of a systematic study of H_2O emission in a large sample of infrared galaxies over a wide range in redshift (from local up to $z \sim 4$) and luminosity ($L_{IR} \sim 10^{10}$–$10^{13}\,L_\odot$). However, our previous high-redshift sample was limited to seven sources and to one $J = 2$ para-H_2O line ($E_{up}/k = 100$–127 K) per source (O13). In order to further constrain the conditions of H_2O excitation, to confirm the dominant role of far-infrared pumping and to learn the physical conditions of the warm dense gas phase in high-redshift starbursts, it is essential to extend the studies to higher excitation lines. We thus present and discuss here the results of such new observations of a strong $J = 3$ ortho-H_2O line with $E_{up}/k = 304$ K in six strongly lensed *H*-ATLAS galaxies at $z \sim 2.8$–3.6, where a second lower-excitation $J = 2$ para-H_2O line was also observed (Fig. 1 for the transitions and the corresponding E_{up}).

We describe our sample, observation and data reduction in Section 2. The observed properties of the high-redshift submm H_2O emission are presented in Sect. 3. Discussions of the lensing properties, L_{H_2O}-L_{IR} correlation, H_2O excitation, comparison between H_2O and CO, AGN contamination will be given in Sect. 4. Section 5 describes the detection of H_2O^+ lines. We summarise our results in Sect. 6. A flat ΛCDM cosmology with $H_0 = 71$ km s^{-1} Mpc^{-1}, $\Omega_M = 0.27$, $\Omega_\Lambda = 0.73$ (Spergel et al. 2003) is adopted throughout this paper.

2. Sample and observation

Our sample consists of eleven extremely bright high-redshift sources with $F_{500\,\mu m} > 200$ mJy discovered by the *H*-ATLAS survey (Eales et al. 2010). Together with the seven similar

[1] The *Herschel*-ATLAS is a project with *Herschel*, which is an ESA space observatory with science instruments provided by European-led Principal Investigator consortia and with important participation from NASA. The *H*-ATLAS website is http://www.h-atlas.org

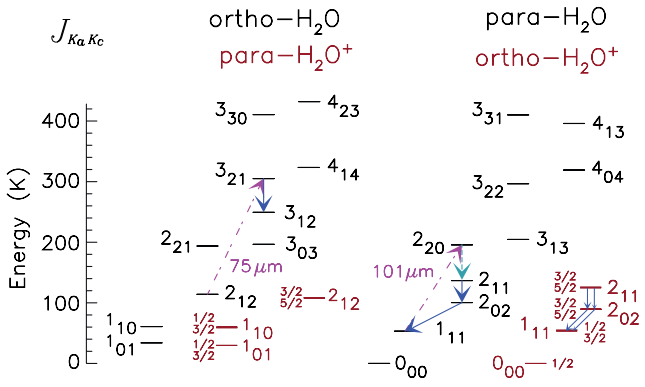

Fig. 1. Energy level diagrams of H_2O and H_2O^+ shown in black and red, respectively. Dark blue arrows are the submm H_2O transitions we have observed in this work. Pink dashed lines show the far-infrared pumping path of the H_2O excitation in the model we use, with the wavelength of the photon labeled. The light blue dashed arrow is the transition from para-H_2O energy level 2_{20} to 2_{11} along the cascade path from 2_{20} to 1_{11}. Rotational energy levels of H_2O and H_2O^+, as well as fine structure component levels of H_2O^+ are also shown in the figure.

sources reported in our previous H_2O study (O13), they include all the brightest high-redshift *H*-ATLAS sources ($F_{500\,\mu m} > 170$ mJy), but two, imaged at 880 μm with SMA by Bussmann et al. (2013, hereafter B13). In agreement with the selection according to the methods of Negrello et al. (2010), the detailed lensing modelling performed by B13 has shown that all of them are strongly lensed, but one, G09v1.124 (Ivison et al. 2013, see below). The sample of our present study is thus well representative of the brightest high-redshift submillimeter sources with $F_{500\,\mu m} > 200$ mJy (with apparent total infrared luminosity $\sim$5–15 $\times\, 10^{13}\, L_\odot$ and $z \sim 1.5$–4.2) found by *H*-ATLAS in its equatorial ("GAMA") and north-galactic-pole ("NGP") fields, in $\sim$300 deg^2 with a density $\sim$0.05 deg^{-2}. In our previous project (O13), we observed H_2O in seven strongly lensed high-redshift *H*-ATLAS galaxies from the B13 sample. In this work, in order to observe the high-excitation ortho-$H_2O(3_{21}$–$3_{12})$ line with rest frequency of 1162.912 GHz with the IRAM/NOEMA, we selected the brightest sources at 500 μm with $z \gtrsim 2.8$ so that the redshifted lines could be observed in a reasonably good atmospheric window at $\nu_{obs} \lesssim 300$ GHz. Eight sources with such redshift were selected from the B13 *H*-ATLAS sample.

B13 provide lensing models, magnification factors (μ) and inferred intrinsic properties of these galaxies and list their CO redshifts which come from Harris et al. (2012); Harris et al. (in prep.); Lupu et al. (in prep.); Krips et al. (in prep.) and Riechers et al. (in prep.).

In our final selection of the sample to be studied in the $H_2O(3_{21}$–$3_{12})$ line, we then removed two sources, SDP 81 and G12v2.30, that were previously observed in H_2O (O13; and also ALMA Partnership, Vlahakis et al. 2015, for SDP 81), because the $J = 2$ H_2O emission is too weak and/or the interferometry could resolve out some flux considering the lensing image. The observed high-redshift sample thus consists of two GAMA-field sources: G09v1.97 and G12v2.43, and four sources in the *H*-ATLAS NGP field: NCv1.143, NAv1.195, NAv1.177 and NBv1.78 (Tables 1 and 2). Among the six remaining sources at redshift between 2.8 and 3.6, only one, NBv1.78, has been observed previously in a low-excitation line, para-$H_2O(2_{02}$–$1_{11})$ (O13). Therefore, we have observed both para-H_2O line 2_{02}–1_{11} or 2_{11}–2_{02} and ortho-$H_2O(3_{21}$–$3_{12})$ in the other five sources, in order to compare their velocity-integrated flux densities.

In addition, we also observed five sources mostly at lower redshifts in para-H_2O lines 2_{02}–1_{11} or 2_{11}–2_{02} (Tables 1 and 2) to complete the sample of our H_2O low-excitation study. They are three strongly lensed sources, G09v1.40, NAv1.56 and SDP11, a hyper-luminous cluster source G09v1.124 (Ivison et al. 2013), and a $z \sim 3.7$ source, NCv1.268 for which we did not propose a $J = 3$ H_2O observation, considering its large linewidth which could bring difficulties in line detection.

As our primary goal is to obtain a detection of the submm H_2O lines, we carried out the observations in the compact, D configuration of NOEMA. The baselines extended from 24 to 176 m, resulting in a synthesised beam with modest/low resolution of $\sim$1.0″ × 0.9″ to $\sim$5.6″ × 3.3″ as shown in Table 1. The H_2O observations were conducted from January 2012 to December 2013 in good atmospheric conditions (seeing of 0.3″–1.5″) stability and reasonable transparency (PWV $\leq$ 1 mm). The total on source time was $\sim$1.5–8 h per source. 2 mm, 1.3 mm and 0.8 mm bands covering 129–174, 201–267 and 277–371 GHz, respectively, were used. All the central observation frequencies were chosen based on previous redshifts given by B13 according to the previous CO detections (Table 2). In all cases but one, the frequencies of our detections of H_2O lines are consistent with these CO redshifts. The only exception is G09v1.40 where our H_2O redshift disagrees with the redshift of $z = 2.0894 \pm 0.0009$ given by Lupu et al. (in prep.), which is quoted by B13. We find $z = 2.0925 \pm 0.0001$ in agreement with previous CO(3–2) observations (Riechers et al., in prep.). We used the WideX correlator which provided a contiguous frequency coverage of 3.6 GHz in dual polarisation with a fixed channel spacing of 1.95 MHz.

The phase and bandpass were calibrated by measuring standard calibrators that are regularly monitored at the IRAM/NOEMA, including 3C 279, 3C 273, MWC349 and 0923+392. The accuracy of the flux calibration is estimated to range from $\sim$10% in the 2 mm band to $\sim$20% in the 0.8 mm band. Calibration, imaging, cleaning and spectra extraction were performed within the `GILDAS`[2] packages `CLIC` and `MAPPING`.

To compare the H_2O emission with the typical molecular gas tracer, CO, we also observed the sources for CO lines using the EMIR receiver at the IRAM 30 m telescope. The CO data will be part of a systematic study of molecular gas excitation in *H*-ATLAS lensed Hy/ULIRGs, and a full description of the data and the scientific results will be given in a following paper (Yang et al., in prep.). The global CO emission properties of the sources are listed in Table 3 where we list the CO fluxes and linewidths. A brief comparison of the emission between H_2O and CO lines will be given in Sect. 4.3.

3. Results

A detailed discussion of the observation results for each source is given in Appendix A, including the strength of the H_2O emission, the image extension of H_2O lines and the continuum (Fig. A.1), the H_2O spectra and linewidths (Fig. 2) and their comparison with CO (Table 3). We give a synthesis of these results in this section.

[2] See `http://www.iram.fr/IRAMFR/GILDAS` for more information about the GILDAS softwares.

Table 1. Observation log.

IAU name	Source	RA (J2000)	Dec (J2000)	RA_{pk} (J2000)	Dec_{pk} (J2000)	H_2O line	ν_{obs} (GHz)	Beam ($''$)	t_{on} (h)
H-ATLAS J083051.0+013224	G09v1.97	08:30:51.02	+01:32:24.88	08:30:51.17	+01:32:24.39	2_{11}–2_{02}	162.286	5.6×3.3	3.5
				08:30:51.17	+01:32:24.09	3_{21}–3_{12}	250.952	2.6×1.1	3.1
H-ATLAS J113526.3−014605	G12v2.43	11:35:26.36	−01:46:05.56	11:35:26.27	−01:46:06.44	2_{02}–1_{11}	239.350	2.3×1.0	6.9
				11:35:26.28	−01:46:06.43	3_{21}–3_{12}	281.754	2.2×1.1	1.5
H-ATLAS J125632.7+233625	NCv1.143	12:56:32.70	+23:36:24.86	12:56:32.56	+23:36:27.92	2_{11}–2_{02}	164.739	3.1×2.9	1.5
				12:56:32.56	+23:36:27.69	3_{21}–3_{12}	254.745	2.1×1.0	1.5
H-ATLAS J132630.1+334410	NAv1.195	13:26:30.12	+33:44:09.90	13:26:30.14	+33:44:09.11	2_{02}–1_{11}	250.045	2.0×1.7	3.8
				13:26:30.14	+33:44:09.09	3_{21}–3_{12}	293.334	1.0×0.9	3.1
H-ATLAS J132859.3+292327	NAv1.177	13:28:59.29	+29:23:27.07	13:28:59.25	+29:23:26.18	2_{02}–1_{11}	261.495	1.9×1.7	2.3
				13:28:59.25	+29:23:26.34	3_{21}–3_{12}	307.812	1.6×0.9	2.3
H-ATLAS J133008.4+245900	NBv1.78	13:30:08.56	+24:58:58.30	13:30:08.56	+24:58:58.55	3_{21}–3_{12}	282.878	1.7×1.1	4.2
H-ATLAS J084933.4+021443	G09v1.124-W	08:49:33.36	+02:14:42.30	08:49:33.59	+02:14:44.68	2_{11}–2_{02}	220.537	1.8×1.2	8.4
	G09v1.124-T			08:49:32.95	+02:14:39.70				
H-ATLAS J085358.9+015537	G09v1.40	08:53:58.90	+01:55:37.00	08:53:58.84	+01:55:37.75	2_{11}–2_{02}	243.425	1.8×1.0	1.9
H-ATLAS J091043.1−000321	SDP11	09:10:43.09	−00:03:22.51	09:10:43.06	−00:03:22.10	2_{02}–1_{11}	354.860	1.9×1.5	3.8
H-ATLAS J125135.4+261457	NCv1.268	12:51:35.46	+26:14:57.52	12:51:35.38	+26:14:58.12	2_{11}–2_{02}	160.864	2.9×2.6	7.7
H-ATLAS J134429.4+303036	NAv1.56	13:44:29.52	+30:30:34.05	13:44:29.46	+30:30:34.01	2_{11}–2_{02}	227.828	1.7×1.7	2.3

Notes. RA and Dec are the J2000 *Herschel* coordinates which were taken as the centres of the NOEMA images displayed in Fig. A.1; RA_{pk} and Dec_{pk} are the J2000 coordinates of the NOEMA dust continuum image peaks; ν_{obs} is the central observed frequency. The rest-frame frequencies of para-H_2O 2_{02}–1_{11}, 2_{11}–2_{02} and ortho-H_2O 3_{21}–3_{12} lines are: 987.927 GHz, 752.033 GHz and 1162.912 GHz, respectively (the rest-frame frequencies are taken from the JPL catalogue: `http://spec.jpl.nasa.gov`); t_{on} is the on-source integration time. The source G09v1.124, which is not resolved by SPIRE, is a cluster that consists of two main components: eastern component W (G09v1.124-W) and western component T (G09v1.124-T) as described in Ivison et al. (2013) (see also Fig. A.3).

Table 2. Previously observed properties of the sample.

Source	z	F_{250} (mJy)	F_{350} (mJy)	F_{500} (mJy)	F_{880} (mJy)	r_{half} (kpc)	Σ_{SFR} ($10^3\,M_\odot\,yr^{-1}\,kpc^{-2}$)	$f_{1.4\ GHz}$ (mJy)	T_d (K)	μ	μL_{IR} ($10^{13}\,L_\odot$)
G09v1.97	3.634	260 ± 7	321 ± 8	269 ± 9	85.5 ± 4.0	0.85	0.91 ± 0.15	±0.15	44 ± 1	6.9 ± 0.6	15.3 ± 4.3
G12v2.43	3.127	290 ± 7	295 ± 8	216 ± 9	48.6 ± 2.3	–	–	±0.15	–	–	(8.3 ± 1.7)
NCv1.143	3.565	214 ± 7	291 ± 8	261 ± 9	97.2 ± 6.5	0.40	2.08 ± 0.77	0.61 ± 0.16	40 ± 1	11.3 ± 1.7	12.8 ± 4.3
NAv1.195	2.951	179 ± 7	279 ± 8	265 ± 9	65.2 ± 2.3	1.57	0.21 ± 0.04	±0.14	36 ± 1	4.1 ± 0.3	7.4 ± 2.0
NAv1.177	2.778	264 ± 9	310 ± 10	261 ± 10	50.1 ± 2.1	–	–	±0.15	–	–	(5.5 ± 1.1)
NBv1.78	3.111	273 ± 7	282 ± 8	214 ± 9	59.2 ± 4.3	0.55	1.09 ± 1.41	0.67 ± 0.20	43 ± 1	13.0 ± 1.5	10.7 ± 3.9
G09v1.124-W[a]	2.410	242 ± 7	293 ± 8	231 ± 9	50.0 ± 3.5	–	–	±0.15	40 ± 1	1	3.3 ± 0.3
G09v1.124-T[a]						–	–	±0.15	36 ± 1	1.5 ± 0.2	2.7 ± 0.8
G09v1.40	2.089[b]	389 ± 7	381 ± 8	241 ± 9	61.4 ± 2.9	0.41	0.77 ± 0.30	0.75 ± 0.15	36 ± 1	15.3 ± 3.5	6.5 ± 2.5
SDP11	1.786	417 ± 6	378 ± 7	232 ± 8	30.6 ± 2.4	0.89	0.22 ± 0.08	0.66 ± 0.14	41 ± 1	10.9 ± 1.3	6.2 ± 1.9
NCv1.268	3.675	145 ± 7	201 ± 8	212 ± 9	78.9 ± 4.4	0.93	0.31 ± 0.14	1.10 ± 0.14	39 ± 1	11.0 ± 1.0	9.5 ± 2.7
NAv1.56	2.301	481 ± 9	484 ± 13	344 ± 11	73.1 ± 2.4	1.50	0.14 ± 0.08	1.12 ± 0.27	38 ± 1	11.7 ± 0.9	11.3 ± 3.1

Notes. z is the redshift inferred from previous CO detection quoted by B13 (see the references therein); F_{250}, F_{350} and F_{500} are the SPIRE flux densities at 250, 350 and 500 μm, respectively (Pascale et al. 2011); F_{880} is the SMA flux density at 880 μm; r_{half} and Σ_{SFR} are the intrinsic half-light radius at 880 μm and the lensing-corrected surface SFR (star formation rate) density (Sect. 4.2); $f_{1.4\ GHz}$ is the 1.4 GHz band flux densities from the VLA FIRST survey; T_d is the cold-dust temperature taken from B13 (note that the errors quoted for T_d are significantly underestimated since the uncertainties from differential lensing and single-temperature dust SED assumption are not fully considered); μ is the lensing magnification factor from B13, except for G09v1.124 which is adopted from Ivison et al. (2013); μL_{IR} is the apparent total infrared luminosity mostly inferred from B13. The μL_{IR} in brackets are not listed in B13, thus we infer them from single modified black body dust SED fitting using the submm photometry data listed in this table. [(a)] The cluster source G09v1.124 includes two main components: G09v1.124-W to the east and G09v1.124-T to the west (Fig. A.3) and the values of these two rows are quoted from Ivison et al. (2013); [(b)] our H_2O observation gives $z = 2.093$ for G09v1.40. This value is slightly different from the value of 2.089 quoted by B13 from Lupu et al. (in prep.) obtained by CSO/Z-Spec, but consistent with CO(3–2) observation by Riechers et al. (in prep.).

3.1. General properties of the H_2O emissions

To measure the linewidth, velocity-integrated flux density and the continuum level of the spectra from the source peak and from the entire source, we extract each spectrum from the CLEANed image at the position of the source peak in a single synthesis beam and the spectrum integrated over the entire source. Then we fit them with Gaussian profiles using `MPFIT` (Markwardt 2009).

We detect the high-excitation ortho-$H_2O(3_{21}$–$3_{12})$ in five out of six observed sources, with high signal to noise ratios ($S/N > 9$) and velocity-integrated flux densities comparable to those of the low-excitation $J = 2$ para-H_2O lines (Table 4 and Figs. 2 and A.1). We also detect nine out of eleven $J = 2$ para-H_2O lines, either 2_{02}–1_{11} or 2_{11}–2_{02}, with $S/N \geq 6$ in terms of their velocity-integrated flux density, plus one tentative detection of $H_2O(2_{02}$–$1_{11})$ in SDP11. We present the values of velocity-integrated H_2O flux density detected at the source peak in a single synthesised beam, $I_{H_2O}{}^{pk}$, and the velocity-integrated H_2O flux density over the entire source, I_{H_2O} (Table 4). The detected H_2O lines are strong, with $I_{H_2O} = 3.7$–14.6 Jy km s^{-1}. Even considering gravitational lensing correction, this is consistent with

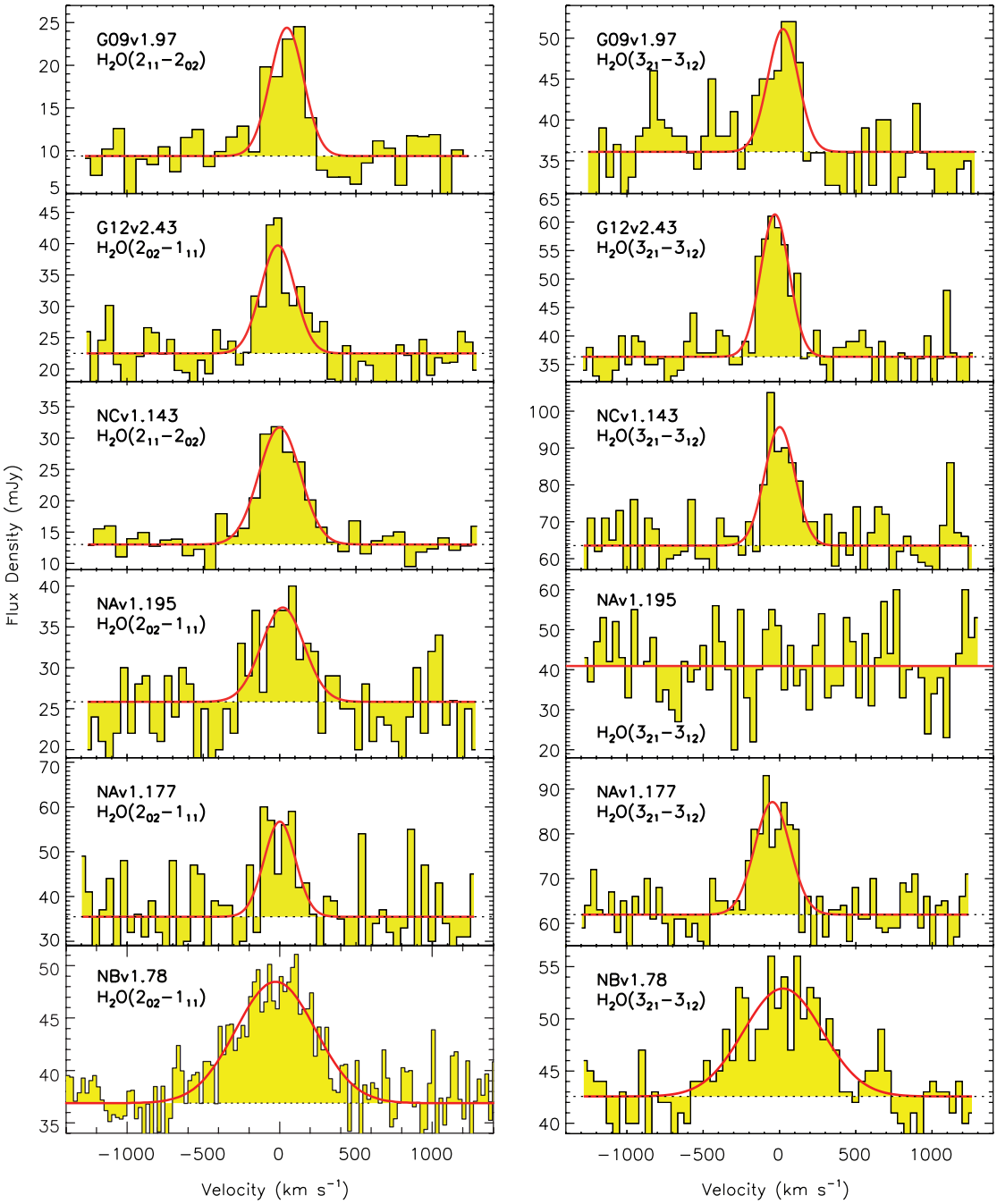

Fig. 2a. Spatially integrated spectra of H_2O in the six sources with both $J = 2$ para-H_2O and $J = 3$ ortho-H_2O lines observed. The red lines represent the Gaussian fitting to the emission lines. The $H_2O(2_{02}–1_{11})$ spectrum of NBv1.78 is taken from O13. Except for $H_2O(3_{21}–3_{12})$ in NAv1.195, all the $J = 2$ and $J = 3$ H_2O lines are well detected, with a high S/N and similar profiles in both lines for the same source.

our previous finding that high-redshift Hy/ULIRGs are very strong H_2O emitters, with H_2O flux density approaching that of CO (Tables 3 and 4 and Sect. 4.3). The majority of the images (7/11 for $J = 2$ lines and 3/4 for $J = 3$) are marginally resolved with $I_{H_2O}{}^{pk}/I_{H_2O} \sim 0.4$–$0.7$. They show somewhat lensed structures. The others are unresolved with $I_{H_2O}{}^{pk}/I_{H_2O} > 0.8$. All continuum emission flux densities ($S_\nu(\mathrm{ct})^{pk}$ for the emission peak and $S_\nu(\mathrm{ct})$ for the entire source) are very well detected ($S/N \geq 30$), with a range of total flux density of 9–64 mJy for $S_\nu(\mathrm{ct})$. Figure A.1 shows the low-resolution images of H_2O and the corresponding dust continuum emission at the observing frequencies. Because the positions of the sources were derived from *Herschel* observation, which has a large beamsize (>17″) comparing to the source size, the position of most of the sources are not perfectly centred at these *Herschel* positions as seen in the maps. The offsets are all within the position error of the *Herschel* measurement (Fig. A.1). G09v1.124 is a complex HyLIRG system including two main components eastern G09v1.124-W and western G09v1.124-T as described in Ivison et al. (2013). In Fig. A.3, we identified the two strong components separated

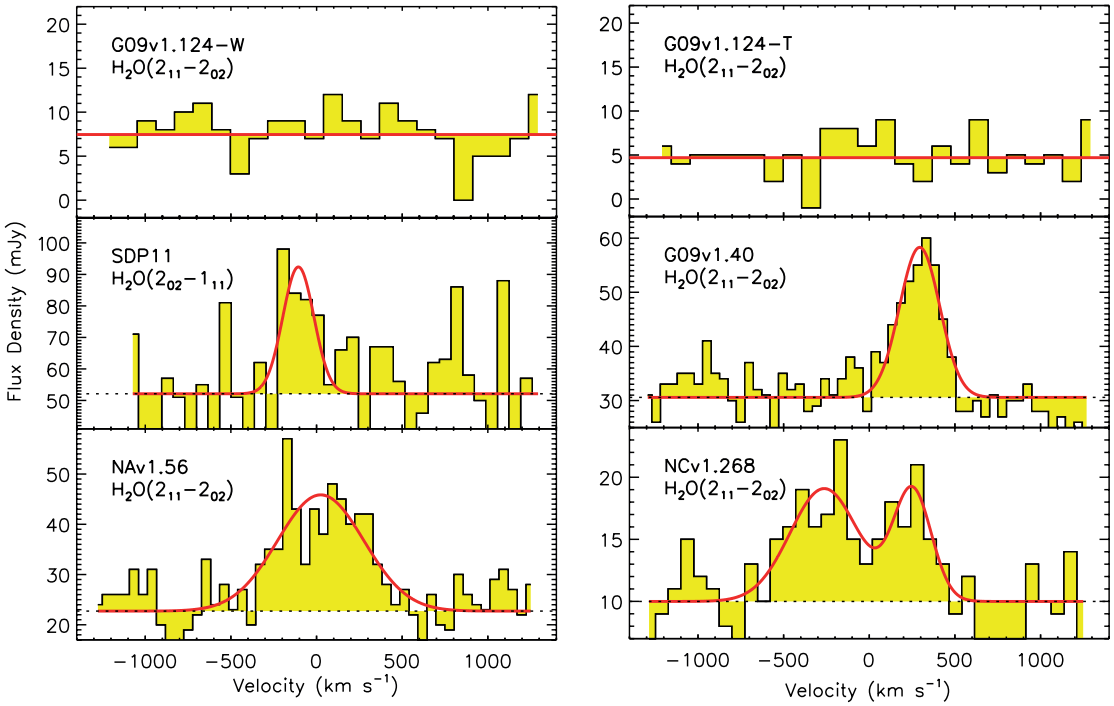

Fig. 2b. Spatially integrated spectra of H_2O of the five sources with only one $J = 2$ para-H_2O line observed. The red lines represent the Gaussian fitting to the emission lines. Except for the H_2O line in G09v1.124, all the $J = 2$ H_2O lines are well detected.

Table 3. Observed CO line properties using the IRAM 30 m/EMIR.

Source	CO line	I_{CO} (Jy km s^{-1})	ΔV_{CO} (km s^{-1})
G09v1.97	5–4	9.5 ± 1.2	224 ± 32
	6–5	10.4 ± 2.3	292 ± 86
NCv1.143	5–4	13.1 ± 1.0	273 ± 27
	6–5	11.0 ± 1.0	284 ± 27
NAv1.195	5–4	11.0 ± 0.6	281 ± 16
NAv1.177	3–2	6.8 ± 0.4	231 ± 15
	5–4	11.0 ± 0.6	230 ± 16
NBv1.78	5–4	10.3 ± 0.8	614 ± 53
	6–5	9.7 ± 1.0	734 ± 85
G09v1.40	4–3	7.5 ± 2.1	198 ± 51
NAv1.56	5–4	17.7 ± 6.6	432 ± 182

Notes. I_{CO} is the velocity-integrated flux density of CO; ΔV_{CO} is the linewidth (FWHM) derived from fitting a single Gaussian to the line profile.

about 10″, in agreement with Ivison et al. (2013). The $J = 2$ H_2O and dust continuum emissions in NBv1.78, NCv1.195, G09v1.40, SDP 11 and NAv1.56, as well as the $J = 3$ ortho-H_2O and the corresponding dust continuum emissions in G09v1.97, NCv1.143 and NAv1.177, are marginally resolved as shown in Fig. A.1. Their images are consistent with the corresponding SMA images (B13) in terms of their spatial distribution. The rest of the sources are not resolved by the low-resolution synthesised beams. The morphological structure of the H_2O emission is similar to the continuum for most sources as shown in Fig. A.1. The ratio $S_\nu(\mathrm{ct})^{\mathrm{pk}}/S_\nu(\mathrm{ct})$ and $S_\nu(\mathrm{H_2O})^{\mathrm{pk}}/S_\nu(\mathrm{H_2O})$ are in good agreement within the error. However, for NCv1.143 in which $S_\nu(\mathrm{ct})^{\mathrm{pk}}/S_\nu(\mathrm{ct}) = 0.55 \pm 0.01$ and $S_\nu(\mathrm{H_2O})^{\mathrm{pk}}/S_\nu(\mathrm{H_2O}) = 0.74 \pm 0.16$, the $J = 3$ ortho-H_2O emission appears more compact than the dust continuum. Generally it seems unlikely that we have a significant fraction of missing flux for our sources. Nevertheless, the low angular resolution (∼1″ at best) limits the study of spatial distribution of the gas and dust in our sources. A detailed analysis of the images for each source is given in Appendix A.

The majority of the sources have H_2O (and CO) linewidths between 210 and 330 km s^{-1}, while the four others range between 500 and 700 km s^{-1} (Table 4). Except NCv1.268, which shows a double-peaked line profile, all H_2O lines are well fit by a single Gaussian profile (Fig. 2). The line profiles between the $J = 2$ and $J = 3$ H_2O lines do not seem to be significantly different, as shown from the linewidth ratios ranging from 1.26 ± 0.14 to 0.84 ± 0.16. The magnification from strong lensing is very sensitive to the spatial configuration, in other words, differential lensing, which could lead to different line profiles if the different velocity components of the line are emitted at different spatial positions. Since there is no visible differential effect between their profiles, it is possible that the $J = 2$ and $J = 3$ H_2O lines are from similar spatial regions.

In addition to H_2O, within the 3.6 GHz WideX band, we have also tentatively detected H_2O^+ emission in 3 sources: NCv1.143, G09v1.97 and G15v2.779 (see Sect. 5).

3.2. Lensing properties

All our sources are strongly gravitationally lensed (except G09v1.124, see Appendix A.11), which increases the line flux densities and allows us to study the H_2O emission in an affordable amount of observation time. However, the complexity of the lensed images complicates the analysis. As mentioned above, most of our lensed images are either unresolved or marginally resolved. Thus, we will not discuss here the spatial distribution of the H_2O and dust emissions through gravitational lensing modelling. However, we should keep in mind that the correction of

Table 4. Observed properties of H_2O emission lines.

Source	H_2O line	ν_{H_2O} (GHz)	$S_\nu(\mathrm{ct})^{\mathrm{pk}}$ ($\frac{\mathrm{mJy}}{\mathrm{beam}}$)	$S_\nu(\mathrm{ct})$ (mJy)	$S^{\mathrm{pk}}_{H_2O}$ ($\frac{\mathrm{mJy}}{\mathrm{beam}}$)	S_{H_2O} (mJy)	$I_{H_2O}{}^{\mathrm{pk}}$ ($\frac{\mathrm{Jy\,km\,s^{-1}}}{\mathrm{beam}}$)	I_{H_2O} (Jy km s^{-1})	ΔV_{H_2O} (km s^{-1})	μL_{H_2O} ($10^8\,L_\odot$)
G09v1.97	2_{11}–2_{02}	162.255	8.9 ± 0.2	9.4 ± 0.2	14.9 ± 2.2	15.0 ± 2.1	3.8 ± 0.4	4.1 ± 0.4	257 ± 27	7.4 ± 0.7
	3_{21}–3_{12}	250.947	21.7 ± 0.3	36.1 ± 0.3	7.8 ± 1.9	15.0 ± 2.6	2.4 ± 0.4	3.7 ± 0.4	234 ± 34	10.4 ± 1.0
G12v2.43	2_{02}–1_{11}	239.388	16.0 ± 0.3	22.5 ± 0.4	10.8 ± 2.1	17.3 ± 3.1	3.2 ± 0.5	4.8 ± 0.6	262 ± 35	8.8 ± 1.0
	3_{21}–3_{12}	281.784	31.5 ± 0.3	36.4 ± 0.3	25.6 ± 3.3	25.0 ± 3.0	4.9 ± 0.4	5.9 ± 0.5	221 ± 20	12.7 ± 1.0
NCv1.143	2_{11}–2_{02}	164.741	11.2 ± 0.1	13.3 ± 0.2	17.4 ± 1.3	18.7 ± 1.3	5.6 ± 0.3	5.8 ± 0.3	293 ± 15	10.1 ± 0.5
	3_{21}–3_{12}	254.739	34.8 ± 0.5	63.5 ± 0.5	23.9 ± 4.3	32.1 ± 4.1	5.2 ± 0.6	8.0 ± 0.7	233 ± 22	21.3 ± 1.8
NAv1.195	2_{02}–1_{11}	250.034	14.0 ± 0.4	25.8 ± 0.4	6.6 ± 2.5	11.6 ± 2.5	2.1 ± 0.6	4.0 ± 0.6	328 ± 51	6.7 ± 1.0
	3_{21}–3_{12}	(293.334)	17.2 ± 0.5	41.2 ± 0.5	<4.2	<7.3	<1.5	<2.6	330[a]	<5.0
NAv1.177	2_{02}–1_{11}	261.489	26.5 ± 0.6	35.5 ± 0.6	16.8 ± 4.9	21.2 ± 4.9	4.4 ± 0.9	5.4 ± 0.9	241 ± 41	8.2 ± 1.2
	3_{21}–3_{12}	307.856	38.2 ± 0.4	62.0 ± 0.4	14.8 ± 2.6	25.2 ± 3.1	4.6 ± 0.5	7.3 ± 0.6	272 ± 24	12.9 ± 1.1
NBv1.78	2_{02}–1_{11}[b]	240.290	15.4 ± 0.3	36.9 ± 0.4	5.0 ± 1.0	12.3 ± 3.2	2.7 ± 0.3	6.7 ± 1.3	510 ± 90	12.2 ± 2.4
	3_{21}–3_{12}	282.863	29.2 ± 0.2	42.6 ± 0.2	8.8 ± 1.0	10.6 ± 1.0	4.8 ± 0.4	6.7 ± 0.5	607 ± 43	14.3 ± 1.0
G09v1.124-W	2_{11}–2_{02}	(220.537)	6.42 ± 0.15	7.6 ± 0.2	<1.4	<1.6	<1.2[c]	<1.4[c]	850[c]	<1.3[c]
G09v1.124-T			4.08 ± 0.15	4.9 ± 0.2	<1.7	<2.0	<1.0[c]	<1.2[c]	550[c]	<1.0[c]
G09v1.40	2_{11}–2_{02}	243.182	16.9 ± 0.2	30.6 ± 0.3	17.5 ± 2.0	27.7 ± 1.9	4.9 ± 0.4	8.2 ± 0.4	277 ± 14	5.7 ± 0.3
SDP11	2_{02}–1_{11}	354.930	29.2 ± 1.3	52.1 ± 1.3	14.8 ± 8.4	40.3 ± 11.7	5.2 ± 2.0	9.2 ± 2.0	214 ± 41	6.3 ± 1.1
NCv1.268	2_{11}–2_{02}	161.013	6.6 ± 0.1	10.0 ± 0.1	5.2 ± 1.1	9.0 ± 1.2	3.7 ± 0.4	7.0 ± 0.7	731 ± 75	12.8 ± 1.2
NAv1.56	2_{11}–2_{02}	227.822	14.0 ± 0.6	22.7 ± 0.6	15.8 ± 3.3	23.2 ± 3.0	7.8 ± 1.1	14.6 ± 1.3	593 ± 56	12.0 ± 1.1

Notes. ν_{H_2O} is the observed central frequency of H_2O lines, and the values in brackets are the H_2O line frequencies inferred from the CO redshifts for the undetected sources; $S_\nu(\mathrm{ct})^{\mathrm{pk}}$ and $S_\nu(\mathrm{ct})$ are the peak and spatially integrated continuum flux density, respectively; $S^{\mathrm{pk}}_{H_2O}$ is the peak H_2O line flux and S_{H_2O} is the total line flux; $I_{H_2O}{}^{\mathrm{pk}}$ and I_{H_2O} are the peak and spatially integrated velocity-integrated flux density of the H_2O lines; ΔV_{H_2O} is the H_2O linewidth; μL_{H_2O} is the apparent luminosity of the observed H_2O line. [(a)] The linewidth of the undetected $H_2O(3_{21}$–$3_{12})$ in NAv1.195 has been set to 330 km s^{-1} by assuming that the widths of the $H_2O(3_{21}$–$3_{12})$ and $H_2O(2_{02}$–$1_{11})$ lines are roughly the same; [(b)] the data of para-$H_2O(2_{02}$–$1_{11})$ in NBv1.78 is taken from O13; [(c)] the 2σ upper limits of I_{H_2O} are derived by assuming that the H_2O linewidths are similar to those of the CO lines (Ivison et al. 2013).

the magnification is a crucial part of our study. In addition, differential lensing could have a significant influence when comparing H_2O emission with dust and even comparing different transitions of same molecular species (Serjeant 2012), especially for the emission from close to the caustics.

In order to infer the intrinsic properties of our sample, especially L_{H_2O} as in our first paper O13, we adopted the lensing magnification factors μ (Table 2) computed from the modelling of the 880 μm SMA images (B13). As shown in the Appendix, the ratio of $S_\nu(\mathrm{ct})^{\mathrm{pk}}/S_\nu(\mathrm{ct})$ and $S_\nu(H_2O)^{\mathrm{pk}}/S_\nu(H_2O)$ are in good agreement within the uncertainties. Therefore, it is unlikely that the magnification of the 880 μm continuum image and H_2O can be significantly different. However, B13 were unable to provide a lensing model for two of our sources, G12v2.43 and NAv1.177, because their lens deflector is unidentified. This does not affect the modelling of H_2O excitation and the comparison of H_2O and infrared luminosities since the differential lensing effect seems to be insignificant as discussed in Sects. 4 and Appendix A.

4. Discussion

4.1. L_{H_2O} – L_{IR} correlation and L_{H_2O} – L_{IR} ratio

Using the formula given by Solomon et al. (1992), we derive the apparent H_2O luminosities of the sources, μL_{H_2O} (Table 4), from I_{H_2O}. For the ortho-$H_2O(3_{21}$–$3_{12})$ lines, μL_{H_2O} varies in the range of 6–22 $\times\,10^8\,L_\odot$, while the μL_{H_2O} of the $J = 2$ lines are a factor ~1.2–2 weaker (Table 4) as discussed in Sect. 4.2.

Using the lensing magnification correction (taking the values of μ from B13), we have derived the intrinsic H_2O luminosities (Table 5). The error of each luminosity consists of the uncertainty from both observation and the gravitational lensing modelling. After correcting for lensing, the H_2O luminosities of our high-redshift galaxies appear to be one order of magnitude higher than those of local ULIRGs, as well as their infrared luminosities (Table 5), so that many of them should rather be considered as HyLIRGs than ULIRGs. Though the ratio of L_{H_2O}/L_{IR} in our high-redshift sample is close to that of local ULIRGs (Y13), with somewhat a statistical increase in the extreme high L_{IR} end (Fig. 3).

As displayed in Fig. 3 for H_2O of the three observed lines, because we have extended the number of detections to 21 H_2O lines, distributed in 16 sources and 3 transitions, we may independently study the correlation of $L_{H_2O(2_{02}-1_{11})}$ and $L_{H_2O(2_{11}-2_{02})}$ with L_{IR}, while we had approximately combined the two lines in O13.

As found in O13, the correlation is slightly steeper than linear ($L_{H_2O} \sim L^{1.2}_{IR}$). To broaden the dynamical range of this comparison, we also included the local ULIRGs from Y13, together with a few other H_2O detections in high-redshift Hy/ULIRGs, for example, HLSJ 0918 (HLSJ 091828.6+514223) (Combes et al. 2012; Rawle et al. 2014), APM 08279 (van der Werf et al. 2011), SPT 0538 (SPT-S J0538165030.8) (Bothwell et al. 2013) and HFLS3 (Riechers et al. 2013, with the magnification factor from Cooray et al. 2014) (Fig. 3). In the fitting, however, we excluded the sources with heavy AGN contamination (Mrk 231 and APM 08279) or missing flux resolved out by the interferometry (SDP 81). We also excluded the $H_2O(3_{21}$–$3_{12})$ line of HFLS3 considering its unusual high $L_{H_2O(3_{21}-3_{12})}/L_{IR}$ ratio as discussed above, that could bias our fitting. We have performed a linear regression in log-log space using the Metropolis-Hastings Markov Chain Monte Carlo (MCMC) algorithm sampler through `linmix_err` (Kelly 2007) to derived the α in

$$L_{H_2O} \propto L^{\alpha}_{IR}. \quad (1)$$

Table 5. IR luminosity, H_2O line luminosity and global dust temperature of the entire sample.

Source	H_2O Transition	L_{IR} ($10^{12}\,L_\odot$)	$L_{H_2O(2_{11}-2_{02})}$ ($10^7\,L_\odot$)	$L_{H_2O(2_{02}-1_{11})}$ ($10^7\,L_\odot$)	$L_{H_2O(3_{21}-3_{12})}$ ($10^7\,L_\odot$)
G09v1.97	2_{11}–2_{02}, 3_{21}–3_{12}	22.1 ± 5.9	10.7 ± 1.4	–	15.0 ± 1.9
G12v2.43	2_{02}–1_{11}, 3_{21}–3_{12}	83.2 ± 16.6/μ	–	88.4 ± 10.7/μ	143.2 ± 11.5/μ
NCv1.143	2_{11}–2_{02}, 3_{21}–3_{12}	11.4 ± 3.1	9.0 ± 1.4	–	18.9 ± 3.3
NAv1.195	2_{02}–1_{11}, 3_{21}–3_{12}	18.0 ± 4.6	–	16.4 ± 3.0	<12.3
NAv1.177	2_{02}–1_{11}, 3_{21}–3_{12}	55.0 ± 11.0/μ	–	82.0 ± 12.8/μ	129.1 ± 10.8/μ
NBv1.78	2_{02}–1_{11}, 3_{21}–3_{12}	8.2 ± 2.2	–	9.4 ± 2.1	11.0 ± 1.5
G09v1.124-W	2_{11}–2_{02}	33.1 ± 3.2	<12.9	–	–
G09v1.124-T	2_{11}–2_{02}	14.5 ± 1.8	<6.9	–	–
G09v1.40	2_{11}–2_{02}	4.2 ± 1.3	3.7 ± 0.9	–	–
SDP11	2_{02}–1_{11}	5.7 ± 1.6	–	5.8 ± 1.4	–
NCv1.268	2_{11}–2_{02}	8.6 ± 2.3	11.5 ± 1.5	–	–
NAv1.56	2_{11}–2_{02}	9.7 ± 2.6	10.3 ± 1.2	–	–
SDP81	2_{02}–1_{11}	6.1	–	3.3	–
NAv1.144	2_{11}–2_{02}	11	9.7	–	–
SDP9	2_{11}–2_{02}	5.2	7.0	–	–
G12v2.30	2_{02}–1_{11}	16	–	13	–
SDP17b	2_{02}–1_{11}	16	–	20	–
G15v2.779	2_{11}–2_{02}	21	26.6	–	–

Notes. L_{IR} is the intrinsic total infrared luminosity (8–1000 μm) taken from B13. The intrinsic H_2O luminosities are inferred from μL_{H_2O} using μ in B13. The first group of the sources are the ones with both $J = 2$ and $J = 3$ H_2O lines observed, the next group are the sources with only $J = 2$ H_2O observed, and the last group are the previous published sources in O13.

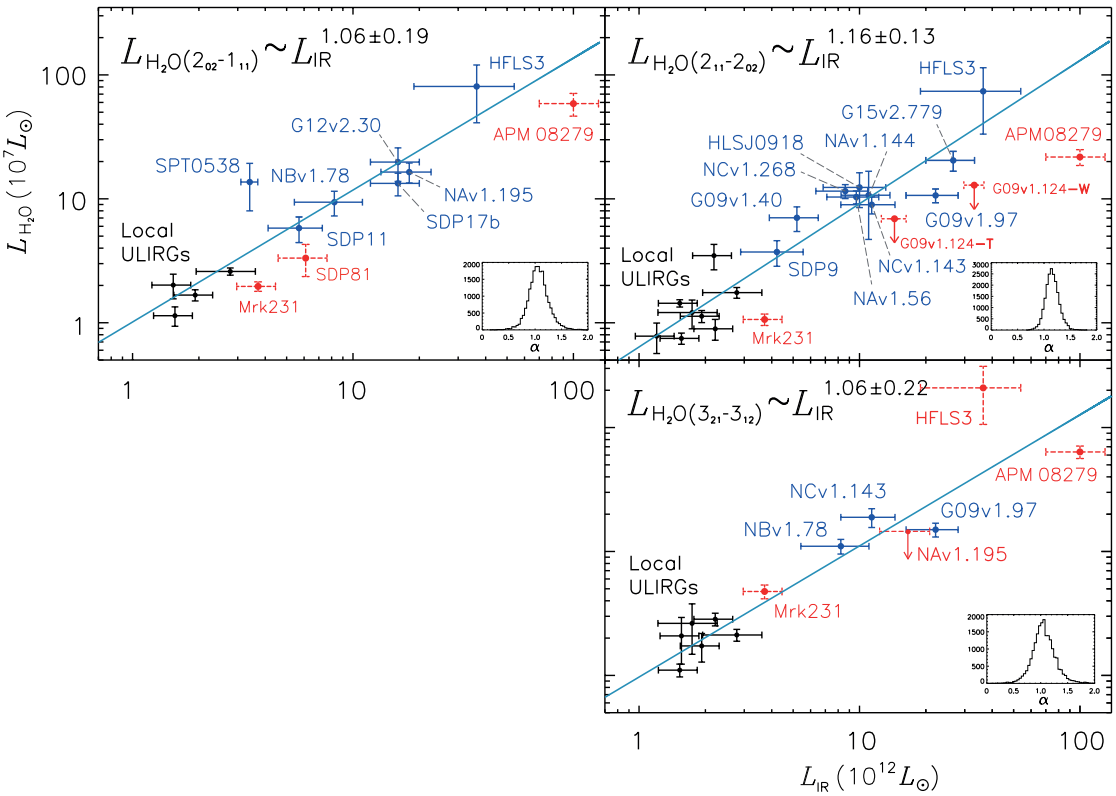

Fig. 3. Correlation between L_{IR} and L_{H_2O} in local ULIRGs and high-redshift Hy/ULIRGs. The black points represent local ULIRGs from Y13. The blue points with solid error bars are the *H*-ATLAS source in this work together with some previously published sources. Red points with dashed error bars are excluded from the fit as described in the text. Upper limits are shown in arrows. The light blue lines show the results of the fitting. The *insets* are the probability density distributions of the fitted slopes α. We find tight correlations between the luminosity of the three H_2O lines and L_{IR}, namely $L_{H_2O} \propto L_{IR}^{1.1-1.2}$.

The fitted parameters are $\alpha = 1.06 \pm 0.19$, 1.16 ± 0.13 and 1.06 ± 0.22 for H_2O line 2_{02}–1_{11}, 2_{11}–2_{02} and 3_{21}–3_{12}, respectively. Comparing with the local ULIRGs, the high-redshift lensed ones have higher L_{H_2O}/L_{IR} ratios (Table 6). These slopes confirm our first result derived from 7 H_2O detections in (O13). The slight super-linear correlations seem to indicate that far-infrared pumping play an important role in the excitation of the submm H_2O emission. This is unlike the high-J CO lines, which are determined by collisional excitation and follow the linear correlation between the CO line luminosity and L_{IR} from the local to the high-redshift Universe (Liu et al. 2015). As demonstrated in G14, using the far-infrared pumping model, the steeper than linear growth of L_{H_2O} with L_{IR} can be the result of an increasing optical depth at 100 μm (τ_{100}) with increasing L_{IR}. In local ULIRGs, the ratio of L_{H_2O}/L_{IR} is relatively low while most of them are likely to be optically thin ($\tau_{100} \sim 0.1$, G14). On the other hand, for the high-redshift lensed Hy/ULIRGs with high values of L_{IR}, the continuum optical depth at far-infrared wavelengths is expected to be high (see Sect. 4.2), indicating that the H_2O emission comes from very dense regions of molecular gas that are heavily obscured.

Similar to what we found in the local ULIRGs (Y13), we find again an anti-correlation between T_d and $L_{H_2O(3_{21}-3_{12})}/L_{IR}$. The Spearman's rank correlation coefficient for the five $H_2O(3_{21}$–$3_{12})$ detected H-ATLAS sources is $\rho = -0.9$ with a two-sided significance of its deviation from zero, $p = 0.04$. However, after including the non-detection of $H_2O(3_{21}$–$3_{12})$ in NAv1.195, the correlation is much weaker, that is to say, $\rho \lesssim -0.5$ and $p \sim 0.32$. No significant correlation has been found between T_d and $L_{H_2O(2_{02}-1_{11})}/L_{IR}$ ($\rho = -0.1$ and $p = 0.87$) nor $L_{H_2O(2_{11}-2_{02})}/L_{IR}$ ($\rho = -0.3$ and $p = 0.45$). As explained in G14, in the optically thick and very warm galaxies, the ratio of $L_{H_2O(3_{21}-3_{12})}/L_{IR}$ is expected to decrease with increasing T_d. And this anti-correlation can not be explained by optically thin conditions. However, a larger sample is needed to increase the statistical significance of this anti-correlation.

Although, it is important to stress that the luminosity of H_2O is a complex result of various physical parameters such as dust temperature, gas density, H_2O abundance and H_2O gas distribution relative to the infrared radiation field, etc, it is striking that the correlation between L_{H_2O} and L_{IR} stays linear from local young stellar objects (YSOs), in which the H_2O molecules are mainly excited by shocks and collisions, to local ULIRGs (far-infrared pumping dominated), extending ~12 orders of magnitudes (San José-García et al. 2016), implying that H_2O indeed traces the SFR proportionally, similarly to the dense gas (Gao & Solomon 2004) in the local infrared bright galaxies. However, for the high-redshift sources, the L_{H_2O} emissions are somewhat above the linear correlations which could be explained by their high τ_{100} (or large velocity dispersion). As shown in Table 6, HFLS3, with a $\tau_{100} > 1$ has extremely large ratios of L_{H_2O}/L_{IR} which are stronger than the average of our H-ATLAS sources by factors ~2 for the $J = 2$ lines and ~4 for $J = 3$ (see Fig. 3). The velocity dispersions of its H_2O lines are ~900 km s^{-1} (with uncertainties from 18% to 36%), which is larger than all our sources. For optically thick systems, larger velocity dispersion will increase the number of absorbed pumping photons, and boost the ratio of L_{H_2O}/L_{IR} (G14).

For the AGN-dominated sources (i.e. APM 08279, G09v1.124-W and Mrk 231) as shown in Fig. 3, most of them (except for the $H_2O(3_{21}$–$3_{12})$ line of Mrk 231) are well below the fitted correlation (see Sect. 4.4). This is consistent with the average value of local strong-AGN-dominated sources. The $J \lesssim 3$ H_2O lines are far-infrared pumped by the 75 and 101 μm photons, thus the very warm dust in strong-AGN-dominated sources is likely to contribute more to the L_{IR} than the $J \lesssim 3$ H_2O excitation (see also Y13).

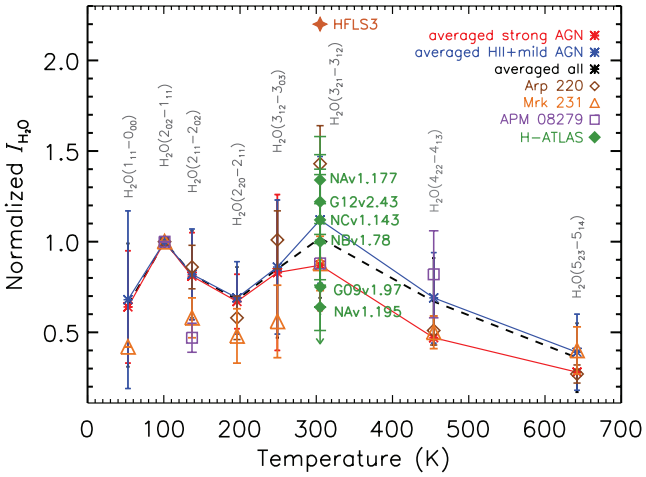

Fig. 4. Velocity-integrated flux density distribution of H_2O normalised to $I_{H_2O(2_{02}-1_{11})}$ adapted from Y13. Local averaged values are shown in black dashed line and marks. Among them, AGN-dominated sources are shown in red and star-forming dominated galaxies are shown in blue. Some individual sources are also shown in this plot as indicated by the legend. Green diamonds are the high-redshift lensed Hy/ULIRGs from this work. HFLS3 is a $z = 6.3$ high-redshift galaxy from Riechers et al. (2013).

4.2. H_2O excitation

We have detected both $J = 2$ and $J = 3$ H_2O lines in five sources out of six observed for $J = 3$ ortho-H_2O lines. By comparing the line ratios and their strength relative to L_{IR}, we are able to constrain the physical conditions of the molecular content and also the properties of the far-infrared radiation field.

To compare the H_2O excitation with local galaxies, we plot the velocity-integrated flux density of ortho-$H_2O(3_{21}$–$3_{12})$ normalised by that of para-$H_2O(2_{02}$–$1_{11})$ in our source on top of the local and high-redshift H_2O SLEDs (spectral line energy distributions) in Fig. 4. All the six high-redshift sources are located within the range of the local galaxies, with a 1σ dispersion of ~0.2. Yet for the $z = 6.34$ extreme starburst HFLS3, the value of this ratio is at least 1.7 times higher than the average value of local sources (Y13) and those of our lensed high-redshift Hy/ULIRGs at $\gtrapprox 3\sigma$ confidence level (Fig. 4). This probably traces different excitation conditions, namely the properties of the dust emission, as it is suggested in G14 that the flux ratio of $H_2O(3_{21}$–$3_{12})$ over $H_2O(2_{02}$–$1_{11})$ is the most direct tracer of the hardness of the far-infrared radiation field which powers the submm H_2O excitation. However, the line ratios are still consistent with the strong saturation limit in the far-infrared pumping model with a $T_{warm} \gtrsim 65$ K. The large scatter of the H_2O line ratio between 3_{21}–3_{12} and 2_{02}–1_{11} indicates different local H_2O excitation conditions. As far-infrared pumping is dominating the H_2O excitation, the ratio therefore reflects the differences in the far-infrared radiation field, for example, the temperature of the warmer dust that excites the H_2O gas, and the submm continuum opacity. It is now clear that far-infrared pumping is the prevailing excitation mechanism for those submm H_2O lines rather than collisional excitation (G14) in infrared bright galaxies in both the local and high-redshift

Table 6. Ratio between infrared and H_2O luminosity, and the velocity-integrated flux density ratio between different H_2O transitions.

Source	H_2O Transition	T_d (K)	$\frac{L_{H_2O(2_{11}-2_{02})}}{L_{IR}}$ ($\times10^{-6}$)	$\frac{L_{H_2O(2_{02}-1_{11})}}{L_{IR}}$ ($\times10^{-6}$)	$\frac{L_{H_2O(3_{21}-3_{12})}}{L_{IR}}$ ($\times10^{-6}$)	$\frac{I_{H_2O(3_{21}-3_{12})}}{I_{H_2O(2_{11}-2_{02})}}$	$\frac{I_{H_2O(3_{21}-3_{12})}}{I_{H_2O(2_{02}-1_{11})}}$
G09v1.97	2_{11}–2_{02}, 3_{21}–3_{12}	44 ± 1	4.8 ± 1.4	–	6.8 ± 2.0	0.9 ± 0.1	(0.8 ± 0.2)
G12v2.43	2_{02}–1_{11}, 3_{21}–3_{12}	(39 ± 2)	–	10.6 ± 2.5	15.3 ± 3.3	–	1.2 ± 0.2
NCv1.143	2_{11}–2_{02}, 3_{21}–3_{12}	40 ± 1	7.9 ± 2.5	–	16.6 ± 5.4	1.4 ± 0.1	(1.1 ± 0.4)
NAv1.195	2_{02}–1_{11}, 3_{21}–3_{12}	36 ± 1	–	9.1 ± 2.9	<6.8	–	<0.7
NAv1.177	2_{02}–1_{11}, 3_{21}–3_{12}	(32 ± 1)	–	14.9 ± 3.8	23.5 ± 5.1	–	1.3 ± 0.2
NBv1.78	2_{02}–1_{11}, 3_{21}–3_{12}	43 ± 1	–	11.4 ± 4.7	13.4 ± 4.9	–	1.0 ± 0.2
G09v1.124-W	2_{11}–2_{02}	40 ± 1	<3.9	–	–	–	–
G09v1.124-T	2_{11}–2_{02}	36 ± 1	<4.8	–	–	–	–
G09v1.40	2_{11}–2_{02}	36 ± 1	8.8 ± 3.5	–	–	–	–
SDP11	2_{02}–1_{11}	41 ± 1	–	10.2 ± 3.8	–	–	–
NCv1.268	2_{11}–2_{02}	39 ± 1	13.4 ± 3.9	–	–	–	–
NAv1.56	2_{11}–2_{02}	38 ± 1	10.7 ± 3.1	–	–	–	
SDP81	2_{02}–1_{11}	34 ± 1	–	5.4	–	–	–
NAv1.144	2_{11}–2_{02}	39 ± 1	9.7	–	–	–	–
SDP9	2_{11}–2_{02}	43 ± 1	13.5	–	–	–	–
G12v2.30	2_{02}–1_{11}	41 ± 1	–	8.1	–	–	–
SDP17b	2_{02}–1_{11}	38 ± 1	–	12.5	–	–	–
G15v2.779	2_{11}–2_{02}	41 ± 1	7.7	–	–	–	–
HFLS3	2_{02}–1_{11}, 2_{11}–2_{02}, 3_{21}–3_{12}	56^{+9}_{-12}	20.3	22.2	57.3	1.8 ± 0.6	2.2 ± 0.5
APM 08279	2_{02}–1_{11}, 2_{11}–2_{02}, 3_{21}–3_{12}	220 ± 30	2.2	6.0	6.4	1.9 ± 0.3	0.9 ± 0.1
HLSJ 0918	2_{02}–1_{11}	38 ± 3	11.4	–	–	–	–
SPT 0538	2_{02}–1_{11}	39 ± 2	–	40.3	–	–	–
local strong-AGN	2_{02}–1_{11}, 2_{11}–2_{02}, 3_{21}–3_{12}	–	3.8	6.4	6.7	1.1 ± 0.4	0.9 ± 0.3
local H II+mild-AGN	2_{02}–1_{11}, 2_{11}–2_{02}, 3_{21}–3_{12}	–	5.8	9.2	10.8	1.4 ± 0.4	1.1 ± 0.3

Notes. The luminosity ratios between each H_2O line and their total infrared, and the velocity-integrated flux density ratio of different H_2O transitions. T_d is the cold-dust temperature taken from B13, except for the ones in brackets which are not listed B13, that we infer them from single modified black-body dust SED fitting using the submm/mm photometry data listed in Table 2. All the errors quoted for T_d are significantly underestimated especially because they do not include possible effects of differential lensing and make the assumption of a single-temperature. Line ratios in brackets are derived based on the average velocity-integrated flux density ratios between 2_{11}–2_{02} and 2_{02}–1_{11} lines in local infrared galaxies. The local strong-AGN sources are the optically classified AGN-dominated galaxies and the local H II+mild-AGN sources are star-forming-dominated galaxies with possible mild AGN contribution (Y13). The first group of the sources are from this work; and the sources in the second group are the previously published sources in O13; the third group contains the previously published high-redshift detections from other works: HFLS3 (Riechers et al. 2013), APM 08279 (van der Werf et al. 2011), HLSJ 0918 (Combes et al. 2012; Rawle et al. 2014) and SPT 0538 (Bothwell et al. 2013); the last group shows the local averaged values from Y13.

Universe. The main path of far-infrared pumping related to the lines we observed here are 75 and 101 μm as displayed in Fig. 1. Therefore, the different line ratios are highly sensitive to the difference between the monochromatic flux at 75 and 101 μm. We may compare the global T_d measured from far-infrared and submm bands (B13). It includes both cold and warm dust contribution to the dust SED in the rest-frame, which is, however, dominated by cold dust observed in SPIRE bands. It is thus not surprising that we find no strong correlation between T_d and $I_{H_2O(3_{21}-3_{12})}/I_{H_2O(2_{02}-1_{11})}$ ($r \sim -0.3$). The Rayleigh-Jeans tail of the dust SED is dominated by cooler dust which is associated with extended molecular gas and less connected to the submm H_2O excitation. As suggested in G14, it is indeed the warmer dust (T_{warm}, as shown by the colour legend in Fig. 5) dominating at the Wien side of the dust SED that corresponds to the excitation of submm H_2O lines.

To further explore the physical properties of the H_2O gas content and the far-infrared dust radiation related to the submm H_2O excitation, we need to model how we can infer key parameters, such as the H_2O abundance and those determining the radiation properties, from the observed H_2O lines. For this purpose, we use the far-infrared pumping H_2O excitation model described in G14 to fit the observed L_{H_2O} together with the corresponding L_{IR}, and derive the range of continuum optical depth at 100 μm (τ_{100}), warm dust temperature (T_{warm}), and H_2O column density per unit of velocity interval ($N_{H_2O}/\Delta V$) in the five sources with both $J = 2$ and $J = 3$ H_2O emission detections. Due to the insufficient number of the inputs in the model, which are L_{H_2O} of the two H_2O lines and L_{IR}, we are only able to perform the modelling by using the pure far-infrared pumping regime. Nevertheless, our observed line ratio between $J = 3$ and $J = 2$ H_2O lines suggests that far-infrared pumping is the dominant excitation mechanism and the contribution from collisional excitation is minor (G14). The $\pm1\sigma$ contours from χ^2 fitting are shown in Fig. 5 for each warm dust temperature component (T_{warm} = 35–115 K) per source. It is clear that with two H_2O lines (one $J = 2$ para-H_2O and ortho-$H_2O(3_{12}$–$3_{12})$), we will not be able to well constrain τ_{100} and $N_{H_2O}/\Delta V$. As shown in the figure, for $T_{warm} \lesssim 75$ K, both very low and very high τ_{100} could fit the observation data together with high $N_{H_2O}/\Delta V$, while the dust with $T_{warm} \gtrsim 95$ K are likely favouring high τ_{100}. In the low continuum optical depth part in Fig. 5, as τ_{100} decreases, the model needs to increase the value of $N_{H_2O}/\Delta V$ to generate sufficient L_{H_2O} to be able to fit the observed L_{H_2O}/L_{IR}. This has been observed in some local sources with low τ_{100}, such as in NGC 1068 and NGC 6240. There are no absorption features in the far-infrared but submm H_2O emission have been detected in these sources (G14). The important feature of such sources is

Table 7. Parameters derived from far-infrared pumping model of H_2O.

Source	τ_{100}	$T_{\rm warm}$ (K)	$N_{\rm H_2O}/\Delta V$ ($\rm cm^{-2}\,km^{-1}\,s$)	$N_{\rm H_2O}$ ($\rm cm^{-2}$)
G09v1.97	1.8	45–55	$(0.3–0.6)\times10^{15}$	$(0.3–1.1)\times10^{17}$
G12v2.43	–	45–95	$\gtrsim0.7\times10^{15}$	$\gtrsim0.7\times10^{17}$
NCv1.143	7.2	45–55	$(2.0–20)\times10^{15}$	$(2.0–60)\times10^{17}$
NAv1.177	–	45–75	$\gtrsim1.0\times10^{15}$	$\gtrsim1.0\times10^{17}$
NBv1.78	2.5	45–75	$\gtrsim0.6\times10^{15}$	$\gtrsim0.6\times10^{17}$

Notes. τ_{100} is derived from Eq. (2) with errors of a few units (see text), while $T_{\rm warm}$ and $N_{\rm H_2O}/\Delta V$ are inferred from the H_2O excitation model. $N_{\rm H_2O}$ is calculated by taking a typical ΔV value range of 100–300 km s^{-1} as suggested by G14.

the lack of $J \geq 4$ H_2O emission lines. Thus, the observation of higher excitation of H_2O will discriminate between the low and high τ_{100} regimes.

Among these five sources, favoured key parameters are somewhat different showing the range of properties we can expect for such sources. Compared with the other four Hy/ULIRGs, G09v1.97 is likely to have the lowest $T_{\rm warm}$ as only dust with $T_{\rm warm} \sim 45-55$ K can fit well with the data. NCv1.143 and NAv1.177 have slightly different diagnostic which yields higher dust temperature as $T_{\rm warm} \sim 45$–75 K, while NBv1.78 and G12v2.43 tend to have the highest temperature range, $T_{\rm warm} \sim 45$–95 K. The values of $T_{\rm warm}$ are consistent with the fact that H_2O traces warm gas. We did not find any significant differences between the ranges of $N_{\rm H_2O}/\Delta V$ derived from the modelling for these five sources, although G09v1.97 tends to have lower $N_{\rm H_2O}/\Delta V$ (Table 7). As shown in Sect. 4.4, there is no evidence of AGN domination in all our sources, the submm H_2O lines likely trace the warm dust component that connect to the heavily obscured active star-forming activity. However, due to the lack of photometry data on the Wien side of the dust SEDs, we will not be able to compare the observed values of $T_{\rm warm}$ directly with the ones derived from the modelling.

By adopting the 100 μm dust mass absorption coefficient from Draine (2003) of $\kappa_{100} = 27.1$ cm^2 g^{-1}, we can derive the dust opacity by

$$\tau_{100} = \kappa_{100}\,\sigma_{\rm dust} = \kappa_{100}\left(\frac{M_{\rm dust}}{A}\right) = \kappa_{100}\left(\frac{M_{\rm dust}}{2\pi r_{\rm half}^2}\right) \quad (2)$$

where $\sigma_{\rm dust}$ is the dust mass column density, $M_{\rm dust}$ is the dust mass, A is the projected surface area of the dust continuum source and $r_{\rm half}$ is the half-light radius of the source at submm. As shown in Table 2, among the five sources in Fig. 5, the values of $M_{\rm dust}$ and $r_{\rm half}$ in G09v1.97, NCv1.143 and NBv1.78 have been derived via gravitational lensing (B13). Consequently, the derived approximate dust optical depth at 100 μm in these three sources is $\tau_{100} \approx 1.8$, 7.2 and 2.5, respectively. One should note that, the large uncertainty in both the κ_{100} and $r_{\rm half}$ of these high-redshift galaxies can bring a factor of few error budget. Nevertheless, by adopting a gas-to-dust mass ratio of $X = 100$ (e.g. Magdis et al. 2011), we can derive the gas depletion time using the following approach,

$$t_{\rm dep} = \frac{M_{\rm gas}}{SFR} = \frac{X\tau_{100}}{\Sigma_{\rm SFR}\kappa_{100}} \approx 1.8\times10^4\left(\frac{\tau_{100}}{\frac{\Sigma_{\rm SFR}}{M_\odot\,{\rm yr^{-1}\,kpc^{-2}}}}\right)\,{\rm Myr} \quad (3)$$

where $M_{\rm gas}$ is the total molecular gas mass and $\Sigma_{\rm SFR}$ is the surface SFR density derived from $L_{\rm IR}$ using Kennicutt (1998) calibration by assuming a Salpeter IMF (B13, and Table 2). The implied depletion time scale is $t_{\rm dep} \approx 35$–60 Myr with errors within a factor of two, in which the dominant uncertainties are from the assumed gas-to-dust mass ratio and the half-light radius. The $t_{\rm dep}$ is consistent with the values derived from dense gas tracers, like HCN in local (U)LIRGs (e.g. Gao & Solomon 2004; García-Burillo et al. 2012). As suggested in G14, the H_2O and HCN likely to be located in the same regions, indicate that the H_2O traces the dense gas as well. Thus, the τ_{100} derived above is likely also tracing the far-infrared radiation source that powers the submm H_2O emissions. B13 also has found that these *H*-ATLAS high-redshift Hy/ULIRGs are expected to be optically thick in the far-infrared. By adding the constrain from τ_{100} above, we can better derive the physical conditions in the sources as shown in Table 7.

From their modelling of local infrared galaxies, G14 find a range of $T_{\rm warm} = 45$–75 K, $\tau_{100} = 0.05$–0.2 and $N_{\rm H_2O}/\Delta V = (0.5–2) \times 10^{15}$ cm^{-2} km^{-1} s. The modelling results for our high-redshift sources are consistent with those in local galaxies in terms of $T_{\rm warm}$ and $N_{\rm H_2O}/\Delta V$. However, the values of τ_{100} we found at high-redshift are higher than those of the local infrared galaxies. This is consistent with the higher ratio between $L_{\rm H_2O}$ and $L_{\rm IR}$ at high-redshift (Y13) which could be explained by higher τ_{100} (G14). However, as demonstrated in an extreme sample, a very large velocity dispersion will also increase the value of $L_{\rm H_2O}/L_{\rm IR}$ within the sources with $\tau_{100} > 1$. Thus, the higher ratio can also be explained by larger velocity dispersion (not including systemic rotations) in the high-redshift Hy/ULIRGs. Compared with local ULIRGs, our *H*-ATLAS sources are much more powerful in terms of their $L_{\rm IR}$. The dense warm gas regions that H_2O traces are highly obscured with much more powerful far-infrared radiation fields, which possibly are close to the limit of maximum starbursts. Given the values of dust temperature and dust opacity, the radiation pressure $P_{\rm rad} \sim \tau_{100}\sigma T_{\rm d}/c$ (σ is Stefan-Boltzmann′s constant and c the speed of light) of our sources is about 0.8×10^{-7} erg cm^{-3}. If we assume a H_2 density $n_{\rm H_2}$ of $\sim10^6$ cm^{-3} and take $T_{\rm k} \sim 150$ K as suggested in G14, the thermal pressure $P_{\rm th} \sim n_{\rm H_2}k_{\rm B}T_{\rm k} \sim 2\times10^{-8}$ erg cm^{-3} ($k_{\rm B}$ is the Boltzmann constant and $T_{\rm k}$ is the gas temperature). Assuming a turbulent velocity dispersion of $\sigma_{\rm v} \sim 20$–50 km s^{-1} (Bournaud et al. 2015) and taking molecular gas mass density $\rho \sim 2\mu n_{\rm H_2}$ (2μ is the average molecular mass) would yield for the turbulent pressure $P_{\rm turb} \sim \rho\sigma_{\rm v}^2/3 \sim 4\times10^{-6}$ erg cm^{-3}. This might be about an order of magnitude larger than $P_{\rm rad}$ and two orders of magnitude larger than $P_{\rm th}$, but we should note that all values are very uncertain, especially $P_{\rm turb}$ which could be uncertain by, at maximum, a factor of a few tens. Therefore, keeping in mind their large uncertainties, turbulence and/or radiation are likely to play an important role in limiting the star formation.

4.3. Comparison between H_2O and CO

The velocity-integrated flux density ratio between submm H_2O and submm CO lines with comparable frequencies is 0.02–0.03 in local PDRs such as Orion and M 82 (Weiß et al. 2010). But this ratio in local ULIRGs (Y13) and in *H*-ATLAS high-redshift Hy/ULIRGs is much higher, from 0.4 to 1.1 (Tables 3 and 4). The former case is dominated by typical PDRs, where CO lines are much stronger than H_2O lines, while the latter sources shows clearly a different excitation regime, in which H_2O traces the central core of warm, dense and dusty molecular gas which is about a few hundred parsec (González-Alfonso et al. 2010) in diameter in local ULIRGs and highly obscured even at far-infrared.

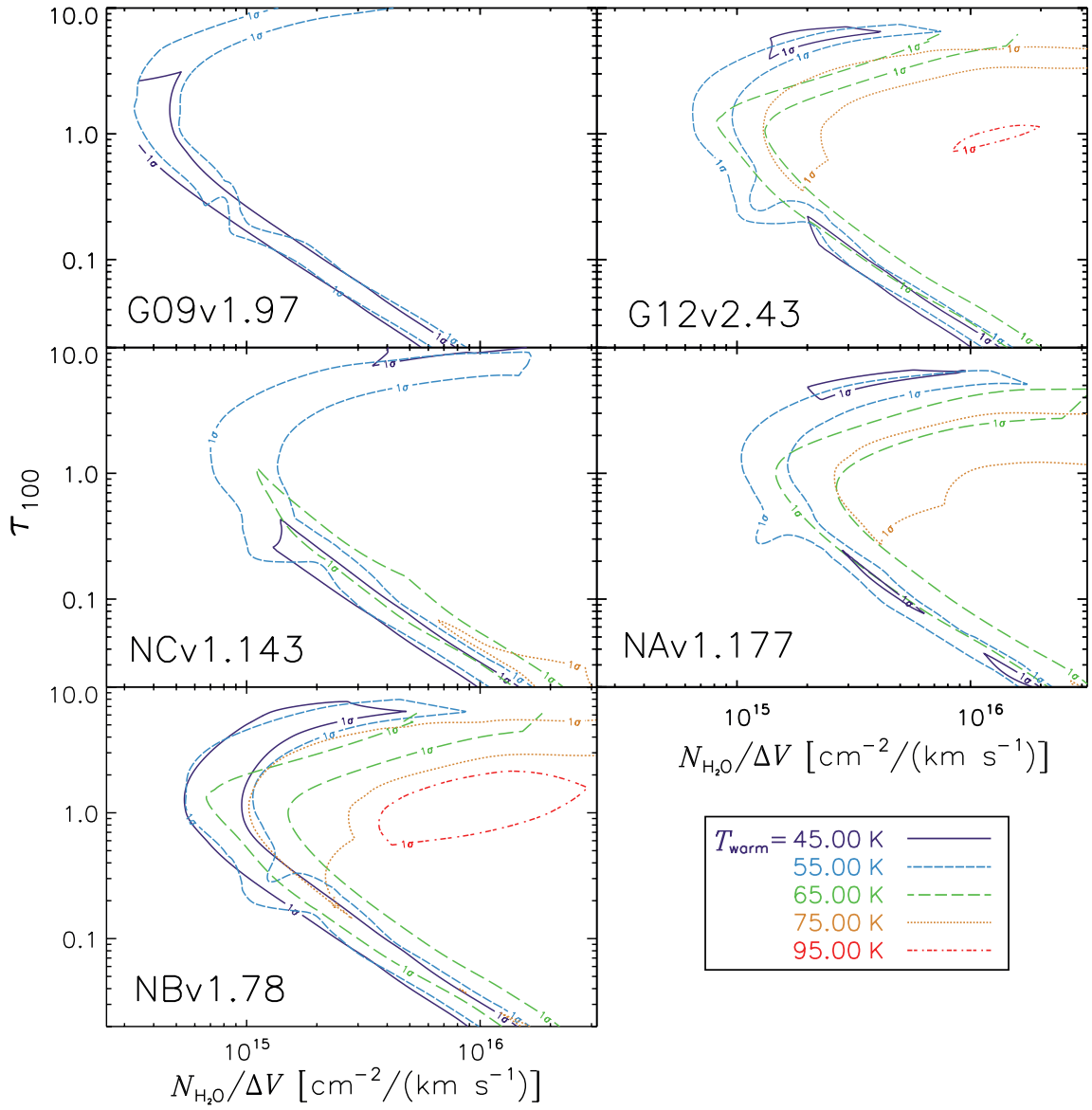

Fig. 5. Parameter space distribution of the H_2O far-infrared pumping excitation modelling with observed para-H_2O 2_{02}–1_{11} or 2_{11}–2_{02} and ortho-$H_2O(3_{21}$–$3_{12})$ in each panel. $\pm1\sigma$ contours are shown for each plot. Different colours with different line styles represent different temperature components of the warm dust as shown in the legend. The explored warm dust temperature range is from 35 K to 115 K. The temperature contours that are unable to fit the data are not shown in this figure. From the figure, we are able to constrain the τ_{100}, T_{warm} and $N_{H_2O}/\Delta V$ for the five sources. However, there are strong degeneracies. Thus, we need additional information, such as the velocity-integrated flux densities of $J \geq 4$ H_2O lines, to better constrain the physical parameters.

Generally, submm H_2O lines are dominated by far-infrared pumping that traces strong far-infrared dust continuum emission, which is different from the regime of molecular gas traced by collisional excited CO lines. In the active star-forming nucleus of the infrared-bright galaxies, the far-infrared pumped H_2O is expected to trace directly the far-infrared radiation generated by the intense star formation, which can be well correlated with the high-J CO lines (Liu et al. 2015). Thus there is likely to be a correlation between the submm H_2O and CO emission. From our previous observations, most of the H_2O and CO line profiles are quite similar from the same source in our high-redshift lensed Hy/ULIRGs sample (Fig. 2 of O13). In the present work, we again find similar profiles between H_2O and CO in terms of their FWHM with an extended sample (Table 3 and 4). In both cases the FWHMs of H_2O and CO are generally equal within typical 1.5σ errors (see special discussion for each source in Appendix A).

As the gravitational lensing magnification factor is sensitive to spatial alignment, the similar line profiles could thus suggest similar spatial distributions of the two gas tracers. However, there are a few exceptional sources, such as SDP 81 (ALMA Partnership, Vlahakis et al. 2015) and HLSJ0918 (Rawle et al. 2014). In both cases, the H_2O lines are lacking the blue velocity component found in the CO line profiles. Quite different from the rest sources, in SDP 81 and HLSJ0918, the CO line profiles are complicated with multiple velocity components. Moreover, the velocity-integrated flux density ratios between these CO components may vary following

the excitation level (different J_{up}). Thus, it is important to analyse the relation between different CO excitation components (from low-J to high-J) and H_2O. Also, high resolution observation is needed to resolve the multiple spatial gas components and compare the CO emission with H_2O and dust continuum emission within each component.

4.4. AGN content

It is still not clear how a strong AGN could affect the excitation of submm H_2O in both local ULIRGs and high-redshift Hy/ULIRGs. Nevertheless, there are some individual studies addressing this question. For example, in APM 08279, van der Werf et al. (2011) found that AGN is the main power source that excites the high-J H_2O lines and also enriches the gas-phase H_2O abundance. Similar conclusion has also been drawn by González-Alfonso et al. (2010) that in Mrk 231 the AGN accounts for at least 50% contribution to the far-infrared radiation that excites H_2O. From the systematic study of local sources (Y13), slightly lower values of L_{H_2O}/L_{IR} are found in strong-AGN-dominated sources. In the present work, the decreasing ratio of L_{H_2O}/L_{IR} with AGN is clearly shown in Fig. 3 where Mrk 231, G09v1.124-W and APM 08279 are below the correlation by factors between 2 and 5 with less than 30% uncertainties (except the $H_2O(3_{21}–1_{23})$ line of Mrk 231).

In the far-infrared pumping regime, the buried AGN will provide a strong far-infrared radiation source that will pump the H_2O lines. However, the very warm dust powered by the AGN will increase the value of L_{IR} faster than the number of $\geq 75\,\mu$m photons that is dominating the excitation of $J \leq 3$ H_2O lines (e.g. Kirkpatrick et al. 2015). If we assume that the strength of the H_2O emission is proportional to the number of pumping photons, then in the strong-AGN-dominated sources, the ratio of L_{H_2O}/L_{IR} will decrease since much warmer dust is present. Moreover, strong radiation from the AGN could dissociate the H_2O molecules.

To evaluate the AGN contribution to the *H*-ATLAS sources, we extracted the 1.4 GHz radio flux from the FIRST radio survey (Becker et al. 1995) listed in Table 2. By comparing the far-infrared and radio emission using the q parameter (Condon 1992), $q \equiv \log(L_{FIR}/3.75 \times 10^{12}\,\mathrm{W}) - \log(L_{1.4\,GHz}/1\,\mathrm{W\,Hz^{-1}})$, we derive values of q from 1.9 to 2.5 in our sources. These values follow the value 2.3 ± 0.1 found by Yun et al. (2001) for non strong-radio AGN. This may suggest that there is also no significant indication of a high radio contribution from AGN. This is also confirmed by the Wide-field Infrared Survey Explorer (WISE, Wright et al. 2010), which does not detect our sources at 12 μm and 22 μm. However, rest-frame optical spectral observations show that G09v1.124-W is rather a powerful AGN (Oteo et al., in prep.), which is the only identified AGN-dominated source in our sample.

5. Detection of H_2O^+ emission lines

H_2O can be formed through both solid-state and gas-phase chemical reactions (van Dishoeck et al. 2013). On dust-grain mantles, surface chemistry dominates the formation of H_2O molecules. Then they can be released into the ISM gas through sublimation. In the gas phase, H_2O can be produced through two routes: the neutral-neutral reaction, usually related to shocks, creates H_2O via $O + H_2 \longrightarrow OH + H$; $OH + H_2 \longrightarrow H_2O + H$ at high temperature ($\gtrsim$300 K). At lower temperature ($\lesssim$100 K), the ion-neutral reactions in photon-dominated regions (PDRs), cosmic-ray-dominated regions and X-ray-dominated regions (e.g. Meijerink & Spaans 2005) generate H_2O from O, H^+, H_3^+ and H_2, with intermediates such as O^+, OH^+, H_2O^+ and H_3O^+, and finally $H_3O^+ + e \longrightarrow H_2O + H$. However, classical PDRs are not likely linked to these highly excited submm H_2O emissions (Y13). Therefore, H_2O^+ lines are important for distinguishing between shock- or ion-chemistry origin for H_2O in the early Universe, indicating the type of physical regions in these galaxies: shock-dominated regions, cosmic-ray-dominated regions or X-ray-dominated regions. Indeed, they can be among the most direct tracers of the cosmic-ray or/and X-ray ionization rate (e.g. Gérin et al. 2010; Neufeld et al. 2010; González-Alfonso et al. 2013) of the ISM, which regulates the chemistry and influences many key parameters, for example, X-factor (Bell et al. 2007) that connects the CO luminosity to the H_2 mass. Moreover, the significant detections of H_2O^+ emission in high-redshift Hy/ULIRGs could help us understanding H_2O formation in the early Universe.

When observing our sources with redshift $z \gtrsim 3.3$, it is possible to cover all the following lines with the NOEMA WideX bandwidth: para-$H_2O(2_{11}–2_{02})$ at 752 GHz and four ortho-H_2O^+ lines (two intertwined fine structure doublets of two different lines whose frequencies almost coincide by chance): $2_{02}–1_{11\,(5/2–3/2)}$ at 742.1 GHz, $2_{11}–2_{02\,(5/2–3/2)}$ at 742.3 GHz, $2_{02}–1_{11\,(3/2–3/2)}$ at 746.3 GHz and $2_{11}–2_{02\,(5/2–5/2)}$ at 746.5 GHz, in the 3.6 GHz band simultaneously (the rest-frame frequencies are taken from the CDMS catalogue: `http://www.astro.uni-koeln.de/cdms`, see energy level diagram of H_2O^+ in Fig. 1 and the full spectra in Fig. 6). Additionally, within this range, we can also cover the $H_2^{18}O(2_{11}–2_{02})$ line at 745.3 GHz. There are three sources of our sample that have been observed in such a frequency setup: NCv1.143, NCv1.268 and G09v1.97. We have also included the source G15v2.779 from our previous observation (O13), in which we have covered both $H_2O(2_{11}–2_{02})$ at 752 GHz and H_2O^+ lines around 746 GHz. We have detected both main lines of H_2O^+ in NCv1.143, and tentatively detected one line in G09v1.97 and G15v2.779 (Fig. 6). For NCv1.268, due to the large noise level and the complex line profile, we were not able to really identify any H_2O^+ line detection.

As shown in Fig. 6, in NCv1.143, the dominant H_2O^+ fine structure lines $2_{11}–2_{02\,(5/2–5/2)}$ at 746.5 GHz and $2_{02}–1_{11\,(5/2–3/2)}$ at 742.1 GHz are well detected. The velocity-integrated flux densities of the two lines from a two-Gaussian fit are 1.9 ± 0.3 and 1.6 ± 0.2 Jy km s^{-1}, respectively. These are the approximate velocity-integrated flux densities of the dominant H_2O^+ lines $2_{11}–2_{02\,(5/2–5/2)}$ and $2_{02}–1_{11\,(5/2–3/2)}$ if neglecting the minor contributions from H_2O^+ lines $2_{02}–1_{11\,(3/2–3/2)}$ at 746.2 GHz and $2_{11}–2_{02\,(5/2–3/2)}$ at 742.3 GHz. However, the H_2O^+ line profile at 746.5 GHz is slightly wider than the H_2O line (Fig. 6), probably due to a contribution from the fairly weak fine structure line $H_2O^+(2_{02}–1_{11})_{(3/2–3/2)}$ at 746.3 GHz. The ratio between total velocity-integrated flux density of the H_2O^+ lines and $H_2O(2_{11}–2_{02})$ is 0.60 ± 0.07 (roughly 0.3 for each dominant H_2O^+ line), being consistent with the average value from the local infrared galaxies (Y13)[3]. In order to derive the velocity-integrated flux density of each fine structure doublets around 742 and 746 GHz, we have also performed a four-Gaussian fit with fixed line positions (equal to $\nu_{rest}/(1+z)$) and linewidth (equals to that of $H_2O(2_{11}–2_{02})$). We find the velocity-integrated

[3] As suggested by González-Alfonso et al. (2013), due to the very limited spectral resolution of *Herschel*/SPIRE FTS, the ortho-$H_2O^+(2_{02}–1_{11})_{(3/2–3/2)}$ line at 746.5 GHz quoted in Y13 is actually dominated by ortho-$H_2O^+(2_{11}–2_{02})_{(5/2–5/2)}$, considering their likely excitation and relative strength.

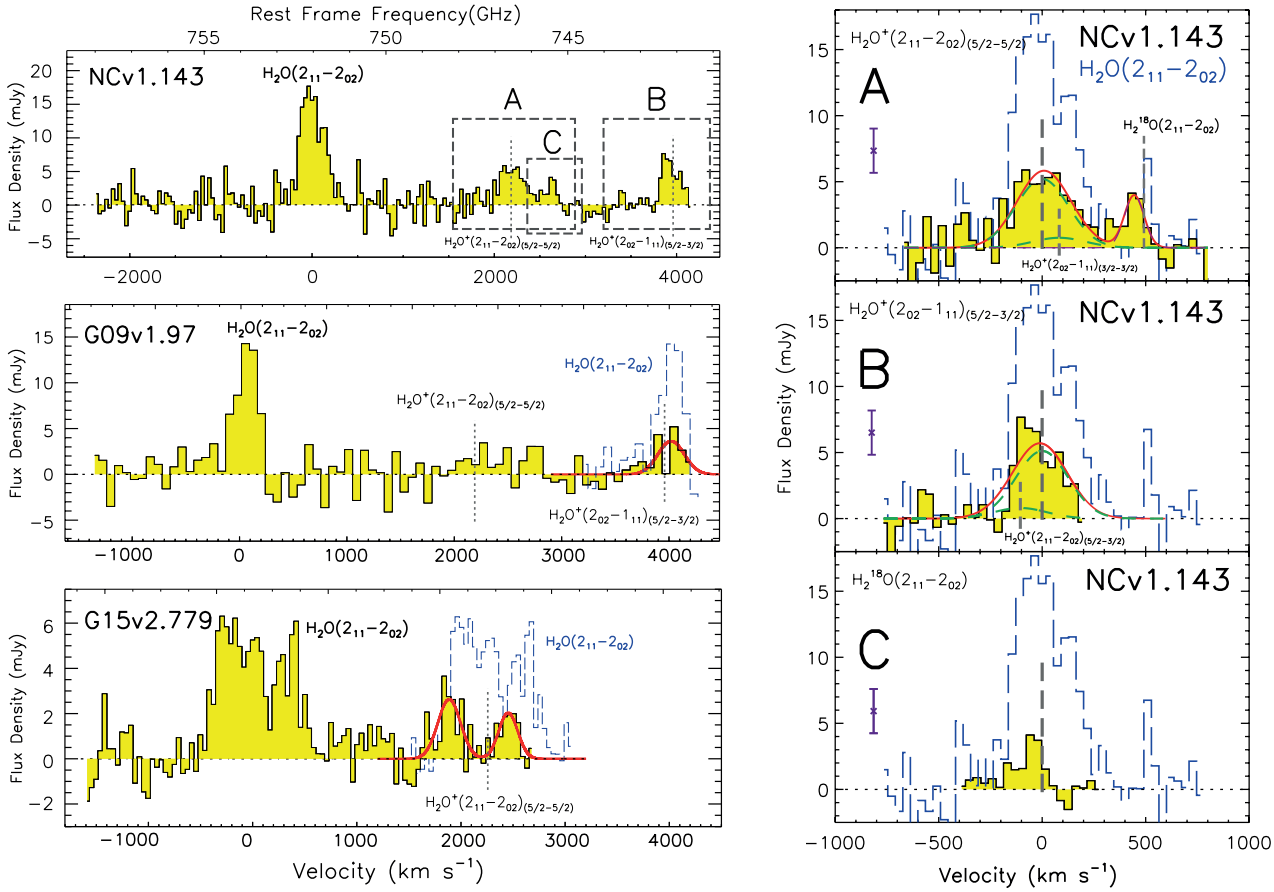

Fig. 6. *Left panel*: *from top to bottom* are the full NOEMA spectrum at $\nu_{\rm rest} \sim 750$ GHz of NCv1.143, G09v1.97 and G15v2.779, respectively. The reference frequency is the redshifted frequency of the line $H_2O(2_{11}–2_{02})$. The frequencies of the main $H_2O^+(2_{11}–2_{02})_{(5/2–5/2)}$ and $H_2O^+(2_{02}–1_{11})_{(5/2–3/2)}$ lines are indicated by grey vertical dashed lines. The three dashed squares in the spectrum of NCv1.143 show the position of each zoom-in spectrum of the H_2O^+ (or the $H_2^{18}O$) as displayed in *the right panel* indicated by the A, B or C. The superposed blue dashed histograms represents the spectra of $H_2O(2_{11}–2_{02})$ centred at the frequencies of the H_2O^+ lines. Note that, in many cases, the observed frequency ranges (yellow histograms) do not include the full expected profiles for the H_2O^+ lines. The red curve represents the Gaussian fitting to the spectra. We have detected both H_2O^+ lines in NCv1.143, and tentatively detected $H_2O^+(2_{02}–1_{11})_{(5/2–3/2)}$ in G09v1.97 and $H_2O^+(2_{11}–2_{02})_{(5/2–5/2)}$ in G15v2.779. *Right panel*: *from top to bottom* are the spectra dominated by lines of $H_2O^+(2_{11}–2_{02})_{(5/2–5/2)}$, $H_2O^+(2_{02}–1_{11})_{(3/2–3/2)}$ and $H_2^{18}O(2_{11}–2_{02})$, respectively, displayed as the filled yellow histograms. The reference frequency is the frequency of each of these lines. Weaker $H_2O^+(2_{02}–1_{11})_{(3/2–3/2)}$ and $H_2O^+(2_{11}–2_{02})_{(5/2–3/2)}$ components are indicated by additional grey vertical dashed lines. The superposed blue dashed histograms represent the spectra of para-$H_2O(2_{11}–2_{02})$ in NCv1.143 centred at each line frequency. The red curve represents the Gaussian fitting to the spectra, and the green dashed curves are the decomposed Gaussian profiles for each fine structure line. The violet error bar indicates the $\pm1\sigma$ uncertainties of the spectrum.

flux densities of the two fine structure lines of $H_2O^+(2_{11}–2_{02})$ are 1.6 ± 0.5 and 0.3 ± 0.4 Jy/km s^{-1}, while they are 1.6 ± 0.4 and 0.2 ± 0.5 Jy/km s^{-1} for the two fine structure lines of $H_2O^+(2_{02}–1_{11})$ (Table 8). We should note that these fitting results have much larger uncertainties due to the blending. Nevertheless, they are consistent with the earlier fitting results without de-blending. The similarity of the velocity-integrated flux densities between the $H_2O^+(2_{02}–1_{11})$ and $H_2O^+(2_{11}–2_{02})$ lines is in good agreement with the regime of far-infrared pumping as submm H_2O (González-Alfonso et al. 2013). As a first approximation, if these H_2O^+ lines are optically thin and we ignore the additional pumping from ortho-H_2O^+ 2_{02} to ortho-H_2O^+ $J = 3$ energy levels, the statistical equilibrium applied to energy level $2_{02\,5/2}$ implies that all population arriving per second at $2_{02\,5/2}$ should be equal to all population leaving the level per second.

After subtracting the Gaussian profiles of all the H_2O^+ lines in the spectrum, we find a 3σ residual in terms of the velocity-integrated flux density around 745.3 GHz ($I = 0.6 \pm 0.2$ Jy km s^{-1}, see Fig. 6). This could be a tentative detection of the $H_2^{18}O(2_{11}–2_{02})$ line at 745.320 GHz. The velocity-integrated flux density ratio of $H_2^{18}O(2_{11}–2_{02})$ over $H_2O(2_{11}–2_{02})$ in NCv1.143 would hence be ~0.1. If this tentative detection was confirmed, it would show that ALMA could easily study such lines. But sophisticated models will be needed to infer isotope ratios.

The spectrum of the $H_2O(2_{11}–2_{02})$ line in G09v1.97 covers both the two main H_2O^+ fine structure lines (Fig. 6). However, due to the limited sensitivity, we have only tentatively detected the $H_2O^+(2_{02}–1_{11})_{(5/2–3/2)}$ line just above 3σ (neglecting the minor contribution from $H_2O^+(2_{11}–2_{02})_{(5/2–3/2)}$), and the velocity-integrated flux density is 1.4 ± 0.4 Jy km s^{-1} using a single Gaussian fit. We did not perform any line de-blending for this source considering the data quality. The H_2O^+ line profile is in good agreement with that of the H_2O (blue dashed histogram

Table 8. Observed ortho-H_2O^+ fine structure line parameters of the high-redshift *H*-ATLAS lensed HyLIRGs.

Source	H_2O^+ transition	ν_{rest} (GHz)	ν_{line} (GHz)	$I_{H_2O^+}$ (Jy km s^{-1})
NCv1.143	2_{11}–2_{02} $_{(5/2-5/2)}$	746.5	163.53	1.6 ± 0.5
	2_{02}–1_{11} $_{(3/2-3/2)}$	746.3	163.48	0.2 ± 0.5
	2_{11}–2_{02} $_{(5/2-3/2)}$	742.3	162.61	0.3 ± 0.4
	2_{02}–1_{11} $_{(5/2-3/2)}$	742.1	162.56	1.6 ± 0.4
G09v1.97	2_{02}–1_{11} $_{(5/2-3/2)}$	742.1	160.14	1.4 ± 0.4
G15v2.779	2_{11}–2_{02} $_{(5/2-5/2)}$	746.5	142.35	1.2 ± 0.3

Notes. The H_2O^+ $(2_{02}$–$1_{11})$ $_{(5/2-3/2)}$ line in G09v1.97 is blended by $(2_{11}$–$2_{02})$ $_{(5/2-3/2)}$, and H_2O^+ $(2_{11}$–$2_{02})$ $_{(5/2-5/2)}$ line in G15v2.779 is blended by $(2_{02}$–$1_{11})$ $_{(3/2-3/2)}$. However, the contribution from the latter in each case is small, likely less than 20% as shown in the case of the H_2O^+ lines in NCv1.143. Note that the quoted uncertainties do not include the missing parts of the spectra cut by the limited observed bandwidth (Fig. 6).

in Fig. 7). The velocity-integrated flux density of the undetected $H_2O^+(2_{11}$–$2_{02})$ $_{(5/2-5/2)}$ line could also be close to this value as discussed in the case of NCv1.143, yet somewhat lower and not detected in this source. More sensitive observation should be conducted to further derive robust line parameters.

We have also tentatively detected the $H_2O^+(2_{11}$–$2_{02})$ $_{(5/2-5/2)}$ line in G15v2.779 ($S/N \sim 4$ by neglecting the minor contribution from the $H_2O^+(2_{02}$–$1_{11})$ $_{(3/2-3/2)}$ line). The line profile is in good agreement with that of $H_2O(2_{11}$–$2_{02})$ (blue dashed histogram in Fig. 6). The velocity-integrated flux density derived from a double-peak Gaussian fit is 1.2 ± 0.3 Jy km s^{-1} (we did not perform any line de-blending for the H_2O^+ doublet considering the spectral noise level). There could be a minor contribution from the $H_2O^+(2_{02}$–$1_{11})$ $_{(3/2-3/2)}$ line to the velocity-integrated flux density. However, such a contribution is likely to be negligible as in the case of NCv1.143. The contribution is also within the uncertainty of the velocity-integrated flux density. Nevertheless, the position of H_2O^+ has a small blue-shift compared with H_2O, but note that the blue part of the line is cut by the limited observed bandwidth (yellow histogram).

After including the local detections of H_2O^+ lines from Y13 (Table B.1), we find a tight linear correlation between the luminosity of H_2O and the two main lines of H_2O^+ (slopes equal to 1.03 ± 0.06 and 0.91 ± 0.07, see Fig. 7). However, one should keep in mind that, because the local measurement done by *Herschel* SPIRE/FTS (Naylor et al. 2010) has rather low spectral resolution, neither $H_2O^+(2_{11}$–$2_{02})$ $_{(5/2-3/2)}$ and $H_2O^+(2_{02}$–$1_{11})$ $_{(5/2-3/2)}$, nor $H_2O^+(2_{11}$–$2_{02})$ $_{(5/2-5/2)}$ and $H_2O^+(2_{02}$–$1_{11})$ $_{(3/2-3/2)}$ can be spectroscopically resolved. In the correlation plot (Fig. 7) and Table B.1, we use the total luminosity from the 742 GHz and 746 GHz lines, by assuming the contribution from $H_2O^+(2_{11}$–$2_{02})$ $_{(5/2-3/2)}$ and $H_2O^+(2_{02}$–$1_{11})$ $_{(3/2-3/2)}$ to the velocity-integrated flux density of the line at 742 GHz and 746 GHz is small (∼18%) and does not vary significantly between different sources. Hence, the velocity-integrated flux density ratio between each of the two dominant H_2O^+ fine structure lines and H_2O in NCv1.143, G15v2.779 and G09v1.97 is ∼0.3 (uncertainties are less than 30%), which is consistent with local galaxies as shown in the figure. This ratio is much larger than the abundance ratio of $H_2O^+/H_2O \sim 0.05$ found in Arp 220, an analogue of high-redshift ULIRGs (Rangwala et al. 2011).

As discussed above, the AGN contribution to the excitation of the submm lines of most of our sources appears to be minor. Thus, the formation of H_2O^+ is likely dominated by cosmic-ray ionization, rather than X-ray ionization. Given the

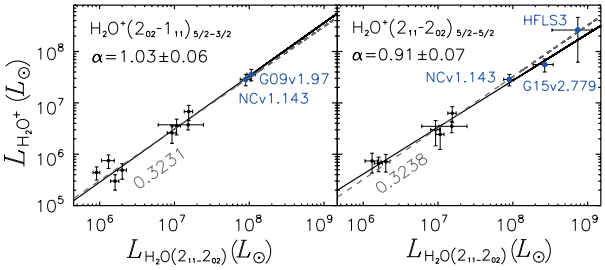

Fig. 7. Correlation between the luminosity of $J = 2$ ortho-H_2O^+ and para-$H_2O(2_{11}$–$2_{02})$. The fitted function is $L_{H_2O^+} \propto L_{H_2O}{}^{\alpha}$. We found a very good correlation between $L_{H_2O^+}$ and L_{H_2O} with a slope close to one. Black points are from the local ULIRGs as listed in Table B.1. Dark blue ones are high-redshift starbursts from this work. Black solid lines indicate the χ^2 fitting results while the grey dashed lines and the grey annotations represent the average ratio between the $L_{H_2O^+}$ and L_{H_2O}.

average luminosity ratio of $H_2O^+/H_2O \sim 0.3 \pm 0.1$ shown in Fig. 7, Meijerink et al. (2011) suggest a cosmic-ray ionization rate of 10^{-14}–10^{-13} s^{-1}. Such high cosmic-ray ionization rates drive the ambient ionization degree of the ISM to 10^{-3}–10^{-2}, rather than the canonical 10^{-4}. Therefore, in the gas phase, an ion-neutral route likely dominates the formation of H_2O. However, H_2O can also be enriched through the water-ice sublimation that releases H_2O into the gas-phase ISM. As the upper part, ∼90 K, of the possible range for T_{warm} is close to the sublimation temperature of water ice. Hence, the high H_2O abundance ($N_{H_2O} \gtrapprox 0.3 \times 10^{17}$ cm^{-2}, see Sect. 4.2) observed is likely to be the result of ion chemistry dominated by high cosmic-ray ionization and/or perhaps water ice desorption. However, further observation of H_2O^+ lines of different transitions and a larger sample is needed to constrain the contribution to H_2O formation from neutral-neutral reactions dominated by shocks.

6. Conclusions

In this paper, we report a survey of submm H_2O emission at redshift $z \sim 2$–4, by observing a higher excited ortho-$H_2O(3_{21}$–$3_{12})$ in 6 sources and several complementary $J = 2$ para-H_2O emission lines in the warm dense cores of 11 high-redshift lensed extreme starburst galaxies (Hy/ULIRGs) discovered by *H*-ATLAS. So far, we have detected an H_2O line in most of our observations of a total sample of 17 high-redshift lensed galaxies, in other words, we have detected both $J = 2$ para-H_2O and $J = 3$ ortho-H_2O lines in five, and in ten other sources only one $J = 2$ para-H_2O line. In these high-redshift Hy/ULIRGs, H_2O is the second strongest molecular emitter after CO within the submm band, as in local ULIRGs. The spatially integrated H_2O emission lines have a velocity-integrated flux density ranging from 4 to 15 Jy km s^{-1}, which yields the apparent H_2O emission luminosity, μL_{H_2O} ranging from ∼6–22 × 10^8 $L_\odot$. After correction for gravitation lensing magnification, we obtained the intrinsic L_{H_2O} for para-H_2O lines 2_{02}–1_{11}, 2_{11}–2_{02} and ortho-$H_2O(3_{21}$–$3_{12})$. The luminosities of the three H_2O lines increase with L_{IR} as $L_{H_2O} \propto L_{IR}{}^{1.1-1.2}$. This correlation indicates the importance of far-infrared pumping as a dominant mechanism of H_2O excitation. Comparing with $J = 3$ to $J = 6$ CO lines, the linewidths between H_2O and CO are similar, and the velocity-integrated flux densities of H_2O and CO are comparable. The similarity in line profiles suggests that these two molecular species possibly trace similar intense star-forming regions.

Using the far-infrared pumping model, we have analysed the ratios between $J = 2$ and $J = 3$ H_2O lines and L_{H_2O}/L_{IR} in 5 sources with both J H_2O lines detected. We have derived the

ranges of the warm dust temperature ($T_{\rm warm}$), the H_2O column density per unit velocity interval ($N_{H_2O}/\Delta V$) and the optical depth at 100 μm (τ_{100}). Although there are strong degeneracies, these modelling efforts confirm that, similar to those of local ULIRGs, these submm H_2O emissions in high-redshift Hy/ULIRGs trace the warm dense gas that is tightly correlated with the massive star forming activity. While the values of $T_{\rm warm}$ and N_{H_2O} (by assuming that they have similar velocity dispersion ΔV) are similar to the local ones, τ_{100} in the high-redshift Hy/ULIRGs is likely to be greater than 1 (optically thick), which is larger than τ_{100} = 0.05–0.2 found in the local infrared galaxies. However, we notice that the parameter space is still not well constrained in our sources through H_2O excitation modelling. Due to the limited excitation levels of the detected H_2O lines, we are only able to perform the modelling with pure far-infrared pumping.

The detection of relatively strong H_2O^+ lines opens the possibility to help understanding the formation of such large amount of H_2O. In these high-redshift Hy/ULIRGs, the H_2O formation is likely to be dominated by ion-neutral reactions powered by cosmic-ray-dominated regions. The velocity-integrated flux density ratio between H_2O^+ and H_2O ($I_{H_2O^+}/I_{H_2O} \sim 0.3$), is remarkably constant from low to high-redshift, reflecting similar conditions in Hy/ULIRGs. However, more observations of H_2O^+ emission/absorption and also OH^+ lines are needed to further constrain the physical parameters of the cosmic-ray-dominated regions and the ionization rate in those regions.

We have demonstrated that the submm H_2O emission lines are strong and easily detectable with NOEMA. Being a unique diagnostic, the H_2O emission offers us a new approach to constrain the physical conditions in the intense and heavily obscured star-forming regions dominated by far-infrared radiation at high-redshift. Follow-up observations of other gas tracers, for instance, CO, HCN, H_2O^+ and OH^+ using the NOEMA, IRAM 30m and JVLA will complement the H_2O diagnostic of the structure of different components, dominant physical processes, star formation and chemistry in high-redshift Hy/ULIRGs.

With unprecedented spatial resolution and sensitivity, the image from the ALMA long baseline campaign observation of SDP 81 (also known as *H*-ATLAS J090311.6+003906, ALMA Partnership, Vlahakis et al. 2015; Dye et al. 2015; Rybak et al. 2015), shows the resolved structure of the dust, CO and H_2O emission in the z = 3 ULIRG. With careful reconstruction of the source plane images, ALMA will help to resolve the submm H_2O emission in high-redshift galaxies into the scale of giant molecular clouds, and provide a fresh view of detailed physics and chemistry in the early Universe.

Acknowledgements. We thank our referee for the very detail comments and suggestions which have improved the paper. This work was based on observations carried out with the IRAM Interferometer NOEMA, supported by INSU/CNRS (France), MPG (Germany), and IGN (Spain). The authors are grateful to the IRAM staff for their support. C.Y. thanks Claudia Marka and Nicolas Billot for their help of the IRAM 30 m/EMIR observation. C.Y. also thanks Zhi-Yu Zhang and Iván Oteo for insightful discussions. C.Y., A.O. and Y.G. acknowledge support by NSFC grants #11311130491, #11420101002 and CAS Pilot B program #XDB09000000. C.Y. and Y.G. also acknowledge support by NSFC grants #11173059. C.Y., A.O., A.B. and Y.G. acknowledge support from the Sino-French LIA-Origin joint exchange program. E.G.-A. is a Research Associate at the Harvard-Smithsonian Center for Astrophysics, and thanks the Spanish Ministerio de Economía y Competitividad for support under projects FIS2012-39162-C06-01 and ESP2015-65597-C4-1-R, and NASA grant ADAP NNX15AE56G. RJI acknowledges support from ERC in the form of the Advanced Investigator Programme, 321302, COSMICISM. US participants in *H*-ATLAS acknowledge support from NASA through a contract from JPL. Italian participants in *H*-ATLAS acknowledge a financial contribution from the agreement ASI-INAF I/009/10/0. SPIRE has been developed by a consortium of institutes led by Cardiff Univ. (UK) and including: Univ. Lethbridge (Canada); NAOC (China); CEA, LAM (France); IFSI, Univ. Padua (Italy); IAC (Spain); Stockholm Observatory (Sweden); Imperial College London, RAL, UCL-MSSL, UKATC, Univ. Sussex (UK); and Caltech, JPL, NHSC, Univ. Colorado (USA). This development has been supported by national funding agencies: CSA (Canada); NAOC (China); CEA, CNES, CNRS (France); ASI (Italy); MCINN (Spain); SNSB (Sweden); STFC, UKSA (UK); and NASA (USA). C.Y. is supported by the China Scholarship Council grant (CSC No. 201404910443).

References

ALMA Partnership, Vlahakis, C., Hunter, T. R., Hodge, J. A., et al. 2015, ApJ, 808, L4
Becker, R. H., White, R. L., & Helfand, D. J. 1995, ApJ, 450, 559
Bell, T. A., Viti, S., & Williams, D. A. 2007, MNRAS, 378, 983
Bothwell, M. S., Aguirre, J. E., Chapman, S. C., et al. 2013, ApJ, 779, 67
Bournaud, F., Daddi, E., Weiß, A., et al. 2015, A&A, 575, A56
Bradford, C. M., Bolatto, A. D., Maloney, P. R., et al. 2011, ApJ, 741, L37
Bussmann, R. S., Pérez-Fournon, I., Amber, S., et al. 2013, ApJ, 779, 25 (B13)
Calanog, J. A., Fu, H., Cooray, A., et al. 2014, ApJ, 797, 138
Casey, C. M., Narayanan, D., & Cooray, A. 2014, Phys. Rep., 541, 45
Combes, F., Rex, M., Rawle, T. D., et al. 2012, A&A, 538, L4
Condon, J. J. 1992, ARA&A, 30, 575
Cooray, A., Calanog, J., Wardlow, J. L., et al. 2014, ApJ, 790, 40
Draine, B. T. 2003, ARA&A, 41, 241
Dye, S., Furlanetto, C., Swinbank, A. M., et al. 2015, MNRAS, 452, 2258
Eales, S., Dunne, L., Clements, D., et al. 2010, PASP, 122, 499
Gao, Y., & Solomon, P. M. 2004, ApJ, 606, 271
Gao, Y., Carilli, C. L., Solomon, P. M., & Vanden Bout, P. A. 2007, ApJ, 660, L93
García-Burillo, S., Usero, A., Alonso-Herrero, A., et al. 2012, A&A, 539, A8
Gérin, M., de Luca, M., Black, J., et al. 2010, A&A, 518, L110
González-Alfonso, E., Smith, H. A., Fischer, J., & Cernicharo, J. 2004, ApJ, 613, 247
González-Alfonso, E., Smith, H. A., Ashby, M. L. N., et al. 2008, ApJ, 675, 303
González-Alfonso, E., Fischer, J., Isaak, K., et al. 2010, A&A, 518, L43
González-Alfonso, E., Fischer, J., Graciá-Carpio, J., et al. 2012, A&A, 541, A4
González-Alfonso, E., Fischer, J., Bruderer, S., et al. 2013, A&A, 550, A25
González-Alfonso, E., Fischer, J., Aalto, S., & Falstad, N. 2014, A&A, 567, A91 (G14)
Harris, A. I., Baker, A. J., Frayer, D. T., et al. 2012, ApJ, 752, 152
Ivison, R. J., Swinbank, A. M., Smail, I., et al. 2013, ApJ, 772, 137
Kamenetzky, J., Glenn, J., Rangwala, N., et al. 2012, ApJ, 753, 70
Kelly, B. C. 2007, ApJ, 665, 1489
Kennicutt, Jr., R. C. 1998, ARA&A, 36, 189
Kessler, M. F., Steinz, J. A., Anderegg, M. E., et al. 1996, A&A, 315, L27
Kirkpatrick, A., Pope, A., Sajina, A., et al. 2015, ApJ, 814, 9
Lis, D. C., Neufeld, D. A., Phillips, T. G., Gerin, M., & Neri, R. 2011, ApJ, 738, L6
Liu, D., Gao, Y., Isaak, K., et al. 2015, ApJ, 810, L14
Lupu, R. E., Scott, K. S., Aguirre, J. E., et al. 2012, ApJ, 757, 135
Magdis, G. E., Daddi, E., Elbaz, D., et al. 2011, ApJ, 740, L15
Markwardt, C. B. 2009, in Astronomical Data Analysis Software and Systems XVIII, eds. D. A. Bohlender, D. Durand, & P. Dowler, ASP Conf. Ser., 411, 251
Meijerink, R., & Spaans, M. 2005, A&A, 436, 397
Meijerink, R., Spaans, M., Loenen, A. F., & van der Werf, P. P. 2011, A&A, 525, A119
Meijerink, R., Kristensen, L. E., Weiß, A., et al. 2013, ApJ, 762, L16
Naylor, D. A., Baluteau, J.-P., Barlow, M. J., et al. 2010, in SPIE Conf. Ser., 7731, 16
Negrello, M., Hopwood, R., De Zotti, G., et al. 2010, Science, 330, 800
Neufeld, D. A., Goicoechea, J. R., Sonnentrucker, P., et al. 2010, A&A, 521, L10
Omont, A., Neri, R., Cox, P., et al. 2011, A&A, 530, L3
Omont, A., Yang, C., Cox, P., et al. 2013, A&A, 551, A115 (O13)
Pascale, E., Auld, R., Dariush, A., et al. 2011, MNRAS, 415, 911
Pellegrini, E. W., Smith, J. D., Wolfire, M. G., et al. 2013, ApJ, 779, L19
Pereira-Santaella, M., Spinoglio, L., Busquet, G., et al. 2013, ApJ, 768, 55
Pilbratt, G. L., Riedinger, J. R., Passvogel, T., et al. 2010, A&A, 518, L1
Rangwala, N., Maloney, P. R., Glenn, J., et al. 2011, ApJ, 743, 94
Rawle, T. D., Egami, E., Bussmann, R. S., et al. 2014, ApJ, 783, 59
Riechers, D. A., Bradford, C. M., Clements, D. L., et al. 2013, Nature, 496, 329
Rybak, M., McKean, J. P., Vegetti, S., Andreani, P., & White, S. D. M. 2015, MNRAS, 451, L40
San José-García, I., Mottram, J. C., van Dishoeck, E. F., et al. 2016, A&A, 585, A103
Serjeant, S. 2012, MNRAS, 424, 2429
Solomon, P. M., Downes, D., & Radford, S. J. E. 1992, ApJ, 387, L55
Spergel, D. N., Verde, L., Peiris, H. V., et al. 2003, ApJS, 148, 175

Spinoglio, L., Pereira-Santaella, M., Busquet, G., et al. 2012, ApJ, 758, 108
van der Werf, P. P., Isaak, K. G., Meijerink, R., et al. 2010, A&A, 518, L42
van der Werf, P. P., Berciano Alba, A., Spaans, M., et al. 2011, ApJ, 741, L38
van Dishoeck, E. F., Herbst, E., & Neufeld, D. A. 2013, Chemical Reviews, 113, 9043
Vieira, J. D., Marrone, D. P., Chapman, S. C., et al. 2013, Nature, 495, 344
Weiß, A., Requena-Torres, M. A., Güsten, R., et al. 2010, A&A, 521, L1
Weiß, A., De Breuck, C., Marrone, D. P., et al. 2013, ApJ, 767, 88
Wright, E. L., Eisenhardt, P. R. M., Mainzer, A. K., et al. 2010, AJ, 140, 1868
Yang, C., Gao, Y., Omont, A., et al. 2013, ApJ, 771, L24 (Y13)
Yun, M. S., Reddy, N. A., & Condon, J. J. 2001, ApJ, 554, 803

[1] Purple Mountain Observatory/Key Lab of Radio Astronomy, Chinese Academy of Sciences, 210008 Nanjing, PR China
e-mail: yangcht@pmo.ac.cn
[2] Institut d'Astrophysique Spatiale, CNRS, Univ. Paris-Sud, Université Paris-Saclay, Bât. 121, 91405 Orsay Cedex, France
[3] Graduate University of the Chinese Academy of Sciences, 19A Yuquan Road, Shijingshan District, 10049 Beijing, PR China
[4] CNRS, UMR 7095, Institut d′Astrophysique de Paris, 75014 Paris, France
[5] UPMC Univ. Paris 06, UMR 7095, Institut d'Astrophysique de Paris, 75014 Paris, France
[6] Universidad de Alcalá, Departamento de Fisica y Matemáticas, Campus Universitario, 28871 Alcalá de Henares, Madrid, Spain
[7] Institut de Radioastronomie Millimétrique (IRAM), 300 rue de la Piscine, 38406 Saint-Martin-d'Hères, France
[8] Leiden Observatory, Leiden University, PO Box 9513, 2300 RA Leiden, The Netherlands
[9] Max Planck Institut für Radioastronomie, Auf dem Hgel 69, 53121 Bonn, Germany
[10] Department of Earth and Space Sciences, Chalmers University of Technology, Onsala Space Observatory, 43992 Onsala, Sweden
[11] Department of Physics and Astronomy, Rutgers, The State University of New Jersey, 136 Frelinghuysen Road, Piscataway, NJ 08854-8019, USA
[12] Astronomy Department, Cornell University, 220 Space Sciences Building, Ithaca, NY 14853, USA
[13] Department of Physics and Astronomy, University of California, Irvine, Irvine, CA 92697, USA
[14] Joint ALMA Observatory, 3107 Alonso de Córdova, Vitacura, Santiago, Chile
[15] Universitat Wien, Institut für Astrophysik, Türkenschanzstrasse 17, 1180 Wien, Austria
[16] School of Physics and Astronomy, University of Nottingham, University Park, Nottingham NG7 2RD, UK
[17] Institute for Astronomy, University of Edinburgh, Royal Observatory, Blackford Hill, Edinburgh, EH9 3HJ, UK
[18] European Southern Observatory, Karl Schwarzschild Straße 2, 85748 Garching, Germany
[19] Kapteyn Astronomical Institute, University of Groningen, 9700 AV Groningen, The Netherlands
[20] School of Physics and Astronomy, Cardiff University, The Parade, Cardiff CF24 3AA, UK

Appendix A: Individual sources

In the Appendix, we describe the observational results of each source, including the lensing model, the H_2O spectrum, mapping of the H_2O and continuum emission (by showing low-resolution NOEMA H_2O and continuum images), the ratio between velocity-integrated flux densities of different H_2O transitions, and the comparison between H_2O and CO emission.

A.1. G09v1.97 at z = 3.634

The galaxy G09v1.97 has the second largest redshift in our sample obtained by CARMA (Riechers et al., in prep.). In the SMA 880 μm image (B13), similar to SDP81 (ALMA Partnership, Vlahakis et al. 2015; Dye et al. 2015), it displays a triple arc structure with an angular size scale of $\sim$2″. However, there are two foreground deflectors at two different redshifts, making this complex mass distribution a very unusual case. B13 estimate a lensing amplification $\mu = 6.9 \pm 0.6$.

We have observed both para-$H_2O(2_{11}$–$2_{02})$ and ortho-$H_2O(3_{21}$–$3_{12})$ lines at 162 GHz and 251 GHz, respectively. The source is clearly unresolved at 162 GHz, but marginally resolved at 251 GHz as displayed in Fig. A.1. The ratio between the peak and the spatially integrated flux density of the continuum ($S_\nu(\mathrm{ct})^{\mathrm{pk}}/S_\nu(\mathrm{ct})$) is 0.95 ± 0.03 and 0.60 ± 0.01 at 162 GHz and 251 GHz, respectively. The H_2O emission line peak to spatially integrated flux densiity ratio ($S^{\mathrm{pk}}_{\mathrm{H_2O}}/S_{\mathrm{H_2O}}$) for $J = 2$ and $J = 3$ are 1.0 ± 0.2 and 0.5 ± 0.2, respectively. Therefore, the spatial concentrations of H_2O and continuum image are in good agreement within the uncertainties.

Both the continuum and the H_2O lines are well detected in this source. The two H_2O lines are well fitted by single Gaussian profiles with similar linewidths (257 ± 27 and 234 ± 34 km s^{-1}, Fig. 2 and Table 4). The difference in linewidth (23 km s^{-1}) is smaller than the errors of the linewidth. Therefore, there is no significant difference between the spectra of the two transitions. The ratio between $I_{\mathrm{H_2O}(3_{21}-3_{12})}$ and $I_{\mathrm{H_2O}(2_{11}-2_{02})}$ is 0.91 ± 0.12, which is the lowest of our five detected sources in both lines. However, this ratio remains consistent with the observations of local galaxies (Y13, and Fig. 4), by taking the uncertainty into account.

From our CO line observations we find a line FWHM of $\Delta V_{\mathrm{CO}} = 224 \pm 32$ and 292 ± 86 km s^{-1} for the CO(5–4) and CO(6–5) lines, respectively, which are within 1σ to the H_2O FWHMs. The observed ratio of $I_{\mathrm{H_2O}}/I_{\mathrm{CO}}$ for both the CO(5–4) and CO(6–5) lines, is about 0.4 with less than 25% uncertainty.

We have tentatively detected an H_2O^+ line in this source as well (see Sect. 5).

A.2. G12v2.43 at z = 3.127

The source is marginally resolved in the SMA 880 μm image (Fig. 2 of B13), with a size $\sim$1.5″, but there is no obvious strongly lensed structures such as multiple images. It is not yet possible to build a lensing model for this source because the search for a deflector by B13 has been unsuccessful.

Both para-$H_2O(2_{02}$–$1_{11})$ and ortho-$H_2O(3_{21}$–$3_{12})$ lines are well detected, as shown in Fig. A.1, and the source is unresolved, consistent with the SMA image. The ratios of $S_\nu(\mathrm{ct})^{\mathrm{pk}}/S_\nu(\mathrm{ct})$ for 239 GHz and 282 GHz are 0.71 ± 0.02 and 0.87 ± 0.01, respectively, while the $S^{\mathrm{pk}}_{\mathrm{H_2O}}/S_{\mathrm{H_2O}}$ for $H_2O(2_{02}$–$1_{11})$ and $H_2O(3_{21}$–$3_{12})$ are 0.6 ± 0.2 and 1.0 ± 0.2, respectively.

The two H_2O lines are both well fitted by a single Gaussian profile. The FWHMs are 201 ± 27 and 221 ± 20 km s^{-1} for para-$H_2O(2_{02}$–$1_{11})$ and ortho-$H_2O(3_{21}$–$3_{12})$, respectively. The difference is within the 1σ uncertainty.

The velocity-integrated flux density ratio of high-lying over low-lying H_2O line of this source, $I_{\mathrm{H_2O}(3_{21}-3_{12})}/I_{\mathrm{H_2O}(2_{02}-1_{11})} = 1.2 \pm 0.2$, which is slightly lower than that of Arp 220 as shown in Fig. 4. The linewidths of the H_2O lines (201 ± 27 and 221 ± 20 km s^{-1}) are the narrowest ones among our sources. The values are also very close to the CO(1–0) linewidth (210±30 km s^{-1}, Harris et al. 2012). Their similarity indicates that there is not likely any strong differential lensing effect between the CO and H_2O emissions in this case.

A.3. NCv1.143 at z = 3.565

Having a redshift of $z = 3.565$ from CO observation by CARMA (Riechers et al., in prep.), this source is one of the brightest (at submm) in our sample. It is resolved by the SMA 880 μm beam (B13) with a size $\sim$ 2″, featured by two components at the northeast and southwest directions. With a single deflector, the lensing model estimates a magnification factor of $\mu = 6.9 \pm 0.6$.

As displayed in Fig. A.1, both the lines and the continuum are very strong and well detected. The ratio $S_\nu(\mathrm{ct})^{\mathrm{pk}}/S_\nu(\mathrm{ct}) = 0.86 \pm 0.02$ shows that the source is unresolved at 165 GHz (for observing para-H_2O line 2_{11}–2_{02}). At 255 GHz, the ratios $S_\nu(\mathrm{ct})^{\mathrm{pk}}/S_\nu(\mathrm{ct}) = 0.55 \pm 0.01$ and $S^{\mathrm{pk}}_{\mathrm{H_2O}}/S_{\mathrm{H_2O}} = 0.7 \pm 0.2$ indicate that the source is partially resolved, consistent with the SMA result.

Both the $H_2O(2_{02}$–$1_{11})$ and $H_2O(3_{21}$–$3_{12})$ lines can be fitted by single Gaussian profiles. The ratio of $I_{\mathrm{H_2O}(3_{21}-3_{12})}/I_{\mathrm{H_2O}(2_{11}-2_{02})}$ is 1.36 ± 0.13, close to the mean ratio found in the nearby star-forming-dominated galaxies (Y13, and Fig. 4). The linewidths of $H_2O(2_{11}$–$2_{02})$ and $H_2O(3_{21}$–$3_{12})$ are 293 ± 15 and 233 ± 22 km s^{-1}, respectively. Although the former is larger, they are compatible within an uncertainty of 1.6σ. Also, the H_2O linewidth agrees well with the CO(5–4) and CO(6–5) linewidths (273±27 and 284±27 km s^{-1}, see Table 3). Therefore, the line ratios are unlikely to be affected by differential magnification. The observed ratio of $I_{\mathrm{H_2O}}/I_{\mathrm{CO}}$ is 0.4–0.5 and 0.6–0.7 (uncertainties are within 13%) for the $J = 2$ para-H_2O and $J = 3$ ortho-H_2O, respectively.

We have also detected ortho-$H_2O^+(2_{11}$–$2_{02})$ and ortho-$H_2O^+(2_{02}$–$1_{11})$ fine structure lines together with para-$H_2O(2_{11}$–$2_{02})$ in this source. The further discussion of the H_2O^+ spectra and its interpretation are given in Sect. 5.

A.4. NAv1.195 at z = 2.951

As quoted in B13, the redshift of this source was first obtained by the CO observation (Harris et al., in prep.). Its SMA image shows a typical lensed feature with two components separated by $\sim$2″ along the northwest and southeast direction. The lensing model suggests a modest magnification factor $\mu = 4.1 \pm 0.3$.

We have robust detections of $H_2O(2_{02}$–$1_{11})$ and the continuum emission at 250 GHz and 293 GHz (Fig. A.1). However, the $H_2O(3_{21}$–$3_{12})$ line isat odds with the other five sources. Therefore, we only show the image of the dust continuum emission at this frequency in Fig. A.1. The source is clearly resolved into two components in the three images, and the northwest component is about 4 times stronger than the southeast one in the continuum images, in agreement with the SMA image (B13). For the continuum at 250 GHz, the peak to total integrated flux density

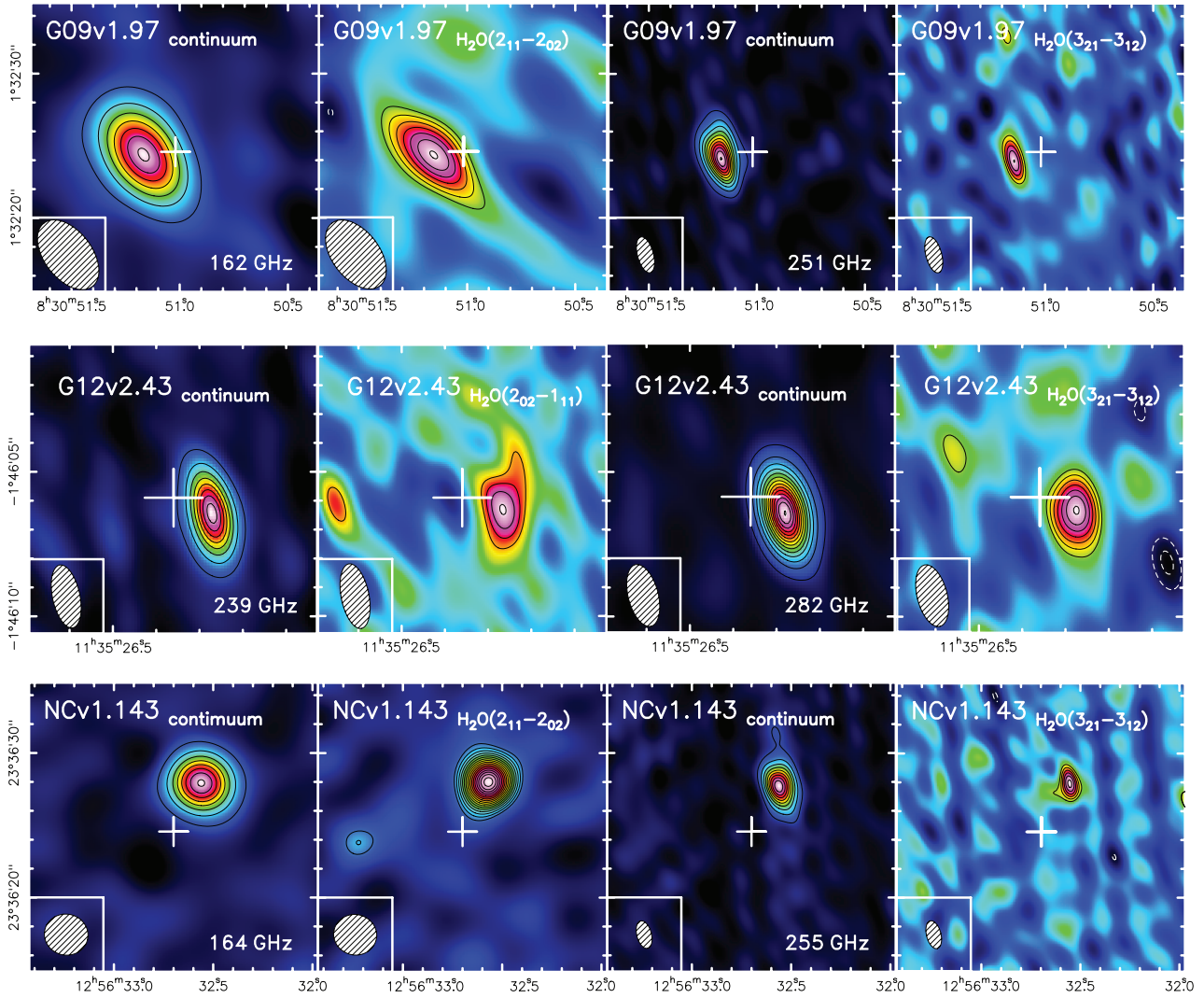

Fig. A.1. Mapping of the H_2O emission lines and the corresponding continuum emission (frequencies have been shown accordingly in the white text) in the sources with both para $J = 2$ and ortho $J = 3$ H_2O lines observed. The contours of the continuum emission start from 6σ in step of 10σ, and the contours of the H_2O emission start from 3σ in step of 1σ. Asymmetric negative contours are shown in white dashed lines. For each observation, the 1σ contours for the continuum (mJy beam^{-1}) and the H_2O emission line (Jy km s^{-1} beam^{-1}) are as follows: G09v1.97 $H_2O(2_{11}–2_{02})$ (0.17/0.57), G09v1.97 $H_2O(3_{21}–3_{12})$ (0.25/0.38), G12v2.43 $H_2O(2_{02}–1_{11})$ (0.29/0.48), G12v2.43 $H_2O(3_{21}–3_{12})$ (0.30/0.53), NCv1.143 $H_2O(2_{11}–2_{02})$ (0.16/0.36) and NCv1.143 $H_2O(3_{21}–3_{12})$ (0.42/0.72).

ratio $S_\nu(\mathrm{ct})^{\mathrm{pk}}/S_\nu(\mathrm{ct}) = 0.54 \pm 0.02$, and for $H_2O(2_{02}–1_{11})$, the ratio $S^{\mathrm{pk}}_{\mathrm{H_2O}}/S_{\mathrm{H_2O}}$ equals to 0.6 ± 0.3. Therefore, the spatial distributions of dust and the H_2O emission are likely to be similar in this source. In the observation at 293 GHz, $S_\nu(\mathrm{ct})^{\mathrm{pk}}/S_\nu(\mathrm{ct}) = 0.42 \pm 0.01$, due to a smaller synthesis beam (Table 1).

Figure 2 shows the spectra corresponding to the two observations of NAv1.195. The $H_2O(2_{02}–1_{11})$ line can be fitted by a single Gaussian profile, with a linewidth equal to 328 ± 51 km s^{-1}. We have not detected the higher excitation $H_2O(3_{21}–3_{12})$ line as mentioned above. By assuming the same linewidth as the lower–J H_2O line, we can infer a 2σ detection limit of 2.56 Jy km s^{-1}. This yields a flux ratio of $H_2O(3_{21}–3_{12})/H_2O(2_{02}–1_{11}) \lesssim 0.6$. This value is significantly lower than that in the five other sources where it ranges from 0.75 to 1.60 (errors are within 25%), but it remains close to the lowest values measured in local galaxies (Y13) as shown in Table 6 and Fig. 4. This low ratio of H_2O lines probably originates from different excitation conditions, especially for the far-infrared radiation field, since the line $H_2O(3_{21}–3_{12})$ is mainly populated through far-infrared pumping via absorbing 75 μm photons (see Sect. 5). The CO(5–4) line of the source has a linewidth of 281 ± 16 km s^{-1}, which is comparable with the H_2O line profile. The observed ratio of $I_{\mathrm{H_2O}}/I_{\mathrm{CO}}$ (CO(5–4)) is $\leq$0.4.

A.5. NAv1.177 at z = 2.778

NOEMA observation of the CO line in this source gives a redshift of $z = 2.778$ (Krips et al., in prep.). The SMA 880 μm image shows a compact structure with two peaks $\sim$1″ away along the eastwest direction, and the western component is the dominant one (Fig. 2 of B13). However, due to the absence of deflector in the foreground optical image from SDSS and lack of the deep optical and near-infrared images, the lensing properties are still unknown (B13).

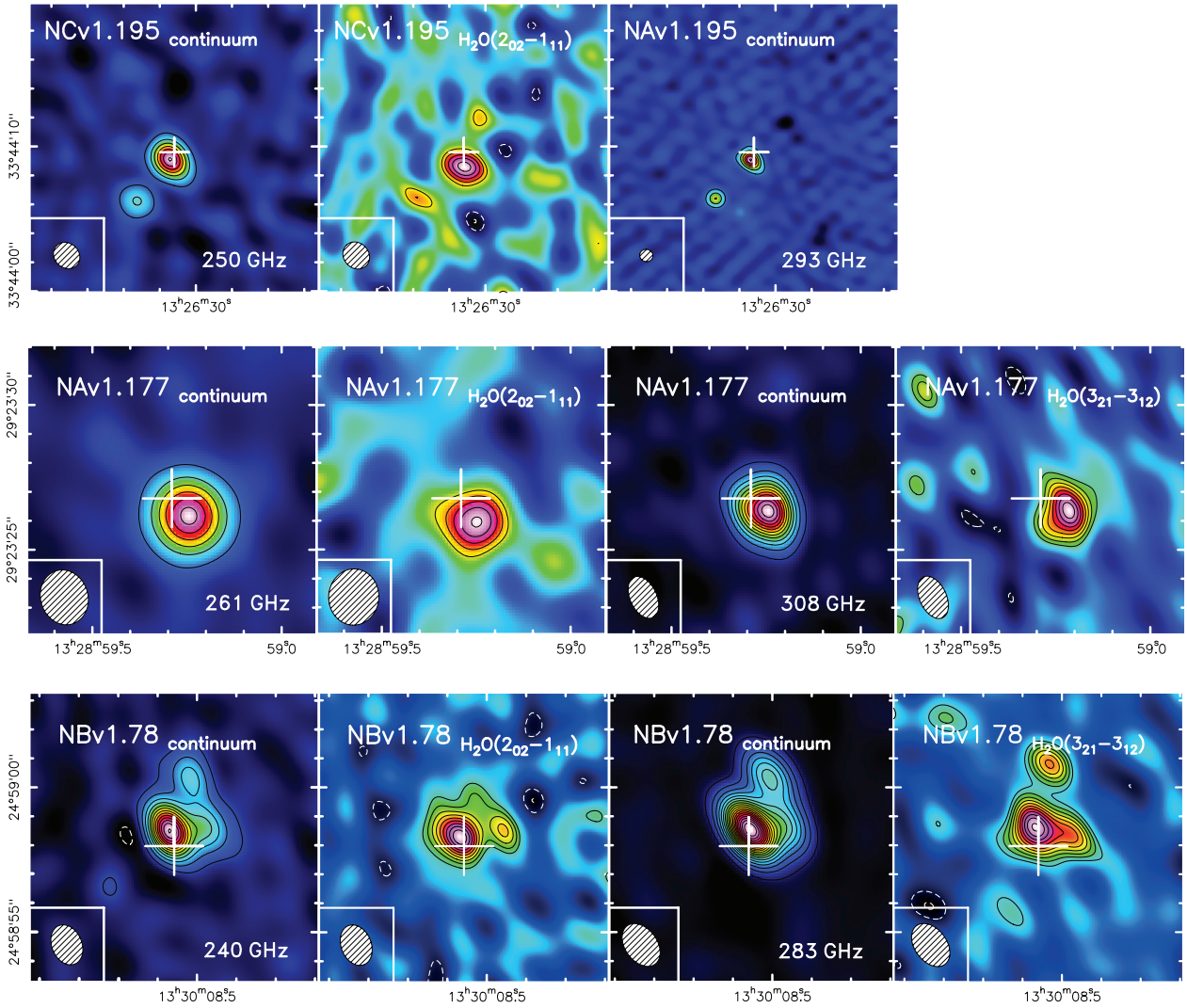

Fig. A.2. (See Fig. A.1 caption.) For each observation, the 1σ contour for the continuum (mJy beam^{-1}) and the H_2O emission line (Jy km s^{-1} beam^{-1}) are as follows: NCv1.195 $H_2O(2_{02}–1_{11})$ (0.34/0.51), NCv1.195 $H_2O(3_{21}–3_{12})$ (0.48/–), NAv1.177 $H_2O(2_{02}–1_{11})$ (0.58/0.65), NAv1.177 $H_2O(3_{21}–3_{12})$ (0.38/0.58), NBv1.78 $H_2O(2_{02}–1_{11})$ (0.28/0.30), NBv1.78 $H_2O(3_{21}–3_{12})$ (0.21/0.29).

As displayed in Fig. A.1, both the lines of $H_2O(2_{02}–1_{11})$ and $H_2O(3_{21}–3_{12})$ and the corresponding dust continuum are well detected. The ratios $S_\nu(\mathrm{ct})^{\mathrm{pk}}/S_\nu(\mathrm{ct})$ are 0.75 ± 0.02 and 0.62 ± 0.01 for observation at 261 GHz and 308 GHz, respectively. One should notice that the direction of the synthesised beam is perpendicular to the alignment of the two components in the image, thus the source is marginally resolved in the $H_2O(2_{02}–1_{11})$ and the corresponding dust continuum images. For the $H_2O(3_{21}–3_{12})$ observation at higher frequency, we can see the partially resolved feature. The peak to total flux ratios of H_2O are $S^{\mathrm{pk}}_{\mathrm{H_2O}}/S_{\mathrm{H_2O}} \sim 0.8 \pm 0.3$ and 0.6 ± 0.1 for the $H_2O(2_{02}–1_{11})$ and $H_2O(3_{21}–3_{12})$ lines, respectively, indicating similar spatial distribution compared with the dust emission.

The H_2O spectra displayed in Fig. 2 show single Gaussian profiles with $FWHM = 241 \pm 41$ and 272 ± 24 km s^{-1} (Table 4). The profiles of the two H_2O lines are similar within the uncertainties. The line ratio, $I_{\mathrm{H_2O(3_{21}–3_{12})}}/I_{\mathrm{H_2O(2_{02}–1_{11})}} = 1.34 \pm 0.24$. This value is close to that found in Arp 220 and it is the largest ratio in our sample. We have also detected the CO(3–2) and CO(5–4) lines using the IRAM 30 m telescope in this source (Table 3), the linewidth of CO is around 230 ± 16 km s^{-1} which is similar to the width of the detected H_2O lines. The ratio of $I_{\mathrm{H_2O}}/I_{\mathrm{CO}}$ is from 0.5 to 1.1 with less than 20% uncertainties.

A.6. NBv1.78 at $z = 3.111$

The CO redshift of NBv1.78 was obtained by Riechers et al. (in prep.) via CARMA, $z = 3.111$, and the data of the $H_2O(2_{02}–1_{11})$ line were obtained by O13. The source is resolved in the SMA 880 μm image (B13) with a somewhat complex morphology, and the size is ~2.5″. There are three main components in the image. The two strong components located at northwest and southeast direction of the image, and the weakest component close to the southeast. The derived lensing magnification is $\mu = 13.5 \pm 1.5$, which is the second largest among our sample. In the near-infrared images, the source has a similar three-component Einstein ring-like structure with a slightly smaller magnification $\mu = 10.8^{+0.3}_{-0.2}$ (Calanog et al. 2014).

Our NOEMA images of both continuums and H_2O lines as shown in Fig. A.1 are consistent with the SMA 880 μm image.

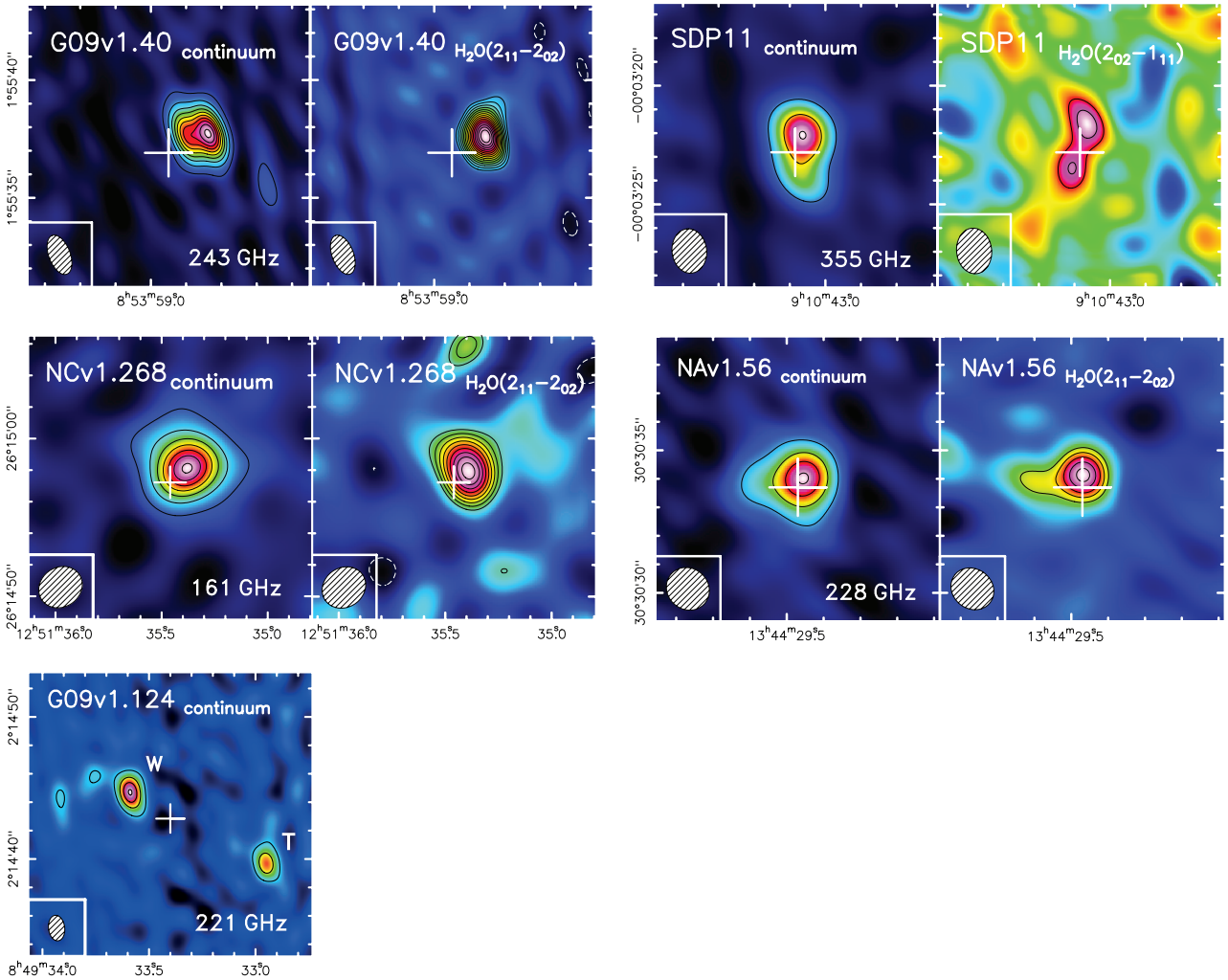

Fig. A.3. (See Fig. A.1 caption.) For each observation, the 1σ contour for the continuum (mJy beam^{-1}) and the H_2O emission line (Jy km s^{-1} beam^{-1}) are as follows: G09v1.124 $H_2O(2_{11}–2_{02})$ (0.17/–), G09v1.40 $H_2O(2_{11}–2_{02})$ (0.19/0.32), SDP11 $H_2O(2_{02}–1_{11})$ (1.30/1.04), NCv1.268 $H_2O(2_{11}–2_{02})$ (0.13/0.39) and NAv1.56 $H_2O(2_{11}–2_{02})$ (0.53/1.02).

The images are resolved into two main parts, while the southern component is extended along the western side. The continuum and H_2O line images have fairly high S/N. From the observation of $H_2O(2_{02}–1_{11})$ at 241 GHz (O13, note that this observation was performed at higher resolution with a $1.4'' \times 1.0''$ beam), the values of $S_\nu(\mathrm{ct})^{\mathrm{pk}}/S_\nu(\mathrm{ct})$ and $S^{\mathrm{pk}}_{\mathrm{H_2O}}/S_{\mathrm{H_2O}}$ agree well, which are 0.42 ± 0.01 and 0.4 ± 0.1, respectively. The continuum image at 283 GHz gives $S_\nu(\mathrm{ct})^{\mathrm{pk}}/S_\nu(\mathrm{ct}) = 0.69 \pm 0.01$, and the image of $H_2O(3_{21}–3_{12})$ gives $S^{\mathrm{pk}}_{\mathrm{H_2O}}/S_{\mathrm{H_2O}} = 0.8 \pm 0.1$. The similarity of the peak to spatially integrated flux density ratios suggest that the spatial distribution of H_2O and submm dust continuum are likely to be consistent. Additionally, the images of $J = 2$ and $J = 3$ images are also consistent within the uncertainty.

NBv1.78 has a very broad linewidth compared with the other sources. As shown in Fig. 2, the linewidth of $H_2O(2_{02}–1_{11})$ and $H_2O(3_{21}–3_{12})$ are 510 ± 90 and 607 ± 43 km s^{-1}, respectively. The two lines have similar profiles. The source has a $I_{\mathrm{H_2O}(3_{21}–3_{12})}/I_{\mathrm{H_2O}(2_{02}–1_{11})}$ ratio equal to 1, within the range of the local galaxies (Fig. 4). The CO(5–4) and CO(6–5) observations (Table 3) give linewidths of 614 ± 53 and 734 ± 85 km s^{-1}, which are wider than the H_2O lines. The observed ratio of $I_{\mathrm{H_2O}}/I_{\mathrm{CO}}$ is about 0.7 with less than 25% uncertainty for $J = 2$ H_2O.

A.7. G09v1.40 at $z = 2.093$

A CO redshift of G09v1.40, $z = 2.0894$ was obtained by CSO/Z-Spec (Lupu et al., in prep.). But, through our H_2O observation, we find a redshift of $z = 2.093$. Our value is consistent with the CO(3–2) observation by Riechers et al. (in prep.), and we have adopted this value. SMA observation of the 880 μm dust continuum shows two close components with a separation of $\sim 1''$ along the east and west direction. The lensing model estimates $\mu = 15.3 \pm 3.5$, which is the largest magnification in our sample. The Keck near-infrared image of the source suggests a magnification of $\mu = 11.4^{+0.9}_{-1.0}$ for the stellar component (Calanog et al. 2014).

The $H_2O(2_{11}–2_{02})$ line is well detected as well as the corresponding dust continuum. As shown by the images of the H_2O and dust continuum (Fig. A.1), the source is partially resolved by the synthesised beam. The two component (east and

west) structure is consistent with the 880 μm image, and the western component is stronger than the eastern one. Both ratios of $S_\nu(\mathrm{ct})^{\mathrm{pk}}/S_\nu(\mathrm{ct})$ and $S^{\mathrm{pk}}_{\mathrm{H_2O}}/S_{\mathrm{H_2O}}$ are found to be 0.6 (uncertainty <13%). However, the eastern component is not detected in the H_2O image.

The $H_2O(2_{11}–2_{02})$ line can be fitted with a single Gaussian profile with a FWHM of 277 ± 14 km s^{-1} (Fig. 2). However, the line has a steeper decline on the red side of the spectrum. The CO(4–3) observation gives a linewidth of 198 ± 51 km s^{-1}, which is 0.7 ± 0.2 times narrower than that of the H_2O line. The velocity-integrated flux density of the H_2O is larger than that of the CO(4–3) in this source with a ratio of $I_{\mathrm{H_2O}}/I_{\mathrm{CO}} = 1.1 \pm 0.3$.

A.8. SDP11 at z = 1.786

The CO observation by Lupu et al. (2012) found $z = 1.786$. The SMA 880 μm image displays a typical strongly lensed morphology with two components, north and south, respectively. The size of the source is ∼2″. The gravitational magnification estimated by B13 is $\mu = 10.9 \pm 1.3$.

As shown in Fig. A.1, the source is partially resolved. The dust continuum image shows an extended structure along the north and south direction, with the brightest peak in the northern part. The noisy images are consistent with the SMA 880 μm observation. The ratio of $S_\nu(\mathrm{ct})^{\mathrm{pk}}/S_\nu(\mathrm{ct})$ is 0.56 ± 0.03. The image shows two distinctive components in the north and south direction. This structure also agrees with the high resolution SMA 880 μm image. Additionally, $S^{\mathrm{pk}}_{\mathrm{H_2O}}/S_{\mathrm{H_2O}} = 0.4 \pm 0.2$ suggests that the H_2O image is slightly resolved compared with the dust emission. This diffierence may come from their different spatial distribution.

Although the noise level of its spectrum is the highest among our sources because of the high frequency, namely 355 GHz, the $H_2O(2_{02}–1_{11})$ line is marginally detected with $S/N = 4.6$. The linewidth is 214 ± 41 km s^{-1} (Fig. 2).

A.9. NCv1.268 at z = 3.675

The redshift of NCv1.268 was obtained by the CO observation of Krips et al. (in prep.). A typical strongly lensed morphology was found by the SMA 880 μm observation (B13), with a strong arc-like component in the south direction. The structure has a size ∼2.5″. The B13 lensing model estimates $\mu = 13.0 \pm 1.5$.

The source is marginally resolved by the NOEMA synthesis beam (Fig. A.1). When comparing the flux ratios between the dust and H_2O emission from the peak and the spatially integrated values, they give $S_\nu(\mathrm{ct})^{\mathrm{pk}}/S_\nu(\mathrm{ct}) = 0.66 \pm 0.01$ and $S^{\mathrm{pk}}_{\mathrm{H_2O}}/S_{\mathrm{H_2O}} = 0.6 \pm 0.1$. The values of dust emission and the H_2O image are in good agreement.

NCv1.268 is the only source in which we have detected a double-peaked line profile from our new observations, with a slightly stronger blue velocity component (Fig. 2). The total linewidth is very large, 731 ± 75 km s^{-1}.

A.10. NAv1.56 at z = 2.301

Harris et al. (2012) give a CO redshift of $z = 2.3010$ for this source. The SMA 880 μm dust continuum image shows a classic strongly lensed morphology with multiple images. It consists of an arc-like component in the western direction and a point-like component toward the east. They are separated ∼2″. The lens model implies that the magnification factor $\mu = 11.7 \pm 0.9$ (B13).

As shown in Fig. A.1, the source is marginally resolved, with an extended morphology in the eastern part. The structures displayed in the dust and H_2O images are similar. The ratios $S_\nu(\mathrm{ct})^{\mathrm{pk}}/S_\nu(\mathrm{ct}) = 0.62 \pm 0.03$ and $S^{\mathrm{pk}}_{\mathrm{H_2O}}/S_{\mathrm{H_2O}} = 0.7 \pm 0.2$ also suggest their similarity within the errors. Most of the fluxes are concentrated in the western part, which agrees with the SMA 880 μm image.

The $H_2O(2_{11}–2_{02})$ line can be fitted by a single Gaussian with a large linewidth equal to 593±56 km s^{-1}. The CO(4–3) line observation by NOEMA (Oteo et al., in prep.) gives a linewidth of 621 ± 47 km s^{-1}. The linewidths of CO and H_2O are in very good agreement. Our noisy detection of CO(5–4) at IRAM 30 m (Table 3) gives a ratio of $I_{\mathrm{H_2O}}/I_{\mathrm{CO}} = 0.8 \pm 0.3$.

A.11. G09v1.124 at z = 2.410

The redshift of this source is measured by CO observation (Harris et al. 2012). This multiple source, with two main components, each with intrinsic $L_{\mathrm{IR}} > 10^{13}\,L_\odot$, separated by 10″ (Fig. A.1), was studied in detail by (Ivison et al. 2013, see also B13 and Oteo et al., in prep.). It is special in our sample since the two main sources are from two very different HyLIRGs rather than multiple images of a single source generated by strong gravitational lensing. The eastern component G09v1.124-W, which contains a powerful AGN (Oteo et al., in prep.), is unlensed and the western component G09v1.124-T is only weakly lensed with a magnification factor $\mu = 1.5 \pm 0.2$. Thus, throughout the discussions, we treat G09v1.124-W and G09v1.124-T as two distinct sources (see Tables 2, 4, 5 and 6).

Probably because of this too small lensing magnification and the smaller values of each μL_{IR} (Table 2), we have only detected the dust continuum emission in this source. The $H_2O(2_{11}–2_{02})$ line is undetected. The 2σ upper limits of the velocity-integrated flux density of the $H_2O(2_{11}–2_{02})$ line show that the values of $I_{\mathrm{H_2O}}$ are more than three times smaller than in the other sources. As seen in Table 4 and Fig. 3, the ratio $L_{\mathrm{H_2O}}/L_{\mathrm{IR}}$ is smaller than all our other sources for G09v1.124-W, probably because of its strong AGN. However, for G09v1.124-T this ratio, albeit small, might be comparable to that of G09v1.97. The dust continuum at 221 GHz follows the same structure as the previously published observations (Fig. A.1 and Ivison et al. 2013). Both the eastern component (W) and the western one (T) are marginally resolved by the synthesised beam. The peak to total continuum flux ratios are $S_\nu(\mathrm{ct})^{\mathrm{pk}}/S_\nu(\mathrm{ct}) = 0.84 \pm 0.03$ and 0.83 ± 0.04, respectively.

Appendix B: H_2O^+ detections in local ULIRGs

The study using the *Herschel* SPIRE/FTS spectra of 167 local galaxies has revealed several emission and absorption lines of H_2O^+, which are ortho-H_2O^+ lines $2_{11}–2_{02\ (5/2–5/2)}$, $2_{02}–1_{11\ (5/2–3/2)}$, $1_{11}–0_{00\ (3/2–1/2)}$, $1_{11}–0_{00\ (1/2–1/2)}$ (Y13, see also Table B.1). All $J \geq 2$ H_2O^+ lines are in emission. Table B.1 gives values of the H_2O^+ flux and luminosity for those among the Y13 sample where H_2O^+ lines are (tentatively) detected with $S/N \gtrsim 2.5$. However, for the $H_2O^+(1_{11}–0_{00})$ lines which connect the ground state, they are often found to be in emission in AGN-dominated sources while they are in absorption in star-forming-dominated ones. A full description of the dataset for this *Herschel* SPIRE/FTS survey will be given in Liu et al. in prep. At high-redshift prior to our study, the $J = 2$ ortho-H_2O^+ doublet lines seem to have only been tentatively detected in two sources, SPT0346-52 (Weiß et al. 2013) and HFLS3 (Riechers et al. 2013).

Table B.1. Beam-matched H_2O^+, H_2O line and infrared luminosities from local detections (*Herschel* SPIRE/FTS archive) and high-redshift *Herschel* lensed galaxies.

Source	2_{02}–1_{11} (5/2–3/2) $10^6\,L_\odot$	2_{11}–2_{02} (5/2–5/2) $10^6\,L_\odot$	$L_{\rm IR-beam}$ $10^{11}\,L_\odot$	$L_{\rm H_2O}$ $10^6\,L_\odot$
Local ULIRGs				
ESO320-G030	0.4 ± 0.1	–	1.5	0.9
CGCG049-057	0.3 ± 0.1	0.7 ± 0.2	1.9	1.6
NGC 2623	0.5 ± 0.2	0.7 ± 0.3	3.5	2.0
Arp299-A	0.8 ± 0.2	0.7 ± 0.3	5.4	1.3
Arp220	3.7 ± 0.8	3.5 ± 0.9	16.2	15.2
IRAS13120-5453	3.6 ± 1.2	2.4 ± 1.0	28.2	10.7
IRASF17207-0014	6.8 ± 2.2	6.3 ± 2.2	24.6	15.5
Mrk231	2.6 ± 1.0	3.0 ± 1.5	32.4	9.3
High-redshift lensed galaxies				
NCv1.143	28.7 ± 7.2	28.6 ± 7.2	113.6	89.7
G09v1.97	35.8 ± 9.0	–	211.4	106.6
G15v2.779	–	55.8 ± 15.9	270.0	266.0
HFLS3	–	261.8 ± 200.3	364.0	737.8

Notes. Luminosity of H_2O^+ fine structure lines 2_{02}–1_{11} (5/2–3/2) (742.1 GHz), 2_{11}–2_{02} (5/2–5/2) (746.5 GHz), and $H_2O(2_{11}$–$2_{02})$. As for the local sources the *Herschel* SPIRE/FTS beam is smaller than the entire source for some galaxies, here $L_{\rm IR-beam}$ represents the $L_{\rm IR}$ from the same beam area as the measured emission line (a full description will be given by Liu et al., in prep.). $L_{\rm H_2O}$ is the luminosity of $H_2O(2_{11}$–$2_{02})$. HFLS3 data are taken from Riechers et al. (2013).

3.3 The excitation of water lines in two strongly lensed SMGs at a look-back time of 12 Gyr

3.3.1 Motivation and source selection

As we presented in Chapter 3.2, in order to further constrain the H_2O excitation, one needs to observe at least one high-J ($J>3$) H_2O line. The line we choose is $H_2O(4_{22}–4_{13})$ which has both detection in local ULIRG and high-z SMGs/QSOs from previous studies (e.g. van der Werf et al., 2011; Yang et al., 2013). This line of higher excitation ($E_{up}/k = 450$ K) is the most stringent probe of extreme far-IR radiation densities, requiring very warm dust ($\gtrsim 70$ K) and high optical depths ($\tau_{100} \gtrsim 1$) to be significantly excited

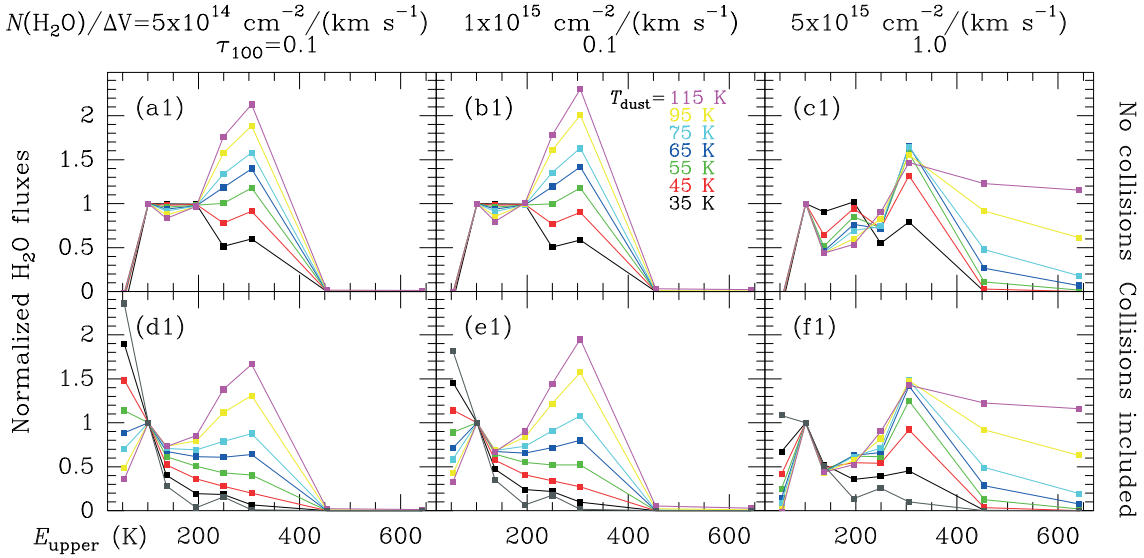

Fig. 3.6 The H_2O SLED generated from far-IR pumping + collisional excitation model of the H_2O lines given by González-Alfonso et al. (2014). The parameter used in generating the H_2O SLED at various dust temperature are given on top of each panel. The upper panels are from the excitation models without considering collisional excitation, while the lower ones are from the models considering both far-IR pumping and collisional excitation.

and thus tracing global conditions similar to the nuclear regions in local ULIRGs. As shown in the work of González-Alfonso et al. (2014) on the submm H_2O line excitation, the J = 3 lines are very sensitive to the dust temperature that is related to the far-IR radiation field. However, as shown in Fig. 3.6, when the water column density is high and the ISM is optically thick, which seems to be the case of our SMGs (see our published paper Yang et al. 2016 in Chapter 3.2, the SMGs usually have $\tau_{100} \gtrsim 1$ and the H_2O column density per velocity interval $N_{H_2O}/\Delta V$ of several 10^{15} cm^{-2} km^{-1} s). Thus, the $H_2O(4_{22}–4_{13})$ line becomes critical for us to derive the reliable $N_{H_2O}/\Delta V$ and τ_{100}. Combining with the $J = 2$ and $J = 3$ H_2O lines, the high optical depths and very warm dust will be better traced by the 4_{22}-4_{13}/3_{21}-3_{12} ratio, while the 3_{21}-3_{12}/2_{02}-1_{11} ratio will extend the diagnostics to more optically thin, extended regions and will potentially probe the presence of widespread, collisionally excited gas.

Nevertheless, because the line is weak comparing with the lower-J H_2O lines, we have chosen up two of the brightest sources with $F_{500} > 260$ mJy at $z \sim 3.6$, NCv1.143 and G09v1.97. The lensing models of these two sources were carefully constructed by Bussmann et al. (2013) based on SMA data, with magnification

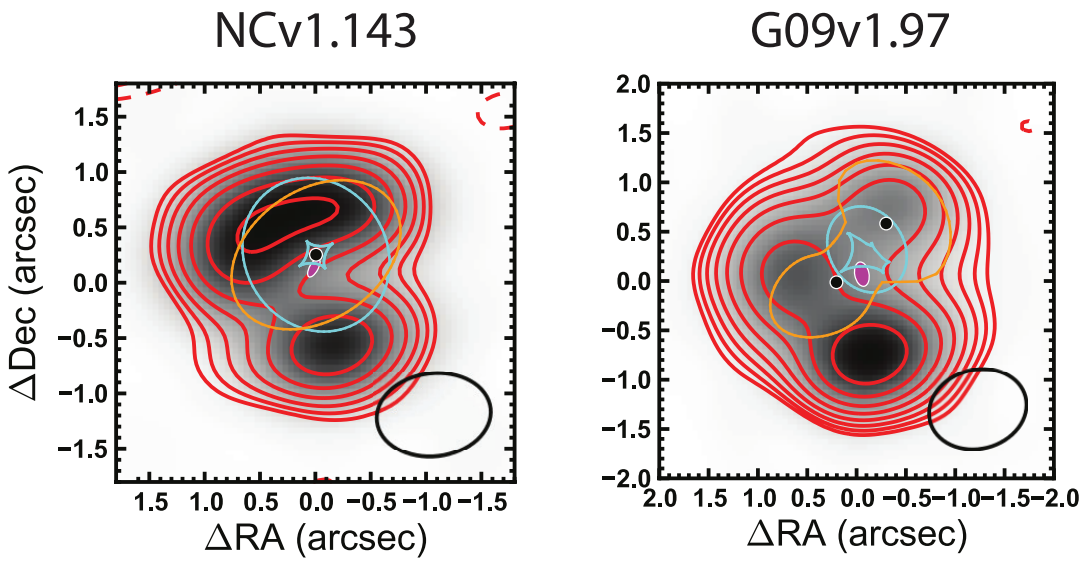

Fig. 3.7 Images from Bussmann et al. (2013): SMA 880 μm continuum of NCv1.143 and G09v1.97. The critical curves are shown in orange, caustics are in cyan, positions of the lens are shown by black circle while reconstructed source plane image is shown by magenta filled ellipses. The resulted lensing magnification for NCv1.143 and G09v1.97 are 11.3 ± 1.7 and 6.9 ± 0.6, respectively.

factors equal to 11.3 ± 1.7 and 6.9 ± 0.6 for NCv1.143 and G09v1.97, respectively. The peak flux of the $J = 2$ H_2O lines in these two sources is above 15 mJy.

3.3.2 Observations and data reduction

The sample is made of two of the brightest sources among our *H*-ATLAS lensed SMGs, NCv1.143 and G09v1.97. As shown in the lens models based on the SMA 880 μm images (Fig. 3.7), for NCv1.143, the foreground source can be modelled with a singular isothermal ellipsoid (SIE) profile. While for G09v1.97, there are two foreground (SIE-profile) sources.

The observations were performed in December 2015 using NOEMA D-configuration, which is chosen for the purpose of line detection. The synthesised beam for NCv1.143 and G09v1.97 are in low resolution of 2.0"×1.6" (PA = 16°) and 2.6"×2.1" (PA = −22°). The baselines extend from 15 m to 145 m. The observations were conducted in the 1.2 mm band (central frequency for NCv1.143 and G09v1.97 are 265 GHz and 260 GHz, respectively) in stable atmospheric conditions with seeing of $\lesssim$ 1.0" and reasonable transparency (PWV ≤ 1 mm). The on-source time spent on NCv1.143 is 3 hours and 2 hours on G09v1.97.

The phase and bandpass were calibrated by measuring standard calibrators that are regularly monitored at the IRAM/NOEMA, including 3C 279, 3C 273, MWC 349 and 0923+392. The accuracy of the flux calibration is estimated to be ∼ 20% in the 1.2 mm band. Calibration, imaging, CLEANing and spectra extraction were performed within the `GILDAS` packages `CLIC` and `MAPPING`.

3.3.3 Results

Fig. 3.8 shows the spatial-integrated $H_2O(4_{22}–4_{13})$ spectra of NCv1.143 and G09v1.97. The spectra are extracted from CLEANed images (natural weighting) of the two sources. To measure the linewidth, velocity-

integrated flux and the continuum level of the spectra, we perform single Gaussian profile fitting to the emission lines using the Levenberg-Marquardt least-square minimisation code `MPFIT` (Markwardt, 2009). Using the relation derived in Solomon et al. (1992), the apparent line luminosities, μL_{H_2O} can be derived from the observed line fluxes by

$$L_{H_2O} = 1.04 \times 10^{-3} I_{H_2O} \nu_{rest} (1+z)^{-1} D_L^2, \tag{3.1}$$

in which I_{H_2O} is the velocity-integrated flux density of $H_2O(4_{22}–4_{13})$, ν_{rest} is the rest-frame frequency of the $H_2O(4_{22}–4_{13})$ line equal to 1207.639 GHz, z and D_L are the redshift and the corresponding luminosity distance of the source, respectively.

The emission line of $H_2O(4_{22}–4_{13})$ has been detected in NCv1.143 at a S/N level ~ 6 and ~ 3 in G09v1.97. As summarised in Table 3.3.3, the velocity-integrated flux density ranges from 1.8 to 2.3 mJy km s^{-1}, which is about 3 to 4 times smaller than that of the $J = 2$ H_2O and $H_2O(3_{21}–3_{12})$ lines. Their linewidth are around 300 km s^{-1}, in agreement with the former H_2O and CO line measurements, although the $H_2O(4_{22}–4_{13})$ linewidth of G09v1.97 is narrower than that of CO, possible due to the non-detected blue part of the emission line that has been confirmed by ALMA observations of line CO and H_2O (see a detailed description of the ALMA data and analysis in Chapter 5).

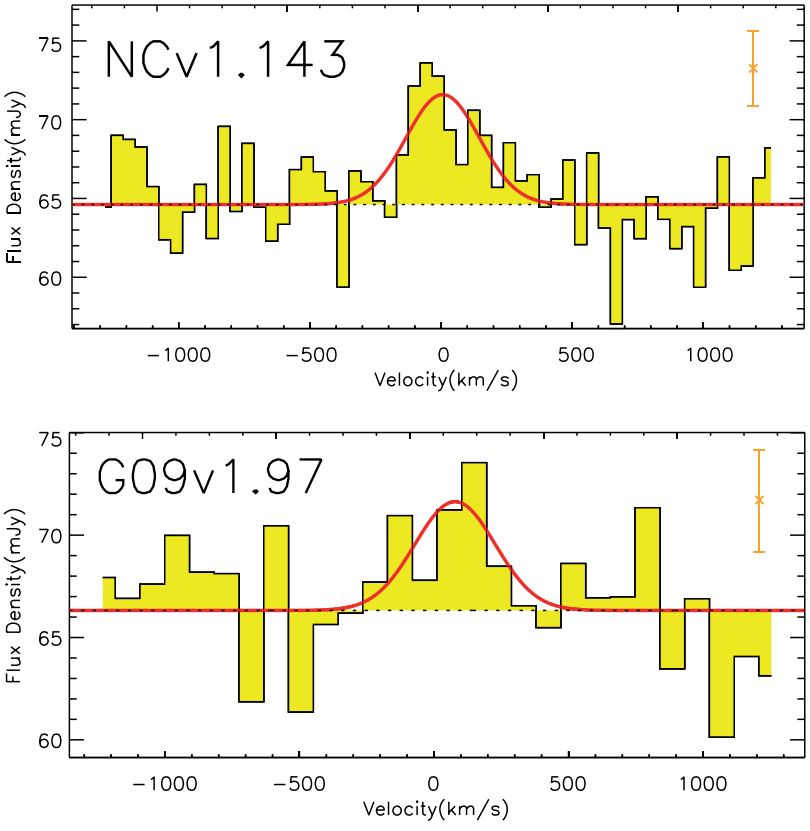

Fig. 3.8 The NOEMA spectra of $H_2O(4_{22}–4_{13})$ line of NCv1.143 and G09v1.97. Zero velocities are set corresponding to the H_2O line frequency calculated based on the CO redshift reported in Table 3.3.3. The typical errors are shown by orange errorbars. Red line indicates the Gaussian fitting to the line profile.

Table 3.1 NOEMA observational results of $H_2O(4_{22}–4_{13})$ (ν_{rest} = 1207.64 GHz and E_{up}/k = 454 K) lines in NCv1.143 and G09v1.97.

Molecule	redshift	ν_{obs} (GHz)	$S_{1.2mm}$ mJy	I_{H_2O} (Jy km s^{-1})	ΔH_2O (km s^{-1})	μL_{H_2O} (10^8 $L_\odot$)
NCv1.143	3.565	264.543	64.8 ± 0.3	2.3 ± 0.4	314 ± 63	6.4 ± 1.2
G09v1.97	3.634	260.604	66.5 ± 0.4	1.8 ± 0.6	328 ± 139	5.3 ± 2.0

Note: the redshifts are from previous CO detections as given in Yang et al. (2016).

3.3.4 Analysis and Discussion

3.3.4.1 Linear correlation between L_{H_2O} and L_{IR}

As argued in Yang et al. (2013) that there exist linear correlations between the luminosities of submm H_2O lines and that of the L_{IR}. For $H_2O(4_{22}–4_{13})$, it is found that $L_{H_2O} \sim L_{IR}^{0.9\pm0.1}$ in local (U)LIRGs. In order to check if the $H_2O(4_{22}–4_{13})$ emission in the two lensed SMGs follows the same linear trend, we plot the two sources in Fig. 3.9.

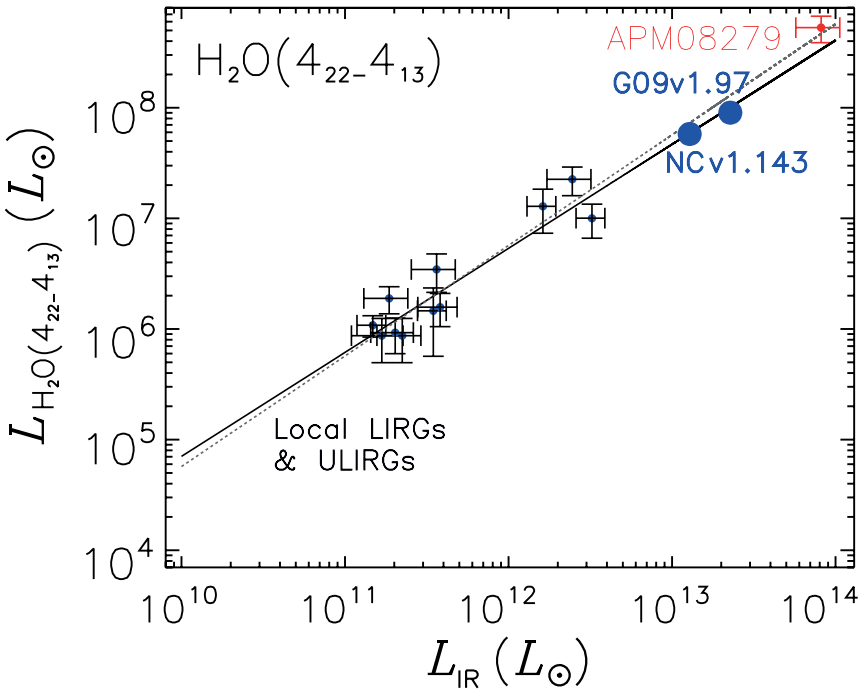

Fig. 3.9 $L_{H_2O(4_{22}–4_{13})}$ plotted against L_{IR} from local (U)LIRGs (Yang et al., 2013) to the lensed high-z SMGs in this work. The lensed QSO APM 08279+5455 (van der Werf et al., 2011) is also included in this plot.

The new fitted slope is also $\sim 0.9 \pm 0.1$, indicating that the two sources follow a similar trend as of the local (U)LIRGs. And after including the lensed QSO source, APM 08279+5455, the slope is ~ 1. This again shows that the H_2O excitation in these two lensed SMGs is likely also dominated by far-IR pumping, especially for the transition $H_2O(4_{22}–4_{13})$, the contribution from far-IR could be close to 100% (González-Alfonso et al., 2014). And more likely, the far-IR radiation field is closely related to the intense star-forming

activities inside. Thus, the linear correlation could be explained as a result of the far-IR pumping. Once absorbing far-IR photons, the upper level H_2O molecules cascade toward the lines we observed in an approximately constant fraction. This will produce a proportional amount of H_2O line photon to the total far-IR radiation intensity. Therefore, dominance of far-IR pumping is likely the main excitation mechanism for the high-J H_2O lines in high-z SMGs.

3.3.4.2 Line ratios and the SLED of H_2O

The ratio between different transitions of the H_2O lines can reflect the excitation condition of the H_2O gas, which traces the physical conditions of the warm dense molecular gas that closely related to the on-going star-forming activities (e.g. González-Alfonso et al., 2014; Omont et al., 2013; Yang et al., 2016). Thus, for NCv1.143 and G09v1.97, in which we have $J = 2$, $J = 3$ and $J = 4$ lines detected, we also plot their SLED to explore the excitation condition of the H_2O lines and compare with other sources.

Table 3.2 H_2O line fluxes and ratios for NCv1.143 and G09v1.97.

observed quantities	unit	NCv1.143	G09v1.97
$I_{H_2O(2_{11}-2_{02})}$	(Jy km s^{-1})	5.8 ± 0.3	4.1 ± 0.4
$I_{H_2O(3_{21}-3_{12})}$	(Jy km s^{-1})	8.0 ± 0.7	3.7 ± 0.4
$\Delta_{H_2O(2_{11}-2_{02})}$	(km s^{-1})	293 ± 15	257 ± 27
$\Delta_{H_2O(3_{21}-3_{12})}$	(km s^{-1})	233 ± 22	234 ± 34
$\mu L_{H_2O(2_{11}-2_{02})}$	($10^8\ L_\odot$)	10.1 ± 0.5	7.4 ± 0.7
$\mu L_{H_2O(3_{21}-3_{12})}$	($10^8\ L_\odot$)	21.3 ± 1.8	10.4 ± 1.0
μL_{IR}	($10^{13}\ L_\odot$)	12.8 ± 4.3	15.3 ± 4.3
$I_{H_2O(3_{21}-3_{12})} / I_{H_2O(2_{11}-2_{02})}$		1.38 ± 0.14	0.90 ± 0.13
$I_{H_2O(4_{22}-4_{13})} / I_{H_2O(2_{11}-2_{02})}$		0.40 ± 0.07	0.44 ± 0.15
$I_{H_2O(4_{22}-4_{13})} / I_{H_2O(3_{21}-3_{12})}$		0.29 ± 0.06	0.49 ± 0.17

Note: the redshifts are from previous CO detections as given in Yang et al. (2016).

For NCv1.143, the fluxes of the two $J \leq 2$ H_2O lines observed by Yang et al. (2016) (see Table 3.2 for the observed quantities) are $I_{H_2O(2_{11}-2_{02})} = 5.8 \pm 0.3$ Jy km s^{-1} and $I_{H_2O(3_{21}-3_{12})} = 8.0 \pm 0.7$ Jy km s^{-1}. And for G09v1.97, the reported value of $I_{H_2O(2_{11}-2_{02})}$ and $I_{H_2O(3_{21}-3_{12})}$ are 4.1 ± 0.4 Jy km s^{-1}and 3.7 ± 0.4 Jy km s^{-1}, respectively. After normalising them with the intensity of $H_2O(2_{02}-1_{11})$ (assuming an average ratio of $I_{H_2O(2_{11}-2_{02})} / I_{H_2O(2_{02}-1_{11})} = 0.8$ in local ULIRGs given by Yang et al. 2013, which will not influence the results within the uncertainties). The left panel of Fig. 3.10 shows the $I_{H_2O(2_{02}-1_{11})}$-normalized H_2O SLED of the two sources overlaid on the average H_2O SLED of the local infrared galaxies. It is clear that the $J = 2/J = 3$ H_2O line ratio of the two sources are within the local average values, albeit G09v1.97 shows a lower ratio of $I_{H_2O(3_{21}-3_{12})} / I_{H_2O(2_{11}-2_{02})} = 0.9$ (i.e. $I_{H_2O(3_{21}-3_{12})} / I_{H_2O(2_{11}-2_{02})} \sim 0.7$). For the ratio $I_{H_2O(4_{22}-4_{13})} / I_{H_2O(2_{11}-2_{02})}$, both sources show low values, which are below 0.5 (corresponding to $I_{H_2O(4_{22}-4_{13})} / I_{H_2O(2_{02}-1_{11})} < \sim 0.4$). Thus the two sources have significantly lower values than those of a large number of local ULIRGs. These low ratios could either raise from higher values of $J = 2$ H_2O and/or lower values of the high excitation H_2O lines. To better compare the difference of the H_2O excitation of these two sources with local ones, we plot the L_{IR}-normalized H_2O SLED on the right panel of Fig. 3.10. As shown in the figure, the

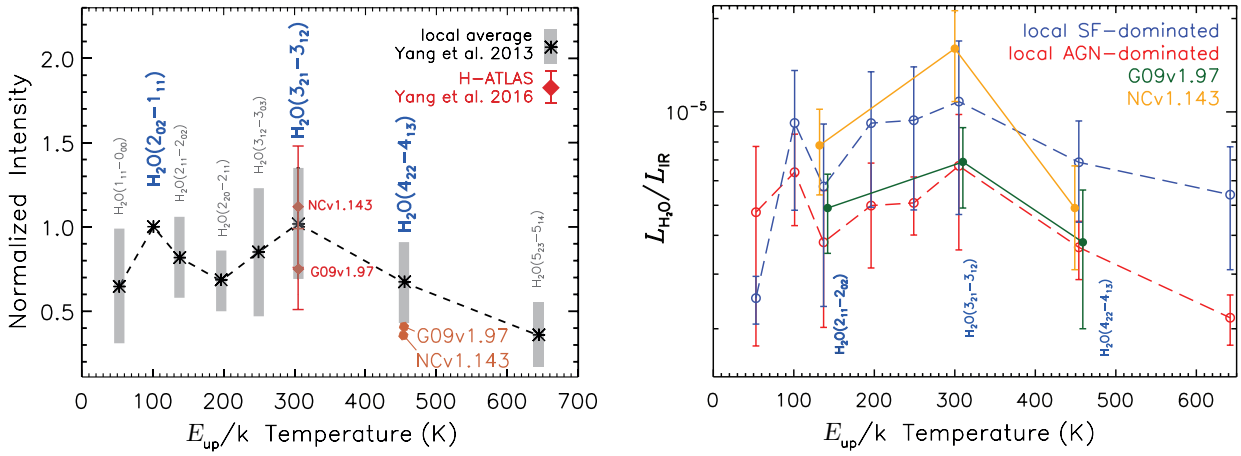

Fig. 3.10 *Left panel*: velocity-integrated flux density distribution of H_2O normalised to $I_{H_2O(2_{02}-1_{11})}$. The $J = 3$ H_2O lines are indicated by the red diamonds, while the data point of $J = 4$ H_2O line are indicated by the orange polygon. *Right panel*: the H_2O SLEDs normalised by L_{IR}Red dashed lines indicates the average values of local AGN-dominated infrared galaxies, while the blue indicates the star-forming-dominated ones. Green line shows the values for G09v1.97 and the yellow one shows the values of NCv1.143.

$H_2O(2_{11}–2_{02})$ line of NCv1.143 is above local star-forming-dominated sources, this could explain the low ratio of $I_{H_2O(4_{22}–4_{13})}/I_{H_2O(2_{11}–2_{02})}$ found. While for the G09v1.97, the $H_2O(2_{11}–2_{02})$ line is within the range of average local value. Nevertheless, the two sources again show a low value of $L_{H_2O(4_{22}–4_{13})}/L_{IR}$, which indicates that comparing to the far-infrared radiation, the $H_2O(4_{22}–4_{13})$ lines are intrinsically weaker.

3.3.5 Modelling the excitation of the multi-J H_2O lines

To fully understand the excitation of the H_2O lines, we apply the far-IR pumping excitation model of González-Alfonso et al. (2014) to extract the physical conditions where the H_2O gas resides. Since the source G09v1.97 is only detected barely at a S/N level of $3\,\sigma$, we will not include the source in the following modelling considering the large uncertainty.

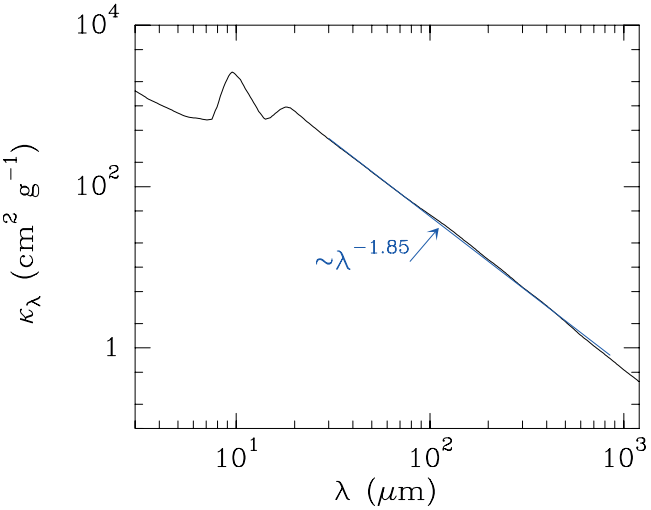

Fig. 3.11 Fig. 2 from González-Alfonso et al. (2014), showing the adopted mass absorption coefficient as a function of wavelength.

The model we use is a spherically symmetric radiative transfer code firstly build by González-Alfonso & Cernicharo (1999). The model considers both the collisional and far-IR pumping excitation of the H_2O lines. For the dust emission, it adopts a composition of a mixture of silicate and amorphous carbon. The optical constants for the dust grains are from Draine (1985) and Preibisch et al. (1993). Fig. 4.2 shows the dust mass opacity coefficient used in the H_2O model. As described in González-Alfonso et al. (2014), the parameters in this model that characterise the physical conditions are the dust temperature T_d from the dust that generates the far-IR radiation field, the continuum optical depth at 100 μm τ_{100}, the gas temperature T_{gas}, the H_2 density n_{H_2}, and H_2O column density per unit of velocity interval $N_{H_2O}/\Delta V$. Collision rates of H_2O with H_2 are taken from Dubernet et al. (2009) and Daniel et al. (2011). In the model we also adopted a typical turbulence velocity of 60 km s^{-1}, which can be found in high-z SMGs (Bournaud et al., 2015). In the practical modelling, the model can be interpreted either as a single spherical source or as an ensemble of such kind of clouds in the clumpy galaxies. Because the τ_{100} can be written as

$$\tau_{100} = \kappa_{abs} n_{H_2} m_{H_2} \chi_{dust} R_{source}, \tag{3.2}$$

in which κ_{abs} is the dust mass opacity coefficient given as shown in Fig. 4.2, m_{H_2} is the mass of molecular hydrogen, χ_{dust} is the dust to gas mass ratio defined as

$$\chi_{dust} = \frac{\rho_{dust}}{n_{H_2} m_{H_2}}, \tag{3.3}$$

and R_{source} is the outer radius of the entire spherical source. Given the gas phase water abundance X_{H_2O} (we assume an ortho-to-para ratio of 3, so that $X_{H_2O} = X_{ortho-H_2O} + X_{para-H_2O}$ could be simplified with only one parameter), we can derive the value of $N_{H_2O}/\Delta V$ by

$$N_{H_2O}/\Delta V = n_{H_2}(X_{ortho-H_2O} + X_{para-H_2O}) R_{source}/\Delta V. \tag{3.4}$$

We, nevertheless, directly use $N_{H_2O}/\Delta V$ as the modelled parameter rather than X_{H_2O} in this work. To take the distance into consideration, we adopt the CO redshift from the work reported in Chapter 4, i.e. $z = 3.5650$. This gives an angular distance of 1530.7 Mpc.

Table 3.3 Model parameters and the best fit model for NCv1.143

observed quantities	unit	explored range	cold model	warm model
T_d	(K)	35–115	~ 35	~ 75
τ_{100}		0.02–12	~ 0.1	~ 0.6
$N_{H_2O}/\Delta V$	(cm^{-2} km^{-1} s)	3×10^{14}–5×10^{17}	$\sim 5\times10^{16}$	$\sim 2\times10^{17}$
n_{H_2}	(cm^{-3})	2×10^{4}–3×10^{5}	$\sim 3\times10^{5}$	$\sim 3\times10^{4}$
T_{gas}	(K)	100–200	150^a	150^a
R_{source}	(pc)	100–2000	~ 700	~ 230

Note: ^{a} This parameter is not constrained, we used a typical value of $T_{gas} \sim 150$ K found in local ULIRGs as reported in González-Alfonso et al. (2014).

After exploring the parameter space we find the observed three H_2O lines can be explained by two components: a cold extended component (defined by the temperature of dust, T_d) that dominates the excitation of H_2O lines with $E_{up} < 200$ K, and a less extended warm component (smaller in size comparing

with the cold one) that dominates the $J \geq 3$ H_2O lines. The modelled parameters are given in Table 3.3. The model predicted values agree with the observational ones within 12% uncertainties.

Table 3.4 Photometric data points of NCv1.143

wavelength (μm)	flux density (mJy)
21.91	22.0 ± 3.0
35.05	94.0 ± 8.0
54.76	214.0 ± 7.0
76.67	291.0 ± 8.0
109.53	261.0 ± 9.0
192.77	97.2 ± 6.5
248.25	64.8 ± 0.3
257.79	63.5 ± 0.5
398.64	13.3 ± 0.2

Note: The wavelengths are the rest-frame values.

In Fig. 3.12, we compare the model predicted H_2O fluxes with the observed ones. It is clearly shown that the cold component dominates the fluxes of the $H_2O(2_{11}–2_{02})$ line, while the other two lines are dominated by the warm component. This points out the importance of far-IR pumping to the excitation of H_2O lines, especially for the lines with $E_{up} > 200$ K. Another important constraint to the model comes from the dust SED. We gathered the photometric data from *Herschel* SPIRE and PACS at sky frequencies of 100, 160, 250, 350, 500 and 880 μm, together with the continuum fluxes acquired from NOEMA observations reported in Yang et al. (2016). In general, the model predicted dust SED fits well with the observed data points. Nevertheless, on the Rayleigh-Jeans side of the dust SED, the model underpredicts the continuum fluxes. This can be explained by the fact that cold dust (normally with $T_d \sim 20$–50 K) has almost no contribution to the H_2O excitation, thus the dust continuum fluxes derived from H_2O excitation model will underpredict the values at long wavelength. As in the case of M 82 and the Orion Bar, the proto-typical photodissociation region (PDR), the H_2O lines from such sources are weak, and the water molecules are mostly locked in icy interstellar dust grains in such cold regions (e.g. Melnick & Bergin, 2005).

For the cold component which dominates the $H_2O(2_{11}–2_{02})$ line, the modelled T_d is about 35 K while the radius is about 700 pc. While for the warm component that dominates the $H_2O(3_{21}–3_{12})$ and $H_2O(4_{22}–4_{13})$ lines, the the modelled $T_d \sim 75$ K and the size is about 230 pc. The size of the cold component agrees with the lensing model built for the NOEMA high-resolution imaging of $H_2O(2_{11}–0_{20})$ (see Chapter 3.3.2 for details of gravitational lensing). For the warm component, the lensing model using the NOEMA images of $H_2O(3_{21}–3_{12})$ predicts a emitting-region size to be about twice smaller than that of the $H_2O(2_{11}–2_{02})$ line. While the size of the warm component derived from the H_2O excitation model is about 3 times smaller than the cold one. This could be due to the fact that the extended component may partially contribute to the $H_2O(3_{21}–3_{12})$ emission as we found in Fig. 3.12, so that the emission size of $H_2O(3_{21}–3_{12})$ will be actually larger than the size of the warm component. This also suggests the importance of the imaging observations of the $J = 4$ H_2O line (or the H_2O lines at even higher energy levels). Since they are totally dominated by the warm component, the constraint of their size will greatly help to constrain the excitation models.

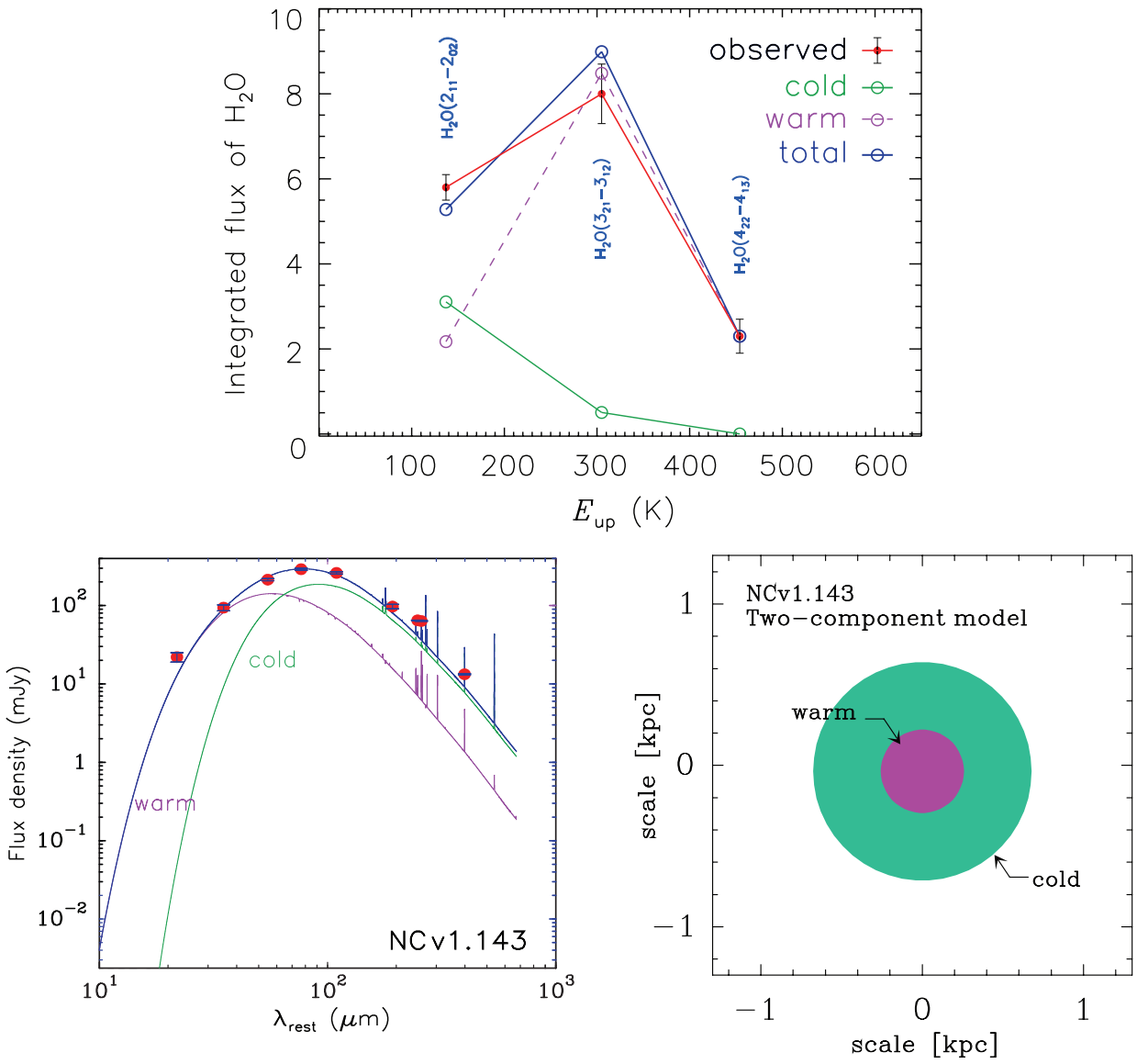

Fig. 3.12 *Upper panel*: The modelled spectral line for the detected three H_2O lines over-plotted on the observed fluxes. The warm excitation component is shown in purple while and the cold one is shown in blue. The total modelled fluxes are shown in blue. Observed fluxes are indicated by the red points with error-bars. *Lower left panel*: The dust SED generated from the FIR-pumping model of the H_2O lines. The warm dust component is shown in purple while the cold one is shown in green. The sum of the two components is shown in blue. The observed FIR fluxes (see Table 3.4) are given in red data points. *Lower right panel*: The schematic figure shows the H_2O-excitation-model-derived structure for the warm and cold components, indicating the approximate sizes derived from the H_2O excitation model.

The molecular gas densities for both components derived tend to agree with the values from the multi-J CO non-LTE modelling results that $T_{\rm gas} \sim 10^{3.0}$–$10^{5.5}$ cm^{-3} reported in Chapter 4. The extended cold component has a value of $N_{\rm H_2O}/\Delta V \sim 5 \times 10^{16}$ cm^{-2} km^{-1} s, which is higher than the results in Yang et al. (2016). Moreover, the fitted τ_{100} from this work is much smaller comparing with the Yang et al. 2016's value. The higher values of τ_{100} in our model will over-predict the flux of dust continuum by a large factor, thus our new constrain favours the low value of τ_{100}. The overestimation of τ_{100} in Yang et al. 2016 could be caused by a underestimation of $N_{\rm H_2O}/\Delta V$ and gas density that was unable to be constrained given the limited observational data points. In Yang et al. (2016), there are only two H_2O lines as inputs to the H_2O excitation models. Therefore, it is difficult to break the degeneracies between the τ_{100} and $N_{\rm H_2O}/\Delta V$ in the model. This brings large uncertainties in deriving the physical conditions from the H_2O excitation model. Nevertheless, in this work, we show that with three H_2O lines, i.e. $H_2O(2_{11}$–$2_{02})$, $H_2O(3_{21}$–$3_{12})$ and $H_2O(4_{22}$–$4_{13})$, we will be able to pinpoint the modelling parameters with much better precisions.

3.3.6 Conclusion

Using the most extended configuration of the NOEMA array, we observed the $H_2O(4_{22}$–$4_{13})$ H_2O line in two of our brightest *H*-ATLAS lensed SMGs, NCv1.143 and G09v1.97. We have detected the H_2O line in NCv1.143 and a tentative detection is achieved for G09v1.97.

We have analysed the H_2O excitation in NCv1.143 using the H_2O far-IR pumping model. We derived the physical conditions of the ISM where the H_2O gas resides. There are likely two components exciting the H_2O lines, one extended (~ 700 pc) cold component with $T_{\rm d} \sim 35$ K, and one less extended warm component (~ 230 pc) with $T_{\rm d} \sim 75$ K. The values of $N_{\rm H_2O}/\Delta V$ are found to be from $\sim 5 \times 10^{16}$ in the cold component to $\sim 2 \times 10^{17}$ in the warm one. The derived dust optical depth at 100 μm τ_{100} are smaller than 1, which is much smaller than that found in the previous work, based on modelling with only two H_2O lines (one $J = 2$ and one $J = 3$ H_2O line). The overestimation can be explained by the degeneracies between $N_{\rm H_2O}/\Delta V$ and τ_{100} in the model, if the input observational constrains are limited. This work shows that, with a $J = 4$ H_2O line, one will be able to break such degeneracies, and help derive the physical conditions with much better precisions.

Chapter 4

Molecular gas in the lensed SMGs as probed by multi-*J* CO and atomic carbon lines

This is the universe. Big, isn't it? Thousands of suns, millions of stars, separated by immense distances and by thin floating clouds of gas.

A Matter of Life and Death (1946)

4.1 Introduction

Thanks to the recent extra-galactic surveys at far-IR and submm bands using space telescope like *Herschel*-Astrophysical Terahertz Large Area Survey (*H*-ATLAS, Eales et al., 2010) and the ground-based telescope at the South Pole, e.g. the South Pole Telescope (SPT) survey (Vieira et al., 2013), large and statistically significant samples of SMGs have been built. Theoretical work has predicted that with a criterion of source flux at 500 μm, namely $S_{500\,\mu m} > 100$ mJy, strongly lensed high-z SMGs can be efficiently selected, and this has been observationally tested (e.g. Nayyeri et al., 2016; Negrello et al., 2017, 2010, 2007; Vieira et al., 2010; Wardlow et al., 2013). The strong lensing effect not only boosts the sensitivity of observations, but also improves the spatial resolution so that it offers us unique opportunity to study the high-z SMGs in unprecedented details (see e.g. Swinbank et al., 2010).

In order to understand the star formation process that shapes the baryonic matter of these SMGs, one of the most direct methods is to study the molecular gas which is the fuel of the star formation. The composition of molecular gas is predominated by molecular hydrogen (H_2). However, H_2 lacks a permanent dipole moment, its rovibrational transitions are thus forbidden. Only at very high temperature, i.e. $\gtrsim 500$ K, the first quadrupole rotational line can be excited. This makes it very difficult to observe the molecular hydrogen directly in common environments of molecular gas in, e.g. GMCs or in extragalactic sources as a global value. Therefore, a tracer of H_2 that can be excited at low temperature is needed. CO, as the most abundant molecule after H_2 in most of the conditions of the ISM, has very low excitation energy and critical density (see Table 1.1 in Chapter 1.2.1). The first energy level of CO is 5.5 K with a critical density of $n_{\rm crit} = 2.4 \times 10^2$ cm^{-3}. The frequency of CO(1–0) is 115.271 GHz, which is well within the 3 mm atmospherical window. Therefore, this line is an ideal molecular gas tracer for the ground-base telescope

observations. The CO lines are important tracers that can help us to understand the physical conditions of the molecular gas.

In the high-z SMGs, Tacconi et al. (2008) found that those galaxies have large reservoirs of molecular gas about 10^{10-11} $M_{\odot}$. The ground state CO line is usually used to trace the molecular gas mass, with the help of a conversion factor between the CO(1–0) flux and molecular gas mass (see Bolatto et al. 2013 for a review). This is also related to one of the key interests of studying star formation at galactic scale across all redshifts from the observation point of view which is to quantify the 'star formation law', namely the correlation between $M_{\rm gas}$ and SFR (or the surface SFR density as originally defined by Kennicutt 1998), as we mentioned in Section 1.2.2. This law is commonly used as an essential input for the cosmological theoretical models of galaxy formation and evolution. It is also a gateway through which we understand the relation between star formation and molecular gas content.

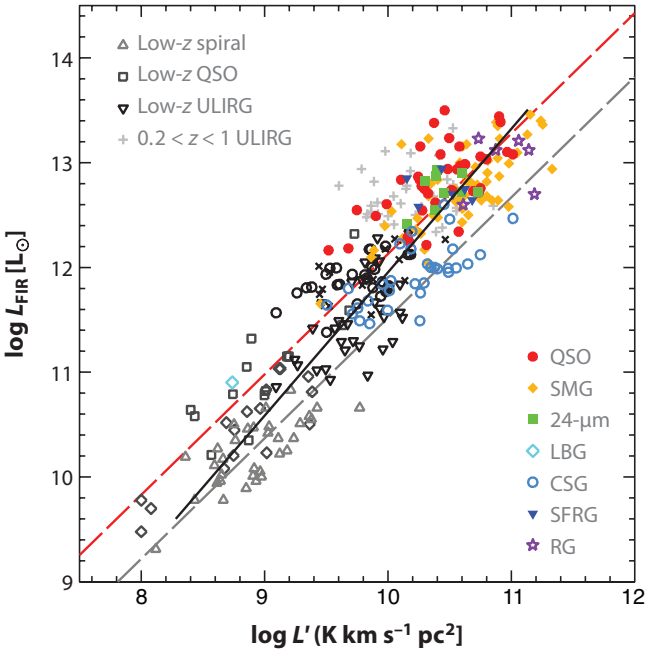

Fig. 4.1 The luminosity of CO(1–0) plotted against far-IR luminosity, one of the interpretations of star formation law (KS law) from local spirals to high-z starbursts. Different types of galaxies at various redshifts are shown in different colours. The figure is adapted from Carilli & Walter (2013).

The excitation of the CO lines can also indicate the physical conditions of the molecular gas. By measuring the multiple-J CO lines, we can constrain the kinetic temperature and the molecular gas density of the emitting regions (e.g Rangwala et al., 2011) using non-local thermodynamic equilibrium (non-LTE) models. From the observations of the aforementioned individual high-z galaxies, the variety of CO spectral line energy distribution shows that multiple molecular gas components in terms of their different gas densities and kinetic temperatures are required to explain the full-J CO SLEDs.The mid-J CO emission can be explained by a warm component with molecular gas volume density of 10^3–10^4 cm^{-3} which is more closely related to the on-going star formation, while there is also an extended cool component with lower metallicity (e.g. Danielson et al., 2011; Ivison et al., 2010). Rosenberg et al. (2015) further quantatively classify the local galaxies into three groups based on the shape of their CO SLEDs, which helps to give hints of the dominant excitation conditions within. Recent works with *Herschel* SPIRE/FTS spectra of 167 local galaxies by Liu et al. (2015) and 121 local LIRGs by Lu et al. (2017) confirm the existence of multiple CO

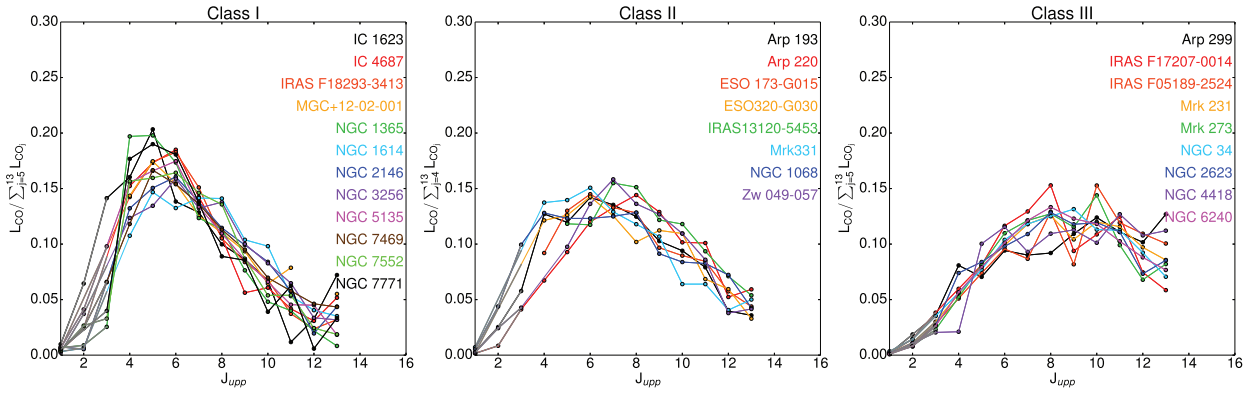

Fig. 4.2 CO SLED for local (U)LIRGs as revealed by *Herschel* SPIRE FTS (Rosenberg et al., 2015). They are divided into three classes. Class I includes galaxies with $\alpha <$,0.33, Class II $0.33 < \alpha < 0.66$; and strong AGN are included in Class III $\alpha > 0.66$ (where alpha is defined as the ratio of high-J ($J_{\rm up}$ = 11+12+13) to mid-J ($J_{\rm up}$ = 5+6++7) CO line luminosities, see Eq. 1 of Rosenberg et al. 2015). It is clearly shown that the presence of a strong AGN warrants a high ratio of high-J vs low-J line intensities.

excitation components. Daddi et al. (2015) reached similar conclusions for $z \sim 1.5$ star-forming galaxies. The differences in $J_{\rm up} \gtrsim 6$ part of the CO SLEDs (normalised by $L_{\rm IR}$) reveal different excitation processes (see e.g. Lu et al., 2017): in most cases the CO emission is insignificant for $J_{\rm up} > 7$ CO lines; in the few cases ($\lesssim 10\%$) where $L_{\rm IR}$ is dominated by an AGN there is a substantial excess of CO emission in the $J_{\rm up} > 10$ CO lines, likely associated with AGN heating of molecular gas; there could also be a very few exceptional cases, like NGC 6240, where shock excitation dominates (Meijerink et al., 2013).

We thus selected a sample of 16 SMGs based on the flux cut at 500 μm. Most of the sources were studied by their H_2O lines are described in Chapter 3. To understand the nature of the SMGs, we study the properties of the ISM within them. We thus targeted multiple-J CO lines in each of them with IRAM 30m telescope. By analysing the CO line profile, we discovered a significant effect of differential lensing that can cause underestimation of the linewidth by a factor of ~ 2. This might heavily influence the estimation of the dynamical mass, since it is proportional to the square of the linewidth. Using the MCMC LVG modelling, the multiple-transition CO line data allowed us to study the molecular gas excitation of the SMGs. The CO SLEDs are mostly peaking around $J_{\rm up}$ = 5–7. Using LVG modelling by fitting the SLEDs via a Bayesian approach, we derive a gas density $n_{\rm H_2}$, gas temperature and CO column density per unit velocity gradient $N_{\rm CO}/{\rm d}v$. Then, we find a correlation between the gas thermal pressure $P_{\rm th}$ and the star formation efficiency. We also study the global properties of the molecular gas and its relation with star formation. We derive gas to dust mass ratios in the approximate range from 30 to 100. The gas depletion time $t_{\rm dep}$ of the *H*-ATLAS SMGs shows no difference compared with other lensed/unlensed SMGs. With the detections of 7 [CI](2–1) lines in our *H*-ATLAS lensed SMGs, we extend the linear correlation between the luminosity of the CO(1–0) line and the [CI](2–1) line found in a sample of local (U)LIRGs. Finally, we compare the linewidths of the CO and H_2O emission lines for a sample of 13 SMGs, using multi-J CO emission lines. We find that the linewidths of the CO lines and H_2O lines agree very well in most cases. This supports our previous argument that the emitting regions of the CO and H_2O lines are likely to be co-spatially located.

The detail content of the work is described in the following Section 4.2.

4.2 Publication (A&A in press)

Astronomy & Astrophysics manuscript no. co-hatlas-2017
September 21, 2017

Molecular gas in the *Herschel*⋆-selected strongly lensed submillimeter galaxies at $z \sim 2$–4 as probed by multi-J CO lines ⋆⋆

C. Yang(杨辰涛)[1,2,3,4,5], A. Omont[4,5], A. Beelen[2], Y. Gao(高煜)[1], P. van der Werf[6], R. Gavazzi[4,5], Z.-Y. Zhang(张智昱)[7,8], R. Ivison[7,8], M. Lehnert[4,5], D. Liu(刘岱钟)[9], I. Oteo[7,8], E. González-Alfonso[10], H. Dannerbauer[11,12], P. Cox[13], M. Krips[14], R. Neri[14], D. Riechers[15], A. J. Baker[16], M.J. Michałowski[17,7], A. Cooray[18], and I. Smail[19]

(Affiliations can be found after the references)

Received .../ Accepted ...

ABSTRACT

We present the IRAM-30 m observations of multiple-J CO ($J_{\rm up}$ mostly from 3 up to 8) and [C I]($^3P_2 \rightarrow {}^3P_1$) ([C I](2–1) hereafter) line emission in a sample of redshift ~ 2–4 submillimeter galaxies (SMGs). These SMGs are selected among the brightest-lensed galaxies discovered in the *Herschel*-Astrophysical Terahertz Large Area Survey (*H*-ATLAS). Forty-seven CO lines and 7 [C I](2–1) lines have been detected in 15 lensed SMGs. A non-negligible effect of differential lensing is found for the CO emission lines, which could have caused significant underestimations of the linewidths, and hence of the dynamical masses. The CO spectral line energy distributions (SLEDs), peaking around $J_{\rm up} \sim 5$–7, are found to be similar to those of the local starburst-dominated ultra-luminous infrared galaxies and of the previously studied SMGs. After correcting for lensing amplification, we derived the global properties of the bulk of molecular gas in the SMGs using non-LTE radiative transfer modelling, such as the molecular gas density $n_{\rm H_2} \sim 10^{2.5}$–$10^{4.1}$ cm^{-3} and the kinetic temperature $T_{\rm k} \sim 20$–750 K. The gas thermal pressure $P_{\rm th}$ ranging from $\sim 10^5$ K cm^{-3} to 10^6 K cm^{-3} is found to be correlated with star formation efficiency. Further decomposing the CO SLEDs into two excitation components, we find a low-excitation component with $n_{\rm H_2} \sim 10^{2.8}$–$10^{4.6}$ cm^{-3} and $T_{\rm k} \sim 20$–30 K, which is less correlated with star formation, and a high-excitation one ($n_{\rm H_2} \sim 10^{2.7}$–$10^{4.2}$ cm^{-3}, $T_{\rm k} \sim 60$–400 K) which is tightly related to the on-going star-forming activity. Additionally, tight linear correlations between the far-infrared and CO line luminosities have been confirmed for the $J_{\rm up} \geq 5$ CO lines of these SMGs, implying that these CO lines are good tracers of star formation. The [C I](2–1) lines follow the tight linear correlation between the luminosities of the [C I](2–1) and the CO(1–0) line found in local starbursts, indicating that [C I] lines could serve as good total molecular gas mass tracers for high-redshift SMGs as well. The total mass of the molecular gas reservoir, $(1\text{–}30) \times 10^{10}\,M_\odot$, derived based on the CO(3–2) fluxes and $\alpha_{\rm CO(1-0)} = 0.8 M_\odot\,(\,{\rm K\,km\,s^{-1}\,pc^2})^{-1}$, suggests a typical molecular gas depletion time $t_{\rm dep} \sim 20$–100 Myr and a gas to dust mass ratio $\delta_{\rm GDR} \sim 30$–100 with ~ 20%–60% uncertainty for the SMGs. The ratio between CO line luminosity and the dust mass $L'_{\rm CO}/M_{\rm dust}$ appears to be slowly increasing with redshift for high-redshift SMGs, which need to be further confirmed by a more complete SMG sample at various redshifts. Finally, through comparing the linewidth of CO and H_2O lines, we find that they agree well in almost all our SMGs, confirming that the emitting regions of the CO and H_2O lines are co-spatially located.

Key words. galaxies: high-redshift – galaxies: ISM – infrared: galaxies – submillimeter: galaxies – radio lines: ISM – ISM: molecules

1. Introduction

The strongest starbursts throughout the star formation history of our Universe are the high-redshift hyper- and ultra-luminous infrared galaxies (HyLIRGs and ULIRGs). With infrared luminosities integrated over 8–1000 μm $L_{\rm IR} \geq 10^{13}\,L_\odot$ and $10^{13}\,L_\odot > L_{\rm IR} \geq 10^{12}\,L_\odot$, respectively, and star formation rate (SFR) around $1000\,M_\odot\,{\rm yr}^{-1}$, they approach the limit of maximum starbursts (Barger et al. 2014). Despite having comparable or slightly higher luminosities than the local ULIRGs (Tacconi et al. 2010), these submillimeter (submm) bright galaxies (SMGs, see reviews of Blain et al. 2002; Casey et al. 2014) are different, being more extended and unlike nuclear starbursts of local ULIRGS. This population of dusty starburst galaxies was first discovered in the submm band using Submillimeter Common-User Bolometer Array (SCUBA, Holland et al. 1999) on the James Clerk Maxwell Telescope (Barger et al. 1998; Hughes et al. 1998; Smail et al. 1997), and later the spectroscopy observations revealed a median redshift of ~ 2.5 (Chapman et al. 2005; Danielson et al. 2017). Their extremely intense star formation activity indicates that these "vigorous monsters" generating enormous energy at far-infrared (FIR) are in the critical phase of rapid stellar mass assembly. They are believed to be the progenitors of the most massive galaxies today (e.g. Simpson et al. 2014). Nevertheless, theoretical models of galaxy evolution have been challenged by the observed large number of high-redshift SMGs (e.g. Casey et al. 2014).

Since the initial discovery of SMGs at 850 μm with SCUBA at the end of the last century, Chapman et al. (2005) carefully studied the properties of this 850 μm-selected SMG population and concluded that those with $S_{850\,\mu{\rm m}} > 1$ mJy contribute a significant fraction to the cosmic star formation around z = 2–3, that is $\gtrsim 10\%$. Several other works have also confirmed that SMGs play a key role in the cosmic star formation at high-redshift (e.g. Murphy et al. 2011; Magnelli et al. 2013; Swinbank et al. 2014; Michałowski et al. 2017). For the ULIRGs studied with a median redshift of 2.2, it can be > 65% according to Le Floc'h et al. 2005 and Dunlop et al. 2017 (see ALMA counts by Karim et al. 2013; Oteo et al. 2016; Aravena et al.

⋆ *Herschel* is an ESA space observatory with science instruments provided by European-led Principal Investigator consortia and with important participation from NASA.

⋆⋆ Based on observations carried out under project number 076-16, 196-15 and 079-15 (PI: C. Yang); 252-11 and 124-11 (PI: P. van de Werf) with the IRAM-30m Telescope. IRAM is supported by INSU/CNRS (France), MPG (Germany) and IGN (Spain).

2016a; Dunlop et al. 2017 and references therein for updated SMG counts; and Casey et al. 2014 for redshift distributions of SMGs selected at 850–870 μm by SCUBA/LABOCA and at 1.1 mm by AzTEC).

It is important to understand the extreme star-forming activity within SMGs through studying their molecular gas content which serves as the basic ingredient for star formation, especially those at the peak of the star formation history (i.e. $z \sim 2$–3, Madau & Dickinson 2014). Nevertheless, due to their great distances, the number of well-studied high-redshift SMGs with several CO transitions at different energy levels is limited (see reviews of Solomon & Vanden Bout 2005; Carilli & Walter 2013) and this is mostly achieved through strong gravitation lensing and/or in quasi-stellar objects (QSOs), including IRAS F10214+4724 (Ao et al. 2008), APM 08279+5455 (Weiß et al. 2007), Cloverleaf (Bradford et al. 2009), SMM J2135-0102 (Danielson et al. 2011), G15v2.779 (Cox et al. 2011) and in the weakly lensed SMG, HFLS3 at $z = 6.34$ (Riechers et al. 2013; Cooray et al. 2014). Our knowledge of the detailed physical and chemical properties and processes related to star formation within these high-redshift Hy/ULIRGs is still limited.

Tacconi et al. (2008) found that high-redshift SMGs have large reservoirs of molecular gas about $10^{10-11}\,M_{\odot}$ (see also Ivison et al. 2011; Riechers et al. 2011c). CO rotational lines are contributing a significant amount of cooling of the molecular gas. By measuring the multiple-J CO lines, we can constrain the kinetic temperature and the gas density of the emitting regions (e.g. Rangwala et al. 2011) using non-local thermodynamic equilibrium (non-LTE) models. From the observations of the aforementioned individual high-redshift galaxies, the variety of CO spectral line energy distribution (SLED) shows that multiple molecular gas components in terms of their different gas densities and kinetic temperatures are required to explain the entire CO SLEDs. The mid/high-J CO emission can be explained by a warm component with molecular gas volume density of 10^3–10^4 cm^{-3} which is more closely related to the ongoing star formation, while there is also an extended cool component dominating the low-J CO (e.g. Ivison et al. 2010; Danielson et al. 2011). Recent works with *Herschel* SPIRE/FTS spectra of 167 local galaxies by Liu et al. (2015) and 121 local LIRGs by Lu et al. (2017) also favour the presence of multiple CO excitation components. Daddi et al. (2015) reached similar conclusions for $z \sim 1.5$ normal star-forming galaxies. The differences in the $J_{\rm up} > 6$ part of the CO SLEDs reveal different excitation processes (e.g. Lu et al. 2017): in most cases, the CO emission is insignificant for $J_{\rm up} > 7$ CO lines; in the few cases ($\lesssim 10\%$) where $L_{\rm IR}$ is dominated by an active galactic nucleus (AGN) there is a substantial excess of CO emission in the $J_{\rm up} > 10$ CO lines (van der Werf et al. 2010), likely associated with AGN heating of molecular gas; there could also be a small number of exceptional cases, like NGC 6240, where shock excitation dominates (Meijerink et al. 2013).

Thanks to the extra-galactic surveys at FIR and submm bands like the *Herschel*-Astrophysical Terahertz Large Area Survey (*H*-ATLAS, Eales et al. 2010), the *Herschel* Multi-tiered Extragalactic Survey (*Her*MES, Oliver et al. 2012) and South Pole Telescope (SPT) survey (Vieira et al. 2013), large and statistically significant samples of SMGs have been built. It was found that with a criterium of source flux at 500 μm, namely $S_{500\,\mu m} > 100$ mJy, (galaxy-galaxy) strongly lensed high-redshift SMGs can be efficiently selected (e.g. Negrello et al. 2007, 2010, 2017; Vieira et al. 2010; Wardlow et al. 2013; Nayyeri et al. 2016). The strong lensing effect not only boosts the sensitivity of observations but also improves the spatial resolution so that we can study the high-redshift galaxies in unprecedented detail (see e.g. Swinbank et al. 2010).

The spectroscopy redshifts (mostly determined from CO lines) have now been determined in more than 24 *Herschel*-selected, lensed *H*-ATLAS SMGs thanks to the combined use of various telescopes; for example, *Herschel* itself, using the SPIRE/FTS (George et al. 2013; Zhang et al., in prep), CSO with Z-Spec (Scott et al. 2011; Lupu et al. 2012), APEX (Ivison et al., in prep), IRAM/PdBI (Cox et al. 2011; Krips et al. in prep.), LMT, ALMA (Asboth et al. 2016) and especially the Zpectrometer on the GBT (Frayer et al. 2011; Harris et al. 2012, and in prep.) and CARMA (Riechers et al. 2011b, and in prep.).

In their parallel work on strongly lensed SMGs (Vieira et al. 2010, 2013; Hezaveh et al. 2013; Spilker et al. 2016, and the references therein), the SPT group used a selection based on the 1.4 mm continuum flux density. The ALMA blind redshift survey of these 1.4 mm-selected SMGs shows a flat redshift distribution in the range $z = 2$–4, with a mean value of $\langle z \rangle = 3.5$, being in contrast to the 850–870 μm SCUBA/LABOCA-selected sample (Weiß et al. 2013; Spilker et al. 2016). This can be explained by the different flux limits of the two samples, namely, the SPT-selected sources are intrinsically brighter than the classic 850–870 μm SCUBA/LABOCA-selected SMGs (Koprowski et al. 2014).

Efficient CO detection in lensed SMGs has significantly enlarged the sample size of multi-J CO detections, with the aim of allowing statistical studies. Thus, we present here our observations of multi-J CO emission lines in 16 *H*-ATLAS lensed SMGs at $z \sim 2$–4, for a better understanding of the physical conditions of the ISM in high-redshift SMGs on a statistical basis.

Although there is a large number of CO observations in high-redshift sources, only a few high-density tracers with high dipole, for example, HCN, have so far been detected, most of which in QSOs (e.g. Gao et al. 2007; Riechers et al. 2010), and even fewer detections in SMGs (e.g. Oteo et al. 2017). Submm H_2O lines, another dense gas tracer, have been reported in 12 *H*-ATLAS lensed SMGs (Omont et al. 2011; Omont et al. 2013, O13 hereafter and Yang et al. 2016, Y16 hereafter) using IRAM NOrthern Extended Millimeter Array (NOEMA), and also in other galaxies (see the review by van Dishoeck et al. 2013). An open question is whether or not the submm H_2O emission lines trace similar regions as traced by mid/high-J CO and HCN. The difficulty of the comparison is coming from the currently limited high-resolution mapping of the submm H_2O lines. However, by comparing line profiles of unresolved observations of lensed SMGs, Y16 argue that the mid-J CO lines originate in similar conditions to the submm H_2O lines. This can be further tested by a larger sample from this work, and more directly, the high angular-resolution mapping of the emissions: see, for example, the cases of SDP81 as probed by ALMA (ALMA Partnership, Vlahakis et al. 2015), NCv1.143 observed by NOEMA and of G09v1.97 through ALMA observations (Yang et al. in prep.).

In this paper, we study the physical properties of the molecular gas in a sample of 16 lensed SMGs at $z \sim 2$–4 by analysing their multiple-J CO emission lines. This paper is organised as follows: we describe our sample, the observations and data reduction in Section 2. The observed properties of the multi-J CO emission lines are presented in Section 3. The global properties of the SMGs together with the differential lensing effect is discussed in Section 4. A detailed discussion of the CO excitation is given in Section 5. Section 5.3 describes the discussion of molecular gas mass and star formation. We compare the emission lines of CO and submm H_2O in Section 5.4. Finally, we summarise our results in Section 6. A spatially-flat ΛCDM cosmology with

$H_0 = 67.8 \pm 0.9\,\mathrm{km\,s^{-1}\,Mpc^{-1}}$, $\Omega_M = 0.308 \pm 0.012$ (Planck Collaboration et al. 2016) and Salpeter's (1955) initial mass function (IMF) has been adopted throughout this paper.

Table 1: Basic information on the CO rotational lines and [C I] ^{3}P fine structure lines used in this paper.

Molecule	Transition $J_U \rightarrow J_L$	$\nu_{\rm rest}$ (GHz)	$E_{\rm up}/k$ (K)	$A_{\rm UL}$ ($\rm s^{-1}$)	$n_{\rm crit}$ ($\rm cm^{-3}$)
CO	$1 \rightarrow 0$	115.271	5.5	7.20×10^{-8}	2.4×10^2
	$2 \rightarrow 1$	230.538	16.6	6.91×10^{-7}	2.1×10^3
	$3 \rightarrow 2$	345.796	33.2	2.50×10^{-6}	7.6×10^3
	$4 \rightarrow 3$	461.041	55.3	6.12×10^{-6}	1.8×10^4
	$5 \rightarrow 4$	576.268	83.0	1.22×10^{-5}	3.6×10^4
	$6 \rightarrow 5$	691.473	116.2	2.14×10^{-5}	6.3×10^4
	$7 \rightarrow 6$	806.652	154.9	3.42×10^{-5}	1.0×10^5
	$8 \rightarrow 7$	921.800	199.1	5.13×10^{-5}	1.5×10^5
	$9 \rightarrow 8$	1036.912	248.9	7.33×10^{-5}	2.1×10^5
	$10 \rightarrow 9$	1151.985	304.2	1.00×10^{-4}	2.9×10^5
	$11 \rightarrow 10$	1267.014	365.0	1.34×10^{-4}	3.9×10^5
[C I]	$^3P_1 \rightarrow {}^3P_0$	492.161	23.6	7.88×10^{-8}	4.9×10^2
	$^3P_2 \rightarrow {}^3P_1$	809.342	62.4	2.65×10^{-7}	9.3×10^2

Notes. Critical density $n_{\rm crit,UL} \equiv A_{\rm UL}/\Sigma_{\rm i \neq U}\gamma_{\rm Ui}$ (e.g. Tielens 2005). $A_{\rm UL}$ is the Einstein coefficient for spontaneous emission from level U to L, and $\gamma_{\rm Ui}$ is the collision rate coefficient. The critical densities ($n_{\rm crit}$) are calculated by assuming a gas temperature $T_{\rm k} = 100$ K, and an ortho-H_2 to para-H_2 ratio of 3 and an optically thin regime. The rest-frame frequencies ($\nu_{\rm rest}$), upper-level energies ($E_{\rm up}/k$) and Einstein A coefficients are taken from the LAMDA database (Schöier et al. 2005). The collision rate coefficients are from Yang et al. (2010). Throughout this paper, we refer to [C I]($^3P_1 \rightarrow {}^3P_0$) as [C I](1–0) and [C I]($^3P_2 \rightarrow {}^3P_1$) as [C I](2–1).

2. Sample, observations, and data reduction

2.1. Selection of the lensed SMGs

Unlike the previously studied SMGs, our sample is drawn from shorter wavelengths using *Herschel* SPIRE photometric data at 250, 350, and 500 μm. In order to find the strongly lensed SMGs, all of our targets were selected from the *H*-ATLAS catalogue (Valiante et al. 2016) with a criterion of $S_{100\,\mu\rm m} > 100$ mJy based on the theoretical models of the submm source number counts (e.g. Negrello et al. 2010, 2017). Then, a Submillimeter Array (SMA) subsample was constructed based on the availability of previously spectroscopically confirmed redshifts obtained by CO observations (Bussmann et al. 2013, hereafter Bu13); it includes all high-redshift *H*-ATLAS sources with $F_{500\,\mu\rm m} > 200$ mJy in the GAMA and NGP fields (300 deg^2). From SMA 880 μm images and the identification of the lens deflectors and their redshifts, Bu13 built lensing models for most of them.

Our sample was thus extracted from Bu13's *H*-ATLAS-SMA sources with the initial goal of studying their H_2O emission lines (see Table 6 of Y16). It consists of 17 lensed SMGs with redshift from 1.6 to 4.2. We have detected submm H_2O emission lines in 16 sources observed with only one non-detection from the AGN-dominated source, G09v1.124 (O13; Y16, Table 2). However, for this CO follow-up observation, we dropped three sources among the H_2O-detected 16: SDP 11 due to its low redshift $z < 2$, NCv1.268 because of its broad linewidth that brings difficulties for line detection in a reasonable observing time, and G15v2.779 because it has already been well observed by Cox et al. (2011). Nevertheless, we included G15v2.779 in discussing the main results to have a better view of CO properties for the whole sample. Our CO sample of 14 sources (13 observed with the IRAM's Eight Mixer Receiver, for example, EMIR, in this work plus G15v2.779 studied by Cox et al. 2011) is thus a good representative for the brightest high-redshift *H*-ATLAS lensed sources with $F_{500\,\mu\rm m} > 200$ mJy and at $z > 2$ (except SDP 81 with $F_{500\,\mu\rm m} \sim 174$ mJy). Besides these 14 sources, we also include two slightly less bright sources, G12v2.890 and G12v2.257, down to $F_{500\,\mu\rm m} > 100$ mJy. In the end, as listed in Table 3, the entire sample includes 16 lensed SMGs from redshift 2.2 to 4.2.

The lensing models for twelve of the SMGs are provided by Bu13 through SMA 880 μm continuum observations. Table 3 lists the magnification factors (μ_{880}) and inferred intrinsic properties of these galaxies together with their CO redshifts from previous blind CO redshift observations. After correcting for the magnification, their intrinsic infrared luminosities are ~ 4–$20 \times 10^{12}\,L_\odot$. Since the lensed nature of these SMGs and their submm selection may bias the sample, we will compare their properties with other SMG samples later from Section 3 to Section 5.3.

In this work, in order to explore the physical properties of the bulk of the molecular gas, we targeted the rotational emission lines of CO, mostly from $J_{\rm up} = 3$ to 8 and up to 11 in a few cases. [C I](2–1) line is also observed "for free" together with CO(7–6). Basic information such as the frequencies, upper-level energies, Einstein A coefficients and critical densities of the CO and [C I] lines are listed in Table 1. The targeted CO lines are selected based on their redshifted frequencies so that they could be observed in a reasonably good atmospheric window in EMIR bands. In total, we observed 55 CO lines, with 8 [C I](2–1) lines acquired simultaneously with CO(7–6) in 15 sources (Table 2).

2.2. Observation and data reduction

The observations were carried out from 2011 June 30th to 2012 March 13th, and from 2015 May 26th to 2016 February 22nd using the multi-band heterodyne receiver EMIR (Carter et al. 2012) on the IRAM-30m telescope. Bands at 3 mm, 2 mm, 1.3 mm and 0.8 mm (corresponding to E090, E150, E230 and E330 receivers, respectively) were used for detecting multiple CO transitions. Each bandwidth covers a frequency range of 8 GHz. We selected the wide-band line multiple auto-correlator (WILMA) with a 2 MHz spectral resolution and the fast Fourier Transform Spectrometer with a 200 kHz resolution (FTS200) as back ends simultaneously during the observations. Given that the angular sizes of our sources are all less than 8″, observations were performed in wobbler switching mode with a throw of 30″. Bright planet/quasar calibrators including Mars, 0316+413, 0851+202, 1226+023, 1253-055, 1308+326 and 1354+195 were used for pointing and focusing. The pointing model was checked every two hours for each source using the pointing calibrators, while the focus was checked after sunrise and sunset. The data were calibrated using the standard dual method. The observations were performed in average weather conditions with $\tau_{225\,\rm GHz} \lesssim 0.5$ during 80% of the observing time.

Data reduction was performed using the `GILDAS`[1] packages `CLASS` and `GREG`. Each scan of the spectrum was inspected by eye and the bad data (up to 10%) were discarded. The baseline-removed spectra were co-added according to the weights derived from the noise level of each. We also note that due to the upgrade of the optical system of the IRAM-30m telescope in November 2015, the telescope efficiency has been changed by small factors for lower band receivers (see the EMIR commissioning report by

[1] See `http://www.iram.fr/IRAMFR/GILDAS` for more information about the GILDAS softwares.

Table 2: Observation log.

Source	IAU name	RA (J2000)	DEC (J2000)	Observed Lines	H_2O observation	H_2O ref
G09v1.97	J083051.0+013224	08:30:51.156	+01:32:24.35	CO(3–2), (5–4), (6–5), (7–6), [C I](2–1)	2_{11}–2_{02}, 3_{21}–3_{12}	1
G09v1.40	J085358.9+015537	08:53:58.862	+01:55:37.70	CO(2–1), CO(4–3), (6–5), (7–6), [C I](2–1)	2_{11}–2_{02}	1
SDP17b	J090302.9−014127	09:03:03.031	−01:41:27.11	CO(3–2), (4–3), (7–6), (8–7), [C I](2–1)	2_{02}–1_{11}	2, 3
SDP81	J090311.6+003906	09:03:11.568	+00:39:06.43	CO(3–2), (5–4), (6–5), (10-9)	2_{02}–1_{11}	2
G12v2.43	J113526.3−014605	11:35:26.273	−01:46:06.55	CO(3–2), (4–3), (5–4), (6–5), (8–7), (10-9)	2_{02}–1_{11}, 3_{21}–3_{12}	1
G12v2.30	J114637.9−001132	11:46:37.980	−00:11:31.80	CO(4–3), (5–4), (6–5), (8–7), (11-10)	2_{02}–1_{11}	2
NCv1.143	J125632.7+233625	12:56:32.544	+23:36:27.63	CO(3–2), (5–4), (6–5), (7–6), (10-9)[a], [C I](2–1)	2_{11}–2_{02}, 3_{21}–3_{12}	1
NAv1.195	J132630.1+334410	13:26:30.216	+33:44:07.60	CO(5–4)	2_{02}–1_{11}, 3_{21}–3_{12}[b]	1
NAv1.177	J132859.3+292317	13:28:59.246	+29:23:26.13	CO(3–2), (5–4), (7–6), (8–7) , [C I](2–1)	2_{02}–1_{11}, 3_{21}–3_{12}	1
NBv1.78	J133008.4+245900	13:30:08.520	+24:58:59.17	CO(5–4), (6–5)	2_{02}–1_{11}, 3_{21}–3_{12}	1
NAv1.144	J133649.9+291801	13:36:49.900	+29:18:01.00	CO(3–2), (4–3), (7–6), (8–7), [C I](2–1)	2_{11}–2_{02}	2
NAv1.56	J134429.4+303036	13:44:29.518	+30:30:34.05	CO(5–4)	2_{11}–2_{02}	1
G15v2.235	J141351.9−000026	14:13:51.900	−00:00:26.00	CO(3–2), (4–3), (5–4), (7–6), (9–8), [C I](2–1)	–	–
G12v2.890	J113243.1−005108	11:32:42.970	−00:51:08.90	CO(3–2), (5–4), (9–8)	–	–
G12v2.257	J115820.2−013753	11:58:20.190	−01:37:55.20	CO(3–2), (4–3), (7–6), (8–7), [C I](2–1)	–	–

Notes. RA and DEC are the J2000 coordinates of the SMA 880 μm images from Bu13 (except for G12v2.890 and G12v2.257 which were not observed by SMA, *Herschel* SPIRE image coordinates in Valiante et al. 2016 are then used instead). These coordinates were used for observations. See in Appendix Table B.1 for the observing frequencies. The H_2O observations for each source are reported in (1) Yang et al. (2016); (2) Omont et al. (2013); (3) Omont et al. (2011). The sources have been divided into two groups as in the table, see Section 2.1 for more details. [(a)] This CO(10-9) data is taken from NOEMA/IRAM project S15CV (Yang et al. in prep.). [(b)] Except for this line, the rest H_2O lines are detected.

Table 3: Previously observed properties of the entire sample.

Source	ID	$z_{\rm spec}$	ref$_{z_{\rm spec}}$	F_{250} (mJy)	F_{350} (mJy)	F_{500} (mJy)	F_{880} (mJy)	$f_{1.4\rm GHz}$ (mJy)	$T_{\rm d}$ (K)	$\mu L_{\rm IR}$ ($10^{13}\,L_\odot$)	μ_{880}	$L_{\rm IR}$ ($10^{12}\,L_\odot$)	$r_{\rm half}$ (kpc)	Σ_{SFR} ($M_\odot\,{\rm yr}^{-1}\,{\rm kpc}^{-2}$)
G09v1.97	1	3.634	1	260 ± 7	321 ± 8	269 ± 9	85.5 ± 4.0	< 0.45	44 ± 1	15.5 ± 4.3	6.9 ± 0.6	22.5 ± 6.5	0.9	910 ± 147
G09v1.40	2	2.0923	1	389 ± 7	381 ± 8	241 ± 9	61.4 ± 2.9	0.75 ± 0.15	36 ± 1	6.6 ± 2.5	15.3 ± 3.5	4.3 ± 1.9	0.4	775 ± 303
SDP17b	3	2.3051	2	347 ± 7	339 ± 8	219 ± 9	54.7 ± 3.1	< 0.51	38 ± 1	7.1 ± 2.6	4.9 ± 0.7	14.5 ± 5.7	3.1	52 ± 36
SDP81	4	3.042	3	138 ± 7	199 ± 8	174 ± 9	78.4 ± 8.2	0.61 ± 0.16	34 ± 1	5.9 ± 1.5	11.1 ± 1.1	5.3 ± 1.5	3.3	14 ± 6
G12v2.43	5	3.1276	4	290 ± 7	295 ± 8	216 ± 9	48.6 ± 2.3	< 0.45	39 ± 2[a]	9.0 ± 0.2[a]	–	–	–	–
G12v2.30	6	3.2592	4	290 ± 6	356 ± 7	295 ± 8	86.0 ± 4.9	< 0.42	41 ± 1	15.6 ± 4.1	9.5 ± 0.6	16.4 ± 4.4	1.6	166 ± 27
NCv1.143	7	3.565	1	214 ± 7	291 ± 8	261 ± 9	97.2 ± 6.5	0.61 ± 0.16	40 ± 1	13.0 ± 4.0	11.3 ± 1.7	11.4 ± 3.9	0.8[b]	1043 ± 384[b]
NAv1.195	8	2.951	5	179 ± 7	279 ± 8	265 ± 9	65.2 ± 2.3	< 0.42	36 ± 1	7.5 ± 2.0	4.1 ± 0.3	18.3 ± 5.1	1.6	213 ± 44
NAv1.177	9	2.778	6	264 ± 9	310 ± 10	261 ± 10	50.1 ± 2.1	< 0.45	32 ± 1[a]	6.2 ± 0.2[a]	–	–	–	–
NBv1.78	10	3.1112	1	273 ± 7	282 ± 8	214 ± 9	59.2 ± 4.3	0.67 ± 0.20	43 ± 1	10.8 ± 3.9	13.0 ± 1.5	8.4 ± 3.1	0.6	1094 ± 1411
NAv1.144	11	2.2024	4	295 ± 8	294 ± 9	191 ± 10	36.8 ± 2.9	< 0.42	39 ± 1	6.0 ± 3.5	4.4 ± 0.8	13.6 ± 8.3	0.9	615 ± 581
NAv1.56	12	2.3010	4	481 ± 9	484 ± 13	344 ± 11	73.1 ± 2.4	1.12 ± 0.27	38 ± 1	11.5 ± 3.1	11.7 ± 0.9	9.8 ± 2.8	1.5	138 ± 82
G15v2.235	13	2.4782	4	190 ± 7	240 ± 8	200 ± 9	33.3 ± 2.6	< 0.59	32 ± 2	2.8 ± 0.7	1.8 ± 0.3	15.6 ± 4.7	1.7	275 ± 101
G12v2.890	14	2.5778	4	74 ± 13	118 ± 19	106 ± 18	–	< 0.45	30 ± 2	2.5 ± 0.3[c]	–	–	–	–
G12v2.257	15	2.1911	4	132 ± 21	152 ± 24	107 ± 18	–	< 0.82	32 ± 2	2.6 ± 0.3[c]	–	–	–	–
G15v2.779	16	4.243	7	115 ± 19	308 ± 47	220 ± 34	90.0 ± 5.0	< 0.46	41 ± 1	10.1 ± 3.0	4.6 ± 0.5	22.0 ± 7.0	3.8	53 ± 11

Notes. $z_{\rm spec}$ is the redshift inferred from previous CO detection as reported by: (1) Riechers et al. (in prep.); (2) Lupu et al. (2012); (3) Fu et al. (2012); (4) Harris et al. (2012); (5) Harris et al. (in prep.); (6) Krips et al. (in prep.); (7) Cox et al. (2011). F_{250}, F_{350} and F_{500} are the *Herschel* SPIRE flux densities at 250, 350 and 500 μm, respectively (Valiante et al. 2016); F_{880} is the 880 μm SMA flux density (Bu13); $f_{1.4\rm GHz}$ is the 1.4 GHz band flux density from the VLA FIRST survey (Becker et al. 1995), and we use 3 σ as upper limits for non-detections; $T_{\rm d}$ is the cold-dust temperature taken from Bu13 (note that the errors quoted here are underestimated since the uncertainties from differential lensing and single-temperature dust SED assumption were not fully considered). $\mu L_{\rm IR}$ is the apparent total infrared luminosity (8–1000 μm) mostly inferred from Bu13. μ_{880} is the lensing magnification factor for the 880 μm images (Bu13); $r_{\rm half}$ and $\Sigma_{\rm SFR}$ are the intrinsic half-light radius at 880 μm and the lensing-corrected surface *SFR* density (*SFR* is derived from $L_{\rm IR}$ using the calibration of Kennicutt 1998a, $SFR = 1.73\times10^{-10} L_{\rm IR}\ M_\odot\,{\rm yr}^{-1}$, by assuming a Salpeter IMF); Since G12v2.890 and G12v2.257 are significantly weaker in submm fluxes compared with other sources, and also they lack SMA 880 μm observation, we put them into a separate group. G15v2.779 is also included in the table for comparison. [(a)] These values of $T_{\rm d}$ and $\mu L_{\rm IR}$ are not given in Bu13, thus we infer them from modified black-body dust SED fitting using the submm/mm photometry data listed in this table. [(b)] This $r_{\rm half}$ is obtained based on the A-configuration NOEMA observation (Yang et al., in prep.), with a better spatial resolution and image quality comparing to the SMA one. [(c)] The values are from Harris et al. (2012).

Marka & Kramer in 2015[2] for details). All our sources are a factor of 3–7 smaller compared with the beamsize of IRAM-30m at the observing frequencies, so that they can be treated as point sources. Accordingly, we apply the different point source conversion factors (in the range of 5.4–9.7 Jy/K depending on the optics and the frequency) that convert $T_{\rm A}^*$ in units of K into flux density in units of Jy for the spectra. A typical absolute flux calibration uncertainty of ~ 10% is also taken into account. We then fit the co-added spectra with Gaussian profiles using the Levenberg-Marquardt least-square minimisation code `MPFIT` (Markwardt 2009) for obtaining the velocity integrated line fluxes, linewidths (FHWM), and the line centroid positions.

[2] Report is available on the IRAM-30m wiki page: https://www.iram.es/IRAMES/mainWiki/Iram30mEfficiencies.

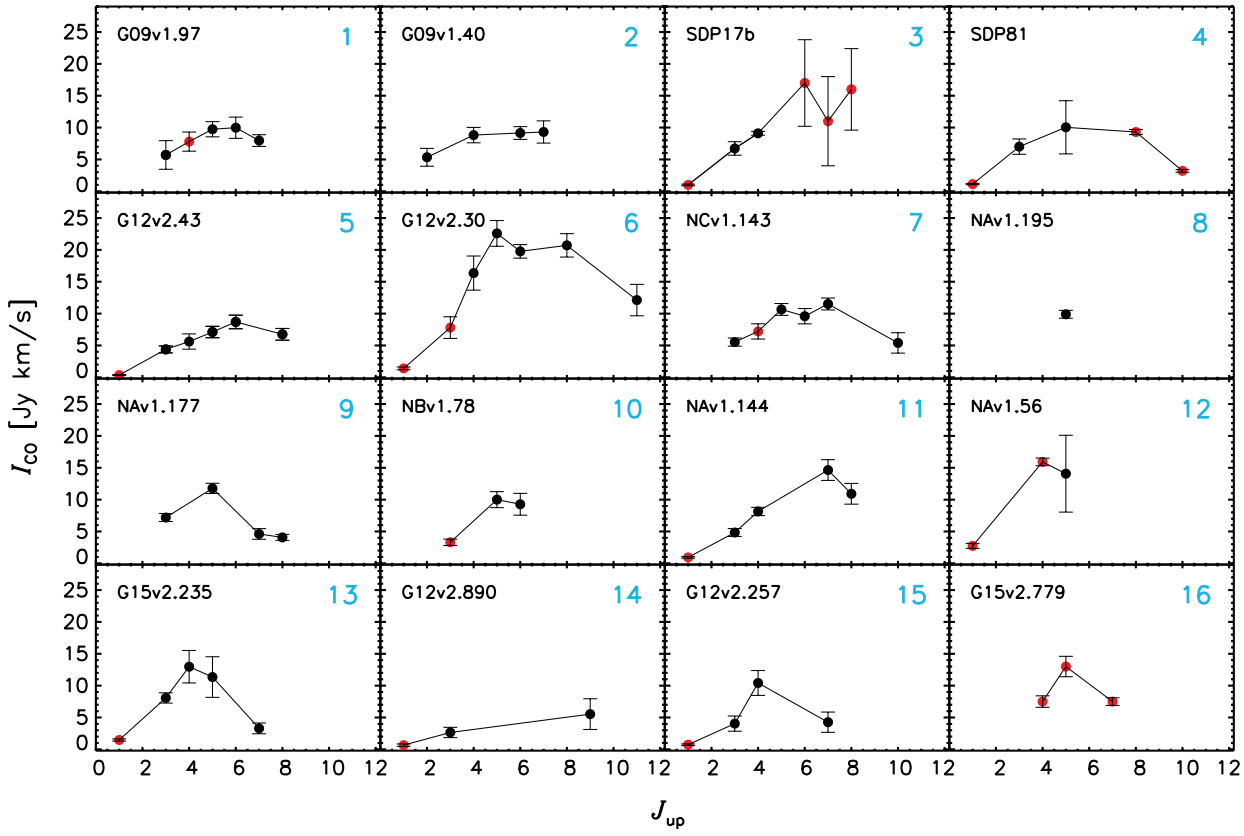

Fig. 1: The distribution of the observed velocity-integrated CO line flux density versus the rotational quantum number J_{up} for each transition, i.e. CO SLEDs. Black dots with error bars are the velocity integrated flux densities from this work. Red dots are the data from other works: all CO(1–0) data are from Harris et al. (2012); CO(4–3) in G09v1.97 is from Riechers et al. (in prep.); CO(6–5), CO(7–6) and CO(8–7) in SDP 17b are from Lupu et al. (2012); CO(8–7) and CO(10-9) in SDP 81 are from ALMA Partnership, Vlahakis et al. (2015); CO(3–2) in G12v2.30, CO(4–3) in NCv1.143 and CO(3–2) in NBv1.78 are from O13; CO(4–3) in NAv1.56 is from Oteo et al. (in prep.). For a comparison, we also plot the CO SLED of G15v2.779 (Cox et al. 2011). We mark an index number for each source in turquoise following Table 3 for the convenience of discussion.

3. Observation results

3.1. Observed CO line properties

We have detected 47 out of 55 $J \geq 2$ CO and 7 out of 8 [C I](2–1) observed emission lines in 15 *H*-ATLAS lensed SMGs (signal to noise ratio S/N $\gtrsim 3$, see Table B.1). The observed spectra are displayed in Fig. A.1 and the fluxes are also shown in the form of CO SLEDs in Fig. 1, indicated by black data points. Detected multi-*J* CO lines are bright with velocity-integrated flux densities ranging from 2 to 22 Jy km s^{-1}. To further compare the CO SLEDs, the CO(3–2) normalised CO SLEDs are plotted in Fig. 2 for all the *H*-ATLAS sources with CO(3–2) detections, overlaid with those of the Milky Way (Fixsen et al. 1999) and the Antennae Galaxy (Zhu et al. 2003). The CO SLEDs are mostly peaking from $J_{up} = 5$ to $J_{up} = 8$. The histogram of the flux ratio between CO(1–0) and CO(3–2) shows that the average $I_{CO(1-0)}/I_{CO(3-2)}$ ratio is 0.17 ± 0.05, which is 1.3 ± 0.4 times smaller than that of the unlensed SMGs (Bothwell et al. 2013, hereafter Bo13). This is likely to be related to differential lensing, in that the magnification factor of CO(3–2) is larger than that of CO(1–0) due to the differences in their emitting sizes. The resulting ratio of $I_{CO(3-2)}/I_{CO(1-0)}$ is thus larger in our lensed sources compared to the unlensed SMGs. We further discuss this in Section 4.3. Here we define the ratio between the lensing magnification factor of CO(3–2) (assumed to be equal to the magnification factor μ_{880} derived from SMA 880 μm images) and CO(1–0) to be

$$\frac{\mu_{CO(3-2)}}{\mu_{CO(1-0)}} = \frac{\mu_{880}}{\mu_{CO(1-0)}} = 1.3 \pm 0.4. \quad (1)$$

We correct for differential lensing for CO(1–0) data using this factor as described in Section 3.3.

One of the most important characteristics of the CO lines is its linewidth. The CO linewidth (FHWM) distribution of our lensed SMGs is displayed by the black solid line in the upper panel of Fig. 3 with the corresponding cumulative fraction shown in the lower panel. This curve shows that the linewidths are distributed between 208 and 830 km s^{-1} (see Table 4 for the weighted average values of the linewidth). Around 50% of the sources have linewidths close to or smaller than 300 km s^{-1}. The median of the whole distribution is 333 km s^{-1} and its average value 418 ± 216 km s^{-1}. Figure 3 also displays the linewidth distributions and the cumulative curves of two other samples of unlensed SMGs (orange dash-dotted lines) and lensed SPT-selected SMGs (green dashed lines) for comparison as discussed in Section 3.2.

Among our 16 sources, 12 of them show a single Gaussian CO line profile. SDP 81, NBv1.78 and G15v2.235 have double Gaussian CO line profiles. Although G09v1.97 might show a

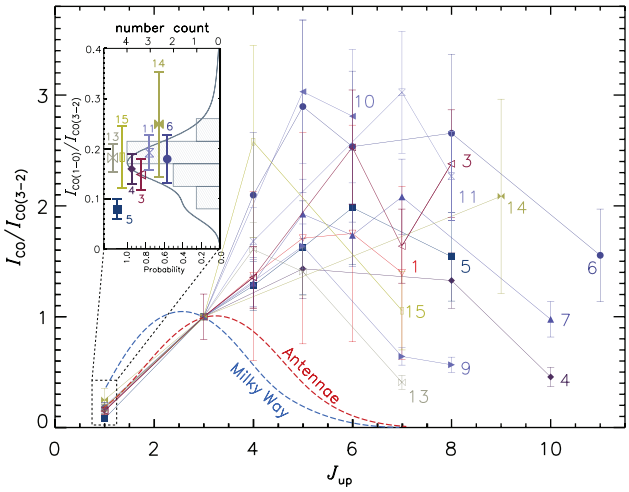

Fig. 2: The observed CO(3–2)-normalised CO SLED (without lensing correction) of the *H*-ATLAS SMGs, in which both $J_{up} = 1$ and $J_{up} = 3$ CO data are available. The inset shows a zoom-in plot of the flux ratio of CO(1–0)/CO(3–2). The grey histogram shows the ratio distribution, while the grey line shows the probability density plot of the line ratio (considering the error). A mean ratio of $I_{CO(1-0)}/I_{CO(3-2)} = 0.17 \pm 0.05$ has been found for our lensed SMGs. This is 1.3 ± 0.4 times smaller than that of the unlensed SMGs of Bo13. For comparison, we also plot the SLED of the Milky Way and the Antennae Galaxy.

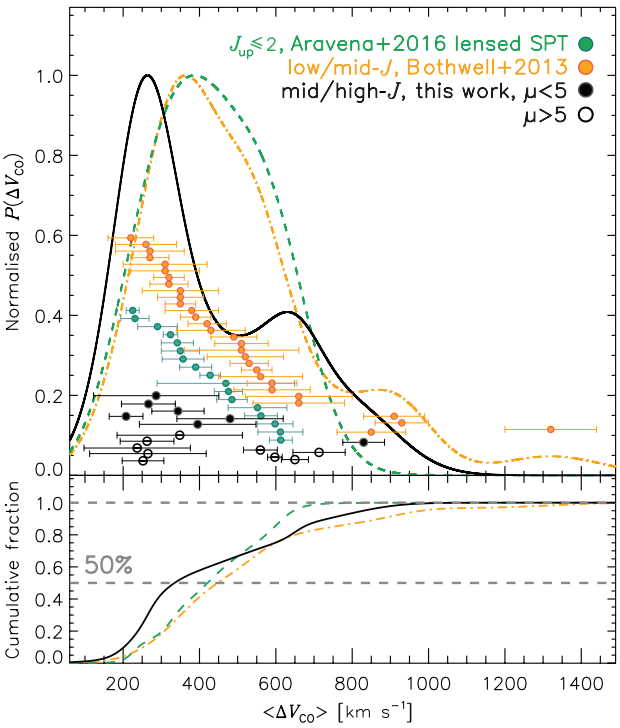

Fig. 3: *Upper panel*: Linewidths with errors from three different samples, with probability distributions obtained by adaptive kernel density estimate (Silverman 1986): black symbols and line are from this work, orange symbols and dashed-dotted line are the $J_{up} \geq 2$ CO linewidth distribution in unlensed SMGs (Bo13) and the green symbols and dashed line represent the linewidth from the $J_{up} \leq 2$ CO lines of the lensed SPT sources (Aravena et al. 2016b). Our lensed sources with $\mu > 5$ are indicated with open circles while the other sources are shown in filled circles. We note that although there is no lensing model for G12v2.43 and NAv1.144, it is suggested that their μ are likely to be ~ 10 (see Section 4.2 and Fig. 6). Thus, they are also marked with open circles. *Lower panel*: Cumulative distribution of $\langle \Delta V_{CO} \rangle$ for the three samples with the same colour code.

single Gaussian line profile, it is likely that there is a weak component in the blue wing, that we have confirmed by a higher sensitivity ALMA observation (Yang et al. in prep.). The high S/N PdBI spectrum of CO(4–3) line in NAv1.56 (Oteo in prep.) also shows a line profile consisting of a narrow blue velocity component and a broad red component. However, due to the limited S/N, we can only identify the CO(5–4) line observed by EMIR with a single Gaussian profile.

The CO line profiles between different J_{up} levels within each source may vary, since their critical density and excitation temperature are different. However, by checking our CO spectral data as displayed in Fig. A.1, we find the differences between the line profiles (mostly by checking the linewidth) are insignificant given the current S/N. Their linewidths generally agree with each other within their uncertainties.

3.2. Comparing our sample to the general SMG population

If we wish to use our sample of lensed sources and the increased sensitivity allowed by magnification to infer general properties of the SMG population, it is important to investigate whether or not it is representative of this population and to recognise the possible biases introduced by lensing selection. For this purpose, we may compare it, especially for CO emission, with the sample of unlensed SMGs of the comprehensive CO study by Bo13. Thanks to early redshift determination, this sample of 32 SMGs initially detected at 850 μm was the object of a large program at IRAM/NOEMA detecting multiple low/mid-*J* CO lines. As discussed by the authors, although not completely free from possible biases, the sample appears to be a good representative of the whole SMG population. Compared to ours, its redshift distribution is similarly concentrated in the redshift range 2 to 3, with a similar extension up to ~ 3.5, but it also extends below 2 down to z$\sim$1 in contrast to our sample. Both samples have very comparable distributions of their FIR luminosity L_{FIR} (a typical ratio between L_{IR} and L_{FIR} is 1.9; e.g. Dale et al. 2001), from a few $10^{12}\,L_\odot$ to just above $10^{13}\,L_\odot$, with a mean value of $6.0 \times 10^{12}\,L_\odot$ for the Bo13 sample and $8.3 \times 10^{12}\,L_\odot$ for ours. As expected from the *Herschel* selection of our sample, its dust temperature T_d (Bu13) is slightly higher ($\langle T_d \rangle = 37$ K) than for typical samples of 850 μm-selected SMGs such as that of Bo13; but there is no obvious evidence of any bias in our lensed sample with respect to the whole *Herschel* SPIRE SMG population.

An important parameter is the extension radii of the dust emission at submm, which is believed to be comparable to that of high-*J* CO emission as discussed by Bo13 (note that the CO(1–0) line is expected to be more extended, see below). Values of this radius for our sources are reported in Table 3 as computed in Bu13 lens models. All values remain $<\sim 3$ kpc, with a mean value of ~ 1.5 kpc. A similar distribution was found by Spilker et al. (2016) for a larger sample of similar strongly lensed sources found in the SPT survey. These authors have compared the intrinsic size distribution of the strongly lensed sources (in-

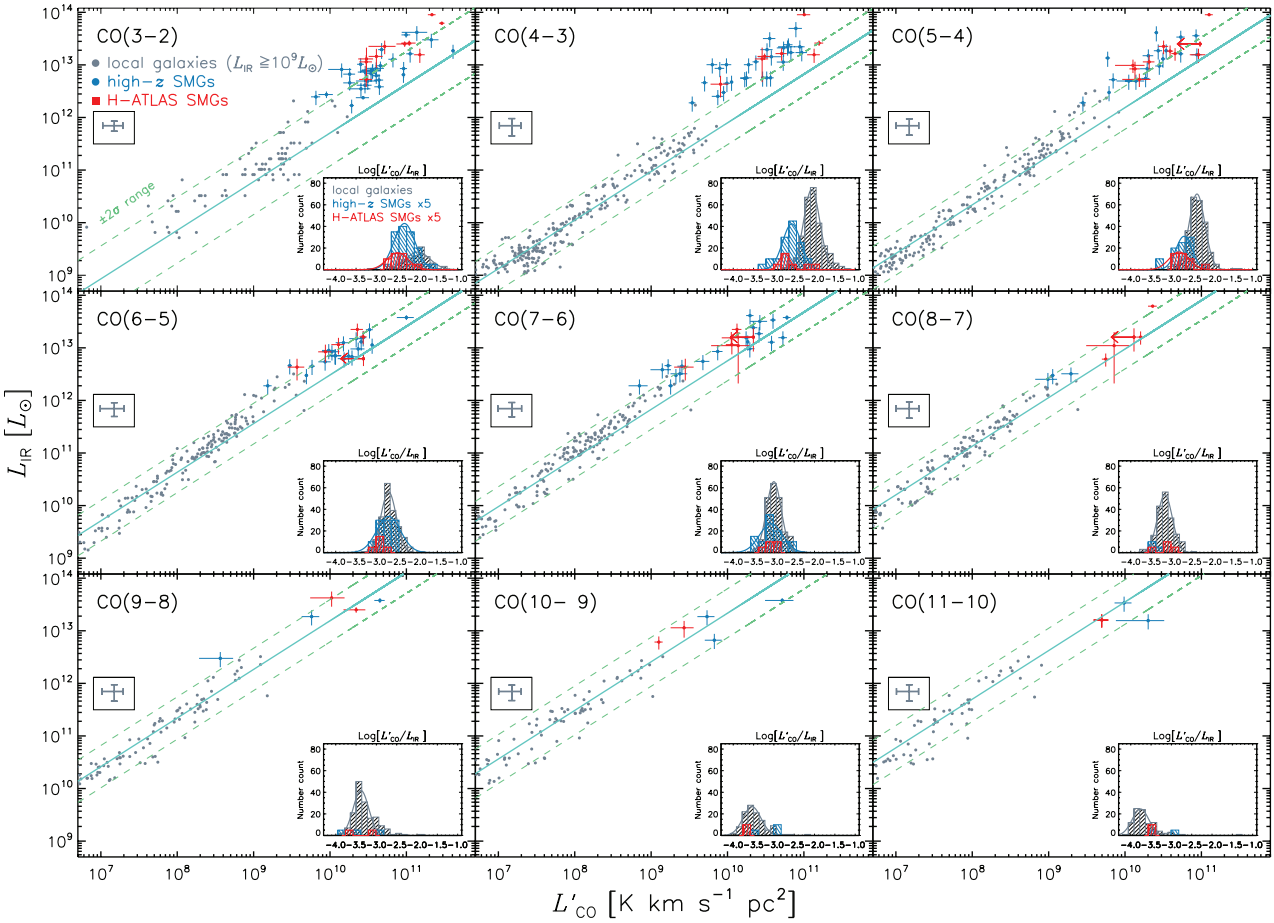

Fig. 4: $L_{\rm IR}$ vs. $L'_{\rm CO}$ from local star-forming galaxies to high-redshift SMGs. The low-z data shown in grey including galaxies with $10^9 \leq L_{\rm IR} \leq 10^{12}\,L_\odot$ (only $<20\%$ of the local sources are ULIRGs) are from Liu et al. (2015) and Kamenetzky et al. (2016), with the typical error shown by the grey error-bars. The high-redshift SMG data in blue are from Carilli & Walter (2013) (including HFLS3 from Riechers et al. 2013). The red data points represent the *H*-ATLAS SMGs from this work. Solid light blue lines are linear fits to the local galaxies, showing the average ratios of $L'_{\rm CO}/L_{\rm IR}$, with the $\pm 2\,\sigma$ limits indicated by the dashed green lines. The insets show the histograms of the distribution of the ratio between $L'_{\rm CO}$ and $L_{\rm IR}$ for the three samples. It is clear from the correlation plots and the histograms that the high-redshift SMGs are above the low-redshift correlation for $J_{\rm up} = 3$ and $J_{\rm up} = 4$, with a significant smaller ratio of $L'_{\rm CO}/L_{\rm IR}$. Our *H*-ATLAS SMGs are located in the same region as other SMGs.

cluding Bu13 ones) to a similar number of unlensed SMGs and found no significant differences.

In contrast with these similarities of lensed and unlensed SMG samples, the CO linewidths of our lensed flux-limited sample appear anomalously low on average as quoted above. This is obvious from the comparison with the Bo13 sample: see Fig. 3 and the comparison of the distribution of the linewidth, the mean values ($\pm 1\,\sigma$) are 418 ± 216 km s^{-1} for our *H*-ATLAS flux-limited sample, 502 ± 249 km s^{-1} for Bo13 sources with z ≥ 2, and 430±140 km s^{-1} for the SPT lensed SMG based on CO(1–0) and CO(2–1) observations by Aravena et al. (2016b). The median values of linewidth for the three samples are 333 km s^{-1}, 445 km s^{-1} and 420 km s^{-1}, respectively, while the mode values are 264 km s^{-1}, 346 km s^{-1} and 328 km s^{-1}, respectively. The range of the CO linewidths of our lensed SMGs are similar to those of the unlensed Bo13 sample, although the former has a concentration towards a narrower linewidth; more precisely, 50% of them have linewidths $\lesssim$ 333 km s^{-1}. In order to further compare these three samples, KS-tests were performed. The value of KS probability $P_{\rm KS}$ will be small if the two comparing data sets are significantly different. For the linewidth of our sample and the unlensed SMG sample, $P_{\rm KS} = 0.23$ with a maximum deviation of 0.3; while for comparing our sample with the SPT lensed SMG sample, $P_{\rm KS} = 0.30$ and the maximum deviation equals 0.3. These values of $P_{\rm KS}$ show that the differences among the samples are not statistically significant, indicating that they could arise from similar distributions. Nevertheless, the shapes of the probability distributions and the accumulative distributions of the linewidth for the three samples show some differences as displayed in Fig. 3. The difference between our lensed sample and the SPT one might be expected since the lensed SPT linewidths come from CO(1–0) and CO(2–1) observations which likely trace a larger velocity range of the gas, and thus tend to have larger linewidths compared with mid/high-*J* CO lines. However, linewidths of the Bo13 SMG sample are also from low/mid-*J* CO observations. The difference between this unlensed sample and our *H*-ATLAS flux-limited sample is rather likely coming from differential lensing, as discussed in the subsequent subsection. We note, nevertheless, that the per-

centage of double-peak CO profiles appears consistent (~25%) for our sources and those of Bo13.

3.3. Intrinsic CO emission properties

We derive the apparent line luminosities, for example, $\mu L_{\rm line}$ (in units of $L_\odot$) and $\mu L'_{\rm line}$ (in units of K km s^{-1} pc^2), from the observed line flux densities using the classical formulae as given by Solomon et al. (1992): $L_{\rm line} = 1.04\times10^{-3} I_{\rm line}\nu_{\rm rest}(1+z)^{-1}D_{\rm L}^2$ and $L'_{\rm line} = 3.25\times10^{7} I_{\rm line}\nu_{\rm obs}^{-2}(1+z)^{-3}D_{\rm L}^2$. The resulting line luminosities are listed in Appendix Table B.1. The range of the apparent line luminosities is $\mu L'_{\rm line}\sim 2$–48×10^{10} K km s^{-1} pc^2. After correcting the lensing magnification, the range of the intrinsic CO line luminosities is $\sim(1$–$60)\times10^7\,L_\odot$ or $\sim(2$–$170)\times10^9$ K km s^{-1} pc^2. As usual, the value of $L'_{\rm CO}$ decreases with increasing $J_{\rm up}$ of the CO lines. Besides CO, we have also derived the instrinsic luminosities of the [C I](2–1) line, observed together with CO(7–6), to be $\sim(3$–$23)\times10^7\,L_\odot$ or $\sim(2$–$13)\times10^9$ K km s^{-1} pc^2.

In the following analysis, we have included multi-J CO data found in the literature for our sources, especially CO(1–0) from Harris et al. (2012), compensating for the absence of this line in our observations (see Caption of Fig. 1). However, due to the differential lensing effect on the CO(1–0) data as discussed in Section 4.3, we only use these CO(1–0) fluxes for the CO line excitation modelling, after applying a factor of 1.3 ± 0.4 to correct the differences between the magnification factors of mid/high-J CO and that of CO(1–0) following Eq. (1) (as argued in Section 4.3, we assumed the magnification of mid/high-J CO lines is equal to μ_{880}, and we use μ as μ_{880} hereafter if not specified).

After correcting for the lensing magnification, Fig. 4 shows the correlation between the intrinsic values of $L_{\rm IR}$ and $L'_{\rm CO}$ lines from $J_{\rm up}=3$ to $J_{\rm up}=11$, over-plotted on the local correlations (Liu et al. 2015, see also Greve et al. 2014; Kamenetzky et al. 2016; Lu et al. 2017). One should note that >80% of the local sources in Liu et al. (2015) are galaxies with $L_{\rm IR}\le10^{12}\,L_\odot$, that is, luminous infrared galaxies (LIRGs) and normal star-forming galaxies. As found previously, most of these local sources can be found well within a tight linear correlation between $L_{\rm IR}$ and $L'_{\rm CO}$ for the mid-J and high-J CO lines, although for the low-J CO lines, the local ULIRGs seem to be lying above the correlation at a $\gtrsim2\,\sigma$ level, having larger $L_{\rm IR}/L'_{\rm CO}$ ratios (e.g. Arp 220). As shown by the histograms of the $L_{\rm IR}/L'_{\rm CO}$ ratios in Fig. 4, comparing with local galaxies (mostly populated by galaxies with $L_{\rm IR}=10^9$–$10^{12}\,L_\odot$), both our H-ATLAS SMGs and the previously studied SMGs are slightly above the correlation with larger $L_{\rm IR}/L'_{\rm CO}$ ratios for $J_{\rm up}=3$ to $J_{\rm up}=5$ CO lines. In contrast, for the $J_{\rm up}\ge6$ CO lines, both the local galaxies and the high-redshift SMGs with $L_{\rm IR}$ from $10^9\,L_\odot$ to a few $10^{13}\,L_\odot$ can be found within tight linear correlations. The H-ATLAS SMGs show no difference with other previously studied SMGs. Among the CO transitions, CO(7–6) has the tightest correlation across different galaxy populations ($\sim$ 0.17 dex), which agrees well with Lu et al. (2015). This again indicates that the dense warm gas traced by the $J_{\rm up}\ge6$ CO lines is more tightly correlated with on-going active star formation (without considering AGN contamination to the excitation of CO), and CO(7–6) may be the most reliable star formation tracer among the CO lines.

We have also compared the CO line ratios in local ULIRGs with those in our lensed SMGs, by taking CO(5–4) and CO(6–5) for example. The ratios of $L'_{\rm CO(5-4)}/L'_{\rm CO(6-5)}$ from the two subsamples turn out to be similar within the uncertainties. Their mean values are 1.6 and 1.4 with the standard deviations of 0.35 and 0.37 for local ULIRGs and high-redshift lensed SMGs, respectively. This suggests that the differential lensing is unlikely introducing a large bias of choosing molecular gas with very different gas conditions.

4. Galactic properties and differential lensing

4.1. Molecular gas mass

One of the most commonly used methods to derive the mass of molecular gas in galaxies is to assume that it is proportional to the luminosity $L'_{\rm CO(1-0)}$ through a conversion factor $\alpha_{\rm CO}$ such as $M_{\rm H_2}=\alpha_{\rm CO}L'_{\rm CO(1-0)}$, where $M_{\rm H_2}$ is the mass of molecular hydrogen and $\alpha_{\rm CO}$ is the conversion factor to convert observed CO line luminosity to the molecular gas mass without helium correction (see Bolatto et al. 2013 for a review). Here we adopt a typical value of $\alpha_{\rm CO}=0.8\,M_\odot\,({\rm K\,km\,s^{-1}\,pc^2})^{-1}$ which is usually found in starbursts as observed in local ULIRGs (Downes & Solomon 1998). The total mass of molecular gas $M_{\rm gas}$ is then inferred by multiplying $M_{\rm H_2}$ by the factor 1.36 to include helium. One should also note that at $z=2.1$–4.2, the cosmic microwave background (CMB) temperature reaches ~ 8.5–14.2 K, which is non-negligible to the low-J CO lines. A typical underestimation of the CO(1–0) luminosity could be around 10%–25% if $T_{\rm k}=50$ K, and for the bulk of the molecular gas, which is normally colder than 50 K and is only bright in the low-J transitions, the CMB effect may be even more severe as pointed out by Zhang et al. (2016) (see also da Cunha et al. 2013). Although far from being settled, recent observations of high-redshift SMGs favour $\alpha_{\rm CO}$ being close to the value of local ULIRGs with large uncertainties (Ivison et al. 2011; Magdis et al. 2011; Messias et al. 2014; Spilker et al. 2015; Aravena et al. 2016b).

Half of our sources were observed in their CO(1–0) line with the Green Bank Telescope (GBT) by Harris et al. (2012). The corresponding apparent luminosities $\mu L'_{\rm CO(1-0)}$ (not corrected for lensing) are reported in Table 5. However, it is impossible to infer the total mass of molecular gas in the absence of a detailed lensing model including the extended part of CO(1–0) emission. We may nevertheless directly compare the CO(3–2) and CO(1–0) apparent luminosities $\mu L'_{\rm CO}$ for the seven Harris' sources for which we observed the CO(3–2) line (Table 5). The error-weighted mean ratio of the luminosity of CO(3–2) to CO(1–0) is 0.65 ± 0.19. This is marginally larger at about the 1σ level by a factor 1.3 ± 0.4 than the median brightness temperature ratios r_{32}/r_{10} of 0.52 ± 0.09 reported for unlensed SMGs by Bo13, and 0.55 ± 0.05 reported by Ivison et al. (2011) (as described in Eq. (1)). This difference seems to suggest an effect of differential lensing, the more compact CO(3–2) emission being more magnified than the extended CO(1–0) emission (see Section 4.3 for a detail discussion).

However, the mass of molecular gas $M_{\rm gas}$ can be directly inferred from higher $J_{\rm up}$ CO lines, mostly CO(3–2), as for cases of other high-redshift SMGs where CO(1–0) observations are lacking. Moreover, comparing with the CO(1–0) line, the CO(3–2) line tends to be less affected by differential lensing because its spatial distribution is closer to that of the submm dust emission upon which the lensing models are built. Therefore, by assuming that our lensed SMGs are similar to the unlensed high-redshift SMGs, the brightness temperature ratio $r_{32}/r_{10}=0.52\pm0.09$ from Bo13 yields $\beta_{\rm CO32}=1.36\times0.8/0.52=2.09\,M_\odot\,({\rm K\,km\,s^{-1}\,pc^2})^{-1}$ for the conversion factor defined as

$$M_{\rm gas}=\beta_{\rm CO32}L'_{\rm CO(3-2)}. \quad (2)$$

The masses of molecular gas (including He) are thus derived and reported in Table 5. [3] These values for $M_{\rm gas}$ are in the same range, 10^{10}–$10^{11}\,M_\odot$, as those derived for unlensed SMGs by Bo13. This is confirmed by the direct comparison of the distributions of $L'_{\rm CO}$ after lensing correction (Fig.6). But one should keep in mind the accumulation of uncertainties about our $M_{\rm gas}$ estimates: to the usual uncertainty on $\alpha_{\rm CO}$ or $\beta_{\rm CO32}$, one should add that of the lensing model, especially in the absence of high-resolution CO imaging. The derived gas mass appears exceptionally high for G15v2.235, about three times larger than for any other source and twice more massive than for any unlensed SMG of Bo13. Either the magnification factor is larger than the low value, 1.8±0.3, derived by Bu13, or this source is an exceptional galaxy.

These masses of gas may be compared with the mass of dust derived, for example, through the gas to dust mass ratio

$$\delta_{\rm GDR} = M_{\rm gas}/M_{\rm dust} \quad (3)$$

The dust masses were taken from Bu13. We recall that they are derived by performing a single component modified black body model with the *Herschel* SPIRE and SMA photometric fluxes, with mass absorption coefficient $\kappa_{\rm dust}$ interpolated from Draine (2003). The values of $\delta_{\rm GDR}$ for our sample are given in Table 5. They range from 31 ± 14 to 100 ± 33 with a mean of 56 ± 28. Our value is generally in agreement with the mean value of $\delta_{\rm GDR} = 75 \pm 10$ for ALESS high-redshift SMGs (Simpson et al. 2014; Swinbank et al. 2014) within 1 σ level. This range is also similar to that of the local ULIRGs (Solomon et al. 1997).

Table 4: Dynamical masses of the sample

Source	$\langle\Delta V_{\rm CO}\rangle$ (km s^{-1})	$r_{\rm half}$ (kpc)	i (deg)	$M_{\rm dyn,vir}$ ($10^{10}\,M_\odot$)	$M_{\rm dyn,rot}$ ($10^{10}\,M_\odot$)
G09v1.97	348 ± 164	0.9 ± 0.1	47 ± 5	2.9 ± 2.7	2.5 ± 2.4
G09v1.40	263 ± 70	0.4 ± 0.1	48 ± 11	0.8 ± 0.5	0.7 ± 0.5
SDP17b	286 ± 44	3.1 ± 0.9	39 ± 11	7.0 ± 3.0	8.3 ± 5.4
SDP81	560 ± 139	3.3 ± 0.7	50 ± 7	29.1 ± 15.6	23.3 ± 13.6
G12v2.43	237 ± 68	3 ± 1	55	4.7 ± 3.2[a]	3.3 ± 2.2[a]
G12v2.30	713 ± 153	1.6 ± 0.1	77 ± 2	22.8 ± 9.9	11.1 ± 4.9
NCv1.143	265 ± 55	0.8 ± 0.2	51 ± 10	1.6 ± 0.8	1.2 ± 0.7
NAv1.195	266 ± 19	1.6 ± 0.2	35 ± 9	3.1 ± 0.6	4.4 ± 2.2
NAv1.177	252 ± 35	3 ± 1	55	5.4 ± 2.3[a]	3.7 ± 1.6[a]
NBv1.78	597 ± 121	0.6 ± 0.2	51 ± 7	5.5 ± 3.3	4.3 ± 2.7
NAv1.144	208 ± 35	0.9 ± 0.3	55 ± 8	1.1 ± 0.5	0.7 ± 0.4
NAv1.56	650 ± 28[b]	1.5 ± 0.4	52 ± 5	17.8 ± 5.0	13.2 ± 4.1
G15v2.235	480 ± 111	1.7 ± 0.3	59 ± 8	11.2 ± 5.6	7.1 ± 3.8
G12v2.890	344 ± 92	3 ± 1	55	10.0 ± 6.3[a]	6.9 ± 4.4[a]
G12v2.257	395 ± 206	3 ± 1	55	13.2 ± 14.4[a]	9.2 ± 10.0[a]
G15v2.779[c]	830 ± 86	3.8 ± 0.4	43 ± 7	73.5 ± 17.0	72.8 ± 22.6

Notes. $\langle\Delta V_{\rm CO}\rangle$ is the average value of the CO linewidths, the errors are from standard deviations. We recall the values of half-light radius $r_{\rm half}$ in this table. i is the inclination angle derived from the major and minor axis ratio from lensing models in Bu13. $M_{\rm dyn,vir}$ and $M_{\rm dyn,rot}$ are the dynamical masses enclosed in $r_{\rm half}$. [(a)] Due to lacking $r_{\rm half}$ and b/a ratio of the rotating disk from lensing models, we use a typical value of $r_{\rm half}$ =3 ± 1 kpc (by assigning a 30% uncertainty) and i = 55° (see text) for the estimation of these dynamical masses. [(b)] Because of the limited data quantity for this source, we take the CO(4–3) data of NAv1.56 from the NOEMA observation (Oteo et al. in prep.), which offers better accuracy. [(c)] The physical properties of G15v2.779 are taken from or computed according to Cox et al. (2011) and O13.

4.2. Dynamical mass

In high-redshift SMGs, an important fraction of the baryonic mass is in the form of molecular gas, and the CO linewidth can serve as a good dynamical mass indicator with an assumption about the dynamical structure and extent of the system (e.g. Tacconi et al. 2006; Bouché et al. 2007). From the measured linewidth of the CO lines, we can in principle derive the dynamical mass within the half-light radius ($r_{\rm half}$) by assuming that the lensed SMG can be treated as either a virialised system or a rotating disk with an inclination angle i.

If the system is virialised, the dynamical mass can be calculated following the approach of Bo13 as

$$M_{\rm dyn,vir} = 1.56 \times 10^6 (\frac{\sigma}{\rm km\,s^{-1}})^2 (\frac{r}{\rm kpc})\,M_\odot, \quad (4)$$

in which the velocity dispersion $\sigma = \Delta V_{\rm CO}/(2\sqrt{2\ln 2})$, r is the radius of the enclosed region for calculating the dynamical mass and $\Delta V_{\rm CO}$ is the CO linewidth. If the system is a rotating disk, the dynamical mass can be derived from

$$M_{\rm dyn,rot} = 2.32 \times 10^5 (\frac{v_{\rm cir}}{\rm km\,s^{-1}})^2 (\frac{r}{\rm kpc})\,M_\odot, \quad (5)$$

following Wang et al. (2013) and Venemans et al. (2016), in which $v_{\rm cir}$ is the circular velocity equal to $0.75\Delta V_{\rm CO}/\sin i$, r is the disk radius and i is the inclination angle of the disk on the sky in a range from 0° to 90°. By assuming an inclined thin-disk geometry, we can derive the inclination angle from the minor to major axis ratio b/a of the rotating disk as $i = \cos^{-1}(b/a)$. When possible, we use the minor to major axis ratio of the source image which was derived in the lensing models of (Bu13). This yields the values of i reported in Table 4. Otherwise, we assume an average inclination angle of 55° as suggested by Wang et al. (2013). However, we also note that $1/\sin i$ can take large values for galactic disks seen close to face on. We can thus calculate the two estimates of the dynamical mass enclosed in the half-light radius $r_{\rm half}$, for example, $M_{\rm dyn,vir}$ and $M_{\rm dyn,rot}$ from the CO linewidth and/or the minor to major axis ratios following Eqs. (4) and (5).

However, it is important to note that there is certainly a significant fraction of the SMG mass distributed outside $r_{\rm half}$. Accordingly, the value of $M_{\rm dyn,vir}$ or $M_{\rm dyn,rot}$ should serve as a lower limit of the dynamical mass of the entire region where molecular gas resides. This is a fortiori true for the total mass of the galaxy including the extended diffuse, cool component beyond ~3 kpc. As suggested by the CO(1–0) observations of a sample of SMGs at $z \sim 2.4$, Ivison et al. (2011) find a typical size of ~7 kpc for the CO(1–0), with a linewidth of ~563 km s^{-1}. Using CO(2–1) data, Hodge et al. (2012) also suggest a rotating disk of molecular gas with a radius of ~7 kpc in GN20 and a CO linewidth equal to 575 ± 100 km s^{-1}. JVLA and ATCA observations of CO(1–0) emission at high-redshift reported by several other works (e.g. Greve et al. 2003; Riechers et al. 2011c; Deane et al. 2013; Emonts et al. 2016; Dannerbauer et al. 2017) also support the existence of such an extended cold gas component. Both their linewidth and the size of the emitting region are larger than those of most of our sources, suggesting an underestimation for the dynamical mass for our sample. But even the mass of the starburst, FIR-emitting core is likely to be underestimated by these formulas for $M_{\rm dyn}$. It is challenging to estimate the ratio between the total dynamical mass within the entire CO-emitting

[3] As stated in the caption of Table 5, when CO(3–2) observation is absent we have used another line with similar factors, $\beta_{\rm CO43} = 2.65\,M_\odot\,({\rm K\,km\,s^{-1}\,pc^2})^{-1}$ for CO(4–3) and $\beta_{\rm CO21} = 1.30\,M_\odot\,({\rm K\,km\,s^{-1}\,pc^2})^{-1}$ for CO(2–1) based on Bo13.

Table 5: Observationally derived physical properties of the *H*-ATLAS SMGs.

Source	z_{CO}	D_L	L_{IR}	$\frac{\mu L'_{CO(1-0),Ha}}{10^{11}}$	$\frac{\mu L'_{CO(1-0)}}{10^{11}}$	μM_{H_2}	$\frac{L'_{CO(1-0)}}{10^{10}}$	M_{gas}	$\frac{M_{gas}}{M_{dyn,vir}}$	δ_{GDR}	t_{dep}
		(Mpc)	($10^{12}\,L_\odot$)	($M_\odot$)	(K km s^{-1} pc^2)	($11^{11}\,M_\odot$)	(K km s^{-1} pc^2)	($10^{10}\,M_\odot$)			(Myr)
G09v1.97	3.6345 ± 0.0001	32751 ± 588	22.5 ± 6.5	–	6.9 ± 3.0	5.5 ± 2.4	10.0 ± 4.4	**1.0 ± 0.5**	3.8 ± 3.9	75 ± 35	28 ± 15
G09v1.40	2.0924 ± 0.0001	16835 ± 283	4.3 ± 1.9	–	3.6 ± 1.1	2.8 ± 0.9	2.3 ± 0.9	2.5 ± 1.0	3.2 ± 2.2	31 ± 14	34 ± 20
SDP17b	2.3053 ± 0.0001	18942 ± 322	14.5 ± 5.7	2.7 ± 0.4	3.8 ± 0.9	3.0 ± 0.7	7.8 ± 2.1	8.5 ± 2.3	1.2 ± 0.6	43 ± 14	34 ± 16
SDP81	3.0413 ± 0.0005	26469 ± 466	5.3 ± 1.5	4.8 ± 0.4	6.4 ± 1.6	5.1 ± 1.2	5.7 ± 1.5	6.2 ± 1.6	0.2 ± 0.1	41 ± 12	68 ± 26
G12v2.43	3.1271 ± 0.0001	27367 ± 484	(90 ± 2)/μ	1.6 ± 0.4	4.2 ± 0.9	3.3 ± 0.7	(41 ± 9)/μ	(45 ± 10)/μ	–	–	–
G12v2.30	3.2596 ± 0.0002	28761 ± 511	16.4 ± 4.4	4.7 ± 0.8	7.9 ± 2.2	6.3 ± 1.8	8.3 ± 2.4	9.1 ± 2.6	0.4 ± 0.2	69 ± 22	32 ± 13
NCv1.143	3.5650 ± 0.0004	32007 ± 574	11.4 ± 3.9	–	6.5 ± 1.4	5.2 ± 1.1	5.7 ± 1.5	6.2 ± 1.6	4.0 ± 2.2	50 ± 15	31 ± 14
NAv1.195	2.9510 ± 0.0001	25528 ± 448	18.3 ± 5.1	–	–	–	–	–	–	–	–
NAv1.177	2.7778 ± 0.0001	23736 ± 414	(62 ± 2)/μ	–	5.6 ± 1.1	4.5 ± 0.9	(56 ± 11)/μ	(61 ± 12)/μ	–	–	–
NBv1.78	3.1080 ± 0.0003	27167 ± 480	8.4 ± 3.1	–	3.1 ± 0.7	2.5 ± 0.6	2.4 ± 0.6	2.6 ± 0.7	0.5 ± 0.3	43 ± 13	18 ± 8
NAv1.144	2.2023 ± 0.0001	17918 ± 303	13.6 ± 8.3	2.3 ± 0.3	2.5 ± 0.6	2.0 ± 0.4	5.8 ± 1.6	6.3 ± 1.8	5.9 ± 3.5	44 ± 16	27 ± 18
NAv1.56	2.3001 ± 0.0009	18890 ± 321	9.8 ± 2.8	7.3 ± 1.1	6.4 ± 1.1[a]	5.1 ± 0.9	5.5 ± 1.1	6.0 ± 1.2	0.3 ± 0.1	52 ± 11	35 ± 12
G15v2.235	2.4789 ± 0.0001	20686 ± 355	15.6 ± 4.7	4.4 ± 0.5	5.2 ± 1.0	4.2 ± 0.8	28.8 ± 7.6	31.4 ± 8.2	2.8 ± 1.6	99 ± 33	117 ± 46
G12v2.890	2.5783 ± 0.0003	21694 ± 375	(25 ± 3)/μ	2.1 ± 0.6	1.8 ± 0.5	1.5 ± 0.4	(18 ± 5)/μ	(19 ± 5)/μ	–	–	–
G12v2.257	2.1914 ± 0.0001	17810 ± 301	(26 ± 3)/μ	1.8 ± 0.3	2.1 ± 0.6	1.7 ± 0.5	(21 ± 6)/μ	(23 ± 7)/μ	–	–	–
G15v2.779[b]	4.243 ± 0.001	39349 ± 718	22.0 ± 7.0	–	8.3 ± 1.8	6.6 ± 1.4	18.0 ± 4.3	19.5 ± 4.6	0.3 ± 0.1	85 ± 23	51 ± 20

Notes. z_{CO} is derived from the error-weighted mean of the multi-*J* CO spectral redshifts from this work. For the double-peak sources, we take an average redshift of the two components. The luminosity distance D_L is calculated using `Cosmology.jl` with the of `Julia` language (Bezanson et al. 2012) and the errors are propagated using `Measurements.jl` (Giordano 2016). We also recall values of L_{IR} in this table. For $\mu L'_{CO(1-0)}$, most of the values are converted from CO(3–2) fluxes as described in the text. For G09v1.40, we use CO(2–1)/CO(1–0) ratio to infer the flux of CO(1–0). And for NAv1.56 and G15v2.779, we use CO(4–3)/CO(1–0) ratio (flux ratios are from Bo13). The calculation of apparent molecular gas mass μM_{H_2} takes a conversion factor $\alpha_{CO} = 0.8$ (see text). $\mu M_{H_2,Ha}$ is the molecular gas mass calculated from CO(1–0) fluxes reported in Harris et al. (2012). Gas mass M_{gas} is calculated by considering a 36% Helium contribution, e.g. $M_{gas} = 1.36 M_{H_2}$. δ_{GDR} and t_{dep} are gas to dust mass ratio and molecular gas depletion time, respectively (see the detail definitions in Section 4 and Section 5.3). [(a)] Because of the limited data quantity, we take the NOEMA CO(4–3) data of NAv1.56, which offers better accuracy (Oteo et al. in prep.). [(b)] The physical properties of G15v2.779 are taken from or computed according to Cox et al. (2011) and O13.

region and the one we calculated from r_{half}, although Tacconi et al. (2006) suggest a value about 5 for such a ratio.

As seen in Table 4, the range of $M_{dyn,vir}$, given by Eqs. (4) and (5), varies from $\sim 10^{10}\,M_\odot$ to $3 \times 10^{11}\,M_\odot$ while values of $M_{dyn,rot}$ are comparable but slightly smaller by a factor of ~ 1.4 on average. This is again $\sim$3–10 times smaller than the value of $M_{dyn,rot}$ given in Ivison et al. (2011) and Hodge et al. (2012). We compare these values with the derived masses of gas and discuss them in the following subsection.

4.3. Possible lensing biases

It is well known that differential lensing may be a serious problem for galaxy-galaxy strong-lensing studies of extended objects, especially for multi-line and continuum comparison (e.g. Serjeant 2012; Hezaveh et al. 2012). Although the problem should be dimmer for the compact cores ($r \lesssim$ 1–3 kpc) emitting the continuum and high-*J* CO lines in our sources, it needs consideration in case of complex caustics at this scale. It may become worse for low-*J* CO studies since they may involve more extended SMG components (Ivison et al. 2011). In addition, the flux-limited selection of our lensed sources may bias our sample towards the most compact objects.

Because different excitation levels of CO trace predominantly regions with different gas density and different temperature (see the critical densities and the energy levels of the CO lines in Table 1), the sizes of the emitting regions of each *J* CO line are expected to be somewhat different. This variation of the emitting region of each CO transition will certainly bring differences in the resulting parameters, such as the total magnification factor, and derived quantities such as the molecular gas mass and line ratios with respect to the intrinsic ratios of the unlensed galaxy. The differential lensing effect could arise in a complex way from the specific spatial configuration of the caustic line with respect to the background emission. However, a detailed modelling of complex effects of differential lensing is beyond the scope of the present study for two main reasons: The low resolution of our single-dish CO data and their limited range of J_{up} values, mostly from 3 to 8. It is expected that the regions emitting such lines will not differ very much with J_{up} for most sources and remain close to that of the observed 880 μm dust continuum. This is also consistent with the similarity that we find for the linewidths of the different CO transitions within each source. We will therefore neglect the effects of differential lensing in estimating the ratios of these different mid/high-*J* emissions. Of course, the validity of this assumption should be verified, taking into account the particularities of each source and its lensing, when high-angular-resolution images are available. However, we can perform a first verification in the only case of our sources, SDP 81, for which ALMA high-resolution CO images have been published, noting that it is one of our most extended sources. These images from the ALMA long baseline campaign observation (ALMA Partnership, Vlahakis et al. 2015) show the resolved structure of the dust and CO. From lens modelling, the studies of Dye et al. (2015) and Rybak et al. (2015a,b) show that the differences between the magnification factors of the CO(5–4) and CO(8–7) lines are within 1 σ and close to that of dust emission.

On the other hand, the effects of differential lensing might be much more severe and non-negligible when comparing CO(1–0) with high-*J* CO lines. Previous high-angular-resolution imaging studies of SMGs show evidence that the cooler, low-density emitting regions of low-*J* CO lines are more extended than the dust continuum emission and that of the high-*J* CO lines (e.g. Tacconi et al. 2008; Bo13; Spilker et al. 2015; Casey et al. 2014). Especially for CO(1–0), JVLA images of high-redshift SMGs

reveal a significant extension, usually several times larger on average, compared to high-J CO (Ivison et al. 2011, see also Engel et al. 2010; Riechers et al. 2011a). This is probably also true for the [CI](1–0) line because its spatial distribution agrees well with that of CO(1–0) (e.g. Ikeda et al. 2002; Glover et al. 2015).

With such an extension, typically ~7 kpc, substantial differential lensing seems unavoidable for most strong lensing configurations, yielding a lower magnification for CO(1–0) compared with more compact mid/high-J CO emission. Indeed, such an effect has already been directly observed in at least two strongly lensed SMGs: SDP 81 (Rybak et al. 2015b) and SPT0538-50 (Spilker et al. 2015). As suggested in Hezaveh et al. (2012) such a difference will be moderate in the low-magnified system with small μ but can be non-negligible for the highly magnified systems where $\mu > 10$, which is likely the case of G09v1.40, SDP 81, NCv1.143, NAv1.144 and NAv1.56 in our sample (Table 3). By assuming that μ for CO(3–2) is similar to the dust continuum, the ratio of the velocity integrated flux density between CO(1–0) (from Harris et al. 2012) and CO(3–2) for our sources has a mean value of 0.17 ± 0.05 (Fig. 2), that is, a factor 1.3 ± 0.4 lower than in other high-redshift unlensed SMGs (Eq. (1)). Such a difference in the ratio of CO(1–0) over CO(3–2) can be explained by differential lensing. Nevertheless, one should note that the difference is not at a very significant level. Because we have no high-resolution maps of the CO lines, it is beyond our ability to reconstruct the exact magnification factor for each emission line. Here we assumed that the magnification factors are the same for all the $J_{\rm up} \geq 3$ CO lines as that of dust emission, and we applied the magnification factor μ_{880} derived from the SMA 880 μm images (Table 3). For the CO(1–0) line, we thus applied the factor $\mu_{880}/1.3$, as derived above for the multi-J CO line excitation modelling as described in Section 5.

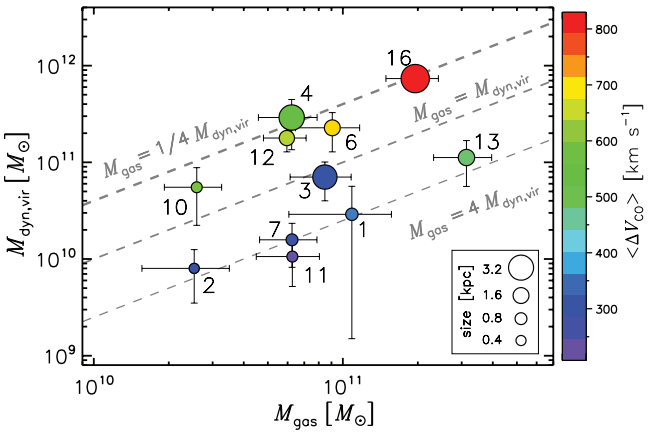

Fig. 5: A comparison between molecular gas mass and dynamical mass of our H-ATLAS lensed sample. The grey dashed lines indicate the ratio of $M_{\rm gas}/M_{\rm dyn,vir}$. Colours are coded according to the average CO linewidth. The size of the symbol represents the value of $r_{\rm half}$ of each source. There is a clear trend that sources with smaller linewidths have large ratios of $M_{\rm gas}/M_{\rm dyn,vir}$. The source index can be found in Fig. 1 and Table B.1.

Another important aspect of differential lensing is the possible distortion of the line profile. As shown in the case of the high-resolution and high-sensitivity CO spectrum of SDP 81, the line profiles show asymmetry features with a prominent red component accompanied by a weaker blue component (ALMA Partnership, Vlahakis et al. 2015). By reconstructing the source in the image plane, Swinbank et al. (2015) show that SDP 81 is a clumpy rotating disk and the red part of the disk is more magnified than the blue part, which causes the line-profile asymmetry. This might also happen to our other sources, especially for the case in which the caustic lines cross only part of the galaxy. It is not impossible that such effects might lead to underestimate the wings of some lines and thus explain at least part of the excess of narrow linewidths that we observed (see the case of G09v1.97 in Sect. 5.4 and Fig.A.1). Another cause of this excess could be a possible bias between the magnification and intrinsic source size (Spilker et al. 2016) which could perhaps bias against composite broad profiles of slightly extended sources in an early merger state. However, it seems that further observation and modelling of high-resolution CO images is needed to progress in completely explaining if this excess is real.

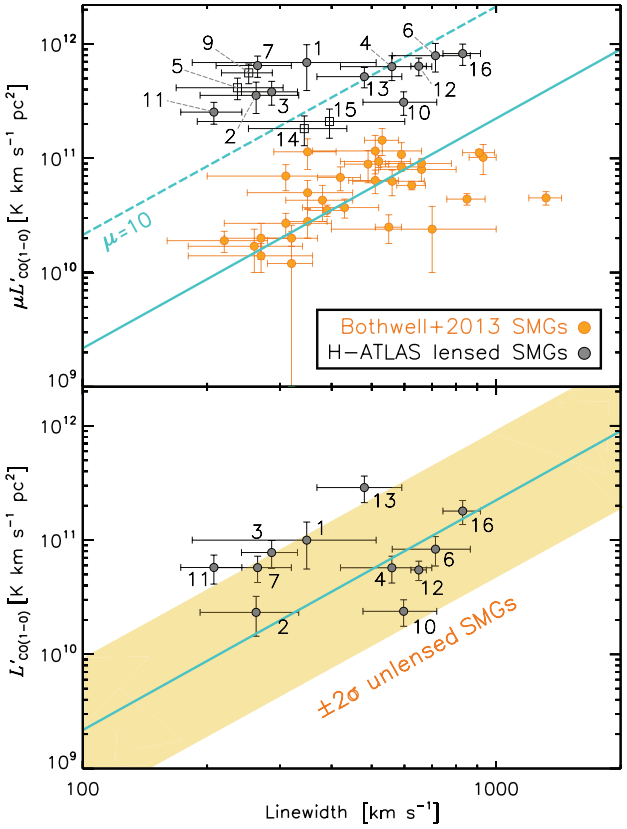

Fig. 6: *Upper panel*: $\mu L'_{\rm CO(1-0)}$ plotted against CO linewidth. Orange data points represent the unlensed SMGs from Bo13, while grey data points (indexed as in Table 2) are from this work, for which the filled circles show the sources with existing lensing model and the black open squares are the ones without lensing models. The solid turquoise line shows the fit proposed by Bo13 for the relation of $L'_{\rm CO}$ vs. linewidth as $L'_{\rm CO} \propto \Delta V^2_{\rm CO}$. The dashed turquoise line indicates the positions for $\mu = 10$ assuming this relation. As shown in the plot, the magnification factors of G12v2.43 (#5) and NAv1.177 (#9) are likely to be large. *Lower Panel*: Intrinsic $L'_{\rm CO(1-0)}$ plotted against the CO linewidth. The light orange region shows the $\pm 2\,\sigma$ range of the scatter derived from the SMGs of Bo13. Our sources generally agree with the correlation.

An effect of underestimating the CO linewidth would be to underestimate dynamical masses. In order to check this, Fig. 5 shows the plot of the relation of $M_{\rm gas}$ and $M_{\rm dyn}$ changes with

CO linewidth and source size. For most broad-line sources, the values of the ratio $M_{\rm gas}/M_{\rm dyn}$ are from 0.2 to 0.5, which appear possible, although the high value for G15v2.235, 2.4 (source #13 as shown in Fig. 5 and 6) seems to point out a problem with its lensing model. On the other hand, for all narrow-line sources, values of $M_{\rm gas}/M_{\rm dyn}$ greater than 1, and even than 3 for most of them (which is equivalent to a 1.7–2 fold underestimation of the linewidth) point out a serious problem. The Spearman's correlation coefficient between CO linewidth and $M_{\rm gas}/M_{\rm dyn}$ is −0.83 with a p-value of 0.0016. The $r_{\rm half}$ value of each source is also indicated by the symbol size. Four of the smallest sources (#1, #2, #7 and #11) have high $M_{\rm gas}/M_{\rm dyn}$ values, since the differential lensing could also potentially affect the estimation of the source size. However, we find a much weaker correlation between $r_{\rm half}$ and $M_{\rm gas}/M_{\rm dyn}$, suggesting that the impact of differential lensing on the source size is much weaker compared to that of the linewidth. It is possible that the sources with narrow linewidth having higher values of $M_{\rm gas}/M_{\rm dyn}$ is partly due to differential lensing since the dynamical mass is proportional to $\Delta V_{\rm CO}{}^2$, as identified in SDP 81 (Rybak et al. 2015b; Dye et al. 2015; Swinbank et al. 2015) and in GO9v1.97 (Yang et al. in prep.) and perhaps in SDP 17b whose CO(4–3) and H_2O profiles are clearly asymmetric (O13). Also, it seems however that at least part of this problem reflects the fact that Eqs.(4) and (5) might underestimate the dynamical mass by a large factor, likely to be up to 5, as quoted, for example, by Tacconi et al. (2006) for unlensed SMGs. It is however obvious that further observation and modelling of high-spatial-resolution CO images is needed to progress in completely explaining such problems.

Acknowledging the possible bias from the narrow-linewidth sources, after excluding the sources with $\Delta V_{\rm CO} < 400$ km s^{-1}, and also G15v2.235 as mentioned before, we derived an average value of $M_{\rm gas}/M_{\rm dyn,vir} = 0.34 \pm 0.10$, in line with the SPT sources (Aravena et al. 2016b), other unlensed SMGs (Bo13) and empirical model predictions (Béthermin et al. 2015). By assuming that the ISM is dominated by molecular content, and a small dark matter contribution within $r_{\rm half}$, the ratio can serve as a proxy of molecular gas mass fraction. Then the molecular gas mass fraction of the H-ATLAS SMGs is thus $\sim$34% with a significant uncertainty, yet it is consistent with Bo13's average value computed from $M_{\rm gas}/(M_{\rm gas}+M_*)$, in which M_* is the stellar mass.

It has been proposed that there exists a simple linear correlation between $L'_{\rm CO}$ and ΔV of the CO(1–0) line (e.g. Harris et al. 2012; Bo13; Goto & Toft 2015; Dannerbauer et al. 2017), $L'_{\rm CO} \propto (\sigma^2 R)/(\alpha_{\rm CO} G)$, where σ is the velocity dispersion of the CO line, R is the CO emitting radius, $\alpha_{\rm CO}$ is the CO luminosity to gas mass conversion factor and G is the gravitational constant. We recall from Eqs. (4) and (5) that the dynamical mass is proportional to $\sigma^2 R$ and $M_{\rm gas} = L'_{\rm CO}\,\alpha_{\rm CO}$; thus this correlation simply reflects the variation of the ratio between gas mass and dynamical mass. In Fig. 6, we overlay both the apparent CO line luminosity $\mu L'_{\rm CO}$ and the intrinsic $L'_{\rm CO}$ plotted against the CO linewidth on those of the Bo13's unlensed sources. The flat distribution of the lensed sources in the upper panel of Fig. 6 shows clearly the lensed feature. After correcting for the magnification, our sources are generally within the 2 σ regions from Bo13's fit. However, it is clear that all the sources with $\Delta V_{\rm CO} < 400$ km s^{-1} are above the correlation and very close to the +2 σ limit. Again, this supports our previous argument that these linewidths are likely being underestimated.

5. Physical properties of molecular gas

5.1. Multi-J CO line excitation and LVG modelling

As indicated by the histograms of $L'_{\rm CO}/L_{\rm IR}$ in Fig. 4, the shape of the average CO SLED of the H-ATLAS SMGs follows the trend of other high-redshift SMGs and both of them depart from the average CO SLED of local galaxies with $L_{\rm IR} < 10^{12}\,L_\odot$ for the low-J ($J_{\rm up} = 3, 4, 5$) part at the $\sim 1\,\sigma$ levels. Fig. 7 shows the $L_{\rm IR}$-normalised CO SLED of the high-redshift SMGs (previous detections in the literature together with H-ATLAS ones) comparing with those of the local galaxies from Liu et al. (2015).

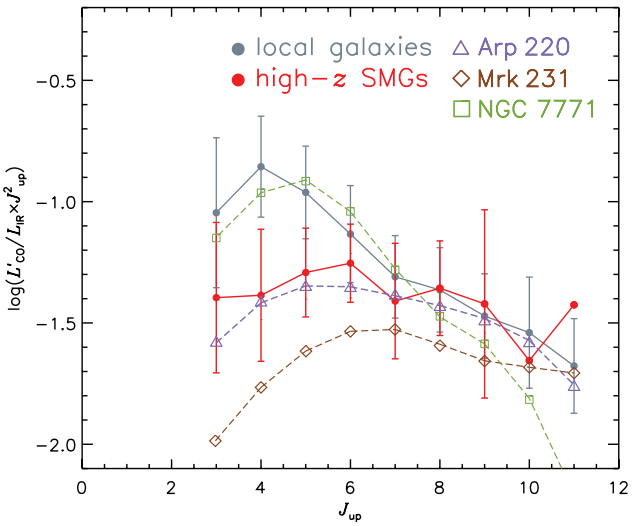

Fig. 7: The CO SLEDs of local galaxies and high-redshift SMGs normalised by $L_{\rm IR}$.[4] Grey symbols indicate the Gaussian mean and deviation of the ratio $L'_{\rm CO}/L_{\rm IR}\times J^2_{\rm up}$ for local galaxies mostly with $10^9\,L_\odot \le L_{\rm IR} \le 10^{12}\,L_\odot$ (Liu et al. 2015). We also include a typical local ULIRG, Arp 220 (purple dashed line and open triangles, Rangwala et al. 2011), an AGN-dominated source, Mrk 231 (red dashed line and open diamond, van der Werf et al. 2010), and a LIRG, NGC 7771 (green dashed line and open square, Liu et al. 2015). Red symbols show high-redshift SMGs from both Carilli & Walter (2013) and from this work. The dots without error bars ($J_{\rm up} = 10$, 11) indicate that the volume of the $L'_{\rm CO}/L_{\rm IR}\times J^2_{\rm up}$ values is insufficient for a normal-distribution fitting. We thus only indicate their mean value here. It is clear that the ratio of $L'_{\rm CO}/L_{\rm IR}\times J^2_{\rm up}$ decreases with increasing $J_{\rm up}$ for local galaxies while it remains flat for high-redshift SMGs and a typical starburst-dominated ULIRG, Arp 220.

Previous studies of global CO excitation in both local and high-redshift galaxies (e.g. Weiß et al. 2007; Rangwala et al. 2011; Deane et al. 2013; Papadopoulos et al. 2014; Zhang et al. 2014; Spilker et al. 2014; Liu et al. 2015; Daddi et al. 2015) show that there are most likely two excitation components dominating the CO emission from ground level up to $J_{\rm up} = 11$, a low-excitation component peaking around $J_{\rm up}$ =3 to $J_{\rm up}$ =4 and a high-excitation component peaking at $J_{\rm up} \gtrapprox 6$. Rosenberg et al. (2015) further quantitively classify the local galaxies into three groups based on the shape of their CO SLEDs, which provides clues towards the dominant excitation conditions within. Com-

[4] The actual value used in y-axis is $L'_{\rm CO}/L_{\rm IR}\times J^2_{\rm up}$. $J^2_{\rm up}$ is included so that the unit of $L'_{\rm CO}\times J^2_{\rm up}$ is comparable to velocity integrated flux density, which is Jy km s^{-1}.

paring the average $L_{\rm IR}$-normalised CO SLED of local galaxies (dominated by normal star-forming galaxies and LIRGs with $L_{\rm IR} = 10^9$–$10^{12}\,L_\odot$) with that of the SMGs in Fig. 7, it is clear that the low-excitation component is more prominent in local galaxies, resulting in the average CO SLED peaking at $J_{\rm up} = 3$ or $J_{\rm up} = 4$, and decreasing with increasing energy levels (as in the case of a local LIRG, NGC 7771, shown in Fig. 7). For the SMGs, the low-excitation component is rather weak while the high-excitation component is comparable to the local normal star-forming galaxies and LIRGs, resulting in a rather flat SLED. To compare the $L_{\rm IR}$-normalised CO SLED of high-redshift SMGs with that of the local ULIRGs, we also overplot a typical local non-AGN-dominated ULIRG (classified as a class II galaxy which is dominated by starburst as in Rosenberg et al. 2015), that is, Arp 220. It is found that the average $L_{\rm IR}$-normalised CO SLED of high-redshift SMGs agrees well with that of Arp 220. Since the average values of $J_{\rm up} = 10$ and $J_{\rm up} = 11$ of high-redshift SMGs are calculated based on only a few sources, the deviations between Arp 220 and high-redshift SMGs for these two lines are not significant from a statistical point of view. Nevertheless, for the AGN-dominated ULIRG, for example, Mrk 231 as shown in Fig.7 (classified as a class-III galaxy which is dominated by AGN powering, Rosenberg et al. 2015), the $L_{\rm IR}$-normalised CO SLED is below that of the high-redshift SMGs. This shows that AGN are contributing much less of the $L_{\rm IR}$ luminosity of our high-redshift SMGs compared to the AGN-dominated ULIRGs. Thus, in the high-redshift SMGs, the average CO gas excitation conditions are likely to be similar to those of local non-AGN-dominated ULIRGs.

To further investigate the CO line excitation and extract the information of physical conditions of the molecular gas, we apply a large velocity gradient (LVG) statistical equilibrium method (e.g. Sobolev 1960; Goldreich & Kwan 1974; Scoville & Solomon 1974) for modelling the fluxes of multiple CO lines. We adopt a one-dimensional (1D) non-LTE radiative transfer code developed by van der Tak et al. (2007), that is, `RADEX`, with an escape probability of $\beta = (1 - {\rm e}^{\tau})/\tau$ derived from an expanding sphere geometry. The CO collisional data are taken from the LAMDA database (Schöier et al. 2005).

As a first step, we use one excitation component in the LVG modelling. Similar to Weiß et al. (2007), the inputs of the code are the molecular gas kinetic temperature ($T_{\rm k}$), the volume density of the molecular hydrogen ($n_{\rm H_2}$), the column density of the CO molecule ($N_{\rm CO}$), and the solid angle ($\Omega_{\rm app}$, note that this solid angle includes the lensing magnification factor) of the source which scales with the resulting fluxes from each CO transition equally, so that the shape of the CO SLED only depends on $T_{\rm k}$, $n_{\rm H_2}$ and $N_{\rm CO}$. We fix the velocity gradient to 1 km s^{-1}, so that the actual input of $N_{\rm CO}$ is column density per unit velocity gradient $N_{\rm CO}/{\rm d}v$ instead.

A Bayesian approach is used to fit our observed flux to the fluxes generated from `RADEX` models given the parameters p (model parameter p includes $T_{\rm k}$, $n_{\rm H_2}$, $N_{\rm CO}/{\rm d}v$ and $\Omega_{\rm app}$). We use the code `emcee` (Foreman-Mackey et al. 2013, see `https://github.com/dfm/emcee`) to perform the Markov chain Monte Carlo (MCMC) calculation with the affine-invariant ensemble sampler (Goodman & Weare 2010). The Bayesian posterior probability of the model parameters given our data $I^{\rm data}$ can thus be written as following (e.g. the notation in Wall & Jenkins 2012),

$$Pr(p|I^{\rm data}) = \frac{Pr(p)Pr(I^{\rm data}|p)}{Pr(I^{\rm data})}, \tag{6}$$

in which $Pr(p|I^{\rm data})$ is the posterior probability of the parameter p given: the prior probability of p as $Pr(p)$; the likelihood of the resulting CO flux $I^{\rm data}$ given the parameter inputs p as $Pr(I^{\rm data}|p)$; and the probability of the data $Pr(I^{\rm data})$, also called evidence, which is commonly treated as a normalising factor. By assuming the noise is independent Gaussian centred, we can write the likelihood as the product of Gaussian probability distributions,

$$Pr(I^{\rm data}|p) = \prod_i \frac{1}{\sqrt{2\pi\sigma_i^2}} \exp\left\{-\frac{\left(I_i^{\rm data} - I_i^{\rm model}(p)\right)^2}{2\sigma_i^2}\right\}, \tag{7}$$

where σ_i is the error associated with each set of measured fluxes $I_i^{\rm data}$, and the `RADEX`-generated results given a set of input parameters p is given by $I_i^{\rm model}(p)$. We note that we use the logarithmic form of Eq.(7) in our practical calculations for convenience, so that the resulting parameters are all in logarithmic form.

Table 6: Single-component MCMC-resulting molecular gas properties of the *H*-ATLAS SMGs.

Source	$\log(n_{\rm H_2})$ $\log({\rm cm^{-3}})$		$\log(T_{\rm k})$ $\log({\rm K})$		$\log(N_{\rm CO}/{\rm d}v)$ $\log({\rm cm^{-2}\,km^{-1}\,s})$	
	$\rm med_{\pm1\sigma}$	$\rm max_{post.}$	$\rm med_{\pm1\sigma}$	$\rm max_{post.}$	$\rm med_{\pm1\sigma}$	$\rm max_{post.}$
G09v1.97	$3.3^{+0.8}_{-0.9}$	3.2	$2.30^{+0.47}_{-0.47}$	2.24	$17.13^{+0.85}_{-0.90}$	17.38
G09v1.40	$2.9^{+0.6}_{-0.5}$	2.4	$2.61^{+0.29}_{-0.49}$	2.89	$17.16^{+0.48}_{-0.57}$	17.26
SDP17b	$3.2^{+2.1}_{-0.8}$	3.1	$2.01^{+0.64}_{-0.64}$	2.57	$17.95^{+0.19}_{-0.67}$	17.34
SDP81	$2.8^{+0.4}_{-0.5}$	3.2	$2.53^{+0.09}_{-0.10}$	2.52	$17.53^{+0.37}_{-0.35}$	17.22
G12v2.43	$2.9^{+0.5}_{-0.5}$	2.7	$2.59^{+0.30}_{-0.43}$	2.88	$17.47^{+0.61}_{-0.34}$	17.43
G12v2.30	$3.0^{+0.3}_{-0.3}$	2.8	$2.88^{+0.09}_{-0.17}$	2.97	$17.43^{+0.29}_{-0.29}$	17.50
NCv1.143	$3.0^{+0.4}_{-0.5}$	2.7	$2.75^{+0.18}_{-0.29}$	2.93	$17.31^{+0.40}_{-0.42}$	17.43
NAv1.195	–	–	–	–	–	–
NAv1.177	$3.0^{+0.6}_{-0.8}$	3.6	$2.50^{+0.18}_{-0.17}$	2.43	$16.73^{+0.85}_{-0.71}$	16.06
NBv1.78	$4.8^{+1.4}_{-1.5}$	4.3	$1.71^{+0.49}_{-0.33}$	1.47	$18.22^{+0.88}_{-1.10}$	17.63
NAv1.144	$3.3^{+1.3}_{-0.8}$	3.3	$1.88^{+0.53}_{-0.36}$	1.98	$18.05^{+0.81}_{-0.62}$	17.98
NAv1.56	$2.5^{+0.5}_{-0.4}$	2.4	$2.35^{+0.43}_{-0.48}$	2.75	$16.38^{+0.72}_{-0.61}$	15.82
G15v2.235	$2.8^{+0.8}_{-0.6}$	3.1	$1.93^{+0.39}_{-0.34}$	1.87	$17.30^{+0.56}_{-0.63}$	17.29
G12v2.890	$3.2^{+1.3}_{-0.8}$	3.4	$2.15^{+0.58}_{-0.57}$	2.43	$17.43^{+1.06}_{-1.38}$	17.49
G12v2.257	$4.0^{+1.8}_{-1.3}$	4.4	$1.35^{+0.37}_{-0.20}$	1.39	$17.84^{+1.02}_{-0.84}$	17.38
G15v2.779	$4.1^{+1.5}_{-1.2}$	5.5	$1.40^{+0.22}_{-0.14}$	1.33	$17.80^{+1.05}_{-0.91}$	17.17

Notes. The value of $\rm med_{\pm1\sigma}$ shows the median value and $\pm1\sigma$ range of the values from the marginal probability distribution of each parameter. The set of parameters with the maximum probability of the posterior distribution within the $\pm1\sigma$ range are shown by the values of $\rm max_{post.}$.

Rather than generating a grid of line fluxes for a range of input parameters from the LVG models (e.g. Kamenetzky et al. 2011; Krips et al. 2011; Spinoglio et al. 2012), we directly use the `Python` package `emcee` to call `pyradex` (a `Python` wrapper of `RADEX` written by A. Ginsburg, see `https://github.com/keflavich/pyradex`) in each iteration for computing the `RADEX` results and passing them to `Python`, and sample the posterior probability distribution function. This can avoid calculations in the unfavourable part of the parameter space, thus saving the total running time of the codes. Following previous works (e.g. Spilker et al. 2014), we adopted flat log-prior within physically reasonable ranges, which are boundaries of the parameter space that we explored. The prior possibilities outside the boundary are set to 0. The parameter-space boundaries are as follows: $n_{\rm H_2} = 10^2$–10^7 cm^{-3}, $T_{\rm k} = T_{\rm CMB}$–10^3 K, $N_{\rm CO}/{\rm d}v = 10^{15.5}$–$10^{19.5}$ cm^{-2} km^{-1} s, in which $T_{\rm CMB}$ is the CMB temperature at the redshift of the source, which can be derived from

$T_{\rm CMB} = 2.7315(1+z)$. We also adopt the range of dv/dr to be 0.1–1000 km s^{-1} pc^{-1} (e.g. Tunnard & Greve 2016), which limits the range of the ratio between $N_{\rm CO}$ and $n_{\rm H_2}$. This prior also puts limits on the ratio between the LVG-solved dv/dr and the dv/dr derived from the virialised state, that is, $K_{\rm vir} = ({\rm d}v/{\rm d}r)_{\rm LVG}/({\rm d}v/{\rm d}r)_{\rm vir}$, in which $({\rm d}v/{\rm d}r)_{\rm vir} = 0.65\alpha^{0.5}(n_{\rm H_2}/(10^3\ {\rm cm^{-3}}))^{-0.5}$ km s^{-1} pc^{-1}, where $\alpha = 0.5$–3 depending on the density profile (Papadopoulos & Seaquist 1999). Additionally, we set the priors to limit the column length to be smaller than the diameter of the entire SMG, which is about 7 kpc. This yields a constraint of the ratio $N_{\rm CO}/n_{\rm H_2}$ that is well outside the range given by the prior from dv/dr. Lastly, the molecular gas mass traced by the CO lines should not exceed the dynamical mass, for example, $\sim 10^{12}\ M_\odot$ (see Sect. 4.2). This yields an upper limit of $N_{\rm CO}$/dv to be smaller than $\sim 10^{20}$ cm^{-2} km^{-1} s (e.g. Rangwala et al. 2011), which is well outside the parameter space as well.

A total of 400 walkers have been deployed to explore the parameter space initiated from the point of solution acquired by the quasi-Newton solver. We ensured proper convergence of the MCMC chains by a burn-in period of 100 iterations and 1000 subsequent iterations. The resulting posterior probability distributions and the marginal distribution of the parameters (generated by `corner.py`, Foreman-Mackey 2016) are shown by the blue density-contour plots and the blue histograms in Fig. C.1. We also indicate the 39% and 68% quantiles of the marginalised probability distribution of the parameter with dashed lines. The solutions with the maximum posterior probability within the 39% and 68% quantiles (the $\pm1\,\sigma$ range) are marked with orange lines and points. The corresponding fit to the CO SLED is also shown in the Figure with an orange line overlaid on the black data points. All the results, the median value, the $\pm1\,\sigma$ range and the maximum posterior probability, are summarised in Table 6, except for NAv1.195 because only one CO line of it has been observed, leading to an unreliable fitting.

From the single excitation component fitting, the range of $n_{\rm H_2}$ is found to be $\approx 10^{2.5}$–$10^{4.1}$ cm^{-3}, $T_{\rm k}$ is from 22 K to 750 K and $N_{\rm CO}/{\rm d}v \approx 10^{17.13}$–$10^{18.22}$ cm^{-2} km^{-1} s for the H-ATLAS SMGs. In most cases, the values are close to those found by single-component LVG modelling of local ULIRGs (e.g. Ao et al. 2008) and high-redshift SMGs (e.g Lestrade et al. 2010; Combes et al. 2012; Riechers et al. 2013). Nevertheless, one should note that the observed CO SLEDs are dominated by the excitation from dense and warm molecular gas as suggested by the CO SLEDs peaking around $J_{\rm up} = 4$–7. Our observed CO SLEDs are biased towards the mid- and high-J CO lines, and thus a single component fit is biased towards the high-excitation component seen in local ULIRGs. Indeed, most of our values of $T_{\rm k}$ from the single component analysis are higher than the low-excitation component seen in local ULIRGs but close to the values of the high-excitation component, for example, the warm molecular gas as found in Arp 220 (Rangwala et al. 2011). The lack of $J_{\rm up} \leq 2$ data will likely lead to overestimations of the values of $T_{\rm k}$ for our SMGs. The under-presentation of the low-excitation component is also shown in the fitted CO SLED to the observed flux: the modelled fluxes of CO(3–2) and CO(1–0) are often underestimated, especially in the cases of G09v1.40, SDP 17b, G12v2.43, NAv1.144 and G12v2.890 shown in Fig. C.1.

Therefore, to fully consider both the low-excitation component with a cooler temperature and the warmer, dense high-excitation component, we perform a two-excitation-component LVG modelling with the CO SLEDs: a low-excitation component with a lower value of $T_{\rm k}$ and a high-excitation component with a higher $T_{\rm k}$. An MCMC method similar to the aforementioned single-component LVG modelling is adopted. We assign two sets of $n_{\rm H_2}$, $T_{\rm k}$, $N_{\rm CO}$/dv and $\Omega_{\rm app}$ to the two excitation components, so that the two components can have different physical conditions. Similar priors are also applied to help constrain the posterior distribution. For the two-excitation-components fit, the number of free parameters can be reduced significantly in some sources, therefore we carefully add some more informative priors. Besides the similar priors such as those used in the single-component analysis, we put additional prior constraints on the two-component LVG modelling as follows: (i) The size of the cooler low-excitation component should be larger than that of the high-excitation component (this has been suggested by the observations of the sizes of the emitting regions of different transitions of the CO lines, e.g. Ivison et al. 2011); and (ii) most importantly, we assume that the temperature of the low-excitation component should be close to the cold dust temperature. At high densities ($n_{\rm H_2} \geq 10^{4.5}$ cm^{-3}), the temperatures of the dust and the gas can be well coupled (Goldsmith 2001). However, the different heating mechanisms do not necessarily produce thermally balanced dust and gas temperature, especially at lower densities ($n_{\rm H_2} \leq 10^{3.5}$ cm^{-3}). So we use rather loose priors for the $T_{\rm k}$ of the cool low-excitation component, that is, a normal distribution with the value of mean and standard deviation equal to the cold dust temperature $Pr(T_{\rm k})_{\rm cool} \sim \mathcal{N}(T_{\rm d}, {T_{\rm d}}^2)$. This prior offers a reasonable guess of the $T_{\rm k}$ for the cooler component in the range of ~ 0 K–90 K (which will be further reduced into the range of $T_{\rm CMB}$–90 K by the aforementioned priors).

We have applied similar MCMC walkers in the parameter space and generated the posterior probability distributions (Fig. C.1). The dark green contours and histograms are the posterior probability distribution and marginal probability distribution for $n_{\rm H_2}$, $T_{\rm k}$ and $N_{\rm CO}$/dv of the low-excitation component, while those shown in light green are for the high-excitation component. The solutions with the maximum posterior probability are shown by the dotted-dash pink line and red dashed line for the low- and high-excitation components, respectively. The corresponding CO SLEDs are over-plotted in Fig. C.1 with dotted-dash pink line and the dashed red lines. The values are summarised in Table 7. We show the histograms of the derived parameters for low- and high-excitation components in Fig.8, together with those of the single component LVG modelling. For the low-excitation component, the density ranges from $\sim 10^{2.8}$ cm^{-3} to $10^{4.6}$ cm^{-3} with large uncertainties, the gas temperature ranges from ~ 20 K to 30 K, and the CO column density per unit velocity gradient ranges from $10^{15.7}$ cm^{-2} km^{-1} s to $10^{17.9}$ km^{-1} s with significant uncertainties. For the high-excitation component, the density ranges from $\sim 10^{2.8}$ cm^{-3} to $10^{4.2}$ cm^{-3}, the gas temperature ranges from ~ 60 K to 400 K, and the CO column density per unit velocity gradient ranges from $10^{17.1}$ cm^{-2} km^{-1} s to $10^{18.1}$ cm^{-2} km^{-1} s. As a comparison, the gas densities of the two components are close, and the differences are within uncertainties. The gas temperatures of the high-excitation component are higher (peaking around ~ 200 K) than those of the low-excitation ones (peaking around ~ 25 K). The $T_{\rm k}$ of the cooler component is $\sim$ 10–15 K lower than the dust temperature $T_{\rm d}$ as shown in Table 3.

As shown in the two-component-model-produced CO SLEDs in Fig. C.1, after including the low-excitation component, the flux of the low-J CO lines can be better reproduced, especially in G09v1.40, SDP 17b, G12v2.43, and NAv1.144. This indicates that to fully explain the CO SLEDs, at least two excitation components are needed. The gas temperatures also decreased comparing the $T_{\rm k}$ from single component LVG modelling with the $T_{\rm k}$ of the high-excitation component from two-

Table 7: Two-component MCMC-resulted molecular gas properties of the *H*-ATLAS SMGs.

Source	low-excitation						high-excitation					
	$\log(n_{H_2})$ $\log(cm^{-3})$		$\log(T_k)$ log(K)		$\log(N_{CO}/dv)$ $\log(cm^{-2}\,km^{-1}\,s)$		$\log(n_{H_2})$ $\log(cm^{-3})$		$\log(T_k)$ log(K)		$\log(N_{CO}/dv)$ $\log(cm^{-2}\,km^{-1}\,s)$	
	$med_{\pm1\sigma}$	$max_{post.}$	$med_{\pm1\sigma}$	$max_{post.}$	$med_{\pm1\sigma}$	$max_{post.}$	$med_{\pm1\sigma}$	$max_{post.}$	$med_{\pm1\sigma}$	$max_{post.}$	$med_{\pm1\sigma}$	$max_{post.}$
G09v1.97	$2.8^{+1.5}_{-0.6}$	2.1	$1.30^{+0.32}_{-0.16}$	1.55	$15.70^{+1.51}_{-0.89}$	14.61	$2.8^{+1.1}_{-0.6}$	3.1	$2.17^{+0.51}_{-0.40}$	2.21	$17.86^{+0.84}_{-1.10}$	17.58
G09v1.40	$3.3^{+1.3}_{-0.9}$	3.6	$1.41^{+0.31}_{-0.30}$	1.55	$16.08^{+1.17}_{-1.07}$	15.22	$3.2^{+1.0}_{-0.8}$	3.5	$2.41^{+0.39}_{-0.38}$	2.46	$17.44^{+0.89}_{-0.69}$	17.20
SDP17b	$3.2^{+1.6}_{-0.9}$	2.5	$1.43^{+0.32}_{-0.30}$	1.65	$16.49^{+1.71}_{-1.41}$	15.69	$3.4^{+1.5}_{-0.9}$	3.8	$2.31^{+0.45}_{-0.45}$	2.38	$17.84^{+0.92}_{-0.90}$	17.30
SDP81	$2.8^{+1.0}_{-0.6}$	2.3	$1.38^{+0.32}_{-0.24}$	1.52	$15.96^{+1.26}_{-1.00}$	15.83	$2.9^{+0.7}_{-0.6}$	3.2	$2.43^{+0.16}_{-0.23}$	2.40	$17.76^{+0.46}_{-0.58}$	17.45
G12v2.43	$4.1^{+1.3}_{-1.3}$	4.0	$1.30^{+0.28}_{-0.19}$	1.44	$15.52^{+1.29}_{-0.72}$	14.74	$3.4^{+1.1}_{-0.9}$	4.2	$1.91^{+0.38}_{-0.28}$	1.60	$18.02^{+0.81}_{-0.83}$	17.90
G12v2.30	$3.6^{+1.3}_{-1.1}$	4.3	$1.42^{+0.31}_{-0.20}$	1.35	$17.22^{+1.04}_{-1.02}$	17.06	$3.3^{+0.8}_{-0.7}$	3.3	$2.57^{+0.33}_{-0.30}$	2.69	$17.70^{+0.83}_{-0.62}$	17.77
NCv1.143	$4.1^{+1.5}_{-1.4}$	4.3	$1.30^{+0.21}_{-0.13}$	1.28	$17.00^{+1.17}_{-0.94}$	16.94	$4.2^{+1.3}_{-1.2}$	5.1	$1.80^{+0.26}_{-0.20}$	1.65	$18.14^{+0.90}_{-0.96}$	17.70
NAv1.195	–	–	–	–	–	–	–	–	–	–	–	–
NAv1.177	$3.9^{+1.2}_{-1.3}$	4.4	$1.40^{+0.27}_{-0.23}$	1.20	$16.96^{+1.18}_{-1.10}$	17.19	$3.0^{+0.9}_{-0.7}$	3.0	$2.60^{+0.28}_{-0.32}$	2.78	$17.25^{+0.58}_{-0.93}$	17.33
NBv1.78	$4.6^{+1.5}_{-1.6}$	4.1	$1.48^{+0.29}_{-0.28}$	1.55	$17.66^{+1.24}_{-1.52}$	17.07	$3.8^{+1.6}_{-1.2}$	4.6	$2.27^{+0.43}_{-0.42}$	2.49	$17.63^{+1.06}_{-1.37}$	16.01
NAv1.144	$3.3^{+1.9}_{-0.1}$	2.6	$1.34^{+0.36}_{-0.29}$	1.34	$16.19^{+1.91}_{-1.19}$	16.16	$3.1^{+0.9}_{-0.7}$	3.4	$2.30^{+0.38}_{-0.34}$	2.09	$17.87^{+0.74}_{-0.62}$	17.90
NAv1.56	$3.0^{+1.0}_{-0.6}$	2.3	$1.42^{+0.34}_{-0.31}$	1.63	$16.24^{+1.08}_{-1.06}$	16.63	$2.7^{+0.9}_{-0.5}$	2.9	$2.31^{+0.45}_{-0.48}$	2.14	$17.44^{+0.83}_{-0.95}$	17.51
G15v2.235	$3.9^{+1.8}_{-1.2}$	3.7	$1.24^{+0.29}_{-0.18}$	1.23	$17.63^{+1.07}_{-1.26}$	17.78	$2.8^{+1.2}_{-0.6}$	3.0	$2.19^{+0.53}_{-0.48}$	2.23	$17.14^{+0.82}_{-1.09}$	17.56
G12v2.890	$4.1^{+1.9}_{-1.5}$	2.8	$1.35^{+0.25}_{-0.25}$	1.48	$17.10^{+1.57}_{-1.59}$	15.80	$3.8^{+1.8}_{-1.2}$	5.1	$2.25^{+0.49}_{-0.49}$	2.55	$17.80^{+1.04}_{-1.36}$	17.47
G12v2.257	$4.5^{+1.5}_{-1.4}$	3.7	$1.28^{+0.26}_{-0.20}$	1.36	$17.54^{+1.10}_{-1.03}$	18.01	$3.5^{+1.8}_{-1.0}$	4.4	$2.17^{+0.55}_{-0.54}$	2.59	$17.34^{+1.19}_{-1.48}$	15.86
G15v2.779	$4.3^{+1.2}_{-1.1}$	4.0	$1.33^{+0.16}_{-0.11}$	1.38	$17.91^{+0.95}_{-0.91}$	17.94	$3.4^{+1.9}_{-1.0}$	5.0	$2.15^{+0.58}_{-0.53}$	2.48	$17.05^{+1.58}_{-1.66}$	16.25

Notes. See caption of Table 6.

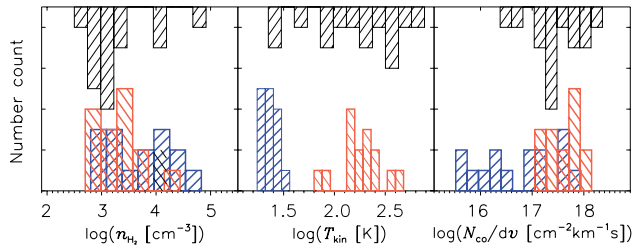

Fig. 8: Histograms of n_{H_2}, T_k and N_{CO}/dv derived from single-component LVG modelling (black), and those of the low- and high-excitation components from two-component LVG modelling as shown in blue and red, respectively.

component analysis, as in the case of G09v1.97, G09v1.40, G12v2.43, G12v2.30, NCv1.143 and NAv1.56. This again suggests that bias could be introduced using only a single excitation component to explain the full CO SLED. The physical properties of both components agree well with other studies of high-redshift SMGs (e.g. Scott et al. 2011; Danielson et al. 2013; Spilker et al. 2014). One has a low gas temperature, while another is smaller in size but with a warmer gas temperature, supporting the idea that there is likely more than one molecular gas excitation component. The latter is thought to be more closely related to the on-going star-forming activity compared with the cooler component. We also note that in the cases of NBv1.78, NAv1.56, G12v2.890 and G15v2.779, due to the very limited number of data points, the two-component fitting is highly reliant upon the priors and does not produce better fitting results than the single-component fittings. Thus, those individual two-component fitting results should be used with caution. Nevertheless, here, for the purpose of a statistical analysis of the physical properties of the gas excitation, we include these results in the discussion below.

We have investigated whether or not the CO linewidth correlates with the derived gas excitation condition. By comparing the linewidth with the parameters derived from LVG modelling, no significant correlation is found, with the absolute values of the correlation coefficient $\lesssim 0.3$.

To further investigate the physical properties from a statistical point of view, we plot the gas thermal pressure P_{th} (defined by $P_{th} \equiv n_{H_2} \times T_k$) sampled from the MCMC posterior probability distributions versus the star formation efficiency (SFE) proxy defined as the ratio between L_{IR} and molecular gas mass in Fig. 9. Because L_{IR} is proportional to the star formation rate (e.g. Kennicutt & Evans 2012), the ratio between L_{IR} and M_{gas} is thus a good representative of SFE as defined by

$$\mathrm{SFE} \equiv \mathrm{SFR}/M_{gas}, \quad (8)$$

representing the SFR per unit molecular gas mass. As displayed in the left panel of Fig. 9, for comparison, we also include the values of the Milky Way (Draine 2011), the Tuffy galaxies (Zhu et al. 2007), the Antennae galaxies (Gao et al. 2001; Zhu et al. 2003), Arp 220 (Rangwala et al. 2011) and the $z \sim 6$ SMG HFLS3 (Riechers et al. 2013) for comparison. For the gas thermal pressure P_{th} versus SFE of the *H*-ATLAS SMGs only (as indicated by the grey dashed square in the left panel of Fig. 9), we find the Pearson's correlation coefficient $R_P = 0.68$ (with the p-value $p = 0.003$), indicating the existence of a strong correlation. The values of the local ULIRG Arp 220 and the high-redshift SMG HFLS3 also follow the similar relation we find in the plot, with similar values of P_{th} and SFE as for the *H*-ATLAS ULIRGs. However, the dynamical range of the P_{th} is small for the SMGs and local ULIRGs; thus the correlation may be biased by a few sources with either very large or very small values of P_{th}. Therefore, we include some nearby galaxies with lower SFE: The Milky Way, the Tuffy galaxies and the Antennae galaxies. After including these sources, we find the Pearson's correlation coefficient increases to $R_P = 0.89$ ($p = 0.001$). With a fit to all the data points from the single component LVG modelling, we get a slope of 1.1 ± 0.5. We have also tested whether this correlation could arise from any relation between n_{H_2} and SFE or between T_k and SFE. For these two pairs of quantities, the correlation coefficient is much weaker, $R_P < 0.33$ ($p > 0.14$), compared with the one between the gas thermal pressure P_{th} and SFE. This rules out the possibility that either n_{H_2} or T_k is dominating the correlation. All these pieces of evidence point out that there is likely

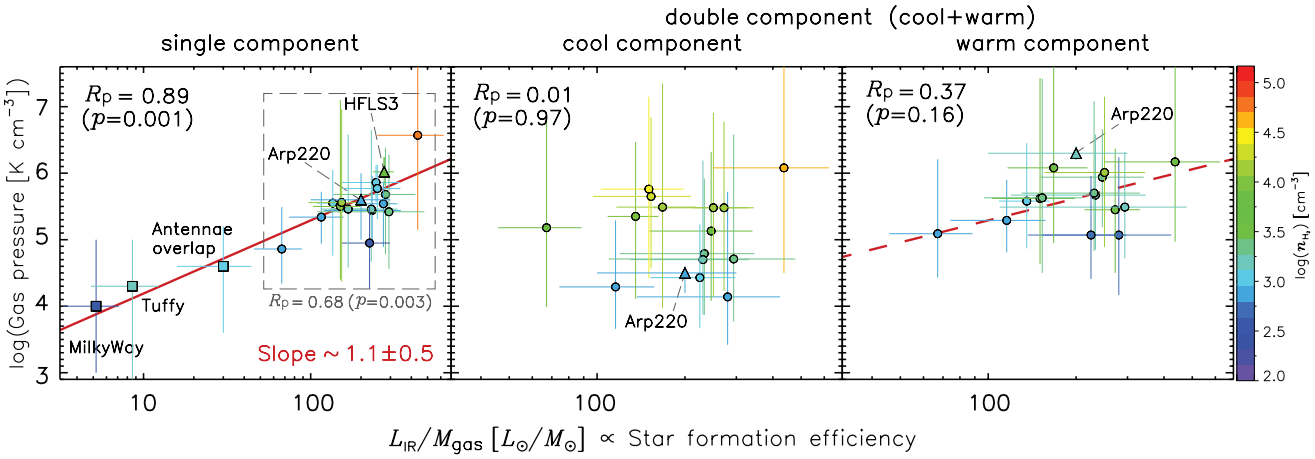

Fig. 9: *Left*: Thermal gas pressure plotted against star formation efficiency as indicated by L_{IR}/M_{gas}. Filled circles are the *H*-ATLAS SMGs. We also plot the values of the Milky Way, the Tuffy galaxies, the Antennae galaxies, Arp 220 and HFLS3 in filled triangles for comparison. The colour is coded based on their values of n_{H_2}. The red line shows the fit to the correlation, which yields a slope of 1.1 ± 0.5 for all the sources. The grey dashed square shows the region where *H*-ATLAS SMGs reside. *Middle*: Similar correlation plot as in the left panel but only for the cool component from the two-component LVG modelling. There is no correlation found ($R_P = 0.01$ and $p = 0.97$). *Right*: Similar correlation plot as in the left panel but only for the warm component in the two-component LVG modelling. The dashed red line is an overlay of exactly the same red line plotted in the left panel. The data points follow the same correlation found in the single component fit with an $R_P = 0.37$ and $p = 0.16$. In all the three panels, the legends show the Pearson's correlation coefficient R_P with corresponding p-value. The values of n_{H_2} for each point are indicated by the colour bar.

a strong close-to-linear correlation between P_{th} of the molecular gas and SFE, suggesting that the thermal pressure of the bulk of molecular gas is playing an important role in regulating the star formation at galactic scale across a range of redshifts. This is in-line with the theoretical works discussing the relation between gas pressure and SFE (e.g. Elmegreen & Efremov 1997; Wong & Blitz 2002).

After decomposing the CO excitation into the low-excitation component and the high-excitation one, we also plot their P_{th} versus SFE separately. The results of the (cool) low-excitation component and the (warm) high-excitation component are shown in the middle and right panel of Fig. 9, respectively. There is likely no correlation between P_{th} and SFE for the low-excitation component, as suggested by the low coefficient $R_P = 0.01$ ($p = 0.97$). Nevertheless, for the high-excitation component there is still evidence of a correlation between P_{th} and SFE with $R_P = 0.37$ ($p = 0.16$). Although, a large dynamical range and smaller uncertainties of P_{th} and SFE are needed to further confirm this correlation. We also overlay the red line from the correlation fit to P_{th} versus SFE of the single component modelling. It is clearly shown in the plot that, the data points of the high-excitation component follow this correlation well. This again shows that the high-excitation component is more closely related to the on-going star formation activity, while the low-excitation gas is much less tied to star formation.

5.2. The [C I](2–1) emission line in the high-redshift SMGs

The ^{3}P fine structure [C I] lines of atomic carbon, [C I](1–0) at 492.2 GHz and [C I](2–1) at 809.3 GHz, are in a simple three-level energy system. The critical densities n_{crit} for the [C I](1–0) and [C I](2–1) lines are both ~ 0.5–1×10^3 cm^{-3}, which is comparable to those of the CO(1–0) and CO(2–1) lines (Table 1). The energy levels for [C I]$^3P_2$ and [C I]$^3P_1$ are 23.6 K and 62.6 K, respectively. Atomic carbon is found to be well-mixed with the bulk of the H_2 gas, making it a promising molecular gas tracer together with low-J CO lines (e.g. Papadopoulos & Greve 2004). From these two optically thin [C I] lines, one can derive the excitation temperature and gas density without relying on other complementary information (e.g. Weiß et al. 2003). In the high-redshift universe, [C I] has only been detected in a small number of systems, mainly gravitationally lensed SMGs and quasars (see the references in Walter et al. 2011; see Bothwell et al. 2017 for recent detections of [C I](1–0) lines in a sample of SPT-selected lensed SMGs; see also Wilson et al. 2017 for detections of [C I](2–1) by stacking *Herschel* SPIRE/FTS spectral data of galaxies at moderate redshifts). In this work, we have detected seven [C I](2–1) lines out of eight observations in our lensed high-redshift SMGs.

Papadopoulos & Greve (2004) find a good agreement between the total molecular gas mass derived from [C I] and CO lines and dust continuum in local ULIRGs. [C I] likely traces H_2 even more robustly than the low-J CO lines (plus standard conversion factor) in extreme conditions on galactic scales (e.g. Zhang et al. 2014). High-redshift observations (e.g. Weiß et al. 2003; Alaghband-Zadeh et al. 2013) also support such an agreement, although Bothwell et al. (2017) recently found that either a larger α_{CO} or a high [C I] abundance is needed to balance the gas mass derived from CO and from [C I] lines. Since the observations of CO(1–0) lines at high-redshift becomes observationally difficult, acquiring the intensities of the [C I] lines, which are usually brighter than the CO(1–0) lines and residing in favourable bands for observation, could help us to better determine the total molecular mass in high-redshift SMGs. Zhang et al. (2016) show that at high-redshift the CO(1–0) line will also suffer observing against the CMB, making the line more difficult to observed. Moreover, they also found that CO can be destroyed by the cosmic rays coming from the intense star-forming activities, suggesting the [C I] lines to be a better tracer of the total molecular gas mass in such environments (Bisbas et al. 2015).

Using *Herschel* spectral data of a sample of local (U)LIRGs, Jiao et al. (2017) find a tight correlation between the CO(1–0)

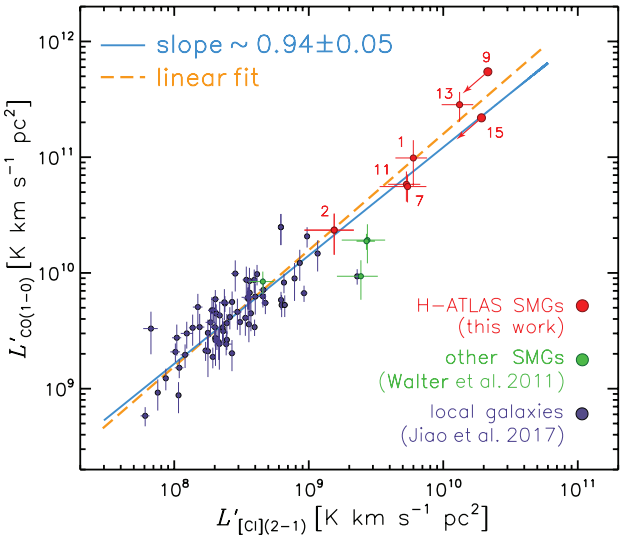

Fig. 10: $L'_{[CI](2-1)}$ versus $L'_{CO(1-0)}$ including (U)LIRGs from Jiao et al. (2017) (dark purple) *H*-ATLAS SMGs (red) and other SMGs from Walter et al. (2011) (green). Two of our sources, NAv1.177 (#9) and G12v2.257 (#15) are lacking lens modelling, thus we plot the limit, and the arrows show the direction for lensing correction. A fit to the correlation from the local to high-redshift galaxies is indicated by the blue line, with a slope of 0.94 ± 0.05. We also show a fit with a fixed slope of 1, that is, a linear fit, by the orange dashed line. The source index ID is indicated in Fig. 1 and Table 3.

line luminosity and the [CI] line luminosities. The tight correlations suggest that the [CI] lines trace the total molecular gas mass as the CO(1–0) line does. Using the empirical correlations, Jiao et al. (2017) derive a conversion factor $\alpha_{[CI](2-1)}$ that converts $L'_{[CI](2-1)}$ into M_{gas} to be $\alpha_{[CI](2-1)} = 27.5 \pm 1.3\,(\mathrm{K\,km\,s^{-1}\,pc^2})^{-1}$. To test whether this correlation can be extended to high-redshift SMGs, we plot the $L'_{[CI](2-1)}$ versus $L'_{CO(1-0)}$ including our lensed SMGs in Fig. 10. The fit to all the galaxies across different redshifts indicates a tight correlation close to linear, that is, the slope equals 0.94 ± 0.05. When fixing the slope to one, we find the fitted linear correlation to be valid both for local sources and high-redshift SMGs. Nevertheless, one would need to know the abundance of [CI] and the excitation temperature for the [CI] lines to properly derive the molecular gas mass from the [CI] lines as in Weiß et al. (2003). This would require the detection of both the [CI](1–0) and [CI](2–1) lines for the *H*-ATLAS SMGs, while we have only detection of the 2–1 line.

5.3. Star formation and the molecular gas content in high-redshift GMGs

One of the key interests of studying star formation at galactic scale across all redshifts from the observation point of view is to quantify the 'star formation law', which is the correlation between M_{gas} and SFR (or the surface SFR density as originally defined by Kennicutt 1998b). This law is not only an essential input for the theoretical models of galaxy formation and evolution but also an important tool to study the relation between star formation and the molecular gas content. As we mentioned in Section 5.1, the SFR per unit molecular gas mass (i.e. SFE) shows how efficiently each unit of molecular gas mass is converted into stars (Eq.(8)). The inverse of SFE can be defined as the molecular gas depletion time,

$$t_{dep} \equiv M_{gas}/\mathrm{SFR}, \quad (9)$$

which indicates the exhausting time-scale of the molecular gas mass with the current SFR. The gas depletion time is a good way of representing the variations of the star formation properties. The value of t_{dep} varies from ~ 1.3–1.5 Gyr for local star-forming galaxies (e.g. Kennicutt 1998b; Daddi et al. 2010; Genzel et al. 2010; Saintonge et al. 2011) to smaller values for high-redshift ones ('main sequence'): ~ 0.7 Gyr (e.g. Tacconi et al. 2013; Sargent et al. 2014) or even smaller values (Saintonge et al. 2013). Indeed, there seems to be a cosmic evolution trend for star-forming galaxies as found by Saintonge et al. (2013). In Fig. 11 (extended from Fig. 7 of Aravena et al. 2016b), we plot the gas depletion time of our sources (see values in Table 5) and compare it with different kinds of galaxies across a range of redshifts, including; the aforementioned evolution track with z of star-forming galaxies (Saintonge et al. 2013); nearby ULIRGs (Solomon et al. 1997) and $z = 0.6$–1 ULIRGs (Combes et al. 2013); other lensed/unlensed SMGs/ULIRGs studied (see Aravena et al. 2016b and the references within). As shown in Fig. 11, unlike star-forming galaxies, for all types of ULIRGs, the depletion time is found to be much smaller, from ~ 10 to 100 Myr (roughly 10 times smaller than that of the star-forming main sequence galaxies), and there seems to be no evidence of a cosmic evolution of t_{dep}. The *H*-ATLAS SMGs show no difference in the t_{dep} compared with SPT lensed ones and other SMGs/ULIRGs studied. They are well below the values for star-forming main sequence galaxies and show no evidence of variation across redshifts.

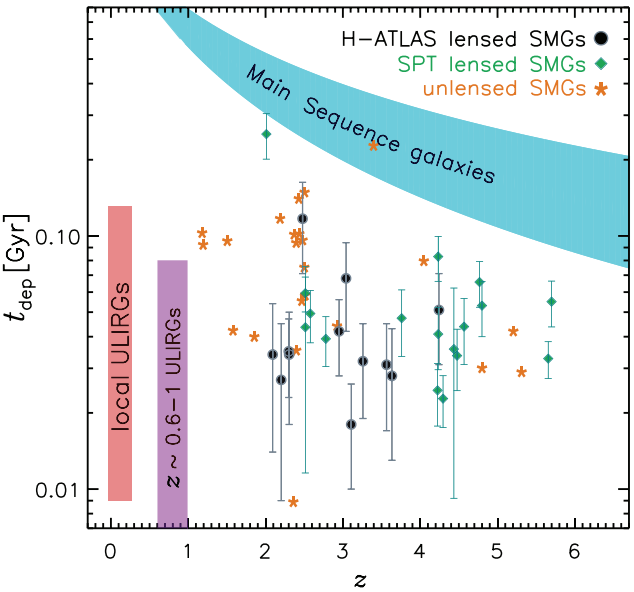

Fig. 11: Extended from Fig. 7 of Aravena et al. 2016b: Molecular gas depletion time of our lensed SMGs (black circles), SPT lensed SMGs (green diamonds), and other unlensed SMGs (orange stars). The ranges of local ULIRGs (Solomon et al. 1997) and z = 0.6–1 ULIRGs (Combes et al. 2013) are also included as the red and purple regions, respectively. The cyan region indicates the main sequence galaxies as described by Saintonge et al. (2013) through the formula $t_{dep} = 1.5(1+z)^{\alpha}$, in which α is from $\alpha = -1.5$ (Davé et al. 2012) to $\alpha = -1.0$ (Magnelli et al. 2013).

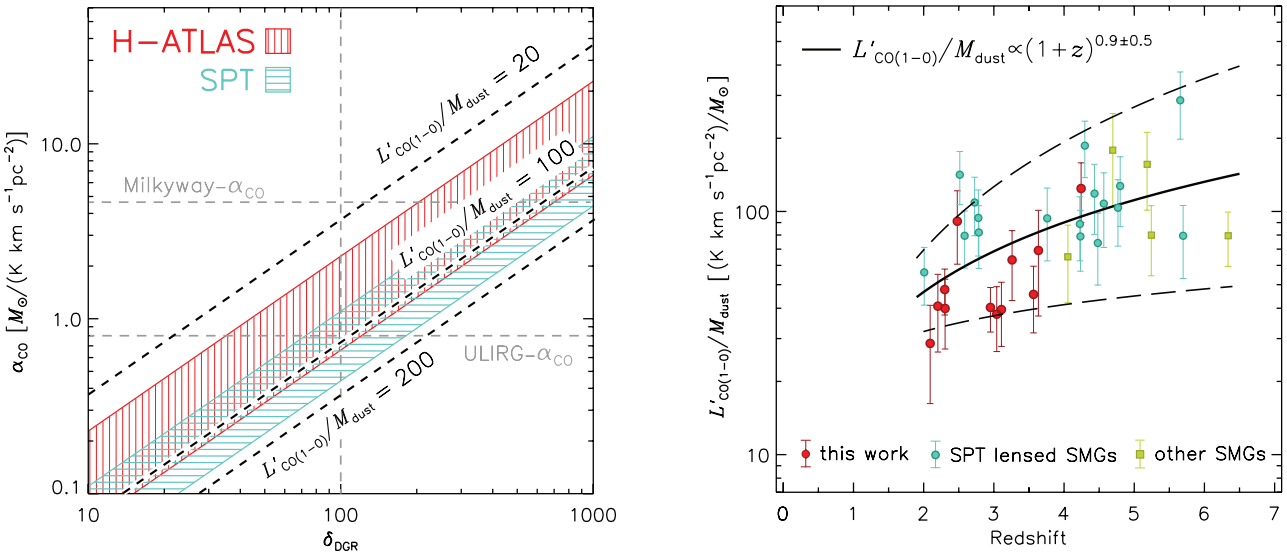

Fig. 12: *Left panel*: The $\pm1\sigma$ range of δ_{GDR} and α_{CO} derived from observed M_{dust} and L'_{CO} using Eq. (10). Red region is from this work while the green region is from Aravena et al. (2016b). Our results generally agree with the SPT sources' albeit having slightly larger α_{CO} or smaller δ_{GDR}. *Right panel*: The ratio between L'_{CO} and M_{dust} of SMGs across the different redshifts. The SPT lensed SMGs in green points are from Aravena et al. (2016b), while our sources are in red. We also plot other SMGs from the literature in yellow filled squares (see references in text). The black line shows a best-fit to all the data points and dashed black lines show the $\pm$ 1σ ranges (for the slope only) from the fit. The resulting relation is shown in the legend.

However, one should note that the values of M_{gas} derived above are based on the assumption of α_{CO} = 0.8 $M_\odot$ (K km s^{-1} pc^2)$^{-1}$. This conversion factor may be different in various types of galaxies. To derive reliable value of α_{CO}, one needs to estimate the molecular gas mass from other methods rather than converting from CO fluxes. One of the most convenient ways is to compute the molecular gas mass from the dust mass by assuming a value for the gas-to-dust mass ratio δ_{GDR}, since the dust continuum is much easier to measure in practical observations (e.g. Scoville et al. 2014, 2017). Nevertheless, δ_{GDR} has no constant value for different galaxies. In fact, both δ_{GDR} and α_{CO} are functions of the metallicity of different galaxies based on both observational results (e.g. Wilson 1995; Leroy et al. 2011; Magdis et al. 2011; Genzel et al. 2012) and theoretical works (e.g. Narayanan et al. 2012). To avoid the uncertainties caused by assuming single values for δ_{GDR} and α_{CO}, we explore a combination of both, which is derived directly from observational quantities. From Eq.(2) and Eq.(3), we can derive

$$\delta_{GDR}/\alpha_{CO} = L'_{CO(1-0)}/M_{dust}, \quad (10)$$

in which $L'_{CO(1-0)}$ is from CO line observations (converted mostly from CO(3–2) in our cases as mentioned in Section 4.1), and M_{dust} is calculated from the observed submm/mm dust continuum flux densities based on a modified black body model (both for our work and the SPT lensed SMGs).

The left panel of Fig. 12 shows the possible $\pm$ 1 σ range of δ_{GDR} versus α_{CO} for *H*-ATLAS SMGs computed using Eq.(10), together with the one from SPT-lensed SMGs for comparison. By taking a common δ_{GDR} of 100, the corresponding α_{CO} for our *H*-ATLAS SMGs is $\sim$0.7–2 $M_\odot$ (K km s^{-1} pc^2)$^{-1}$, while for the SPT sources, α_{CO} is slightly smaller, $\sim$0.4–1 $M_\odot$ (K km s^{-1} pc^2)$^{-1}$. Nevertheless, one need to accurately measure either δ_{GDR} or α_{CO} in order to break the degeneracies between these two quantities. Normally, one could use the calibration of the relation between the metallicity Z and δ_{GDR} (e.g. Magdis et al. 2011), to derive the latter from the former by observing the optical emission lines. But for the high-redshift SMGs, due to the extreme dust obscuration, it is very challenging to measure the metallicity from optical observation, making it thus difficult to accurately pinpoint the value of δ_{GDR} and α_{CO}.

By including other published SMGs at different redshifts (Magdis et al. 2011; Combes et al. 2012; Salomé et al. 2012; Walter et al. 2012; Riechers et al. 2013), we have plotted the $L'_{CO(1-0)}/M_{dust}$ versus redshift for all of them in the right panel of Fig. 12 similarly to Tan et al. (2014). There seems to be an increasing trend for the SMGs across the cosmic time, from nearby to the high-redshift Universe. The best fit to this trend is $L'_{CO(1-0)}/M_{dust} \propto (1+z)^{0.9\pm0.5}$, in the redshift range from $z \approx 2$ up to $z \approx 6$. This agrees with the fact that the average SPT sources have higher values of δ_{GDR}/α_{CO} (i.e. $L'_{CO(1-0)}/M_{dust}$), since the SPT sources have a higher average redshift compared with the *H*-ATLAS one. It has been suggested that δ_{GDR} is linearly anti-correlated with Z, that is, $\delta_{GDR} \propto Z^{-1}$ (e.g. Santini et al. 2010; Leroy et al. 2011; Magdis et al. 2011), while the dependence of α_{CO} seems to be steeper (e.g. $\alpha_{CO} \propto Z^{-1.4}$, calibration from Leroy et al. 2011). Combining these two calibrations, one would derive a correlation between the ratio δ_{GDR}/α_{CO} ($L'_{CO(1-0)}/M_{dust}$) and Z (e.g. Magdis et al. 2012). This offers one possible explanation for the observed correlation, if the higher-redshifted SMGs in this plot have larger values of metallicity Z. Considering the cosmic enrichment of metallicity at high-redshift (e.g. Troncoso et al. 2014), the higher-redshifted SMGs in the plot are unlikely to be evolutionally linked with the lower redshifted ones. At given redshifts, Z increases with stellar masses (see a summary in Tan et al. 2014). Therefore, this increasing value of $L'_{CO(1-0)}/M_{dust}$ could rather be explained by a selection bias towards the high-mass systems which correspond to those higher-redshifted SMGs in the Figure.

5.4. CO gas and H_2O gas comparison

The systematic study of local galaxies (from normal star-forming galaxies to nearby ULIRGs) shows the close relation between the submm H_2O emission and the star-forming activity (Yang et al. 2013). A similar conclusion has been extended to the high-redshift by the study of a group of lensed SMGs (O13 and Y16). The submm H_2O lines are dominated by FIR pumping, which is closely related to the warm dust ($T_d \sim 40$–90 K, see e.g. González-Alfonso et al. 2014). One may compare the gas content traced by these submm H_2O lines with the CO lines we observed. The H_2O column density derived is around $\sim 0.3 \times 10^{15}$ cm^{-2} km^{-1} s to $\sim 2 \times 10^{16}$ cm^{-2} km^{-1} s (Y16), which is about several tens up to several thousand times smaller than the CO column density (from single component LVG modelling).

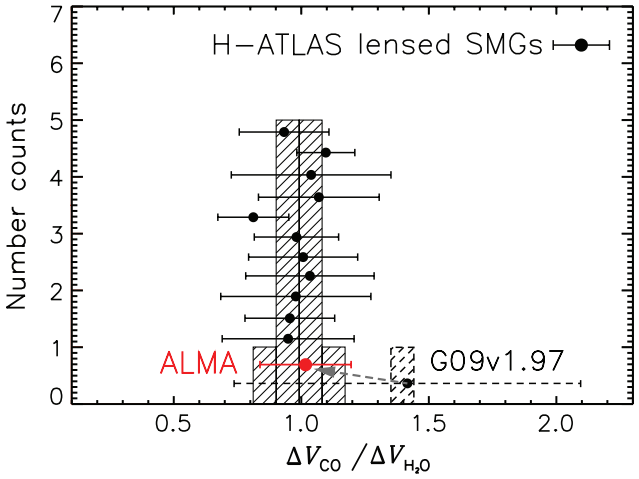

Fig. 13: Histogram showing the distribution of the ratio (indicated by black data points) between the linewidths of CO and H_2O. The H_2O linewidth are from Y16 and O13. It is clear that most of our sources have similar CO and H_2O linewidth, with an average ratio of 1.0 ± 0.1. For G09v1.97, the IRAM-30m spectrum shows that the asymmetric CO line is ~ 1.5 times larger than that of the H_2O line (Y16) as shown by the dashed error bar and histogram. However, using the ALMA high S/N CO and H_2O spectral data of G09v1.97 (Yang et al. in prep.), we find a ratio of the linewidth to be very close to 1 as indicated by the red point. The source of SDP 81 is not shown here because it is a special case as discussed in the text.

Comparing the linewidths between CO and H_2O is instructive. As shown in Fig. 13, most of the *H*-ATLAS sources have similar CO and H_2O linewidths. This suggests that they are possibly coming from similar regions as found in O13 and Y16. However, for SDP 81 and G09v1.97, the CO linewidth obtained using the IRAM-30m data is approximately two times larger than that of the H_2O lines. As shown in O13, the blue component of the CO line of SDP 81 is much weaker compared with the red component, and this component is not even detected by ALMA long baseline observations (ALMA Partnership, Vlahakis et al. 2015). Thus, here the linewidth ratio only accounts for the H_2O linewidth of the red component, which results in the CO linewidth being about twice larger than that of the H_2O line in SDP 81. However, if the S/N of the spectral data is improved, one will detect the weakly magnified velocity component as described in Section 4.3. From the ALMA data of CO(6–5) and $J = 2$ H_2O lines of G09v1.97 (Yang et al., in prep.), we find asymmetrical CO and H_2O line profiles that are very similar, showing a dominant red velocity component with an approximately six times weaker blue velocity component (see Fig. A.1 for the ALMA CO(6–5) spectrum). The linewidth ratio, acquired by the high S/N ALMA data, is found very close to 1 as indicated by the red data point in Fig. 13. The case of G09v1.97 clearly shows that the low/mid-S/N spectral data may suffer from the bias caused by differential lensing effect as mentioned in Section 4.3. Besides the line profiles between H_2O and CO, Oteo et al. (2017) find similar line profiles for H_2O and mid-J CO and HCN lines in a $z \sim 1.6$ lensed SMG, SDP 9.

The similarity of the line profile strongly suggests that the emitting regions are co-spatially located. Both the gas tracers are closely linked to the on-going star formation activities. However, further detailed studies combining the gas excitation, dust emission, and the far-infrared pumping of the H_2O lines is needed to fully incorporate the complex physical processes in these SMGs.

6. Summary

In this work, we report a survey of multiple J_{up} (mostly from $J_{up} = 3$ up to $J_{up} = 8$) CO lines in a sample of *Herschel*-selected lensed SMGs at $z \sim 2$–4. We have detected 47 CO lines and 7 [C I] lines in these SMGs using the IRAM-30m telescope.

Comparing the CO linewidth with those of the SPT lensed SMGs and an unlensed sample, we find evidence of a significant bias introduced by differential lensing that distorts the line profile, resulting in underestimation of the linewidth (usually by a factor of 2). This induces underestimation of the dynamical mass if one uses the observed linewidth measured for the lensed SMGs blindly. Differential lensing also slightly affects flux estimates of the lowest-J CO lines. This is mostly due to the difference in spatial distribution, since the lowest-J lines, especially CO(1–0), are usually several times more extended than the mid-J to high-J CO lines. By comparing the CO(1–0) to CO(3–2) flux ratio of the SMGs for our lensed SMGs and the ones of the unlensed SMGs, we find that the differential lensing could cause a $\sim 1.3 \pm 0.4$ times overestimation of the magnification of the CO(1–0).

We also calculate the dynamical mass of the *H*-ATLAS SMGs; if one did not correct for differential lensing effects, this would lie in the range of 0.1–7×10^{11} $M_\odot$, with a large uncertainty due to the unknown extension and sky inclination (if assuming a rotating-disk scenario) of the CO emission. But for the sources with a narrow linewidth, due to the aforementioned differential lensing effect, their dynamical masses might be underestimated. Nevertheless, for the sources with broad linewidth, the ratio between gas mass and dynamical mass equals about 0.34 ± 0.10, that is, a gas fraction of $\sim 34\%$, which is close to the values of other SMGs and empirical model predictions.

The multiple-transition CO line data allow us to study the molecular gas excitation of the SMGs. The CO SLEDs are mostly peaking around $J_{up} = 5$–7, thus dominated by the warm dense gas. Using LVG modelling by fitting the SLEDs with a single excitation component via a Bayesian approach, we derive a gas density $n_{H_2} \approx 10^{2.5}$–$10^{4.1}$ cm^{-3}, gas temperature $T_k \approx 20$–750 K and CO column density per unit velocity gradient $N_{CO}/dv \approx 10^{16.4}$–$10^{17.8}$ cm^{-2} km^{-1} s. But we notice that the $J_{up} \leq 3$ CO lines are likely under-predicted by the single-component LVG model. This indicates the existence of a low-excitation component. We have thus performed a two-component LVG modelling and derived the gas density, temperature, and the CO column density per unit velocity gradient for

each component. The low-excitation component has a cooler gas temperature of about 20–30 K with a gas density of about $10^{2.8}$–$10^{4.6}$ cm^{-3}, while for the high-excitation component, the gas temperature is higher, ∼ 60–400 K, with a gas density of about $10^{2.7}$–$10^{4.2}$ cm^{-3}. We find a correlation between the gas thermal pressure $P_{\rm th}$ derived from single component LVG modelling and the star formation efficiency. The warm high-excitation component also follows a similar trend while the cool low-excitation component is much less correlated with the on-going star formation. This shows that the high-excitation warm dense gas is more closely related to the star formation than the cool gas in the SMGs. This agrees with previous studies of a large sample of local galaxies.

We also study the global properties of the molecular gas and their relation with star formation. By assuming a conversion from CO luminosity to gas mass, $\alpha_{\rm CO} = 0.8\,M_\odot\,({\rm K\,km\,s^{-1}\,pc^2})^{-1}$, we derive gas to dust mass ratios in the approximate range from 30 to 100. The gas depletion time $t_{\rm dep}$ of the *H*-ATLAS SMGs shows no difference compared with other lensed/unlensed SMGs; the value is also close to that of the local ULIRG. Furthermore, no cosmic evolution trend is found for $t_{\rm dep}$. However, in order to avoid the uncertainties from the assumptions of the values of $\alpha_{\rm CO}$ (and $\delta_{\rm GDR}$), we study the quantity $L'_{\rm CO(1-0)}/M_{\rm dust}$ which is proportional to the ratio $\delta_{\rm GDR}/\alpha_{\rm CO}$. We find for the SMGs, this ratio is increasing with increasing redshift, which could be caused by a selection bias.

With the detections of seven [C I](2–1) lines in our *H*-ATLAS lensed SMGs, we extend the correlation between the luminosity of the CO(1–0) line and the [C I](2–1) line found in a sample of local (U)LIRGs. All of them can be well fitted with a single linear correlation, indicating that the [C I] lines can be good indicators of the total molecular gas mass, both for nearby (U)LIRGs and the high-redshift SMGs. However, [C I](1–0) data are needed to properly derive the gas mass from the [C I] lines.

Finally, we compare the linewidths of the CO and H_2O emission lines for a sample of 13 SMGs, using multi-*J* CO emission lines. We find that the linewidths of the CO lines and H_2O lines agree very well in most cases. This supports our previous argument that the emitting regions of the CO and H_2O lines are likely to be co-spatially located.

This work reports for the first time, a systematic study of the CO gas excitation in a sample of high-redshift lensed SMGs. However, deriving accurate values for the physical properties of the molecular gas is challenging. To model the CO excitation with two excitation components, eight free parameters are needed. A rather complete sample of the CO SLED is thus required to better constrain the models. Also, for strongly lensed systems, due to differential lensing, the line profile can be easily distorted (e.g. the case of SDP 81 Dye et al. 2015), namely the magnification factor at different velocity components of the emission line can be rather different. One could overcome this disadvantage by increasing the S/N of the spectrum using a telescope with better sensitivities such as ALMA and future NOEMA.

Acknowledgements. We would like to thank the anonymous referee for constructive comments. The authors are grateful to the IRAM staff for their support. CY thanks Claudia Marka and Nicolas Billot for their help of the IRAM-30m/EMIR observation. The authors also thank Yinhe Zhao for kindly sharing the local [C I] line data. CY and YG acknowledge support by National Key R&D Program of China (2017YFA0402700) and the CAS Key Research Program of Frontier Sciences. CY, AO and YG acknowledge support by NSFC grants 11311130491 and 11420101002. CY, AO, AB and YG acknowledge support from the Sino-French LIA-Origins joint exchange program. CY is supported by the China Scholarship Council grant (CSC No.201404910443). E.G-A is a Research Associate at the Harvard-Smithsonian Center for Astrophysics, and thanks the Spanish Ministerio de Economía y Competitividad for support under projects FIS2012-39162-C06-01 and ESP2015-65597-C4-1-R, and NASA grant ADAP NNX15AE56G. ZYZ, RJI and IO acknowledges support from ERC in the form of the Advanced Investigator Programme, 321302, COSMICISM. H.D. acknowledges financial support from the Spanish Ministry of Economy and Competitiveness (MINECO) under the 2014 Ramón y Cajal program MINECO RYC-2014-15686. MJM acknowledges the support of the National Science Centre, Poland through the POLONEZ grant 2015/19/P/ST9/04010. This project has received funding from the European Union's Horizon 2020 research and innovation programme under the Marie Skłodowska-Curie grant agreement No. 665778. IRS acknowledges support from STFC (ST/P000541/1), the ERC Advanced Grant DustyGal (321334) and a Royal Society/Wolfson Merit Award. US participants in *H*-ATLAS acknowledge support from NASA through a contract from JPL. Italian participants in *H*-ATLAS acknowledge a financial contribution from the agreement ASI-INAF I/009/10/0. SPIRE has been developed by a consortium of institutes led by Cardiff Univ. (UK) and including: Univ. Lethbridge (Canada); NAOC (China); CEA, LAM (France); IFSI, Univ. Padua (Italy); IAC (Spain); Stockholm Observatory (Sweden); Imperial College London, RAL, UCL-MSSL, UKATC, Univ. Sussex (UK); and Caltech, JPL, NHSC, Univ. Colorado (USA). This development has been supported by national funding agencies: CSA (Canada); NAOC (China); CEA, CNES, CNRS (France); ASI (Italy); MCINN (Spain); SNSB (Sweden); STFC, UKSA (UK); and NASA (USA). Extensive use was made of the NASA IDL (Interactive Data Language) Astronomy User's Library (https://idlastro.gsfc.nasa.gov) and the Coyote Graphics Library.

References

Alaghband-Zadeh, S., Chapman, S. C., Swinbank, A. M., et al. 2013, MNRAS, 435, 1493
ALMA Partnership, Vlahakis, C., Hunter, T. R., Hodge, J. A., et al. 2015, ApJ, 808, L4
Ao, Y., Weiß, A., Downes, D., et al. 2008, A&A, 491, 747
Aravena, M., Decarli, R., Walter, F., et al. 2016a, ApJ, 833, 68
Aravena, M., Spilker, J. S., Bethermin, M., et al. 2016b, MNRAS, 457, 4406
Asboth, V., Conley, A., Sayers, J., et al. 2016, MNRAS, 462, 1989
Barger, A. J., Cowie, L. L., Chen, C.-C., et al. 2014, ApJ, 784, 9
Barger, A. J., Cowie, L. L., Sanders, D. B., et al. 1998, Nature, 394, 248
Becker, R. H., White, R. L., & Helfand, D. J. 1995, ApJ, 450, 559
Béthermin, M., Daddi, E., Magdis, G., et al. 2015, A&A, 573, A113
Bezanson, J., Karpinski, S., Shah, V. B., & Edelman, A. 2012, ArXiv e-prints [arXiv:1209.5145]
Bisbas, T. G., Papadopoulos, P. P., & Viti, S. 2015, ApJ, 803, 37
Blain, A. W., Smail, I., Ivison, R. J., Kneib, J.-P., & Frayer, D. T. 2002, Phys. Rep., 369, 111
Bolatto, A. D., Wolfire, M., & Leroy, A. K. 2013, ARA&A, 51, 207
Bothwell, M. S., Aguirre, J. E., Aravena, M., et al. 2017, MNRAS, 466, 2825
Bothwell, M. S., Smail, I., Chapman, S. C., et al. 2013, MNRAS, 429, 3047 (Bo13)
Bouché, N., Cresci, G., Davies, R., et al. 2007, ApJ, 671, 303
Bradford, C. M., Aguirre, J. E., Aikin, R., et al. 2009, ApJ, 705, 112
Bussmann, R. S., Pérez-Fournon, I., Amber, S., et al. 2013, ApJ, 779, 25 (Bu13)
Carilli, C. L. & Walter, F. 2013, ARA&A, 51, 105
Carter, M., Lazareff, B., Maier, D., et al. 2012, A&A, 538, A89
Casey, C. M., Narayanan, D., & Cooray, A. 2014, Phys. Rep., 541, 45
Chapman, S. C., Blain, A. W., Smail, I., & Ivison, R. J. 2005, ApJ, 622, 772
Combes, F., García-Burillo, S., Braine, J., et al. 2013, A&A, 550, A41
Combes, F., Rex, M., Rawle, T. D., et al. 2012, A&A, 538, L4
Cooray, A., Calanog, J., Wardlow, J. L., et al. 2014, ApJ, 790, 40
Cox, P., Krips, M., Neri, R., et al. 2011, ApJ, 740, 63
da Cunha, E., Groves, B., Walter, F., et al. 2013, ApJ, 766, 13
Daddi, E., Dannerbauer, H., Liu, D., et al. 2015, A&A, 577, A46
Daddi, E., Elbaz, D., Walter, F., et al. 2010, ApJ, 714, L118
Dale, D. A., Helou, G., Contursi, A., Silbermann, N. A., & Kolhatkar, S. 2001, ApJ, 549, 215
Danielson, A. L. R., Swinbank, A. M., Smail, I., et al. 2013, MNRAS, 436, 2793
Danielson, A. L. R., Swinbank, A. M., Smail, I., et al. 2011, MNRAS, 410, 1687
Danielson, A. L. R., Swinbank, A. M., Smail, I., et al. 2017, ApJ, 840, 78
Dannerbauer, H., Lehnert, M. D., Emonts, B. H. C., et al. 2017, ArXiv e-prints [arXiv:1701.05250]
Davé, R., Finlator, K., & Oppenheimer, B. D. 2012, MNRAS, 421, 98
Deane, R. P., Heywood, I., Rawlings, S., & Marshall, P. J. 2013, MNRAS, 434, 23
Downes, D. & Solomon, P. M. 1998, ApJ, 507, 615
Draine, B. T. 2003, ARA&A, 41, 241

Draine, B. T. 2011, Physics of the Interstellar and Intergalactic Medium (Princeton University Press)
Dunlop, J. S., McLure, R. J., Biggs, A. D., et al. 2017, MNRAS, 466, 861
Dye, S., Furlanetto, C., Swinbank, A. M., et al. 2015, MNRAS, 452, 2258
Eales, S., Dunne, L., Clements, D., et al. 2010, PASP, 122, 499
Elmegreen, B. G. & Efremov, Y. N. 1997, ApJ, 480, 235
Emonts, B. H. C., Lehnert, M. D., Villar-Martín, M., et al. 2016, Science, 354, 1128
Engel, H., Tacconi, L. J., Davies, R. I., et al. 2010, ApJ, 724, 233
Fixsen, D. J., Bennett, C. L., & Mather, J. C. 1999, ApJ, 526, 207
Foreman-Mackey, D. 2016, The Journal of Open Source Software, 1
Foreman-Mackey, D., Hogg, D. W., Lang, D., & Goodman, J. 2013, PASP, 125, 306
Frayer, D. T., Harris, A. I., Baker, A. J., et al. 2011, ApJ, 726, L22
Fu, H., Jullo, E., Cooray, A., et al. 2012, ApJ, 753, 134
Gao, Y., Carilli, C. L., Solomon, P. M., & Vanden Bout, P. A. 2007, ApJ, 660, L93
Gao, Y., Lo, K. Y., Lee, S.-W., & Lee, T.-H. 2001, ApJ, 548, 172
Genzel, R., Tacconi, L. J., Combes, F., et al. 2012, ApJ, 746, 69
Genzel, R., Tacconi, L. J., Gracia-Carpio, J., et al. 2010, MNRAS, 407, 2091
George, R. D., Ivison, R. J., Hopwood, R., et al. 2013, MNRAS, 436, L99
Giordano, M. 2016, ArXiv e-prints [arXiv:1610.08716]
Glover, S. C. O., Clark, P. C., Micic, M., & Molina, F. 2015, MNRAS, 448, 1607
Goldreich, P. & Kwan, J. 1974, ApJ, 189, 441
Goldsmith, P. F. 2001, ApJ, 557, 736
González-Alfonso, E., Fischer, J., Aalto, S., & Falstad, N. 2014, A&A, 567, A91 (G14)
Goodman, J. & Weare, J. 2010, Communications in applied mathematics and computational science, 5, 65
Goto, T. & Toft, S. 2015, A&A, 579, A17
Greve, T. R., Ivison, R. J., & Papadopoulos, P. P. 2003, ApJ, 599, 839
Greve, T. R., Leonidaki, I., Xilouris, E. M., et al. 2014, ApJ, 794, 142
Harris, A. I., Baker, A. J., Frayer, D. T., et al. 2012, ApJ, 752, 152
Hezaveh, Y. D., Marrone, D. P., Fassnacht, C. D., et al. 2013, ApJ, 767, 132
Hezaveh, Y. D., Marrone, D. P., & Holder, G. P. 2012, ApJ, 761, 20
Hodge, J. A., Carilli, C. L., Walter, F., et al. 2012, ApJ, 760, 11
Holland, W. S., Robson, E. I., Gear, W. K., et al. 1999, MNRAS, 303, 659
Hughes, D. H., Serjeant, S., Dunlop, J., et al. 1998, Nature, 394, 241
Ikeda, M., Oka, T., Tatematsu, K., Sekimoto, Y., & Yamamoto, S. 2002, ApJS, 139, 467
Ivison, R. J., Papadopoulos, P. P., Smail, I., et al. 2011, MNRAS, 412, 1913
Ivison, R. J., Smail, I., Papadopoulos, P. P., et al. 2010, MNRAS, 404, 198
Jiao, Q., Zhao, Y., Zhu, M., et al. 2017, ApJ, 840, L18
Kamenetzky, J., Glenn, J., Maloney, P. R., et al. 2011, ApJ, 731, 83
Kamenetzky, J., Rangwala, N., Glenn, J., Maloney, P. R., & Conley, A. 2016, ApJ, 829, 93
Karim, A., Swinbank, A. M., Hodge, J. A., et al. 2013, MNRAS, 432, 2
Kennicutt, R. C. & Evans, N. J. 2012, ARA&A, 50, 531
Kennicutt, Jr., R. C. 1998a, ARA&A, 36, 189
Kennicutt, Jr., R. C. 1998b, ApJ, 498, 541
Koprowski, M. P., Dunlop, J. S., Michałowski, M. J., Cirasuolo, M., & Bowler, R. A. A. 2014, MNRAS, 444, 117
Krips, M., Martín, S., Eckart, A., et al. 2011, ApJ, 736, 37
Le Floc'h, E., Papovich, C., Dole, H., et al. 2005, ApJ, 632, 169
Leroy, A. K., Bolatto, A., Gordon, K., et al. 2011, ApJ, 737, 12
Lestrade, J.-F., Combes, F., Salomé, P., et al. 2010, A&A, 522, L4
Liu, D., Gao, Y., Isaak, K., et al. 2015, ApJ, 810, L14
Lu, N., Zhao, Y., Díaz-Santos, T., et al. 2017, ApJS, 230, 1
Lu, N., Zhao, Y., Xu, C. K., et al. 2015, ApJ, 802, L11
Lupu, R. E., Scott, K. S., Aguirre, J. E., et al. 2012, ApJ, 757, 135
Madau, P. & Dickinson, M. 2014, ARA&A, 52, 415
Magdis, G. E., Daddi, E., Béthermin, M., et al. 2012, ApJ, 760, 6
Magdis, G. E., Daddi, E., Elbaz, D., et al. 2011, ApJ, 740, L15
Magnelli, B., Popesso, P., Berta, S., et al. 2013, A&A, 553, A132
Markwardt, C. B. 2009, in Astronomical Society of the Pacific Conference Series, Vol. 411, Astronomical Data Analysis Software and Systems XVIII, ed. D. A. Bohlender, D. Durand, & P. Dowler, 251
Meijerink, R., Kristensen, L. E., Weiß, A., et al. 2013, ApJ, 762, L16
Messias, H., Dye, S., Nagar, N., et al. 2014, A&A, 568, A92
Michałowski, M. J., Dunlop, J. S., Koprowski, M. P., et al. 2017, MNRAS, 469, 492
Murphy, E. J., Chary, R.-R., Dickinson, M., et al. 2011, ApJ, 732, 126
Narayanan, D., Krumholz, M. R., Ostriker, E. C., & Hernquist, L. 2012, MNRAS, 421, 3127
Nayyeri, H., Keele, M., Cooray, A., et al. 2016, ApJ, 823, 17
Negrello, M., Amber, S., Amvrosiadis, A., et al. 2017, MNRAS, 465, 3558
Negrello, M., Hopwood, R., De Zotti, G., et al. 2010, Science, 330, 800
Negrello, M., Perrotta, F., González-Nuevo, J., et al. 2007, MNRAS, 377, 1557
Oliver, S. J., Bock, J., Altieri, B., et al. 2012, MNRAS, 424, 1614
Omont, A., Neri, R., Cox, P., et al. 2011, A&A, 530, L3
Omont, A., Yang, C., Cox, P., et al. 2013, A&A, 551, A115 (O13)
Oteo, I., Zhang, Z., Yang, C., et al. 2017, ArXiv e-prints [arXiv:1701.05901]
Oteo, I., Zwaan, M. A., Ivison, R. J., Smail, I., & Biggs, A. D. 2016, ApJ, 822, 36
Papadopoulos, P. P. & Greve, T. R. 2004, ApJ, 615, L29
Papadopoulos, P. P. & Seaquist, E. R. 1999, ApJ, 516, 114
Papadopoulos, P. P., Zhang, Z.-Y., Xilouris, E. M., et al. 2014, ApJ, 788, 153
Planck Collaboration, Ade, P. A. R., Aghanim, N., et al. 2016, A&A, 594, A13
Rangwala, N., Maloney, P. R., Glenn, J., et al. 2011, ApJ, 743, 94
Riechers, D. A., Bradford, C. M., Clements, D. L., et al. 2013, Nature, 496, 329
Riechers, D. A., Carilli, L. C., Walter, F., et al. 2011a, ApJ, 733, L11
Riechers, D. A., Cooray, A., Omont, A., et al. 2011b, ApJ, 733, L12
Riechers, D. A., Hodge, J., Walter, F., Carilli, C. L., & Bertoldi, F. 2011c, ApJ, 739, L31
Riechers, D. A., Weiß, A., Walter, F., & Wagg, J. 2010, ApJ, 725, 1032
Rosenberg, M. J. F., van der Werf, P. P., Aalto, S., et al. 2015, ApJ, 801, 72
Rybak, M., McKean, J. P., Vegetti, S., Andreani, P., & White, S. D. M. 2015a, MNRAS, 451, L40
Rybak, M., Vegetti, S., McKean, J. P., Andreani, P., & White, S. D. M. 2015b, MNRAS, 453, L26
Saintonge, A., Kauffmann, G., Wang, J., et al. 2011, MNRAS, 415, 61
Saintonge, A., Lutz, D., Genzel, R., et al. 2013, ApJ, 778, 2
Salomé, P., Guélin, M., Downes, D., et al. 2012, A&A, 545, A57
Salpeter, E. E. 1955, ApJ, 121, 161
Santini, P., Maiolino, R., Magnelli, B., et al. 2010, A&A, 518, L154
Sargent, M. T., Daddi, E., Béthermin, M., et al. 2014, ApJ, 793, 19
Schöier, F. L., van der Tak, F. F. S., van Dishoeck, E. F., & Black, J. H. 2005, A&A, 432, 369
Scott, K. S., Lupu, R. E., Aguirre, J. E., et al. 2011, ApJ, 733, 29
Scoville, N., Aussel, H., Sheth, K., et al. 2014, ApJ, 783, 84
Scoville, N., Lee, N., Vanden Bout, P., et al. 2017, ApJ, 837, 150
Scoville, N. Z. & Solomon, P. M. 1974, ApJ, 187, L67
Serjeant, S. 2012, MNRAS, 424, 2429
Silverman, B. W. 1986, Density estimation for statistics and data analysis (Chapman and Hall)
Simpson, J. M., Swinbank, A. M., Smail, I., et al. 2014, ApJ, 788, 125
Smail, I., Ivison, R. J., & Blain, A. W. 1997, ApJ, 490, L5
Sobolev, V. V. 1960, Moving envelopes of stars
Solomon, P. M., Downes, D., & Radford, S. J. E. 1992, ApJ, 387, L55
Solomon, P. M., Downes, D., Radford, S. J. E., & Barrett, J. W. 1997, ApJ, 478, 144
Solomon, P. M. & Vanden Bout, P. A. 2005, ARA&A, 43, 677
Spilker, J. S., Aravena, M., Marrone, D. P., et al. 2015, ApJ, 811, 124
Spilker, J. S., Marrone, D. P., Aguirre, J. E., et al. 2014, ApJ, 785, 149
Spilker, J. S., Marrone, D. P., Aravena, M., et al. 2016, ApJ, 826, 112
Spinoglio, L., Pereira-Santaella, M., Busquet, G., et al. 2012, ApJ, 758, 108
Swinbank, A. M., Dye, S., Nightingale, J. W., et al. 2015, ApJ, 806, L17
Swinbank, A. M., Simpson, J. M., Smail, I., et al. 2014, MNRAS, 438, 1267
Swinbank, A. M., Smail, I., Longmore, S., et al. 2010, Nature, 464, 733
Tacconi, L. J., Genzel, R., Neri, R., et al. 2010, Nature, 463, 781
Tacconi, L. J., Genzel, R., Smail, I., et al. 2008, ApJ, 680, 246
Tacconi, L. J., Neri, R., Chapman, S. C., et al. 2006, ApJ, 640, 228
Tacconi, L. J., Neri, R., Genzel, R., et al. 2013, ApJ, 768, 74
Tan, Q., Daddi, E., Magdis, G., et al. 2014, A&A, 569, A98
Tielens, A. G. G. M. 2005, The Physics and Chemistry of the Interstellar Medium (Cambridge University Press)
Troncoso, P., Maiolino, R., Sommariva, V., et al. 2014, A&A, 563, A58
Tunnard, R. & Greve, T. R. 2016, ApJ, 819, 161
Valiante, E., Smith, M. W. L., Eales, S., et al. 2016, MNRAS, 462, 3146
van der Tak, F. F. S., Black, J. H., Schöier, F. L., Jansen, D. J., & van Dishoeck, E. F. 2007, A&A, 468, 627
van der Werf, P. P., Isaak, K. G., Meijerink, R., et al. 2010, A&A, 518, L42
van Dishoeck, E. F., Herbst, E., & Neufeld, D. A. 2013, Chemical Reviews, 113, 9043
Venemans, B. P., Walter, F., Zschaechner, L., et al. 2016, ApJ, 816, 37
Vieira, J. D., Crawford, T. M., Switzer, E. R., et al. 2010, ApJ, 719, 763
Vieira, J. D., Marrone, D. P., Chapman, S. C., et al. 2013, Nature, 495, 344
Wall, J. V. & Jenkins, C. R. 2012, Practical Statistics for Astronomers (Cambridge University Press)
Walter, F., Decarli, R., Carilli, C., et al. 2012, Nature, 486, 233
Walter, F., Weiß, A., Downes, D., Decarli, R., & Henkel, C. 2011, ApJ, 730, 18
Wang, R., Wagg, J., Carilli, C. L., et al. 2013, ApJ, 773, 44
Wardlow, J. L., Cooray, A., De Bernardis, F., et al. 2013, ApJ, 762, 59
Weiß, A., De Breuck, C., Marrone, D. P., et al. 2013, ApJ, 767, 88
Weiß, A., Downes, D., Neri, R., et al. 2007, A&A, 467, 955
Weiß, A., Henkel, C., Downes, D., & Walter, F. 2003, A&A, 409, L41
Wilson, C. D. 1995, ApJ, 448, L97

Wilson, D., Cooray, A., Nayyeri, H., et al. 2017, ArXiv e-prints [arXiv:1705.00734]
Wong, T. & Blitz, L. 2002, ApJ, 569, 157
Yang, B., Stancil, P. C., Balakrishnan, N., & Forrey, R. C. 2010, ApJ, 718, 1062
Yang, C., Gao, Y., Omont, A., et al. 2013, ApJ, 771, L24 (Y13)
Yang, C., Omont, A., Beelen, A., et al. 2016, A&A, 595, A80
Zhang, Z.-Y., Henkel, C., Gao, Y., et al. 2014, A&A, 568, A122
Zhang, Z.-Y., Papadopoulos, P. P., Ivison, R. J., et al. 2016, Royal Society Open Science, 3, 160025
Zhu, M., Gao, Y., Seaquist, E. R., & Dunne, L. 2007, AJ, 134, 118
Zhu, M., Seaquist, E. R., & Kuno, N. 2003, ApJ, 588, 243

[1] Purple Mountain Observatory/Key Lab of Radio Astronomy, Chinese Academy of Sciences, Nanjing 210008, PR China
e-mail: yangcht@pmo.ac.cn
[2] Institut d'Astrophysique Spatiale, CNRS, Univ. Paris-Sud, Université Paris-Saclay, Bât. 121, 91405 Orsay cedex, France
[3] Graduate University of the Chinese Academy of Sciences, 19A Yuquan Road, Shijingshan District, 10049, Beijing, PR China
[4] CNRS, UMR 7095, Institut d'Astrophysique de Paris, F-75014, Paris, France
[5] UPMC Univ. Paris 06, UMR 7095, Institut d'Astrophysique de Paris, F-75014, Paris, France
[6] Leiden Observatory, Leiden University, P.O. Box 9513, NL-2300 RA Leiden, The Netherlands
[7] Institute for Astronomy, University of Edinburgh, Royal Observatory, Blackford Hill, Edinburgh, EH9 3HJ, UK
[8] European Southern Observatory, Karl Schwarzschild Straße 2, 85748, Garching, Germany
[9] Max Planck Institute for Astronomy, Konigstuhl 17, D-69117 Heidel- berg, Germany
[10] Universidad de Alcalá, Departamento de Física y Matemáticas, Campus Universitario, 28871 Alcalá de Henares, Madrid, Spain
[11] Instituto de Astrofísica de Canarias (IAC), E-38205 La Laguna, Tenerife, Spain
[12] Universidad de La Laguna, Dpto. Astrofísica, E-38206 La Laguna, Tenerife, Spain
[13] Joint ALMA Observatory, Alonso de Córdova 3107, Vitacura, Santiago, Chile
[14] Institut de Radioastronomie Millimétrique (IRAM), 300 rue de la Piscine, 38406 Saint-Martin-d'Hères, France
[15] Astronomy Department, Cornell University, 220 Space Sciences Building, Ithaca, NY 14853, USA
[16] Department of Physics and Astronomy, Rutgers, The State University of New Jersey, 136 Frelinghuysen Road, Piscataway, NJ 08854-8019, USA
[17] Astronomical Observatory Institute, Faculty of Physics, Adam Mickiewicz University, ul. Słoneczna 36, 60-286 Poznań, Poland
[18] Department of Physics and Astronomy, University of California, Irvine, Irvine, CA 92697, USA
[19] Centre for Extragalactic Astronomy, Durham University, Department of Physics, South Road, Durham DH1 3LE, UK

Appendix A: Spectral data.

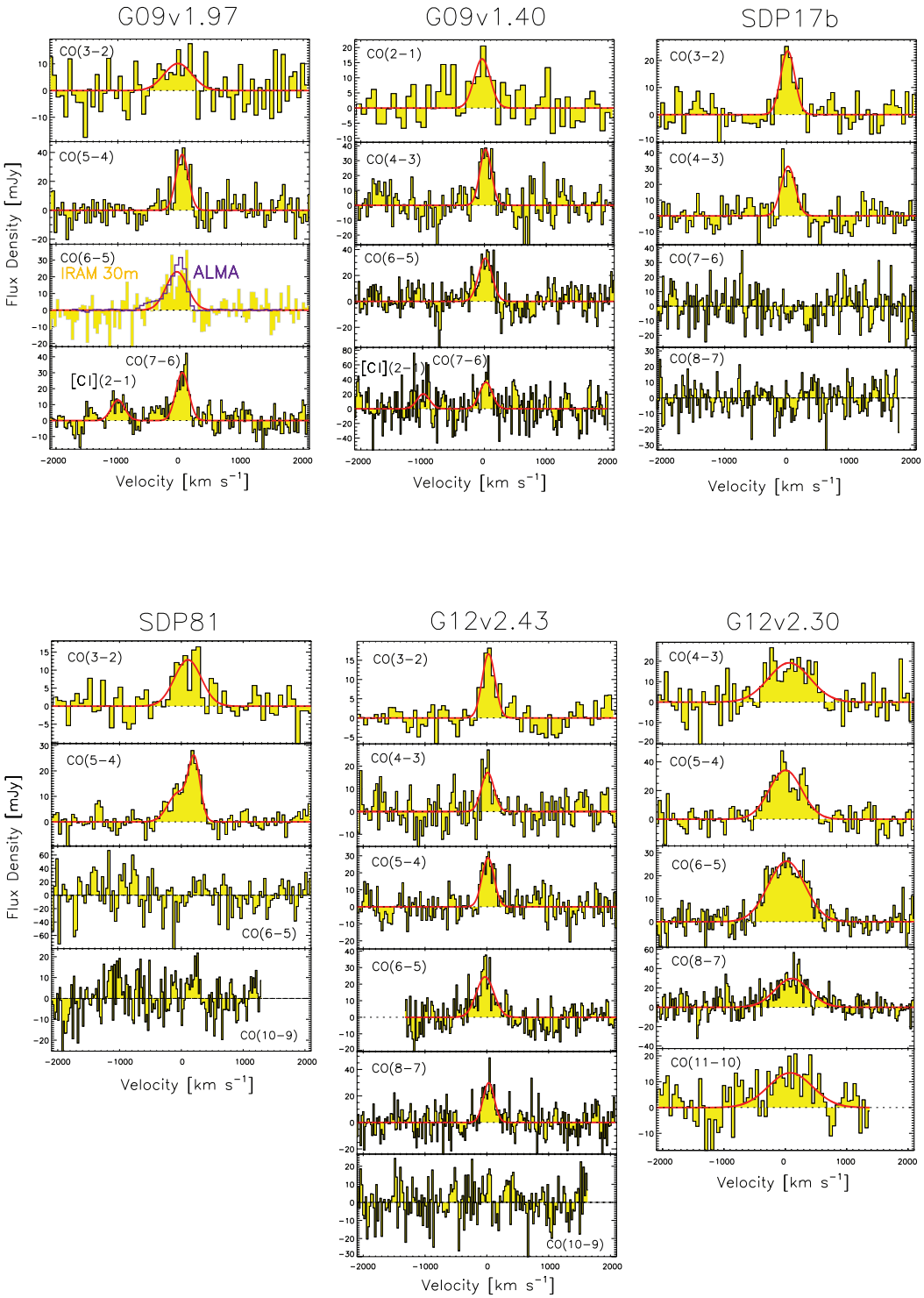

Fig. A.1: Spatially integrated spectra of CO lines in the *H*-ATLAS sources. The red lines represent the Gaussian fitting to the emission lines. The detections are $\gtrsim 3\,\sigma$. Zero velocity is set to the CO line sky frequency according to the previously measured spectroscopy redshifts $z_{\rm spec}$ given in Table 3. For CO(6–5) in G09v1.97, we also overlaid the ALMA spectral data (Yang et al., in prep.) in purple for comparison.

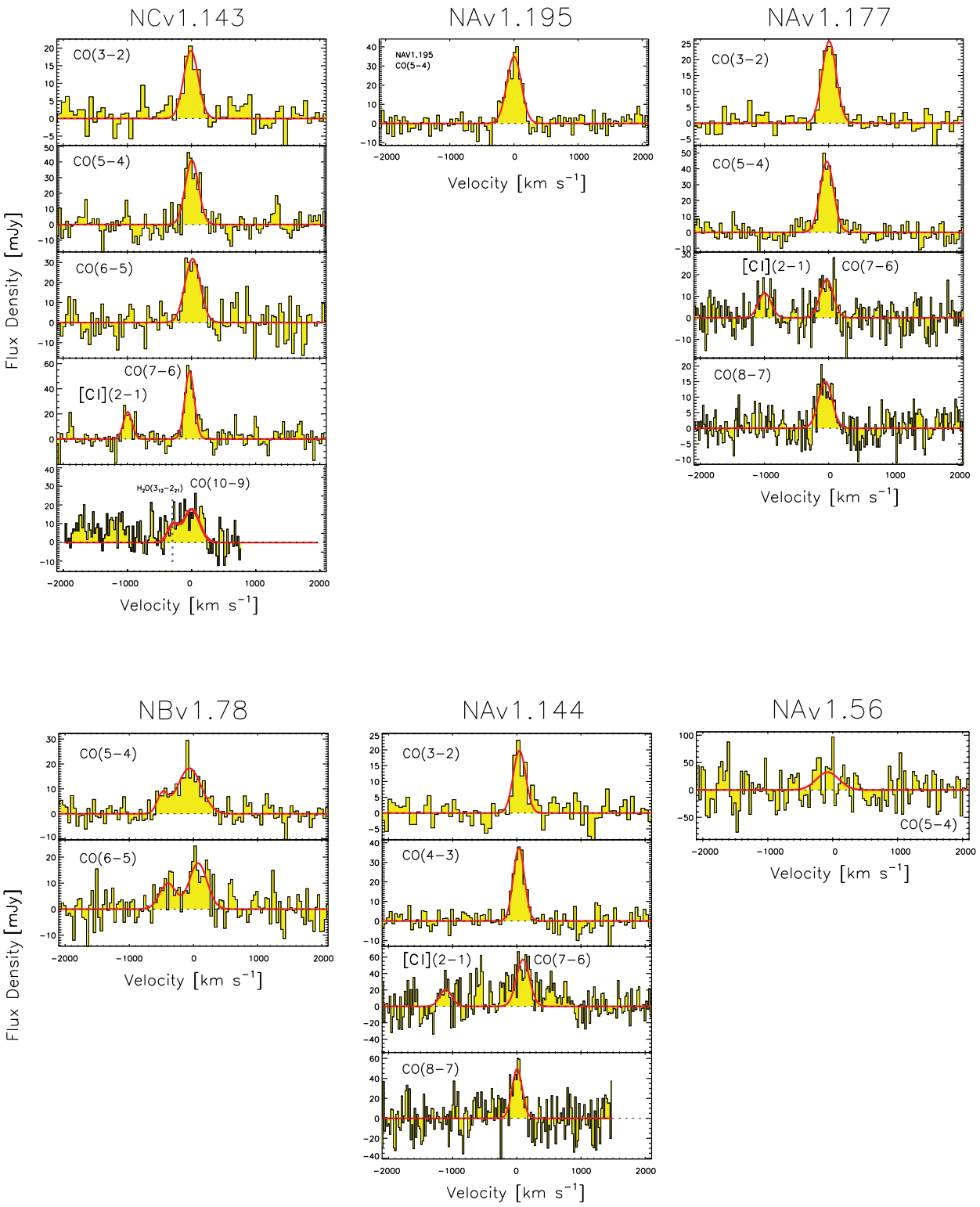

Fig. A.1. Continued.

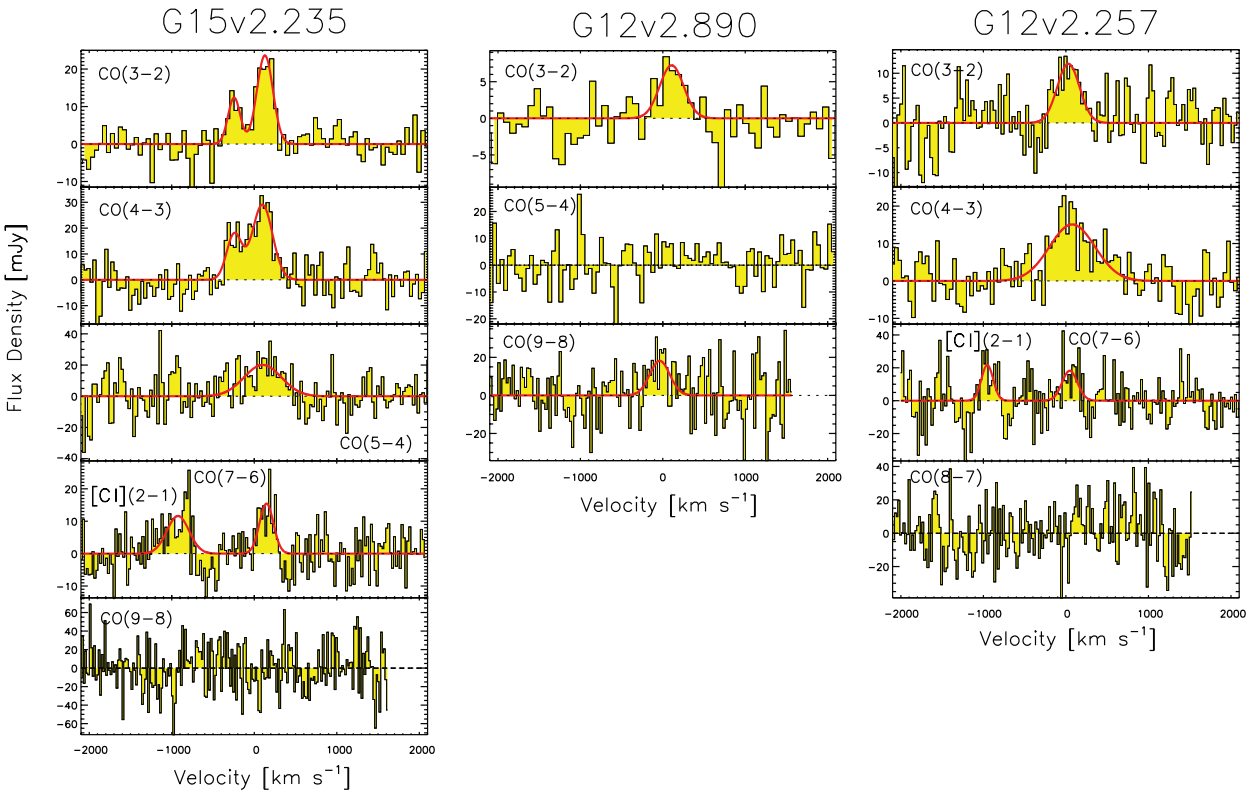

Fig. A.1. Continued.

Appendix B: Tables

Table B.1: The observed parameters of the CO and [C I] emission lines.

Source	Line	$\nu_{\rm sky}$ (GHz)	$t_{\rm on}$ (hour)	Band	$z_{\rm Line}$	$z_{\rm CO}$	$D_{\rm L}$ (Mpc)	ΔV (km s^{-1})	$I_{\rm Line}$ (Jy km s^{-1})	$\mu L_{\rm IR}$ (10^{13} $L_\odot$)	$L_{\rm IR}$ (10^{12} $L_\odot$)	$\mu L_{\rm Line}$ (10^8 $L_\odot$)	$\mu L'_{\rm Line}$ (10^{10} K km s^{-1} pc^2)	$L_{\rm Line}$ (10^7 $L_\odot$)	$L'_{\rm Line}$ (10^9 K km s^{-1} pc^2)
G09v1.97	CO(3–2)	74.621	0.9	E090	3.634 ± 0.002	3.6345 ± 0.0001	32751 ± 588	529 ± 241	5.7 ± 2.2	15.5 ± 4.3	22.5 ± 6.5	4.7 ± 1.9	35.9 ± 14.2	6.9 ± 2.8	52.0 ± 21.0
	CO(5–4)	124.356	1.4	E150	3.6346 ± 0.0002			237 ± 33	9.7 ± 1.2			13.5 ± 1.6	22.1 ± 2.7	19.6 ± 2.9	32.0 ± 4.8
	CO(6–5)	149.217	2.0	E150	3.6333 ± 0.0005			408 ± 79	10.0 ± 1.7			16.6 ± 2.8	15.7 ± 2.6	24.1 ± 4.5	22.8 ± 4.3
	CO(7–6)	174.072	1.6	E150	3.6340 ± 0.0005			249 ± 33	8.0 ± 0.9			15.5 ± 1.8	9.2 ± 1.1	22.4 ± 3.2	13.3 ± 1.9
	[C I](2–1)	174.653		E150	3.6347 ± 0.0002			261 ± 79	3.6 ± 0.9			6.9 ± 1.8	4.1 ± 1.1	10.0 ± 2.8	6.0 ± 1.7
G09v1.40	CO(2–1)	74.552	1.6	E090	2.0919 ± 0.0004	2.0924 ± 0.0001	16835 ± 283	309 ± 93	5.3 ± 1.4	6.6 ± 2.5	4.3 ± 1.9	1.2 ± 0.3	29.9 ± 7.8	0.8 ± 0.3	19.6 ± 6.8
	CO(4–3)	149.108	3.6	E150	2.0925 ± 0.0002			222 ± 35	8.8 ± 1.2			3.9 ± 0.5	12.4 ± 1.7	2.5 ± 0.7	8.1 ± 2.2
	CO(6–5)	223.611	1.2	E230	2.0924 ± 0.0001			259 ± 33	9.2 ± 1.0			6.0 ± 0.7	5.7 ± 0.6	3.9 ± 1.0	3.7 ± 0.9
	CO(7–6)	260.858	1.6	E230	2.0924 ± 0.0005			240	9.3 ± 1.7			7.2 ± 1.3	4.3 ± 0.8	4.7 ± 1.4	2.8 ± 0.8
	[C I](2–1)	261.729		E230	2.0926 ± 0.0003			240	5.2 ± 1.7			4.0 ± 1.3	2.4 ± 0.8	2.6 ± 1.1	1.6 ± 0.6
SDP17b	CO(3–2)	104.628	2.8	E090	2.3052 ± 0.0002	2.3053 ± 0.0001	18942 ± 322	269 ± 49	6.7 ± 1.1	7.1 ± 2.6	14.5 ± 5.7	2.6 ± 0.4	19.8 ± 3.1	5.4 ± 1.1	40.5 ± 8.6
	CO(4–3)	139.498	2.8	E150	2.3053 ± 0.0002			271 ± 42	9.0 ± 1.2			4.7 ± 0.6	15.0 ± 2.0	9.6 ± 1.9	30.6 ± 6.0
	CO(7–6)	244.070	1.8	E230	–			(300)	< 19.0			< 17.6	< 10.6	< 35.9	< 21.8
	[C I](2–1)	244.885	1.8	E230	–			(300)	< 19.0			< 17.6	< 10.6	< 35.9	< 21.8
	CO(8–7)	278.911	1.8	E330	–			(300)	< 15.7			< 16.3	< 6.5	< 33.3	< 13.1
SDP81	CO(3–2)	85.593	2.3	E090	3.0414 ± 0.0006	3.0413 ± 0.0005	26469 ± 466	513 ± 101	7.0 ± 1.2	5.9 ± 1.5	5.3 ± 1.5	4.4 ± 0.7	33.0 ± 5.6	3.9 ± 0.8	29.8 ± 5.9
	CO(5–4)	142.641	1.8	E150	3.0393 ± 0.0016			222 ± 49	5.4 ± 2.9			5.6 ± 3.0	9.2 ± 4.9	5.1 ± 2.7	8.3 ± 4.5
		142.641			3.0428 ± 0.0003			384 ± 199	4.6 ± 3.0			4.8 ± 3.1	7.8 ± 5.1	4.3 ± 2.9	7.1 ± 4.7
	CO(6–5)	171.157	2.3	E150	–			(500)	< 26.2			< 32.2	< 30.4	< 28.9	< 27.4
	CO(10-9)	285.145	1.8	E330	–			(500)	< 8.8			< 18.6	< 3.8	< 16.8	< 3.4
G12v2.43	CO(3–2)	83.789	1.8	E090	3.1274 ± 0.0002	3.1271 ± 0.0001	27367 ± 484	247 ± 35	4.4 ± 0.5	9.0 ± 0.2	–	2.9 ± 0.3	21.6 ± 2.6	–	–
	CO(4–3)	111.713	3.8	E090	3.1270 ± 0.0001			240	5.6 ± 1.2			4.8 ± 1.1	15.5 ± 3.2	–	–
	CO(5–4)	139.634	3.8	E150	3.1273 ± 0.0002			232 ± 34	7.1 ± 0.9			7.7 ± 1.0	12.6 ± 1.6	–	–
	CO(6–5)	167.549	1.6	E150	3.1266 ± 0.0003			334 ± 47	8.7 ± 1.1			11.4 ± 1.4	10.7 ± 1.3	–	–
	CO(8–7)	223.358	1.8	E230	3.1274 ± 0.0002			212 ± 33	6.7 ± 0.9			11.7 ± 1.6	4.7 ± 0.6	–	–
	CO(10-9)	279.134	1.6	E330	–			(300)	< 10.0			< 21.5	< 4.2	–	–
G12v2.30	CO(4–3)	108.251	1.4	E090	3.2599 ± 0.0009	3.2596 ± 0.0002	28761 ± 511	801 ± 151	16.4 ± 2.7	15.6 ± 4.1	16.4 ± 4.4	15.2 ± 2.5	48.6 ± 7.9	16.0 ± 2.8	51.1 ± 8.9
	CO(5–4)	135.306	1.4	E150	3.2591 ± 0.0004			621 ± 64	22.6 ± 2.0			26.3 ± 2.3	42.9 ± 3.8	27.4 ± 3.0	45.2 ± 4.9
	CO(6–5)	162.356	1.8	E150	3.2593 ± 0.0003			704 ± 43	19.8 ± 1.1			27.6 ± 1.5	26.1 ± 1.4	29.1 ± 2.4	27.5 ± 2.3
	CO(8–7)	216.436	1.8	E230	3.2606 ± 0.0004			655 ± 67	20.7 ± 1.8			38.6 ± 3.3	15.4 ± 1.4	40.6 ± 4.4	16.2 ± 1.8
	CO(11-10)	297.491	1.8	E330	3.260 ± 0.001			848 ± 199	12.1 ± 2.5			31.0 ± 6.0	4.8 ± 1.0	32.7 ± 6.9	5.0 ± 1.1
NCv1.143	CO(3–2)	75.749	2.1	E090	3.5649 ± 0.0002	3.5650 ± 0.0004	32007 ± 574	270 ± 36	5.5 ± 0.6	12.9 ± 4.0	11.4 ± 3.9	4.5 ± 0.5	33.7 ± 3.9	3.9 ± 0.7	29.9 ± 5.7
	CO(5–4)	126.236	1.2	E150	3.5651 ± 0.0002			243 ± 24	10.7 ± 0.9			14.3 ± 1.2	23.4 ± 2.0	12.7 ± 2.2	20.7 ± 3.6
	CO(6–5)	151.473	1.4	E150	3.5653 ± 0.0003			283 ± 41	9.6 ± 1.2			15.5 ± 1.9	14.6 ± 1.8	13.7 ± 2.7	13.0 ± 2.5
	CO(7–6)	176.704	5.7	E150	3.5654 ± 0.0005			250	11.5 ± 0.9			21.7 ± 1.7	12.9 ± 1.0	19.2 ± 3.3	11.4 ± 1.9
	[C I](2–1)	177.293		E150	3.5646 ± 0.0002			250	4.4 ± 0.9			8.2 ± 1.7	4.9 ± 1.0	7.3 ± 1.9	4.2 ± 1.1
	CO(10-9)	252.352	4.3	*NOEMA*	–			288 ± 65	5.4 ± 1.2			14.6 ± 2.9	3.0 ± 0.6	12.8 ± 5.1	2.6 ± 1.0
NAv1.195	CO(5–4)	145.854	4.0	E150	2.9510 ± 0.0001	2.9510 ± 0.0001	25528 ± 448	266 ± 19	9.9 ± 0.6	7.5 ± 2.0	18.3 ± 5.1	9.8 ± 0.6	16.0 ± 1.0	23.8 ± 2.3	38.9 ± 3.7
NAv1.177	CO(3–2)	91.529	1.4	E090	2.7781 ± 0.0001	2.7778 ± 0.0001	23736 ± 414	262 ± 26	7.2 ± 0.6	6.2 ± 0.2	–	3.9 ± 0.3	29.1 ± 2.5	–	–
	CO(5–4)	152.533	1.4	E150	2.7777 ± 0.0001			248 ± 19	11.8 ± 0.8			10.5 ± 0.7	17.2 ± 1.2	–	–
	CO(7–6)	213.513	2.9	E230	2.7780 ± 0.0004			244 ± 51	4.6 ± 0.8			5.8 ± 1.1	3.4 ± 0.6	–	–
	[C I](2–1)	214.225	2.9	E230	2.7776 ± 0.0003			233 ± 77	2.9 ± 0.8			3.6 ± 1.0	2.1 ± 0.6	–	–
	CO(8–7)	243.991	3.7	E230	2.7773 ± 0.0002			255 ± 34	4.1 ± 0.5			5.8 ± 0.7	2.3 ± 0.3	–	–
NBv1.78	CO(5–4)	140.170	2.5	E150	3.1102 ± 0.0003	3.1080 ± 0.0003	27167 ± 480	196 ± 89	1.6 ± 0.8	10.8 ± 3.9	8.4 ± 3.1	1.7 ± 0.8	2.8 ± 1.3	1.3 ± 0.6	2.1 ± 1.1
		140.170			3.1044 ± 0.0005			434 ± 63	8.4 ± 1.0			9.1 ± 1.1	14.8 ± 1.7	7.0 ± 1.1	11.4 ± 1.9
	CO(6–5)	168.193	5.4	E150	3.1055 ± 0.0007			328 ± 78	3.1 ± 1.2			7.9 ± 1.6	7.5 ± 1.4	6.1 ± 1.4	5.8 ± 1.3
		168.193			3.1120 ± 0.0004			297 ± 131	6.1 ± 1.2			4.0 ± 1.5	3.8 ± 1.4	3.1 ± 1.2	2.9 ± 1.2
NAv1.144	CO(3–2)	107.994	2.2	E090	2.2024 ± 0.0002	2.2023 ± 0.0001	17918 ± 303	230 ± 34	4.8 ± 0.6	6.0 ± 3.5	13.0 ± 8.3	1.7 ± 0.2	13.2 ± 1.7	4.0 ± 0.9	30.0 ± 6.7
	CO(4–3)	143.985	2.2	E150	2.2023 ± 0.0001			205 ± 19	8.1 ± 0.6			3.9 ± 0.3	12.5 ± 1.0	8.9 ± 1.8	28.4 ± 5.6
	CO(7–6)	251.921	1.3	E230	2.2008 ± 0.0005			205	14.6 ± 1.6			12.3 ± 1.4	7.3 ± 0.8	28.0 ± 6.0	16.7 ± 3.5

Table B.1: continued.

Source	Line	$\nu_{\rm sky}$ (GHz)	$t_{\rm on}$ (hour)	Band	$z_{\rm Line}$	$z_{\rm CO}$	$D_{\rm L}$ (Mpc)	ΔV ($\rm km\,s^{-1}$)	$I_{\rm Line}$ ($\rm Jy\,km\,s^{-1}$)	$\mu L_{\rm IR}$ ($10^{13}\,L_\odot$)	$L_{\rm IR}$ ($10^{12}\,L_\odot$)	$\mu L_{\rm Line}$ ($10^{8}\,L_\odot$)	$\mu L'_{\rm Line}$ ($10^{10}\,\rm K\,km\,s^{-1}\,pc^2$)	$L_{\rm Line}$ ($10^{7}\,L_\odot$)	$L'_{\rm Line}$ ($10^{9}\,\rm K\,km\,s^{-1}\,pc^2$)
	[C1](2–1)	252.762	1.3	E230	2.2030 ± 0.0002			205	4.8 ± 1.6			4.1 ± 1.4	2.4 ± 0.8	9.3 ± 3.5	5.5 ± 2.1
	CO(8–7)	287.882	3.8	E330	2.2020 ± 0.0002			205	11.8 ± 1.9			10.4 ± 1.7	4.1 ± 0.7	23.6 ± 5.8	9.4 ± 2.3
NAv1.56	CO(5–4)	174.574	3.7	E150	2.3001 ± 0.0009	2.3001 ± 0.0009	18890 ± 321	409 ± 201	14.1 ± 6.0	11.5 ± 3.1	9.8 ± 2.8	9.1 ± 3.9	14.9 ± 6.4	7.8 ± 3.4	12.7 ± 5.5
G15v2.235	CO(3–2)	99.418	1.9	E090	2.4797 ± 0.0001	2.4789 ± 0.0001	20686 ± 355	176 ± 47	2.3 ± 0.6	2.8 ± 0.7	15.6 ± 4.7	1.0 ± 0.2	7.7 ± 1.8	5.7 ± 1.6	42.9 ± 12.2
		99.418			2.4754 ± 0.0002			229 ± 28	5.8 ± 0.6			2.5 ± 0.3	19.3 ± 2.0	14.2 ± 2.8	107.0 ± 21.1
	CO(4–3)	132.552	1.3	E150	2.4793 ± 0.0003			216 ± 73	4.0 ± 1.3			2.4 ± 0.8	7.6 ± 2.4	13.2 ± 4.8	42.2 ± 15.3
		132.552			2.4754 ± 0.0004			289 ± 55	8.9 ± 1.4			5.3 ± 0.8	16.8 ± 2.7	29.3 ± 6.8	93.3 ± 21.6
	CO(5–4)	165.680	0.7	E150	2.4794 ± 0.0006			531 ± 131	11.3 ± 2.4			8.4 ± 1.8	13.7 ± 2.9	46.5 ± 12.6	75.9 ± 20.6
	CO(7–6)	231.916	1.8	E230	2.4791 ± 0.0004			201 ± 45	3.3 ± 0.6			3.4 ± 0.7	2.0 ± 0.4	18.9 ± 4.9	11.2 ± 2.9
	[C1](2–1)	232.690	1.8	E230	2.4799 ± 0.0002			316 ± 76	3.9 ± 0.8			4.1 ± 0.8	2.4 ± 0.5	22.5 ± 6.0	13.4 ± 3.6
	CO(9–8)	298.118	1.6	E330	–			(300)	< 24.1			< 32.0	< 9.0	< 177.9	< 50.0
G12v2.890	CO(3–2)	96.653	1.7	E090	2.5790 ± 0.0005	2.5783 ± 0.0003	21694 ± 375	344 ± 92	2.7 ± 0.6	2.5 ± 0.3	–	1.3 ± 0.3	9.5 ± 2.2	–	–
	CO(5–4)	161.072	1.7	E150	–			(300)	< 7.4			< 5.7	< 9.6	–	–
	CO(9–8)	289.827	1.8	E330	2.5773 ± 0.0006			286 ± 109	5.5 ± 1.8			7.8 ± 2.6	2.2 ± 0.7	–	–
G12v2.257	CO(3–2)	108.369	1.4	E090	2.1912 ± 0.0004	2.1914 ± 0.0001	17810 ± 301	318 ± 82	4.0 ± 0.9	2.6 ± 0.3	–	1.4 ± 0.3	10.9 ± 2.4	–	–
	CO(4–3)	144.486	2.5	E150	2.1917 ± 0.0005			648 ± 106	10.4 ± 1.5			5.0 ± 0.7	15.8 ± 2.2	–	–
	CO(7–6)	252.798	1.2	E230	2.1914 ± 0.0003			220 ± 95	4.3 ± 1.6			3.6 ± 1.3	2.1 ± 0.8	–	–
	[C1](2–1)	253.641		E230	2.1914 ± 0.0004			168 ± 70	3.9 ± 1.4			3.2 ± 1.2	1.9 ± 0.7	–	–
	CO(8–7)	288.884	1.5	E330	–			(300)	< 15.4			< 14.6	< 5.8	–	–

Notes. $\nu_{\rm sky}$ is the observed frequency at zero velocity in each spectrum; $t_{\rm on}$ is the on source time spent during the observation; E090, E150, E230 and E330 EMIR bands were used, and the total time used during the observations is less than the sum of all the $t_{\rm on}$ because some of the lines were observed simultaneously utilising different EMIR receiver band combinations; $z_{\rm line}$ is the redshift derived according to the detected lines; ΔV is the linewidth; $z_{\rm CO}$ is the error-weighted average CO line redshift for each source; ΔV with no errors are fixed values used for more accurately inferring the integrated flux density of each line and the ΔV in brackets are the one used for inferring the upper limits for non-detections; $I_{\rm line}$ is the velocity-integrated flux density.

Appendix C: Bayesian approach of the radiative transfer modelling.

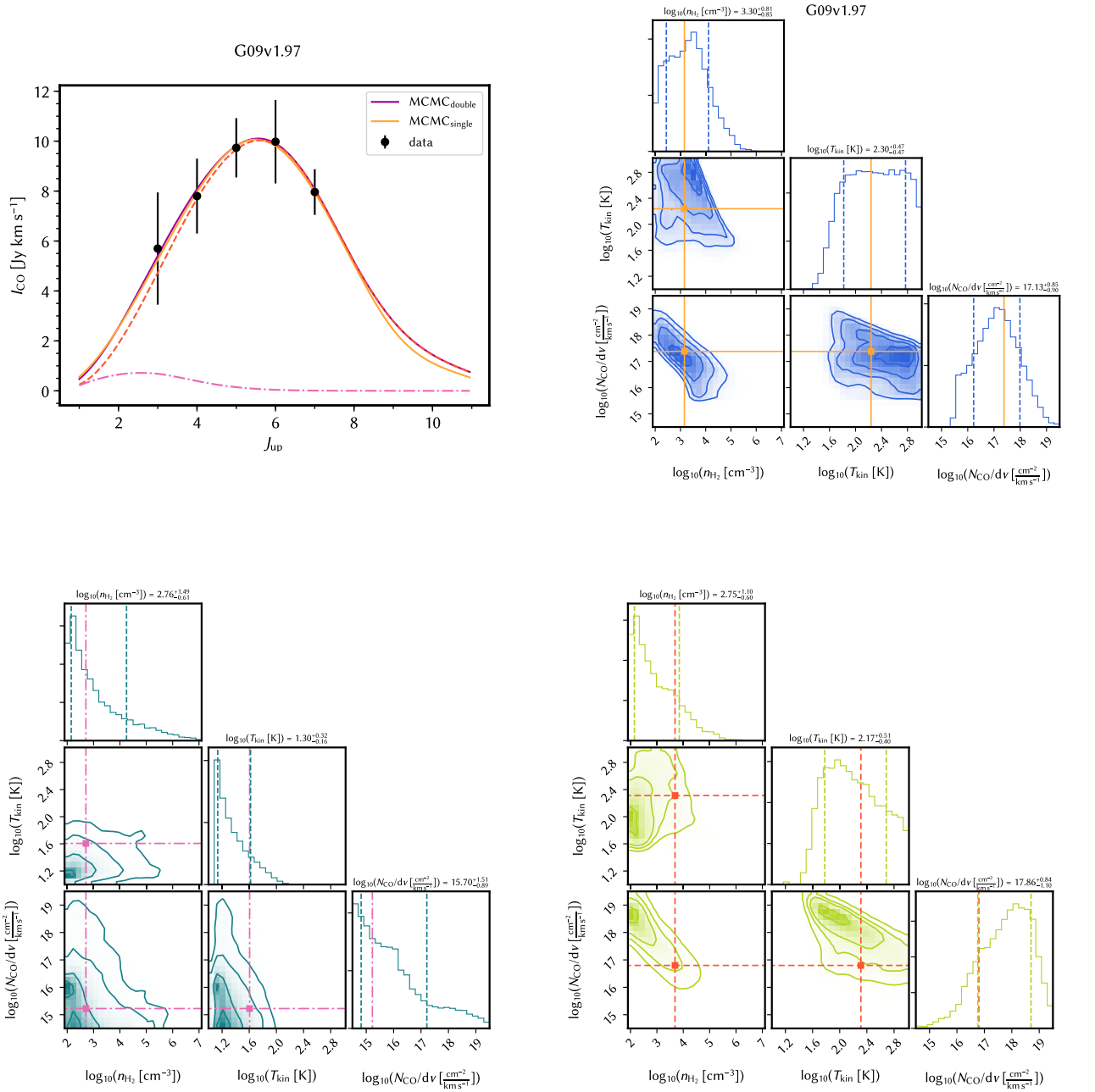

Fig. C.1: *Upper left panel*: The CO SLED (without correcting for lensing magnification) of each source is plotted in black. The flux of CO(1–0) has been corrected for differential lensing effect as discussed in the text. The solid orange curve shows the best fit from the single component model corresponding to the maximum posterior possibility, while the solid purple line shows the best fit of the two-component model. Dashed red line shows the warmer component and the dashed-dotted line shows the cooler component fit. The upper limits are shown in grey open circles with downward arrows. *Upper right panel*: The posterior probability distributions of molecular gas density n_{H_2}, gas temperature T_{kin} and CO column density per velocity N_{CO}/dv of the source, with the maximum posterior possibility point in the parameter space shown in orange lines and points. The contours are in steps of 0.5 σ starting from the centre. *Lower panels*: The posterior probability distributions for n_{H_2}, T_{kin} and N_{CO}/dv of the cooler (dark green) and warmer (light green) component of the two-component model.

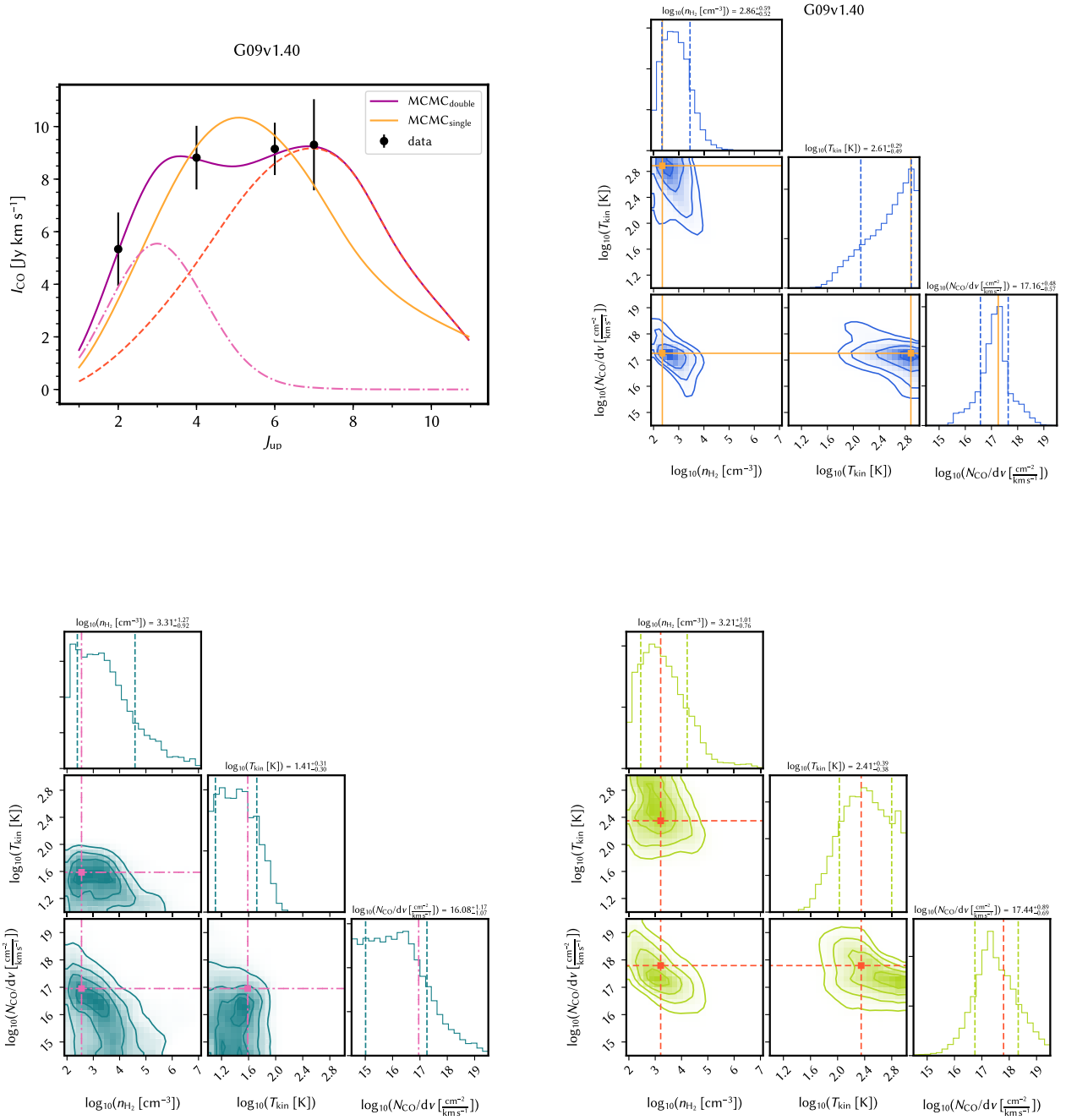

Fig. C.1. Continued.

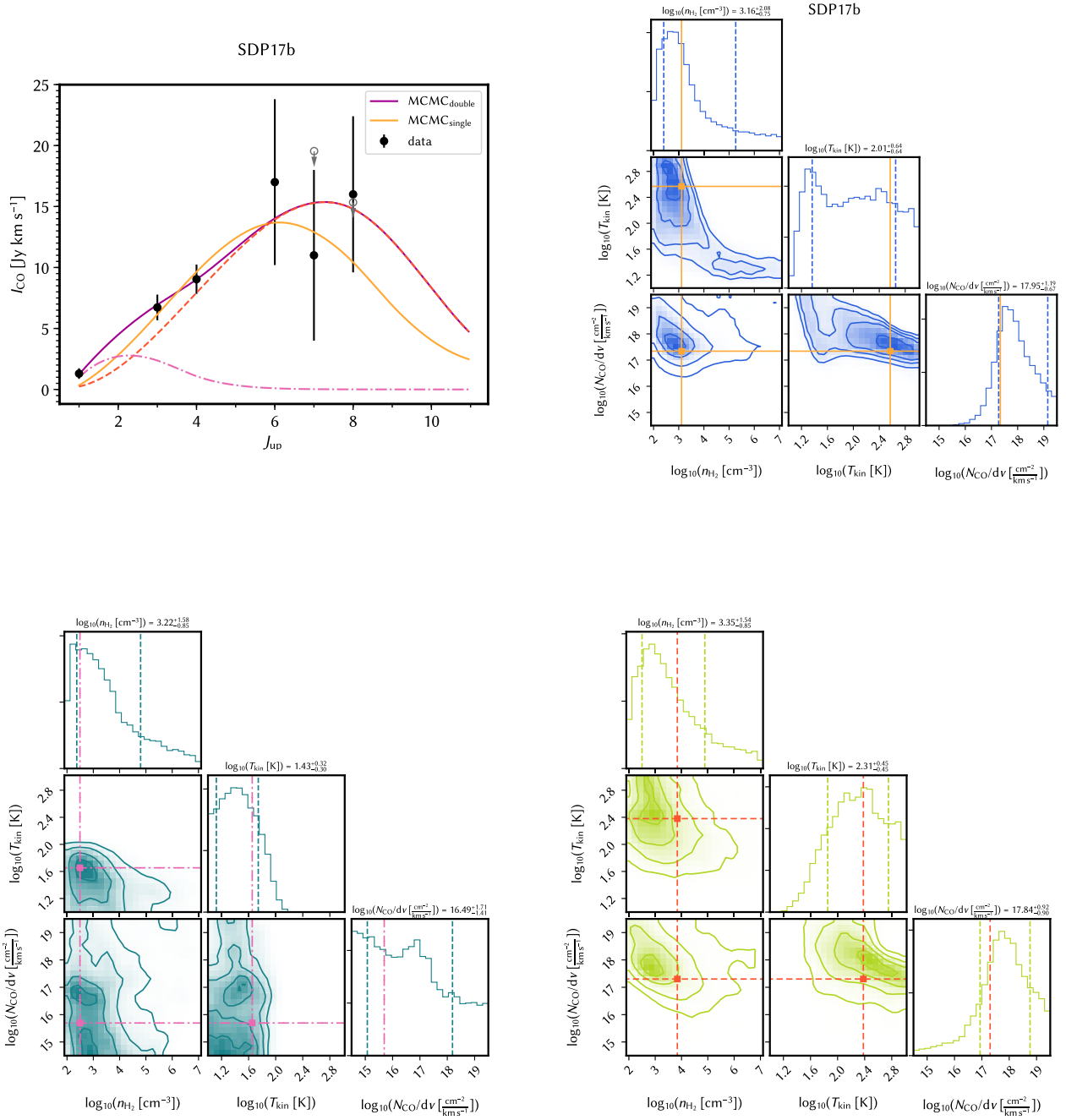

Fig. C.1. Continued.

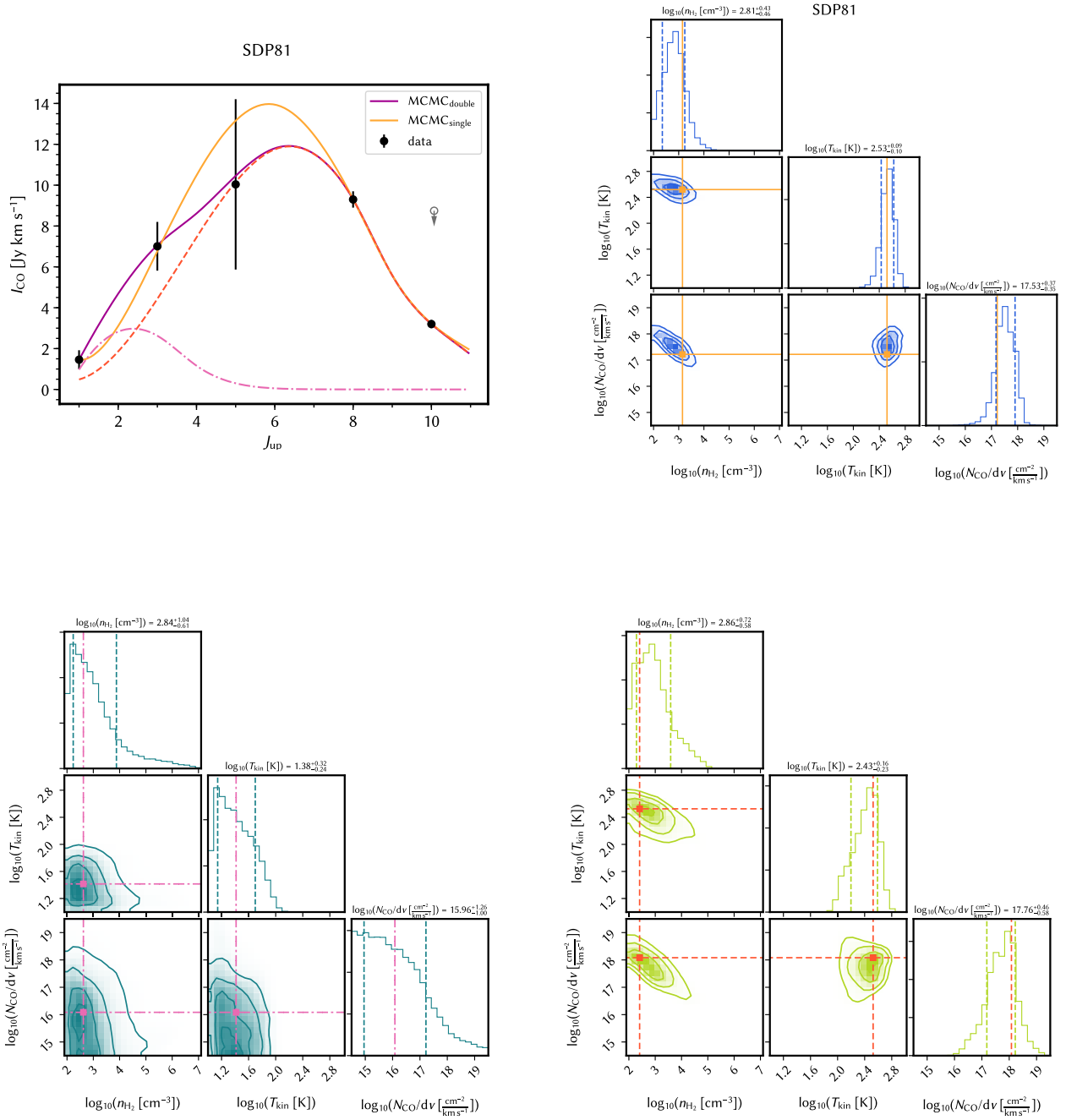

Fig. C.1. Continued.

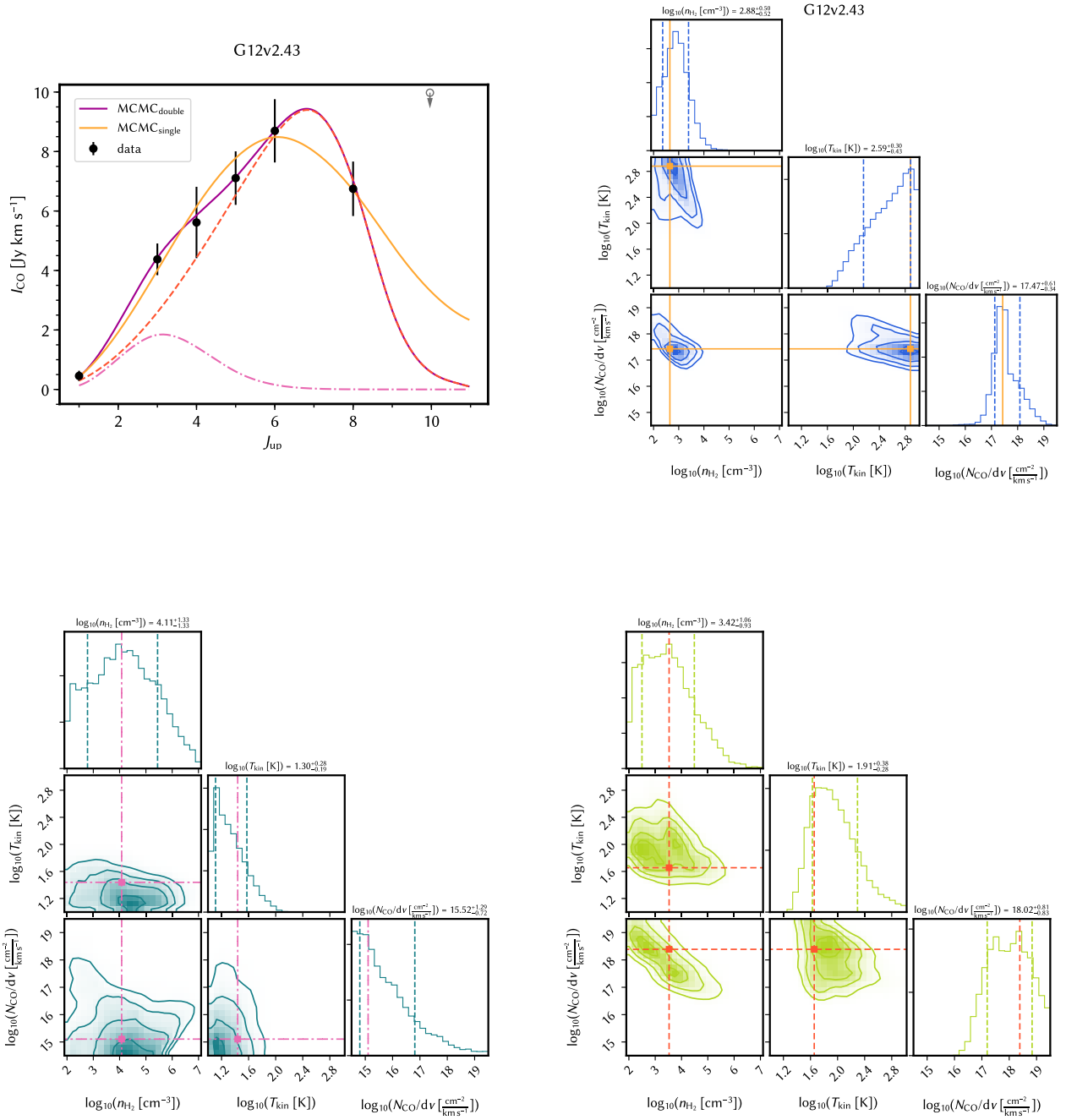

Fig. C.1. Continued.

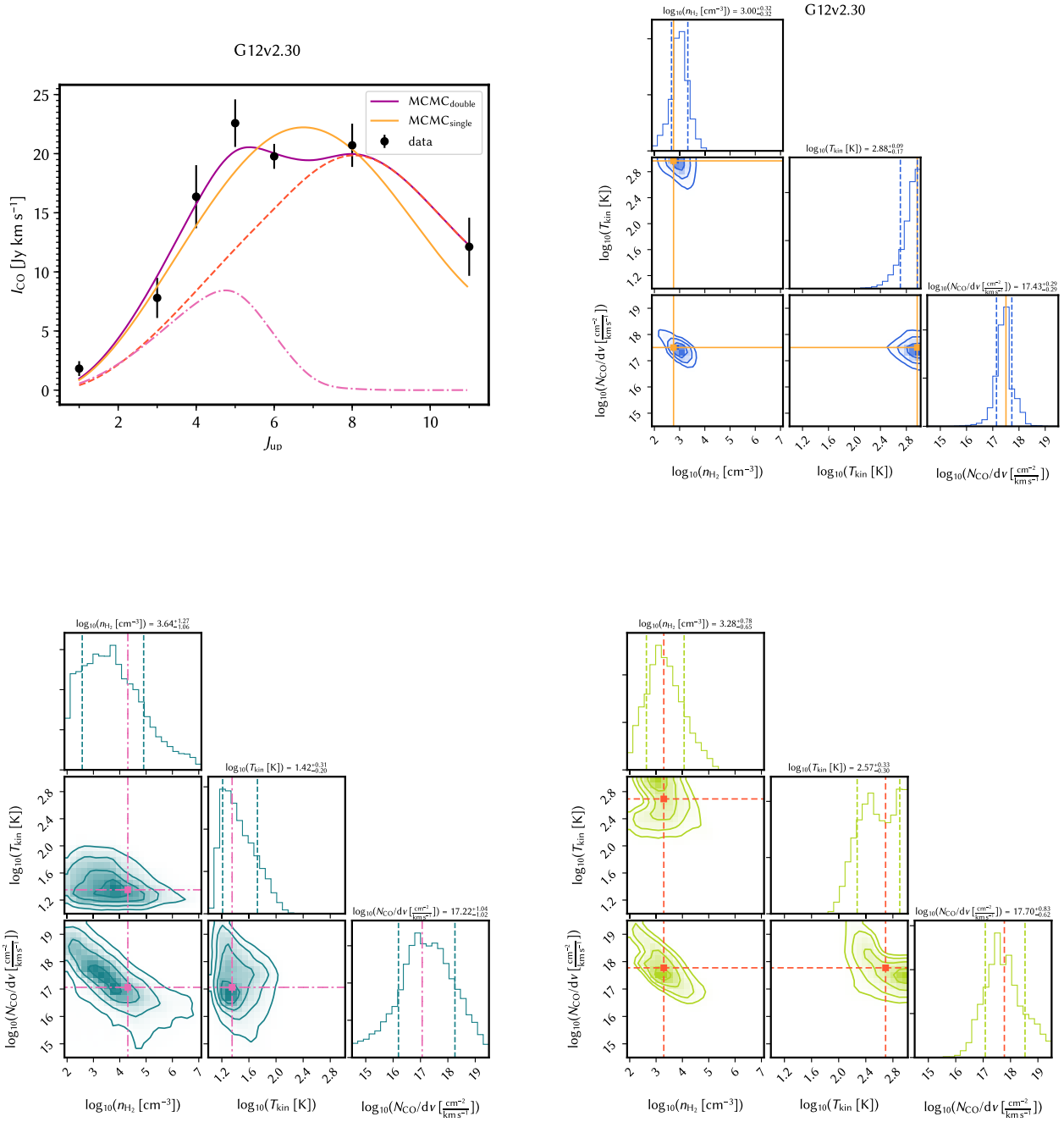

Fig. C.1. Continued.

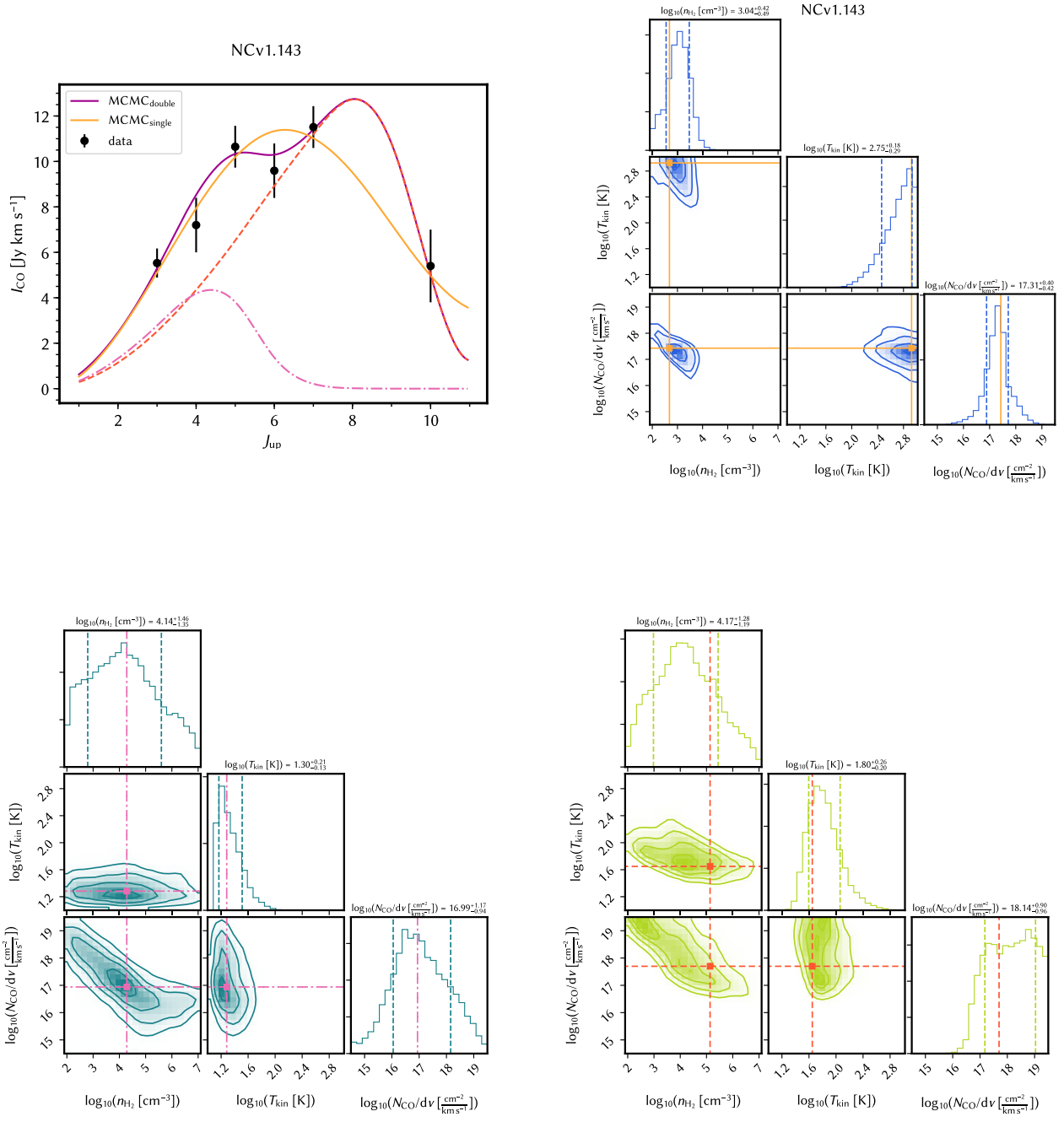

Fig. C.1. Continued.

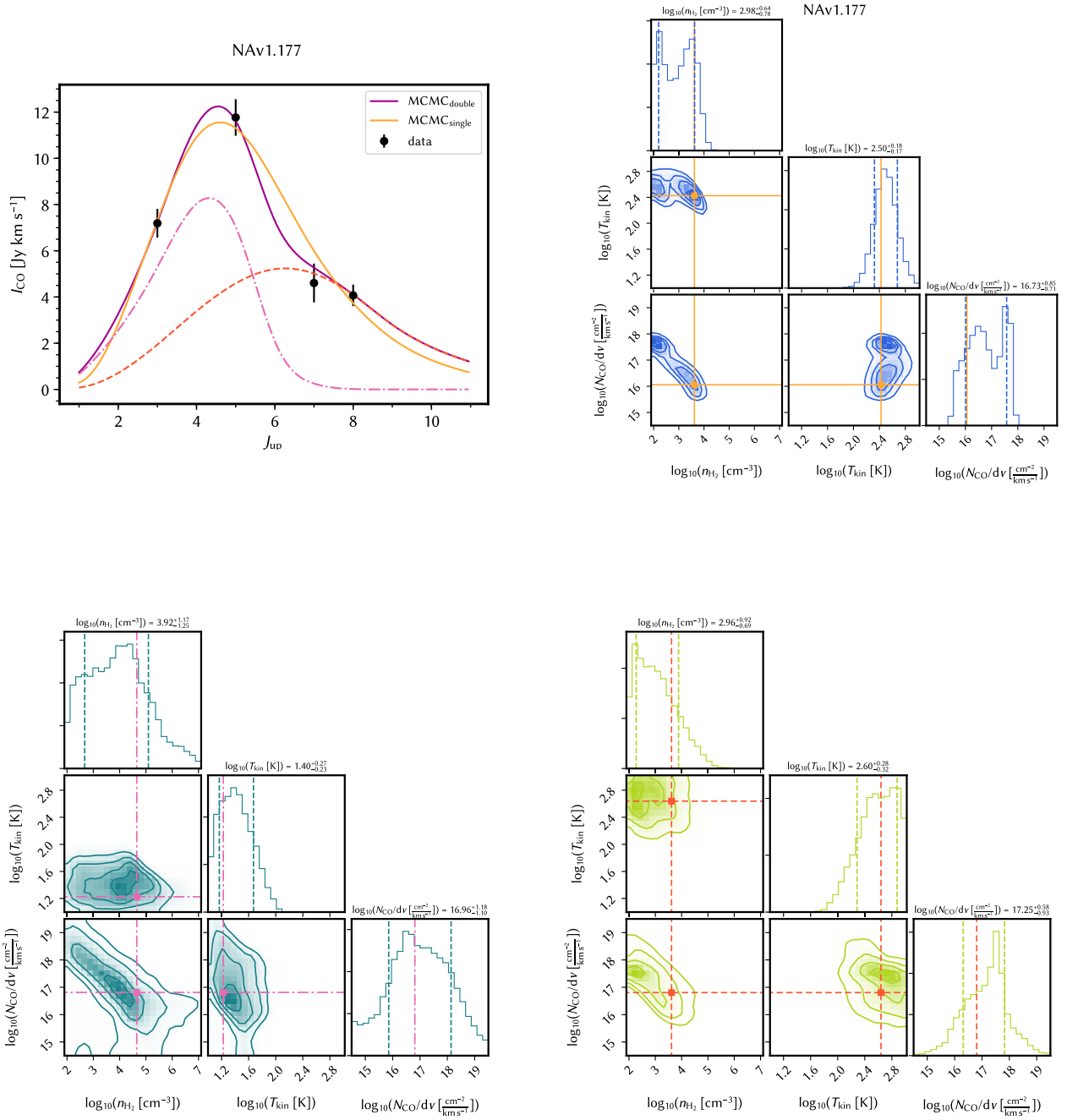

Fig. C.1. Continued.

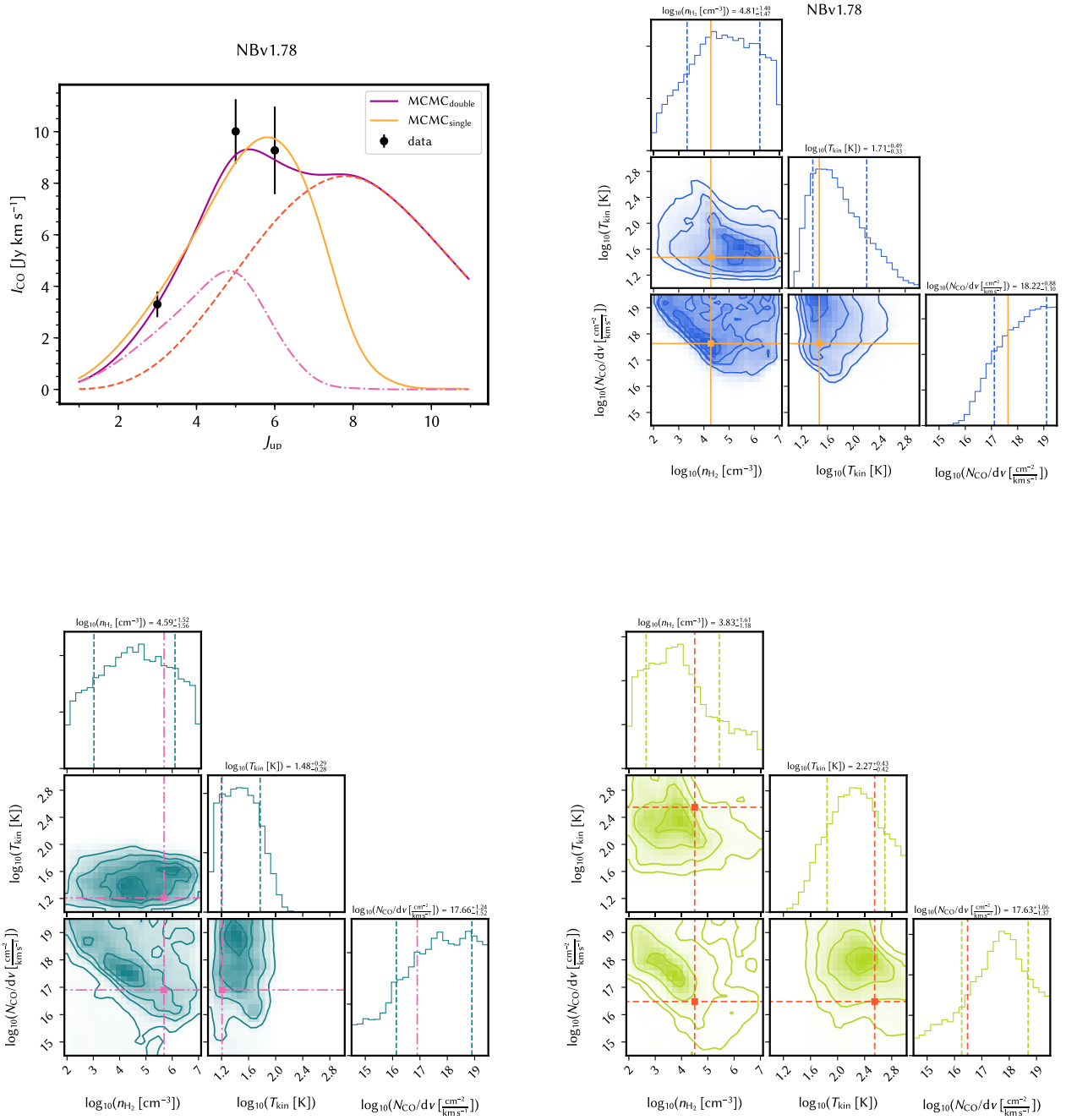

Fig. C.1. Continued.

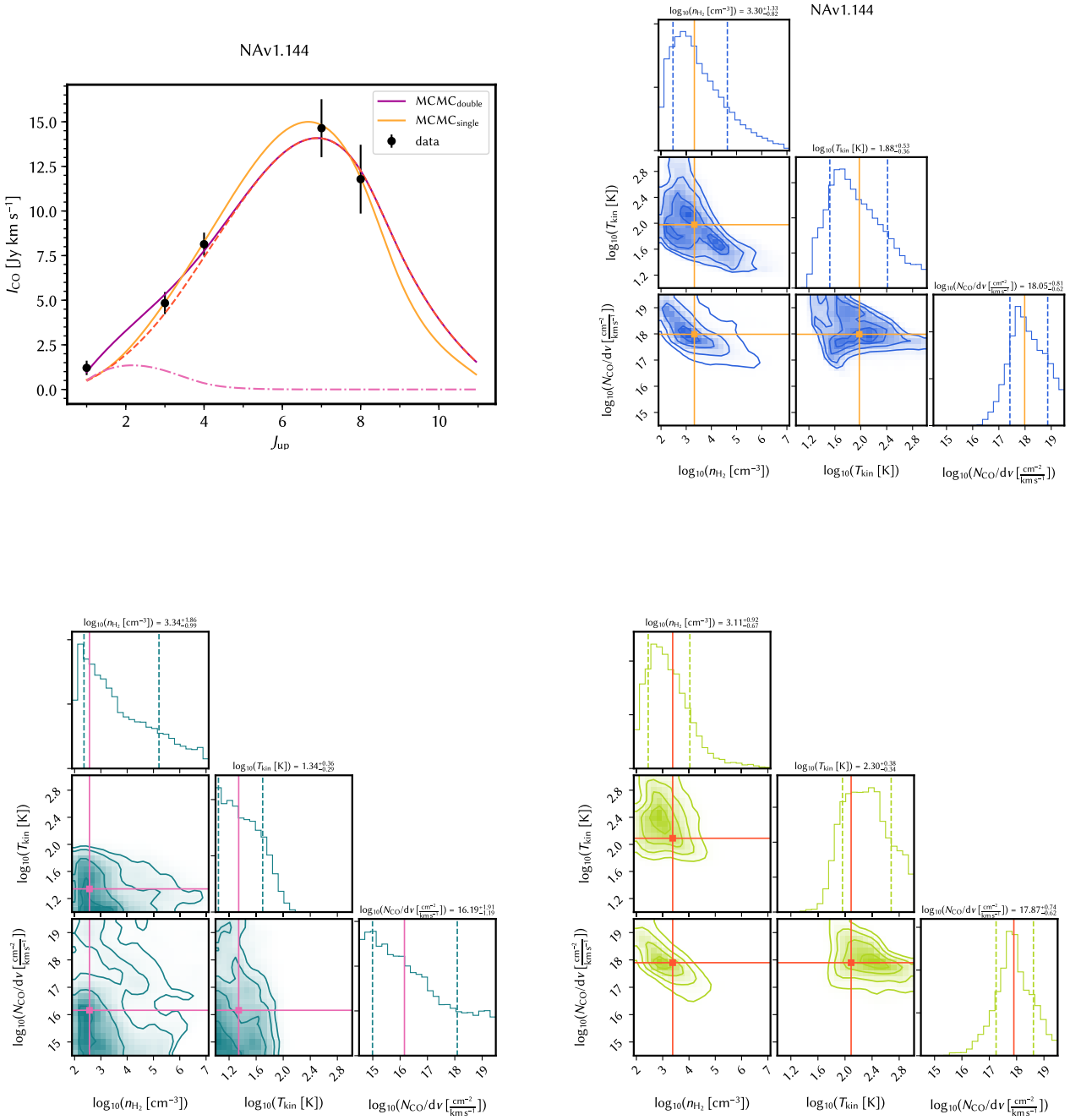

Fig. C.1. Continued.

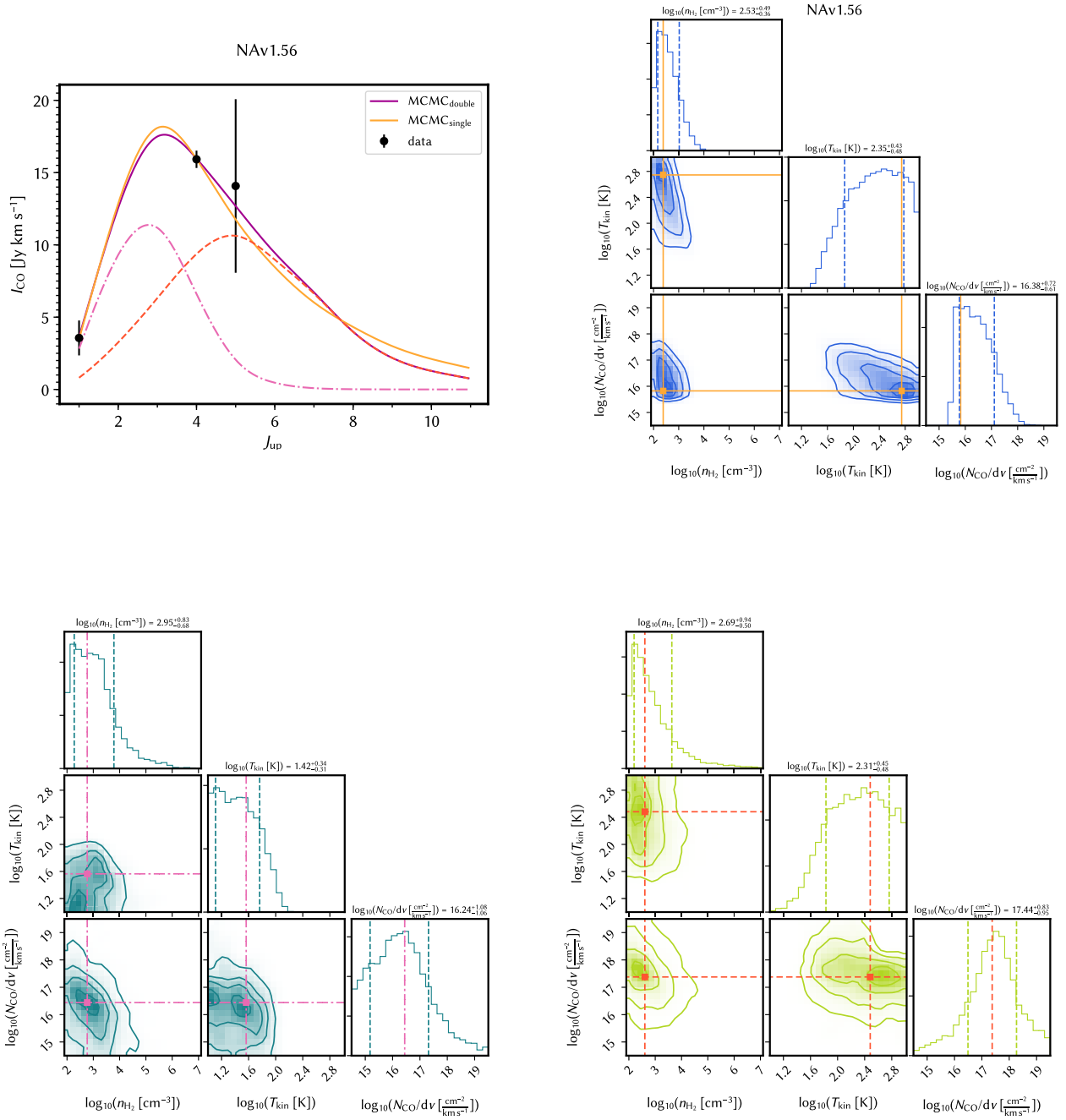

Fig. C.1. Continued.

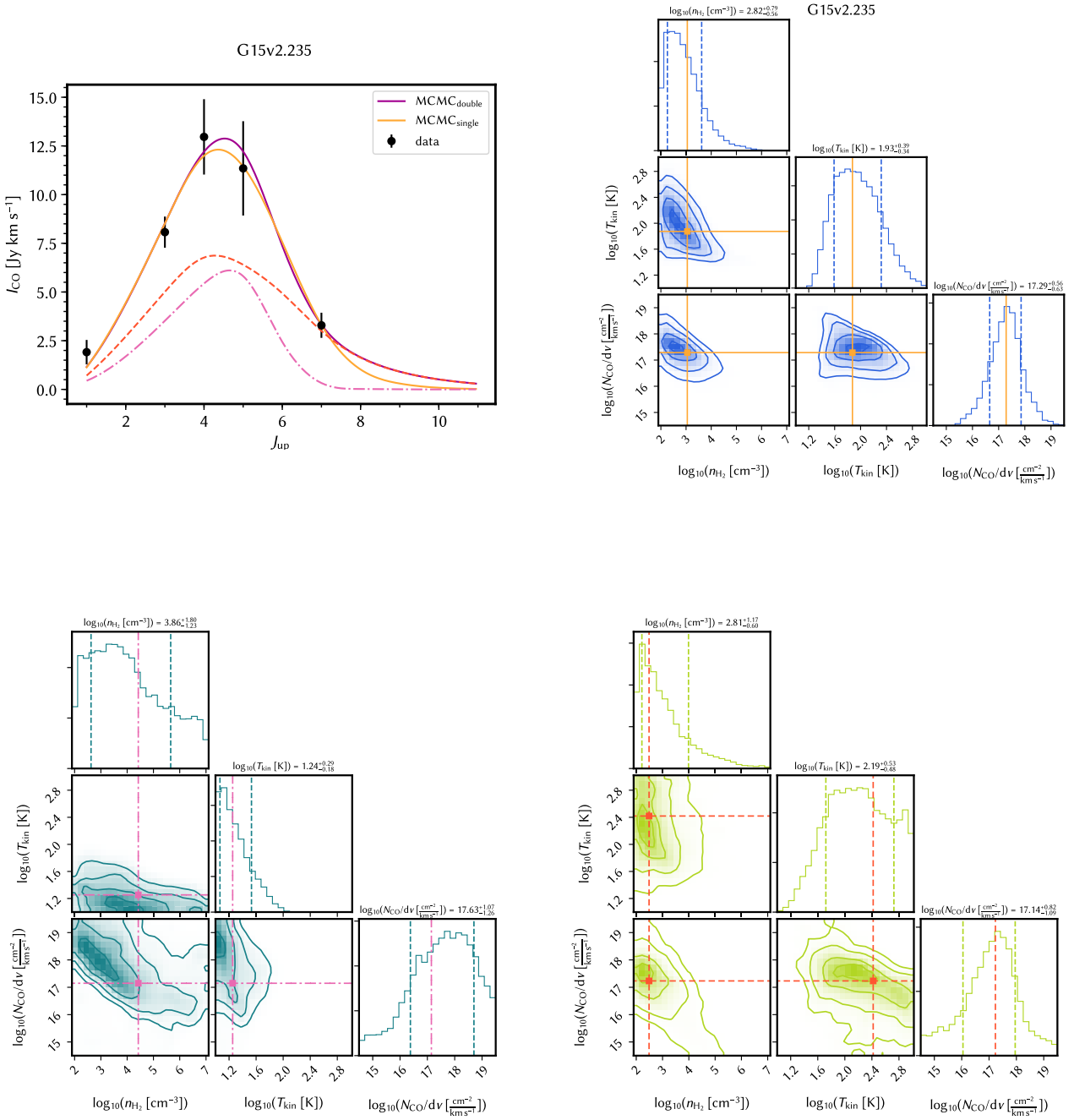

Fig. C.1. Continued.

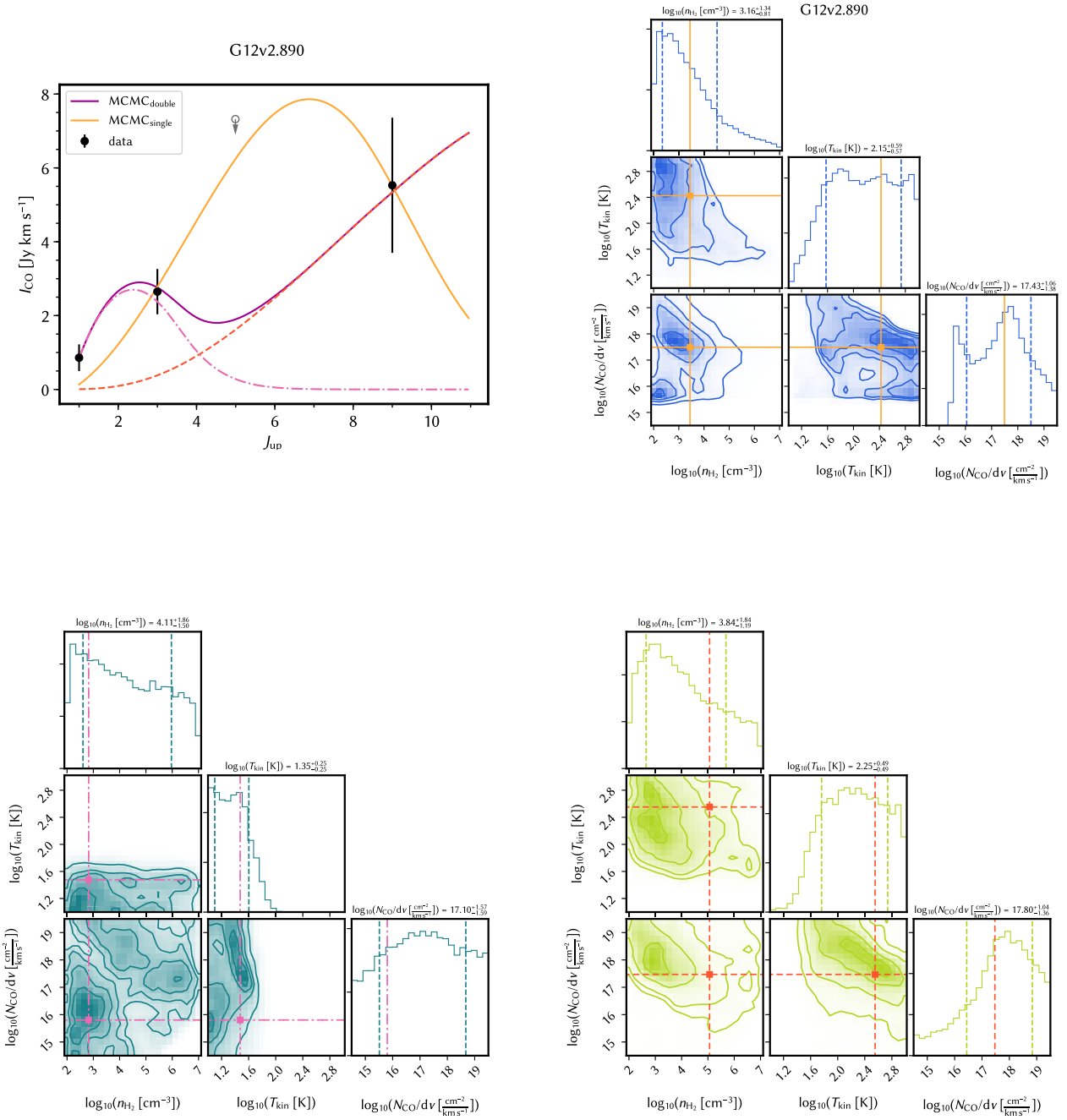

Fig. C.1. Continued.

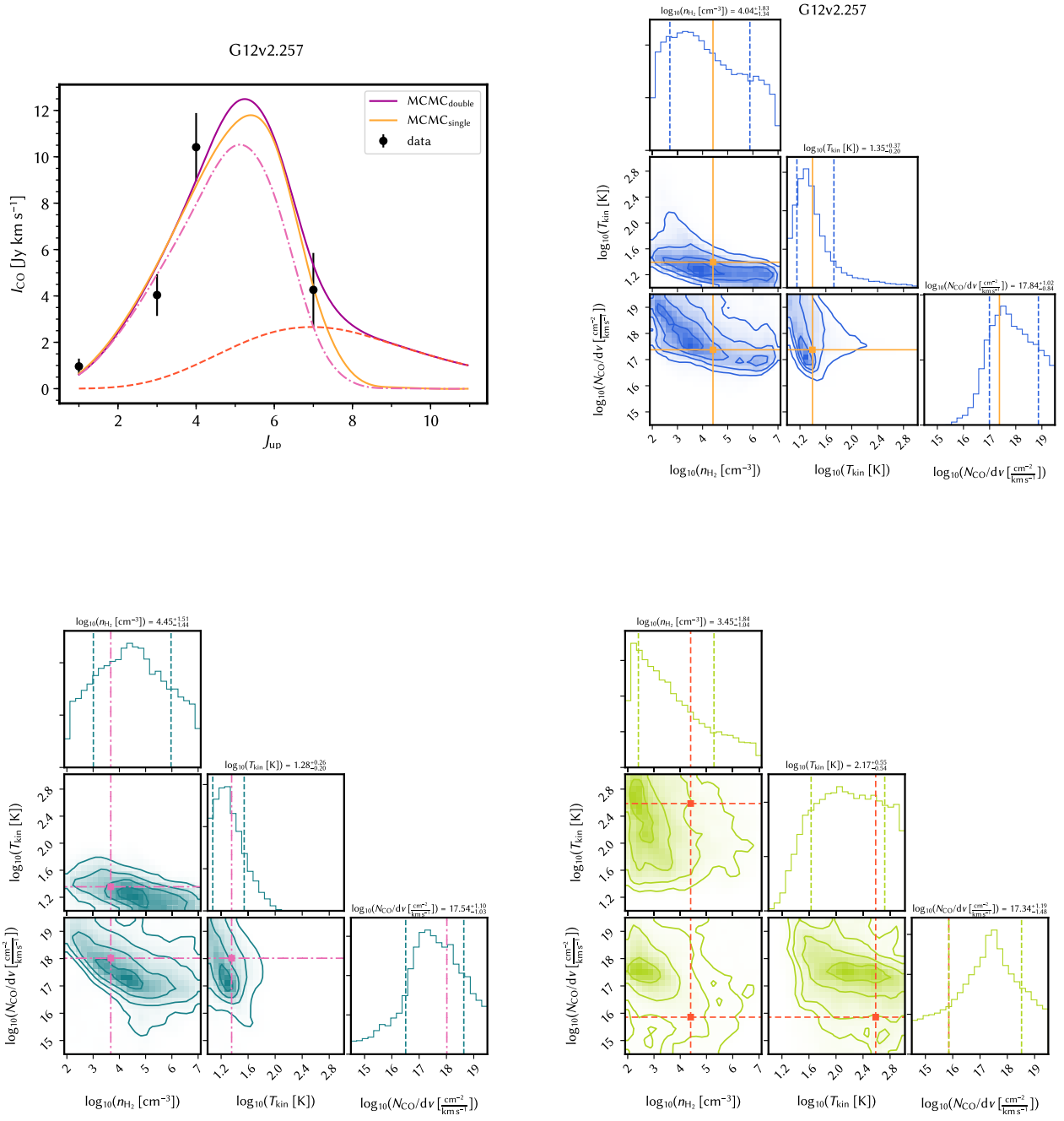

Fig. C.1. Continued.

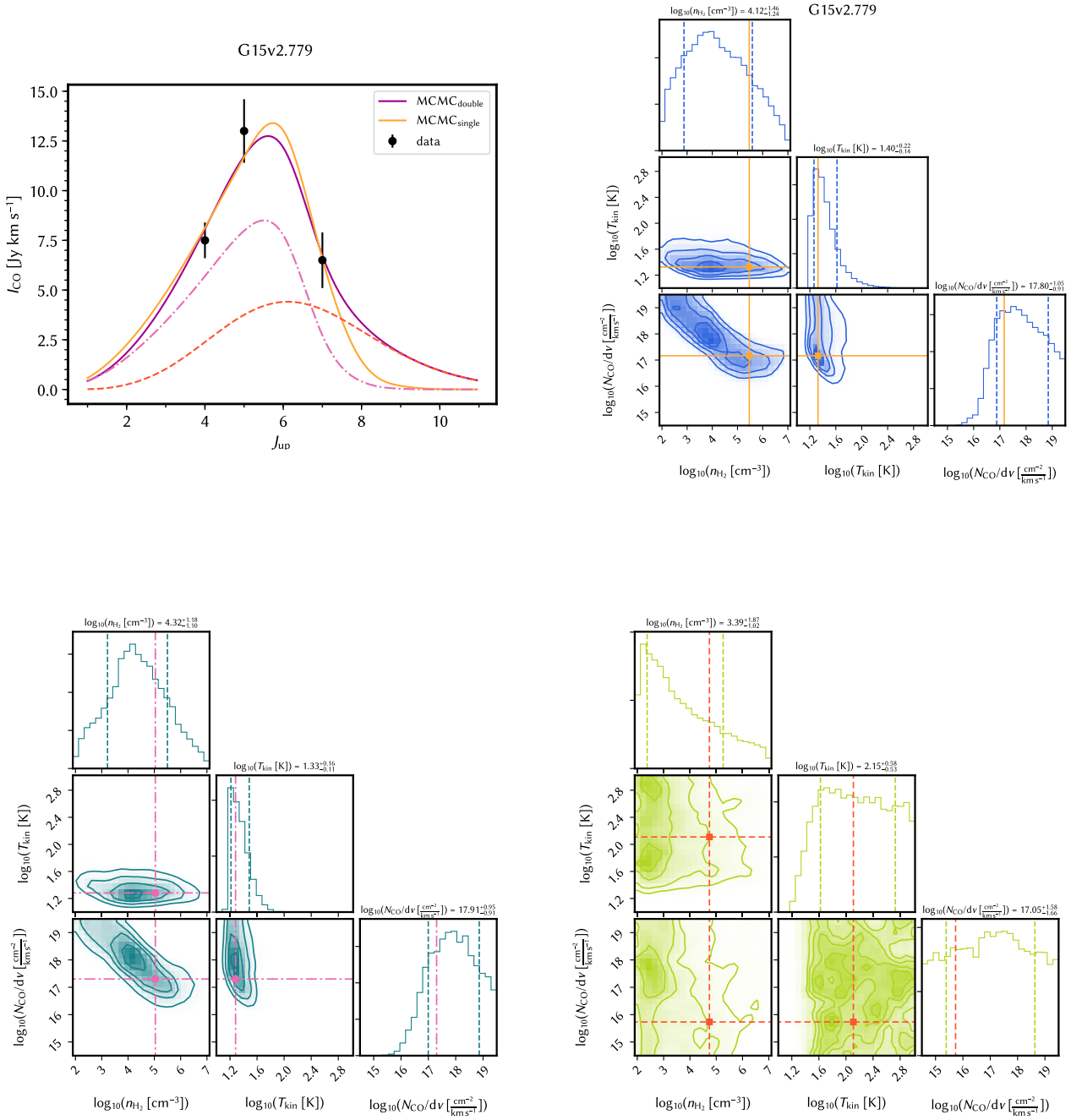

Fig. C.1. Continued.

Chapter 5

Dissecting two strongly lensed starbursts at redshift 3.6 with kiloparsec-scale imaging

Of course, there is no hope of observing this phenomenon directly. First, we shall scarcely ever approach closely enough to such a central line. Second, the angle β will defy the resolving power of our instruments.

Einstein, A. 1936, Science, 84, 506

5.1 Background, motivation and source selection

As discussed in Chapters 3 and 4, in order to understand the properties of molecular emission in high-z SMGs, and more generally, the structure and the dynamical properties of these galaxies, it is crucial to acquire high-resolution images of the emission in the various molecular lines and in the dust continuum. The comparison of these images may then provide fundamental information about the spatial structure of key physical properties (gas density, temperature, molecular excitation, etc.) and also about the dynamical state of the molecular clouds. All this information will greatly help us to understand the nature of the SMGs. However, high spatial-resolution observation of their ISM remains technically challenging mostly because of their great distances. Indeed, such observations can only be achievable using interferometric observations using long baselines. At $z = 2$ and $z = 6$, a 1" beam offers a resolution of ~ 8.5 kpc and 5.8 kpc, respectively, which is normally a bit larger than the size of the molecular gas content within an SMG (e.g. Ivison et al., 2011). Thus, observing with ~ 0.1" resolution is needed for a resolved study under kiloparsec scale of the SMGs around $z \sim 2$–6. This requirement is beyond the limit of most of the interferometric arrays working at mm/submm such as SMA and PdBI (former version of NOEMA). The recently accomplished ALMA is the most powerful facility working at submm/mm that can reach a resolution of several 0.01". Besides, the future (in 2019) NOEMA will also offer a high resolution ~ 0.15" at 1 mm. But still, such high-resolution observation will cost very long integration time to reach detections since the fluxes have been resolved into several beams. The balance between the spatial resolution and the sensitivity is often hard to achieve. However, with the help of strong gravitational lensing effect (Section 1.3), that not only boosts the flux of the background source but also magnifies its size, we will be able to achieve very high spatial resolution observations with reasonable integration time on source.

Therefore, we chose two of our brightest lensed high-z SMGs for such high-resolution studies. Under the help of boosted angular resolution, with a fairly high spatial resolution and sensitivity with millimeter interferometers such as ALMA, NOEMA and SMA, e.g. 0.5" resolution for a $\mu = 11$ source at $z = 3$, the reconstructed source plane image can reach a resolution of ~ 1 kpc. However, to correctly infer the spatial properties of the source in the source plane, special care is also needed for building elaborate galaxy-galaxy strongly lensing models. As mentioned in the previous chapters, continuum imaging was performed at 880 μm with SMA by (Bussmann et al., 2013) for all our sources, but with a moderate angular resolution ~ 0.6" and sensitivity. Although these images have allowed the authors to build robust lens models for most sources (for those with optical/NIR images of the deflectors), providing values for the magnification factor μ and the extension radius $r_{\rm eff}$ of the continuum dust emission from the background source (see Table 3 in the publication shown in Section 4.2), the ~ 0.6" resolution and moderate sensitivity prevent to provide any further detail about the source structure. Clearly, more powerful subm/mm interferometers, such has NOEMA and especially ALMA, with long baselines, both in the dust continuum and in molecular lines, are required to provide details about the source structure and dynamics, and thus about the spatial distribution of star formation, molecular gas and its excitation and various physical properties.

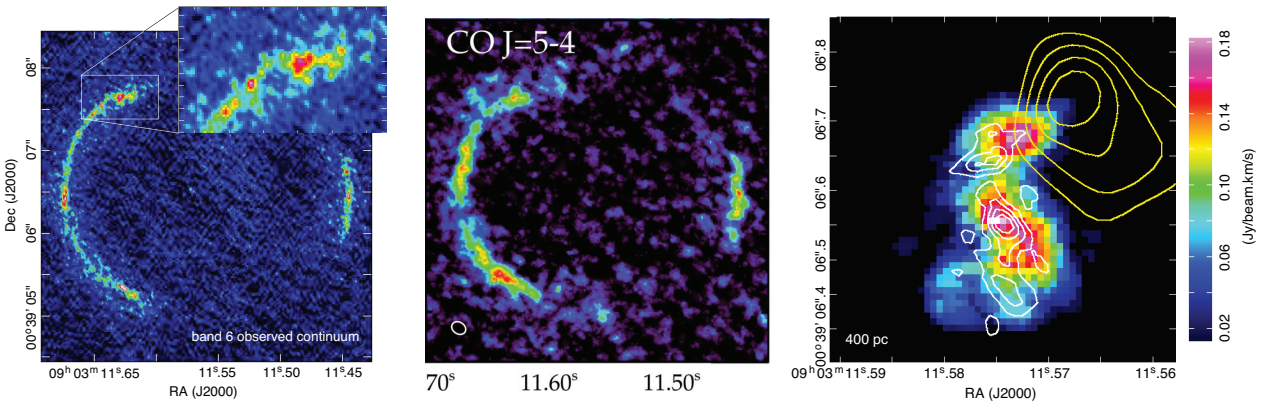

Fig. 5.1 *From left to right:* 1) ALMA observed continuum image of the high-z lensed source SDP 81 at 1.4 mm (ALMA Partnership, Vlahakis et al., 2015). 2) Figure taken from Wong et al. (2015). ALMA image of CO(5–4) of SDP81. 3) Reconstructed images by Dye et al. (2015) in the source plane of: the CO(5–4) line (colour background), dust continuum (white contours). The orange contours in the right image show the NIR image as observed by HST reconstructed in the source plane, see Dye et al. (2015).

This is best illustrated by the case of SDP 81 (H-ATLAS J090311.6+003906), as one of our sources which has been imaged with ALMA long baseline up to ~ 15 km (ALMA Partnership, Vlahakis et al., 2015). Such a unique image with synthetic beams as small as ~ 0.03"–0.05" has been analysed through lensing modelling by several groups (Dye et al., 2015; Hatsukade et al., 2015; Hezaveh et al., 2016; Inoue et al., 2016; Rybak et al., 2015a,b; Swinbank et al., 2015; Tamura et al., 2015; Wong et al., 2015). The interests are focused on both the lensing structure itself and also the star formation properties of the background source. For instance, Dye et al. (2015) published a detailed lens model of this strong lensed system. Using pixelated lens models, they have reconstructed the distribution of the dust continuum emission in SDP 81 and have determined the kinematic properties of the SMG by reconstructing CO(5–4) and CO(8–7) line emission. The source plane dust continuum image reveals a highly non-uniform distribution of dust with clumps on scales of 200 pc (right panel of Fig. 5.1). Comparing with the source plane image of the stellar emission in the NIR (yellow contours in Fig. 5.1), there exists a significant offset between the stellar emission and the dust/CO emission. With the help of strong gravitational lensing and the ALMA long baseline with

unprecedented sensitivity, Swinbank et al. (2015) studied this $z = 3$ SMG on scales of 0.05–0.1 kpc. Unlike the dust emission, the CO emission is more smoothly distributed in the source plane. The reconstructed images suggest that the dynamics can be described as a disk-like velocity field which is well fit by a rotating disk model and an asymptotic inclination-corrected rotation velocity of 320 km s^{-1} (Fig. 5.4). The inferred dynamical mass within a radius of 1.5 kpc is $(3.5\pm0.5)\times10^{10}\,M_{\odot}$ which is comparable to the total molecular gas masses of $(2.7\pm0.5)\times10^{10}\,M_{\odot}$ and $(3.5\pm0.6)\times10^{10}\,M_{\odot}$ from the dust continuum emission and CO

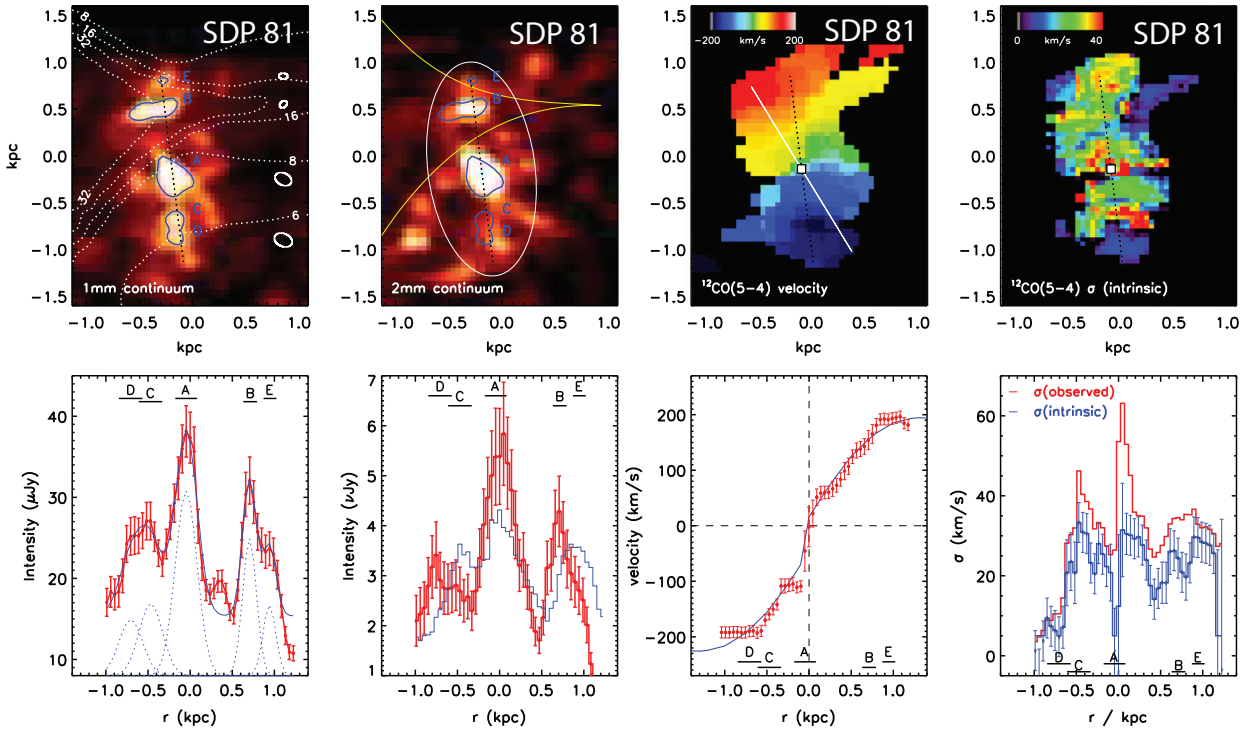

Fig. 5.2 Figures adapted from Swinbank et al. (2015). *The first row from left to right:* 1) source plane dust emission at 1 mm with contours indicating the magnification at various spatial positions, the clumps are marked with letters from A to E; 2) source plane dust emission at 2 mm with the caustic and critical line; 3) reconstructed velocity field of CO(5–4) with the axis indicated by the white line; 4) velocity dispersion of the CO(5–4) line as seen in the source plane. *The second row from left to right:* 1) radial brightness profile of of 1 mm dust emission, while the dashed line are the fit to the profiles of the individual clumps; 2) radial brightness profile of 2 mm dust emission overlaid with the profile of CO(5–4) indicated by the blue histogram; 3) velocity curve along the major axis with the model indicated by the blue line; 4) observed and reconstructed velocity dispersion.

emission respectively. This value of the dynamical mass is smaller and much more accurate than our single-dish values of Table 4 in our publication (i.e. $2\times10^{11}\,M_{\odot}$, see Chapter 4.2 for Yang et al. submitted) probably due to a smaller inclination angle and a smaller radius comparing to the single-dish results, while the mass of gas is consistent with our value. The clumpy nature of the dust and a low value of the Toomre parameter (Toomre, 1964) of $Q \sim 0.3$ suggest that the disk is in a state of collapse. These findings favour a merger induced starburst for this source.

From the recently published ALMA high-resolution (synthetic beam ~ 0.03") images of SDP 9, another lensed SMG at $z \sim 1.6$, Wong et al. (2017) find that there also exists an offset between the reconstructed stellar emission (as seen from the HST Wide Field Camera 3 data) and that of the dust and molecular gas

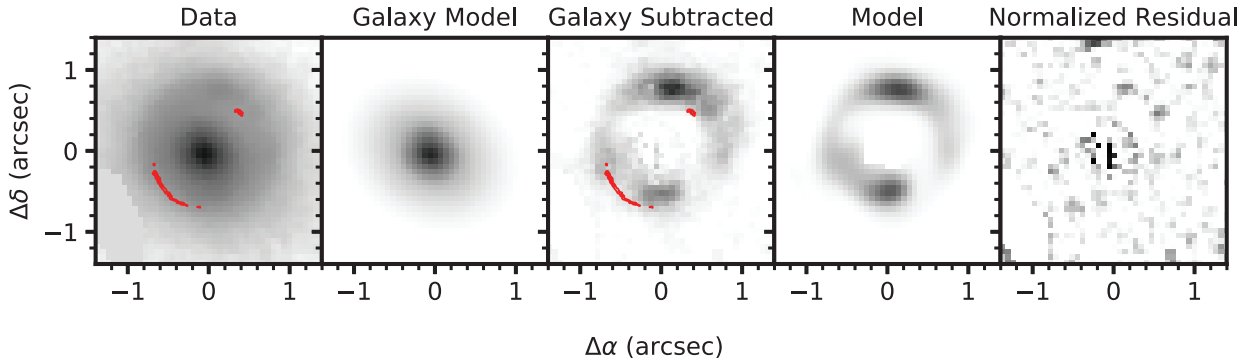

Fig. 5.3 The ALMA data of SDP 9's 1 mm continuum shown in red contours overlaid on the HST image of the entire gravitational lensing system. The model of the lens and the lensed background SMG are as shown in the second and fourth sub-figure. This figure is adapted from Wong et al. (2017).

(Fig. 5.3) as found in SDP 81 (Fig 5.1). This indicates that such an offset could be commonly seen in high-z SMGs.

Besides the $\lesssim$0.05" spatial resolution imaging data of SDP 81 and SDP 9, there are also other published studies observing high-z SMGs with resolution below 1", using mostly ALMA and NOEMA. Three sources of our H_2O sample, G15v2.779 (H-ATLAS J142413.9+022303), SDP 9 and SDP 11 (H-ATLAS J090740.0-004200 and H-ATLAS J091043.1-000321), for which we therefore did not observe the CO lines reported in Chapter 4, have been observed with ALMA or NOEMA. The observations allowed improved lens models compared to Bussmann et al. (2013). Dye et al. (2017) studied G15v2.779 in the continuum at 870 μm with ~0.1" resolution, finding a magnification factor $\mu = 6.6 \pm 0.5$. Oteo et al. (2017) have modelled the lensed CO(3–2) emission observed with NOEMA at about 1.0" ×0.4", together with the 7 GHz radio continuum emission from JVLA observations in SDP 9 and SDP 11 .

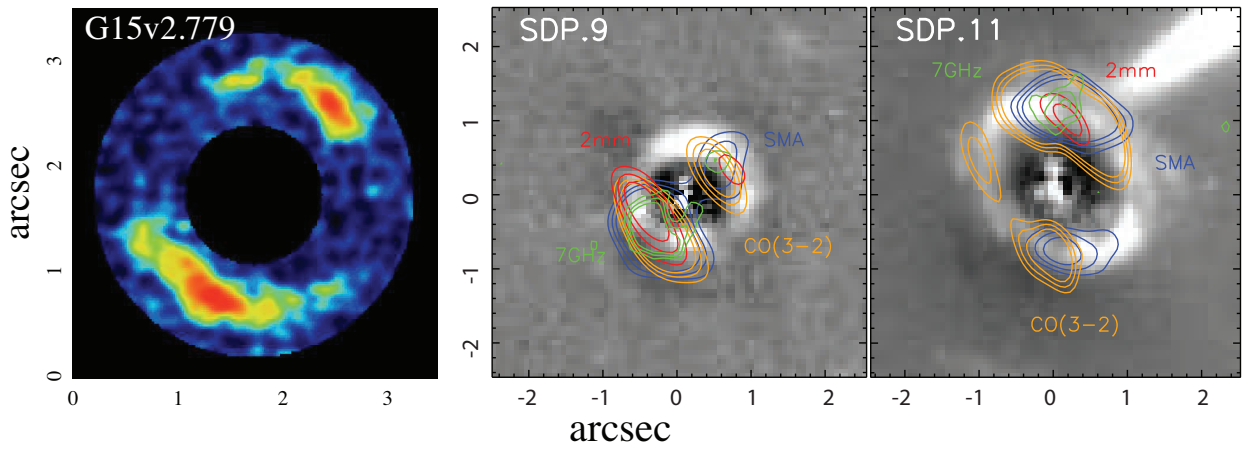

Fig. 5.4 *Left*: ALMA images of dust 870 μm continuum emission of G15v2.779 from Dye et al. (2017). *Centre*: dust 2 mm emission (from NOEMA) and 880 μm from SMA, radio (from JVLA) and CO lines (from NOEMA) emission from SDP 9 (Oteo et al., 2017). *right*: similar data for SDP 11 (Oteo et al., 2017).

In parallel, the number of lensed high-z SMGs imaged at moderate resolution with ALMA and NOEMA is constantly increasing. For instance, Spilker et al. (2016) have published 0.5" resolution 870 μm ALMA

continuum imaging of a sample of 47 SMGs selected from the SPT survey spanning $z = 1.9$–5.7, and constructed gravitational lens models of these sources.

As we concluded in Chapters 3 and 4, such high spatial resolution imaging not only of the continuum, but also of molecular lines of lensed high-z SMGs is mandatory, together with elaborate lensing modelling, to actually probe the structure and the dynamics of such complicated sources and their starburst mostly induced by mergers. Waiting for extremely high-resolution images with ALMA long baselines such as those of Fig. 5.1, we have thus begun applying for moderate angular-resolution (typically ~ 0.4") multi-line imaging of the best sources of our sample with ALMA or NOEMA.

Table 5.1 Source properties from previous *Herschel* and SMA observations

Source	$z_{\rm spec}$	F_{250} (mJy)	F_{350} (mJy)	F_{500} (mJy)	F_{880} (mJy)	$f_{1.4\rm GHz}$ (mJy)	$T_{\rm d}$ (K)	$\mu L_{\rm IR}$ ($10^{13}\,L_\odot$)	μ_{880}	$L_{\rm IR}$ ($10^{12}\,L_\odot$)	$r_{\rm half}$ (kpc)	Σ_{SFR} ($M_\odot\,{\rm yr}^{-1}\,{\rm kpc}^{-2}$)
G09v1.97	3.634	260 ± 7	321 ± 8	269 ± 9	85.5 ± 4.0	<0.45	44 ± 1	15.5 ± 4.3	6.9 ± 0.6	22.5 ± 6.5	0.9	910
NCv1.143	3.565	214 ± 7	291 ± 8	261 ± 9	97.2 ± 6.5	0.61 ± 0.16	40 ± 1	13.0 ± 4.0	11.3 ± 1.7	11.4 ± 3.9	0.4	2086

Note: *Herschel* 250, 350, 500 μm photometric data are from Valiante et al. (2016) while the SMA results (880 μm data, lens model and the star formation properties) are from Bussmann et al. (2013). The 1.4 GHz radio data is taken from the VLA FIRST survey (Becker et al., 1995).

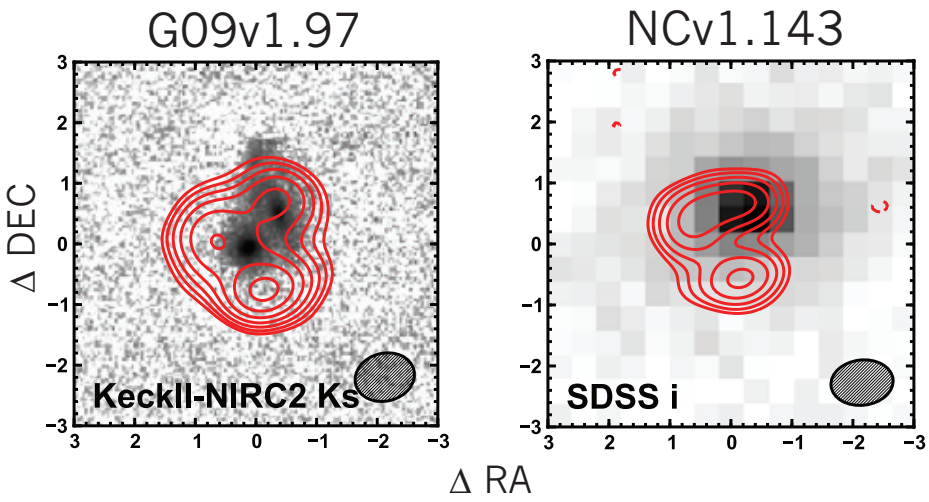

Fig. 5.5 SMA 880 μm images of *H*-ATLAS strongly lensed galaxies NCv1.143 and G09v1.97 (Bussmann et al., 2013). The background image of NCv1.143 is from KECK-NIRC2 NIR observation and the one for G09v1.97 is from SDSS.

For this purpose, we first favoured two prominent sources, G09v1.97 (H-ATLAS J083051.0+013224) and NCv1.143 (H-ATLAS J125632.7+233625), whose highest redshift ($z = 3.6$) allows multi-line observations in good atmospheric windows. In table 5.1, we summarise the previously known properties of these two sources. Bussmann et al. 2013's SMA 880 μm images are also shown in Fig. 5.5. Both of them have a 500 μm flux about 260 mJy. Their intrinsic $L_{\rm IR}$ are larger than $10^{13}\,L_\odot$. In order to optimise the imaging conditions, the equatorial source, G09v1.97 was proposed for ALMA observation, while the northern source, NCv1.143 was submitted to NOEMA. We thus proposed a comprehensive study in three different frequency bands at each facility, aiming firstly at mapping the FIR continuum and CO at ~ 0.3"–0.4" in order to provide details of the source structure at ~ 600–700 pc resolution in the source plane, and relate H_2O emission and excitation to the overall structure and dynamics of the gas disk. In addition, the full project would have

allowed us to observe 5 H_2O lines providing the full diagnostic power of H_2O. But only one observation (in the 2 mm band) was allocated with ALMA and two observations (in the 2 mm and 1.2 mm bands) with NOEMA. Nevertheless, the high-quality data from these state-of-art submm/mm instruments has allowed us to access a rich information about the physical properties of the sources. These results demonstrate that such high angular resolution observations are promising for studying the high-z SMGs with an affordable observation time, and such observations should be extended to a much larger sample size.

In this Chapter 5, we report the observation results, analysing a dozen of images of the dust continuum and molecular line emission with $\lesssim 1$" angular resolution. The high quality space-integrated line spectral data allow us to study the physical conditions of the ISM globally and the star formation properties. We also discuss the kinematic structure and dynamical states of the two sources with the velocity map derived from the imaging data. However, as repeatedly stressed, the exploitation of such high-quality data, mostly depends on the quality of elaborate lens models. The latter, however, also needs high quality optical/near-infrared images for better constraining the gravitational potential of the deflector, which we will propose in future observations. We thus present lens models based on our high-resolution images of the background source and their application to the reconstruction of the structure of the various emissions in the source plane of the two distant SMGs. We conclude by applying such a detailed modelling for inferring the best diagnostic of the properties of the young, perturbed galaxies and their starbursts.

The following contents are organised as follows. Section 5.2 describes the observation and data reduction of G09v1.97 with ALMA and those of NCv1.143 with NOEMA. Section 5.3 presents the observation results : line spectra and main images (continuum and lines). The basic properties of the lens models are described in Section 5.4, together with their application to the continuum images of both sources. In Section 5.5, we analyse the reconstructed velocity structure and the gas dynamics for G09v1.97. Finally Section 5.6 discusses the general properties of the sources revealed by the observed various gas tracers and the dust continuum, together with those inferred from published images of other high-z SMGs, such as SDP81, and in reference to the results of Chapters 3 and 4.

5.2 Observations and data reduction

Table 5.2 Observation log.

Source	telescope	RA (J2000)	DEC (J2000)	target	ν_{obs} (GHz)	Beam size (arcsec)	PA (°)	t_{on} (h)
G09v1.97	ALMA	08:30:51.17	+01:32:24.39	CO(6–5)	149.207	0.36×0.33	70.2	1.2
				$H_2O(2_{11}–2_{02})$	161.946	0.38×0.37	71.4	–
				H_2O^+	160.124	0.40×0.36	80.4	–
				continuum	148.009	0.40×0.38	106.9	–
NCv1.143	NOEMA	12:56:32.56	+23:36:27.92	$H_2O(2_{11}–2_{02})$, H_2O^+	162.286	0.76×0.41	26.9	3.3
				$H_2O(3_{21}–3_{12})$, CO(10–9)	250.952	0.54×0.30	13.7	2.4

Note: The coordinates are the central observing position. The four frequencies of G09v1.97 correspond to the central frequencies of the spectral windows located in the upper and lower sidebands with one tuning of ALMA observation, while for NCv1.143, the two bands are from two single sidebands using two tunings at NOEMA. We note that the continuum has been observed in NCv1.143 at the same frequencies as the molecular lines

5.2.1 ALMA observation and data reduction of G09v1.97

G09v1.97 was observed using ALMA band 4 (see Table 5.2), in the 2 mm window (Program ID: 2015.1.01320.S; PI: A. Omont). Data were acquired with two observing sessions on 2016-08-04 and 2016-08-25, respectively. The on-source time spent is 36.9 min for each, thus, a total 73.8 min on-source time was used, in addition to a total amount of 42 min overhead including calibration – pointing, phase, flux density and bandpass. J0750+1231 and J0825+0309 were used as flux calibrators, while two other calibrators, J0839+0104 and J0854+2006, were also used in the phase/bandpass calibration and pointing. The ALMA spectral setup used comprised band 4 observations in four spectral windows, each of width 1875 MHz. The central frequencies are listed in Table 5.2. In each spectral window, there are 128 frequency channels giving a resolution of 15.6 MHz. 38 and 39 12m antennas were used during the two observation sessions, respectively. ALMA C36-5 configuration provides baselines from 15.1 m up to about 1.5 km. This results in an angular resolution of 0.4" and an RMS of approximately 0.21 mJy in 50 km s^{-1} channel width. Data were calibrated using the ALMA pipeline, with only minor flagging required. The calibrated data were then imaged and CLEANed within `CASA` (Common Astronomy Software Applications)[1] version 4.7.0-1, using the natural weighting scheme to maximise sensitivity.

5.2.2 NOEMA observation and data reduction of NCv1.143

The source NCv1.143 is at declination of +23:36:28, making it suitable to be observed from the northern hemisphere. Observations of this source were carried out in the most extended A-configuration of NOEMA. The baselines extended from 93 to 760 m, resulting in a synthesised beam with a resolution of ~0.5"×0.3" at 1.2 mm and ~0.7"×0.4" at 1.8 mm as shown in Table 5.2. The observations were conducted from February to March 2016 in good atmospheric conditions (seeing of 0.3"–1.0"), stability and reasonable transparency (PWV≤1 mm). The number of antennas was 7, and the total on source time was 3.3 h at 1.8 mm, and 2.4 h at 1.2 mm. All the central observation frequencies were chosen based on the redshift $z = 3.565$ given by Bussmann et al. (2013) according to the previous CO(4–3) detection by Riechers et al. (in prep) using CARMA, and confirmed by our H_2O low-resolution observations (Yang et al., 2016). We used the WideX correlator which provided a contiguous frequency coverage of 3.6 GHz in dual polarisation with a fixed channel spacing of 1.95 MHz. The phase and bandpass were calibrated by measuring standard calibrators that are regularly monitored at the IRAM/NOEMA, including 3C279, 3C273, MWC349 and 0923+392. The accuracy of the flux calibration is estimated to range from ~10% in the 2 mm band to ~15% in the 1.2 mm band. Calibration, imaging, cleaning and spectra extraction were performed within the `GILDAS` packages `CLIC` and MAPPING[2].

5.3 Results

For both sources, the primary goal of these observations is to acquire high resolution maps of submm dust continuum emission and of a few important molecular lines, e.g. CO, H_2O and H_2O^+ (remind that in Chapters 3 and 4, we have detections of CO lines and H_2O/H_2O^+ lines in our targets with observations from compact interferometry array and/or single-dish telescopes whose spatial resolutions are beyond several arcseconds). In this section, we first present these observed lensed images (without any lensing corrections) and compare them in the image plane. We defer to following sections the reconstruction of

[1] see https://casa.nrao.edu/ for more information.
[2] see http://www.iram.fr/IRAMFR/GILDAS for more information about the `GILDAS` softwares.

the maps of the corresponding emissions in the source plane from lensing models, as well as the discussion of velocity effects.

Table 5.3 Observation results from the integrated spectra of the entire source.

Source	redshift	$\nu_{\rm center}$ (GHz)	Line	$S_{\rm pk}$ (mJy)	$I_{\rm CO}$ (Jy km s^{-1})	$\Delta V_{\rm CO}$ (km s^{-1})
G09v1.97	3.634	149.217	CO(6–5)-blue	8.6 ± 0.5	4.0 ± 0.2	497 ± 20
			CO(6–5)-red	31.4 ± 1.0	7.0 ± 0.2	237 ± 3
		162.286	$H_2O(2_{11}–2_{02})$-blue	5.5 ± 0.8	2.5 ± 0.3	481 ± 38
			$H_2O(2_{11}–2_{02})$-red	12.5 ± 1.7	2.4 ± 0.3	204 ± 10
			$^a H_2O^+$	$^a 1.8 \pm 0.4$	$^a 0.6 \pm 0.1$	$^a 348 \pm 41$
			$H_2^{18}O(2_{11}–2_{02})$	1.8 ± 0.4	0.6 ± 0.1	360 ± 46
			$^b H_2O^+$-blue	1.8 ± 1.0	0.7 ± 0.3	413 ± 141
			$^b H_2O^+$-red	3.8 ± 1.7	0.7 ± 0.3	197 ± 34
		2 mm continuum flux = 8.8 ± 0.2 (mJy)				
NCv1.143	3.565	164.739	$H_2O(2_{11}–2_{02})$	19.6 ± 2.1	6.0 ± 0.4	326 ± 27
			$^a H_2O^+$	7.3 ± 1.6	2.2 ± 0.3	319 ± 52
			$^b H_2O^+$	8.4 ± 1.8	1.9 ± 0.3	240 ± 35
			$H_2^{18}O(2_{11}–2_{02})$	4.5 ± 1.0	0.5 ± 0.1	117 ± 55
		2 mm continuum flux = 13.3 ± 0.2 (mJy)				
		252.351	CO(10–9)	15.2 ± 6.7	4.2 ± 1.3	293 ± 91
			$H_2O(3_{12}–2_{21})$	8.2 ± 6.6	2.5 ± 1.4	323 ± 183
			$^c H_2O(3_{21}–3_{12})$	$^c 34.1 \pm 1.1$	$^c 9.3 \pm 0.2$	$^c 290 \pm 7$
		1.2 mm continuum flux^c = 69.0 ± 2.0 (mJy)				

Note: $\nu_{\rm center}$ is the sky frequency corresponding to the zero velocity. Because the line $H_2O(3_{12}–2_{21})$ is very close to CO(10–9) in frequency, we fixed the central frequency of the observed 1.2 mm band of NCv1.143 midway between the two lines (Fig. 5.9). $S_{\rm pk}$ is the peak flux of the emission line after subtracting the continuum emission. See Fig. 5.6 for the fitted spectra of G09v1.97 and Fig. 5.9 for the results of NCv1.143. $^{(a)}$: This H_2O^+ line is dominated by the line $H_2O^+(2_{11}–2_{02})_{(5/2–5/2)}$ with rest-frame frequency of 746.5 GHz. Considering the similarity between the H_2O line and the H_2O^+ lines in the line profiles (Yang et al., 2016, and this work), this line is expected to have similar red+blue component structure. However, due to a gap between the two spectral windows (indicated by the green stripe) where the red component of the line resides, the fitted values in the table should rather serve as lower limits. $^{(b)}$: The H_2O^+ line of G09v1.97 fitted here is dominated by $H_2O^+(2_{02}–1_{11})_{(5/2–3/2)}$ (rest-frame frequency at 742.1 GHz). As argued in Chapter 3, there could be a small contribution from the 742.3 GHz line $H_2O^+(2_{11}–2_{02})_{(5/2–3/2)}$. Nevertheless, considering the complex velocity structure and the flux ratio we found in NCv1.143 in Chapter 3, the contribution from the latter in G09v1.97 can be neglected. $^{(c)}$: In order to recover the true flux, we merge both the compact D-configuration data of NCv1.143 with our new high spatial resolution data. The measurement of the $H_2O(3_{21}–3_{12})$ line fitting results and the continuum flux is then performed on the merged uv-data.

In addition, although this was not the primary goal of our high angular-resolution observations, the spatial integration of the spectra provides high-quality line profiles which have been used for completing the information of Chapters 3 and 4 on calculating line intensities, analysing line profiles and detecting weak lines such as $H_2^{18}O$. After extracting spectra integrated over the entire source region, we then fit each of the emission line with Gaussian profiles using the Levenberg-Marquardt least-square minimization code `MPFIT` (Markwardt, 2009) for obtaining the velocity integrated line fluxes, linewidths and the line centroid positions. The results are displayed in Table 5.3.

After comparing the line strength derived from our high-resolution data with the IRAM 30m single-dish or low angular-resolution data of NOEMA, we find that the ALMA data of G09v1.97 do not suffer any significant missing flux. The integrated fluxes of CO(6–5) and $H_2O(2_{11}–2_{02})$ from the ALMA data are comparable with those from single-dish and low resolution observations. Similar fluxes have also been found between the NOEMA compact configuration and extended configuration results for the 2 mm observations for NCv1.143 (for the $H_2O(2_{11}–2_{02})$ and H_2O^+ lines). However, for the source NCv1.143, the NOEMA high resolution data of the 1.2 mm spectrum covering CO(10–9), $H_2O(3_{12}–2_{21})$ and $H_2O(3_{21}–3_{12})$ seems somewhat resolving out the source, mostly due to the shortest baseline used during the observation which is ~ 100 m, thus the information of larger scales are difficult to recover. Comparing the integrated flux of $H_2O(3_{21}–3_{12})$ to the value of 8.0 Jy km s^{-1} reported in Chapter 3, with the compact D-configuration results, the A-configuration NOEMA data recovers ~ 80% of the total flux, i.e. roughly 20% of the total flux is resolved out. Nevertheless, after merging with the NOEMA compact configuration data, the fluxes are able to be recovered for the 1.2 mm dust continuum and the $H_2O(3_{21}–3_{12})$ line, as reported in Table 5.3 (the CO(10–9) and $H_2O(3_{12}–2_{21})$ lines were not covered by the compact array observations, thus we only use the spectral data extracted from the high-resolution observation for these two lines without correcting them for missing flux).

5.3.1 G09v1.97

5.3.1.1 Spectral line profiles and intensities of G09v1.97

Figure 5.6 displays the space-integrated ALMA spectra in the three observed 2 mm windows. Their sky frequencies ranges are 161.083–162.937 GHz for the H_2O line, 159.160–161.019 GHz for the H_2O^+ lines and 148.240–150.184 GHz for the CO line. The first and second spectral windows are designed to target the $H_2O(2_{11}–2_{02})$ and its neighbouring H_2O^+ lines, while the third window is set to observe the CO(6–5) line. The high-quality spectral data of CO(6–5) and $H_2O(2_{11}–2_{02})$ show a pronounced asymmetry between a strong red peak and a weak blue wing. It can be well fitted by two Gaussian lines as shown in the figure. The peak flux ratio between the red and blue component is about 3.7 for the CO(6–5), 2.3 for $H_2O(2_{11}–2_{02})$ and 2.1 for the H_2O^+ line. The possible origin of such an asymmetry is discussed in Section 5.5, where it is shown that it might not be easy to disentangle the effect of differential lensing from an intrinsic asymmetry including perhaps that due to an outflow. One should also notice that there exists a small velocity shift as seen in the overlaid line profiles of CO(6–5) and $H_2O(2_{11}–2_{02})$ in Fig. 5.7. The peak of the H_2O line profile is seen more red-shifted (roughly by 50 km s^{-1}) comparing to that of the CO line. Similar difference is also seen in the lens-model-reconstructed source plane images of the CO and H_2O emission that we present in Section 5.4. Comparing the flux ratio between the blue and red components of the CO(6–5) and $H_2O(2_{11}–2_{02})$ lines, they are found to be in good agreement. Nevertheless, by carefully building a lens model upon both these high angular-resolution images and a reliable gravitational potential based on the optical/NIR images, one may have a better understanding of the source structure and dynamics that could explain such a line profile. We will further discuss this issue in the sections below. The observed properties and the inferred parameters from the spectral lines are reported in Table 5.3.

As reported in our work about H_2O in Chapter 3, the 738–755 GHz observed range includes the very strong para-$H_2O(2_{11}–2_{02})$ line, two strong H_2O^+ lines ($H_2O^+(2_{11}–2_{02})$ $_{(5/2-5/2)}$ and $H_2O^+(2_{02}–1_{11})$ $_{(3/2-3/2)}$), two weak H_2O^+ lines ($H_2O^+(2_{02}–1_{11})$ $_{(5/2-3/2)}$ and $H_2O^+(2_{11}–2_{02})$ $_{(5/2-3/2)}$) and line $H_2^{18}O(2_{11}–2_{02})$. Within the same band of the H_2O observation, we also have detected these lines thanks to the high S/N (noise level down to 0.2 mJy with 50 km s^{-1} resolution) spectra from ALMA. The observed properties of the

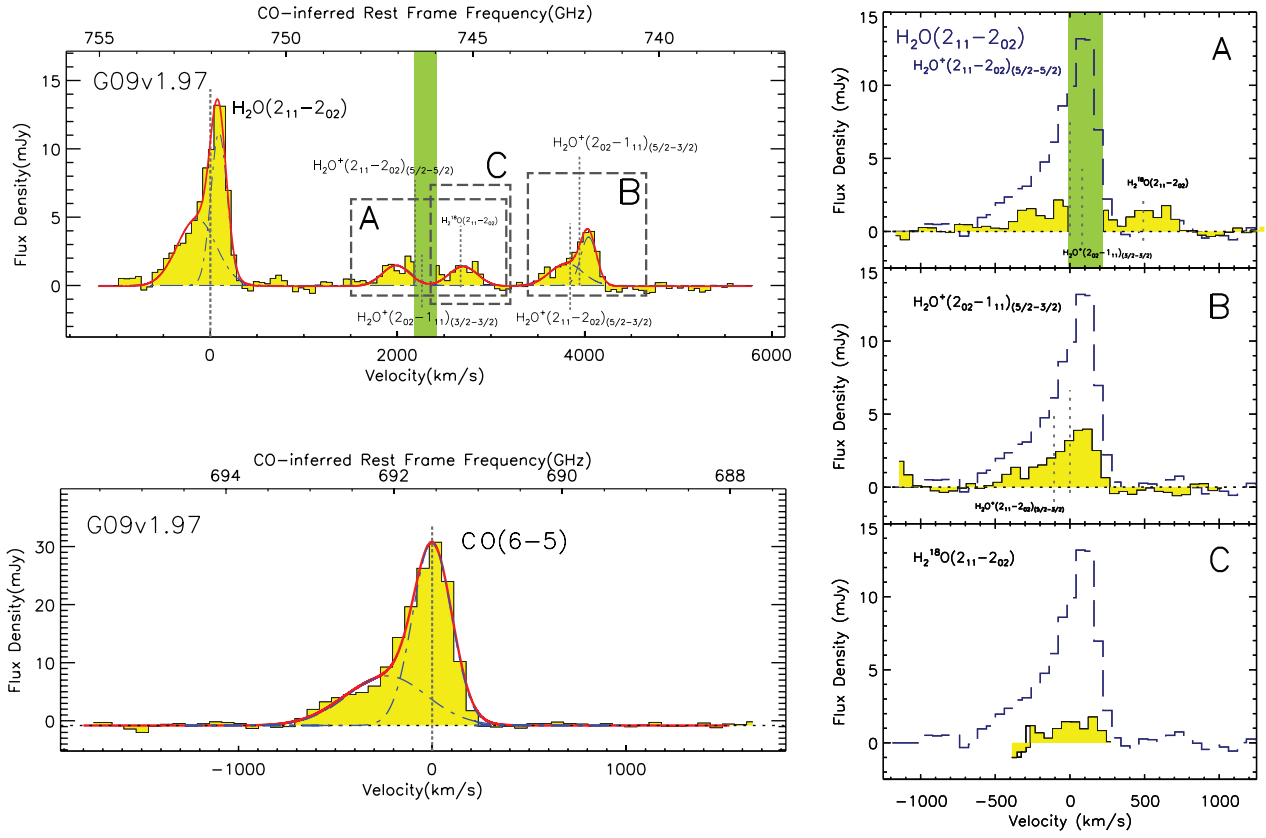

Fig. 5.6 Spatially integrated (continuum subtracted) spectra of molecular lines observed in G09v1.97 using ALMA. The vertical dotted lines represent the expected central line frequencies, based on a $z = 3.634$. The red curve represents the fitting to the spectrum with Gaussian profiles, and the blue dashed curves are the decomposed Gaussian profiles for two components. The average noise level of the spectra is about 0.2 mJy with a spectral resolution of 50 km s^{-1}. *Bottom left*, spectrum of the CO(6–5) line. *Top left*, 738–755 GHz rest frequency range with H_2O, H_2O^+ and $H_2^{18}O$ lines from two spectral windows of the ALMA observation (see text for details). Green stripe shows the gap between the two spectral windows from 746 to 746.5 GHz. The three dashed rectangles show the position of each H_2O^+ (or $H_2^{18}O$) spectrum displayed in rows A, B or C of the right column: *First row A*: Spectra of $H_2O^+(2_{11}–2_{02})_{(5/2–5/2)}$, $H_2O^+(2_{02}–1_{11})_{(3/2–3/2)}$ and, possibly $H_2^{18}O(2_{11}–2_{02})$ displayed as the filled yellow histograms. The reference frequency is the frequency of the line $H_2O^+(2_{11}–2_{02})_{(5/2–5/2)}$. $H_2O^+(2_{02}–1_{11})_{(3/2–3/2)}$ and $H_2^{18}O(2_{11}–2_{02})$ lines are indicated. *Second row B*: Spectra of $H_2O^+(2_{02}–1_{11})_{(5/2–3/2)}$ and $H_2O^+(2_{11}–2_{02})_{(5/2–3/2)}$. The reference frequency is the frequency of the line $H_2O^+(2_{02}–1_{11})_{(5/2–3/2)}$. The grey vertical dashed line represents the position of the $H_2O^+(2_{11}–2_{02})_{(5/2–3/2)}$ line. *Third row C*: Spectrum of $H_2^{18}O(2_{11}–2_{02})$ after subtracting the H_2O^+ lines, with the reference frequency set as the frequency of the $H_2^{18}O(2_{11}–2_{02})$ line. For all panels, the superposed blue dashed histograms represent the spectra of para-$H_2O(2_{11}–2_{02})$ in each source.

spectral lines are reported in Table 5.3. In panels A, B and C of Fig. 5.6, we overlaid the spectrum of $H_2O(2_{11}–2_{02})$ on top of the weaker H_2O^+ and $H_2^{18}O(2_{11}–2_{02})$ lines, by centering their line profiles. It is seen that the strong lines of H_2O and H_2O^+ display asymmetrical profiles (although the red velocity part of the $H_2O^+(2_{11}–2_{02})_{(5/2–5/2)}$ line falls in the gap between the two spectral windows). And the profile of the H_2O^+ line in panel B agrees very well with that of the H_2O line. These profiles seem also mainly similar to that of CO(6–5) (Figure 5.7). This suggests that the CO, H_2O and H_2O^+ may rise from very similar regions/dynamical conditions (however, see below) that might be tightly related to the active star formation.

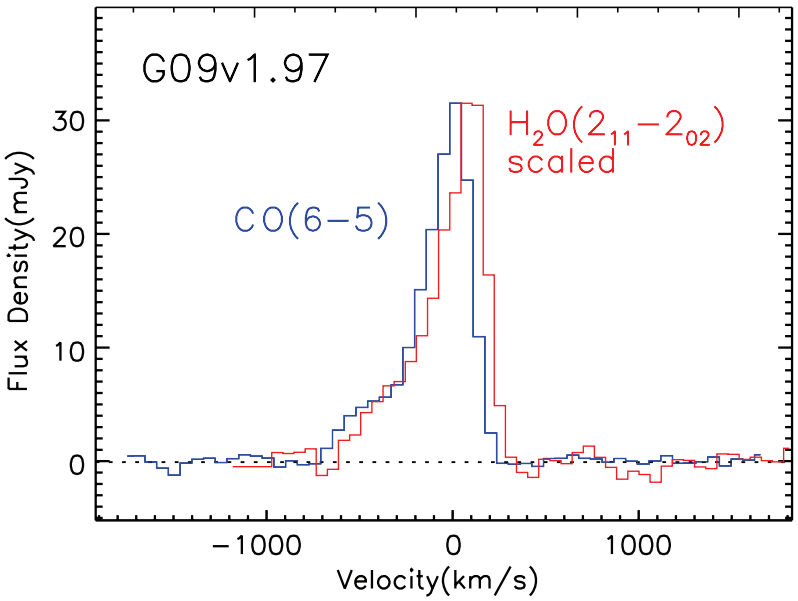

Fig. 5.7 The CO(6–5) and scaled $H_2O(2_{11}–2_{02})$ spectra overlaid at zero velocity according to a redshift of $z \sim 3.634$.

5.3.1.2 Images of G09v1.97: continuum and lines

The ~ 0.35"-resolution ALMA images of G09v1.97 are displayed in Fig. 5.8, for the dust continuum emitted at ~440 μm in the rest frame, the CO(6–5) line, the para-$H_2O(2_{11}–2_{02})$ line and its neighbouring H_2O^+ line emission. The images show a similar broken Einstein ring with radius ~ 1" and three sub-images, the south one being by far the strongest. This agrees with the former SMA 880 μm imaging results (Bussmann et al., 2013). Nevertheless, there is also a small central image component as seen in the dust continuum, CO and H_2O emission, which was unseen in the SMA observations. As shown in the SMA+KECK images of G09v1.97 from Bussmann et al. (2013) (see also Fig. 5.5), the foreground deflector of G09v1.97 is made of two massive galaxies residing at $z = 0.626$ and $z = 1.002$ (Bussmann et al., 2013). This makes the system a special case and also complicates the model of the gravitational potential, which creates another rarely seen small component in the image plane close to the centre. The similarity of the redshift and emission line profile in this central emission component rules out its origin from the two foreground sources. Comparing the extension of the images, the continuum emission is a bit more concentrated in the sub-images, while the CO image forms a more continuous ring, and the H_2O image might be intermediate, but with a smaller S/N ratio. Comparing the ratio between the brightest southern component with the two weaker ones in the north, the dust continuum of the southern component is about twice as bright, while for the CO

line emission, the ratio is about 1.3–1.7, and 1.5 for the H_2O emission. This shows further evidence that the rest-frame dust emission at ~440 μm is a bit more concentrated as compared to the CO and H_2O line emission. When comparing the spatial distribution of the CO and H_2O line in the image plane, it is also noticeable that, for the two northern components, the CO emission from the north west component is stronger than the one from north east, while for the H_2O line the two components are comparable. The H_2O^+ emission is only seen in the brightest image component.

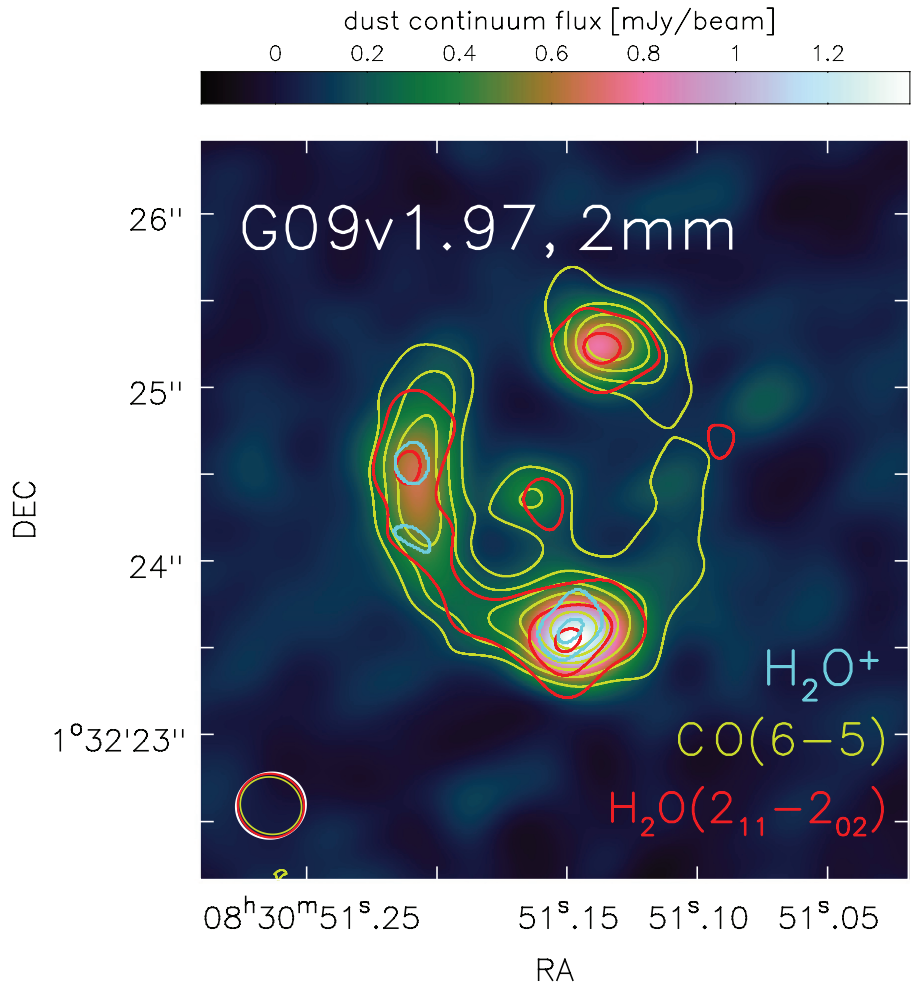

Fig. 5.8 ALMA images of G09v1.97 with angular resolution ~ 0.33"–0.40": The background colour image shows the dust continuum observed at ~ 2 mm, i.e. at ~440 μm in the rest frame. The flux scale is indicated by the colour bar above. Red contours show the emission of $H_2O(2_{11}–2_{02})$ starting from $\pm 4\,\sigma$ in steps of $4\,\sigma$. CO(6–5) line emission is indicated with yellow contours starting from $\pm 4\,\sigma$ in steps of $4\,\sigma$. Cyan contours display the sum of the emission of the series of H_2O^+ lines starting from $\pm 3\,\sigma$ in steps of $1\,\sigma$.

5.3.2 NCv1.143

The 2 mm high-resolution NOEMA data have been merged with that obtained in the same bands with NOEMA in a compact configuration (D-configuration) reported in Chapter 3. This has allowed us to improve the quality of the images and the S/N ratio of the line spectral profiles and intensities. However for the 1.2 mm data, due to the different tuning frequency, only a small frequency range is overlapped. Thus,

we do not merge the high resolution data in this work with the D-configuration data from published works in Chapter 3. Nevertheless, the calculation of the fluxes of $H_2O(3_{21}–3_{12})$ and the 1.2 mm dust continuum were performed on the merged uv-dataset as reported in Section 5.3 and Table 5.3.

5.3.2.1 Spectral line profiles and intensities of NCv1.143

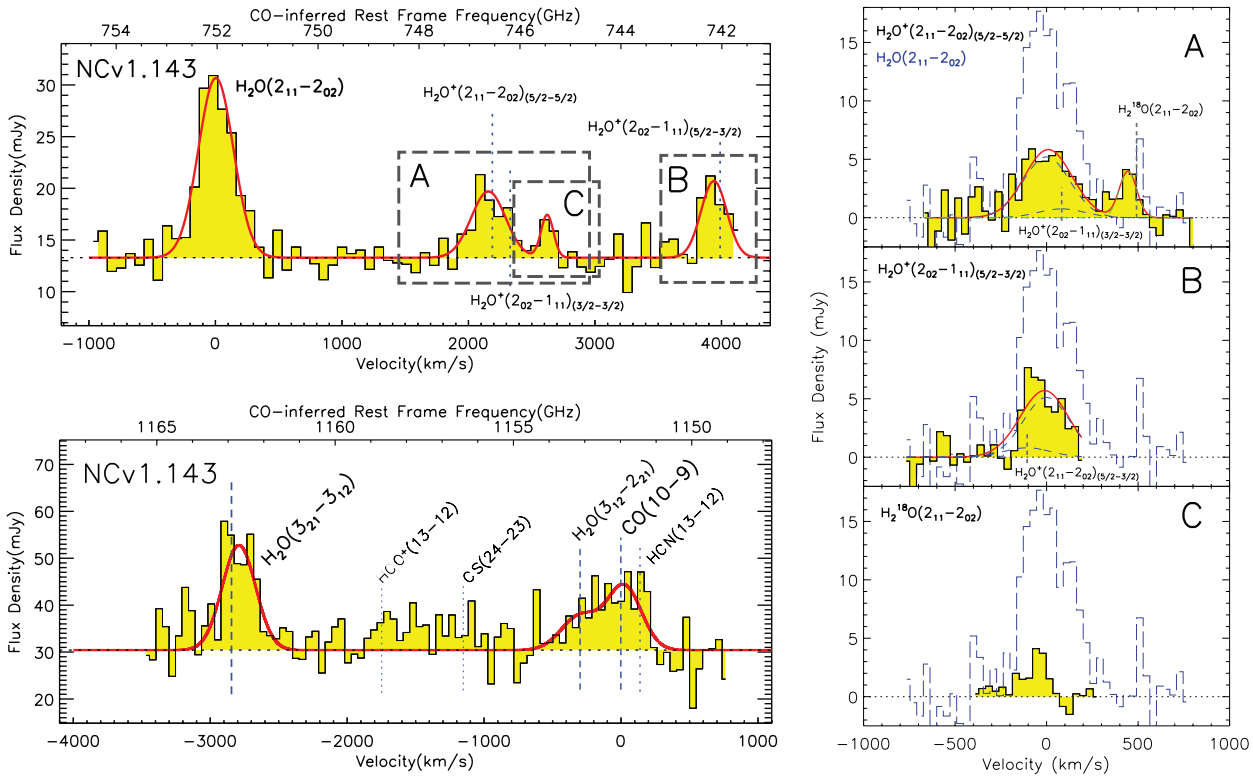

Fig. 5.9 NOEMA space integrated spectra of molecular lines. The red curve represents the Gaussian fitting to the spectra, and the green dashed curves are the decomposed Gaussian profiles for each fine structure line. *Top left*, 738–755 GHz rest frequency range with H_2O, H_2O^+ and $H_2^{18}O$ lines (merged data of extended and compact configurations). The three dashed rectangles show the position of each H_2O^+ (or $H_2^{18}O$) spectrum displayed in rows A, B or C of the right column: *First row A*: Spectra of $H_2O^+(2_{11}–2_{02})$ $_{(5/2–5/2)}$, $H_2O^+(2_{02}–1_{11})$ $_{(3/2–3/2)}$ and, possibly $H_2^{18}O(2_{11}–2_{02})$ displayed as the filled yellow histograms. The reference frequency is the frequency of the line $H_2O^+(2_{11}–2_{02})$ $_{(5/2–5/2)}$. $H_2O^+(2_{02}–1_{11})$ $_{(3/2–3/2)}$ and $H_2^{18}O(2_{11}–2_{02})$ lines are indicated by gray vertical dashed lines. *Second row B*: Spectra of $H_2O^+(2_{02}–1_{11})$ $_{(5/2–3/2)}$ and $H_2O^+(2_{11}–2_{02})$ $_{(5/2–3/2)}$. The reference frequency is the frequency of the line $H_2O^+(2_{02}–1_{11})$ $_{(5/2–3/2)}$. The grey vertical dashed line represents the position of the $H_2O^+(2_{11}–2_{02})$ $_{(5/2–3/2)}$ line. *Third row C*: Spectrum of $H_2^{18}O(2_{11}–2_{02})$ after subtracting the H_2O^+ lines, with the reference frequency set as the frequency of the $H_2^{18}O(2_{11}–2_{02})$ line. For all panels, the superposed blue dashed histograms represents the spectra of para-$H_2O(2_{11}–2_{02})$ in each source. *Bottom left*, 1149-1165 GHz rest frequency range with CO(10-9), blended with $H_2O(3_{12}–2_{21})$, and $H_2O(3_{21}–3_{12})$ (extended configuration data only). The positions are also indicated for HCN(13–12), HCO^+(13–12) and CS(24–23).

Figure 5.9 displays the space-integrated NOEMA spectra in the two observed windows: at 2 mm corresponding to the range 742–754 GHz in the rest frame, and at 1.2 mm corresponding to rest-frame frequency range of 1159–1166 GHz. As already shown in Chapter 3 and also in the previous Section 5.3.1.1,

the 742–754 GHz rest-frame frequency range includes not only one of the strongest H_2O lines, para-$H_2O(2_{11}–2_{02})$ line, but also two strong H_2O^+ lines ($H_2O^+(2_{11}–2_{02})_{(5/2–5/2)}$ and $H_2O^+(2_{02}–1_{11})_{(3/2–3/2)}$), two weak H_2O^+ lines ($H_2O^+(2_{02}–1_{11})_{(5/2–3/2)}$ and $H_2O^+(2_{11}–2_{02})_{(5/2–3/2)}$) and also the line $H_2^{18}O(2_{11}–2_{02})$. The high S/N spectrum from 2 mm observations allows us to acquire good-quality profile of $H_2O(2_{11}–2_{02})$, which can be well fitted by a single narrow Gaussian profile. (see Table 5.3 for a summary of the resulted velocity-integrated flux and linewidth). The values are consistent with those reported in our previous work, Yang et al. (2016), summarised in Chapter 3. The same is true for the two strong lines of H_2O^+ with improved S/N ratios. These new data slightly improve the tentative detection of $H_2^{18}O(2_{11}–2_{02})$ with NOEMA in this source with a velocity integrated flux 0.51 ± 0.14 Jy km s^{-1}with peak flux around ~ 4.5 mJy, in agreement with the value of integrated flux 0.6 ± 0.2 Jy km s^{-1} reported in Yang et al. (2016) (see also Section 3.2).

The signal to noise ratio of our 1.2 mm spectrum is worse than the 2 mm one, due to the limited on-source observing time and the less favourable atmospheric transmission at 1.2 mm. The bottom left panel of Fig. 5.9 shows the spectral data, which includes the two strong lines CO(10–9) and $H_2O(3_{21}–3_{12})$. Close to the line of CO(10–9), there is another weak H_2O line of the transition $3_{12}–2_{21}$. To deblend the contribution of this line to the CO, we fix the centre velocity of the $H_2O(3_{12}–2_{21})$ line while performing the Gaussian fitting to the spectrum. The contribution from the $H_2O(3_{12}–2_{21})$ is thus up to 30%. Their inferred velocity-integrated line flux and linewidth are reported in Table 5.3. Comparing with the continuum flux and the line flux from NOEMA compact D-configurations (Yang et al., 2016), we find that the continuum flux from our extended A-configuration data is about $\sim 50\%$ weaker. For the H_2O line, as mentioned in Section 5.3, the flux is also weaker by about 20%. This suggests that our long-baseline NOEMA observation at 1.2 mm has resolved out the extended emission from both the dust and the H_2O (see Fig. 5.10 for a comparison of the 1.2 mm dust continuum image between the before-combination and after-combination data). Moreover, from the fraction of the missing flux, one may expect that the dust emission has more extended structure comparing with that of H_2O. To further check if the missing flux is caused by the missing information from the short spacing sampling in the uv-plane (recall that the shortest

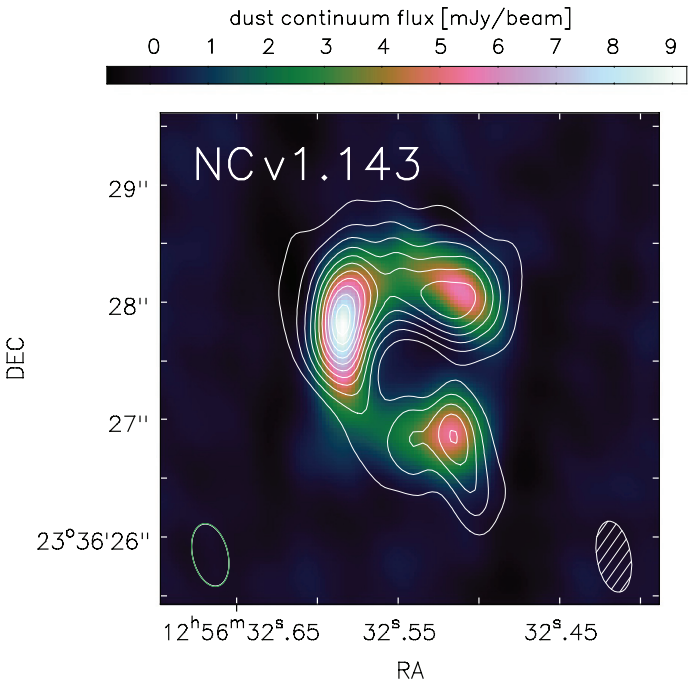

Fig. 5.10 Effect of the NOEMA A-configuration filtering the extended emission. NOEMA 1.2 mm continuum imaging data of NCv1.143 with angular resolution ~0.5" ×0.3" (using only A-configuration data) shown by the background colour image and the A- and D-configuration data combined interferometric data image of the dust continuum with an angular resolution ~0.6" ×0.3" shown in white contours (in steps of 6σ). It is shown that there is extended emission from the dust that might be resolved out by the A-configuration data only. Green ellipse indicates the beam for the A-configuration data only, while the white one shows the beam from the combined data.

baseline used in this observation is about 90 m), we combined the low resolution 1.2 mm data, and created a new visibility table for the overlapping frequency range between these two datasets. The combined data only cover the $H_2O(3_{21}–3_{12})$ emission, while we find the flux now agrees well with the results from low resolution observations. Here we recall again, NCv1.143's fluxes of CO(10–9) and $H_2O(3_{12}–2_{21})$ reported in Table 5.3 are affected by the missing fluxes.

Also note that there seems to be an excess of broad emission in the frequency range between these two lines (lower panel of Fig. 5.9), whose strength is around 1–2 σ noise level. Although such an excess is not significant considering the noise level, the continuous positive excess should raise some caution on interpreting the spectrum. This could be explained by an underestimation of the continuum level or the emergence of weak emission lines around 1155 GHz to 1160 GHz at the rest frame. However, deeper observations are needed to confirm the latter.

5.3.2.2 Images of NCv1.143: continuum and lines

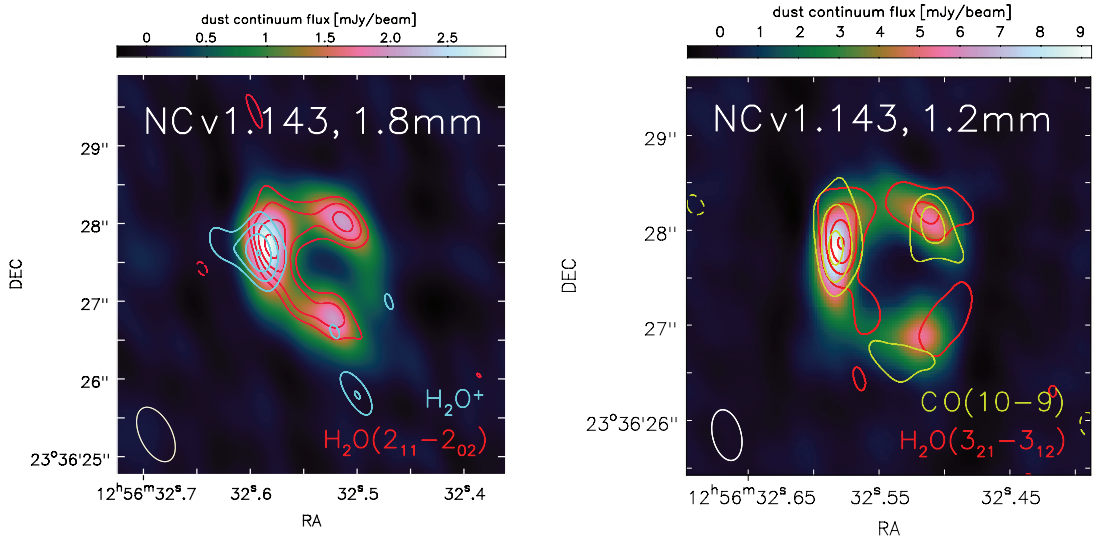

Fig. 5.11 NOEMA images of NCv1.143: 1) Dust continuum observed at ~1.8 mm and ~1.2 mm, i.e. at ~390 μm and ~260 μm, respectively, in the rest frame, represented by colour images with colour code displayed on top of the images. 2) CO(10–9) line, green contours. 3) $H_2O(2_{11}–2_{02})$ and $H_2O(3_{21}–3_{12})$ lines, red contours. 4) Sum of the four H_2O^+ lines, cyan contours. The beamsize can be found in Table 5.2. The contour levels are: in steps of 1 σ started from $\pm 3\,\sigma$ for the $H_2O(2_{11}–2_{02})$ and the H_2O^+ lines; and in steps of 3 σ started from $\pm 3\,\sigma$ for the $H_2O(3_{21}–3_{12})$ and the CO(10–9) lines.

The 0.7"×0.4" and 0.5"×0.3" resolution NOEMA images of NCv1.143 at 1.8 mm and 1.2 mm band, respectively, are displayed in Fig. 5.11. The images show the dust continuum emission at ~ 390 μm (left) and ~ 260 μm (right) in the rest frame, and also several line emissions including the CO(10-9) line, the $H_2O(2_{11}–2_{02})$ and $H_2O(3_{21}–3_{12})$ lines and the total emission from the four H_2O^+ lines (see section 5.3.2.1). In almost all the images, we find typical gravitationally lensed structures as multiple emission components with arc-like morphologies. This source is a typical galaxy-galaxy lensing system, although we lack high quality image of the foreground source (Fig. 5.5). The three emission components agree with the moderate resolution images from Bussmann et al. 2013's SMA 880 μm observations. Among the three components the East one is by far the strongest, while the two West ones are comparable in strength in dust emission. Nevertheless, for both H_2O lines and the CO line, the northern one is a bit stronger than the southern one as shown in Fig. 5.11. The broken Einstein ring has a radius ~ 1".

These images of the dust continuum and those of the CO and H_2O lines will be further analysed in Section 5.4 and used there to reconstruct the source structure from lensing modelling. We will discuss in the following sections whether any apparent differences between these images are significant and might provide important information about the source properties.

5.4 Lens models and continuum image reconstruction

5.4.1 Lens models

In order to derive the intrinsic properties of the background lensed SMGs, lens models need to be built upon both the high-resolution imaging data of the background $z \sim 3.6$ SMGs, but also the optical/NIR images that help us modelling the gravitational potential of the foreground deflectors. We stress here that the study of the detail structure of the deflector or the methodology of solving the lensing parameters is beyond the scope of this work. The core interest is rather to learn about the properties of the lensed SMGs.

As already identified in Bussmann et al. (2013) and in the previous sections and chapters, both G09v1.97 and NCv1.143 are identified as cases of macrolensing, in radius of the order of arcsecs (Treu 2010 and Fig. 5.5). In this type of galaxy-galaxy lensing, with a simple lens model, e.g. a singular isothermal ellipsoid (SIE) model (Kormann et al., 1994), one could reproduce the positions and fluxes of the multiple lensed signatures (or recover the intrinsic source positions and fluxes from the observed lensed images), and also derive the properties of the deflector(s) based on the assumptions of the mass profiles. With the ~ 1.0" SMA beam, Bussmann et al. (2013) used the `GRAVLENS` software (Keeton, 2001) to derive the emission of the image plane from the source plane and compare it with the SMA CLEANed images. SIE profiles were used for the foreground deflectors while the authors assumes that the emission from the background sources can be well described by Sérsic profiles (Sersic, 1968). Then, they derive the parameters of both the deflectors' SIE profiles (position of the deflector, its velocity dispersion which is related to the Einstein radius, the ellipticity and the position angle) and the lensed-sources' Sérsic profiles (Sérsic index, the position of the background source, half-light major axis length, ellipticity and position angle) using a χ^2 fitting technique.

Here we stress again that the best images of G09v1.97 and NCv1.143 reported in this chapter have a resolution of 0.3"–0.4", being about twice better than the SMA images from Bussmann et al. (2013). Besides the dust continuum images, we also acquired the datacubes including the images from the line emission at different velocity channels. These rich datasets offer great information about the lensed systems.

We followed a similar approach as described in Gavazzi et al. (2011) for the modelling of Lock01, another *Herschel* lensed SMG. As Bussmann et al. 2013, we assume that deflectors are made of one (for NCv1.143) or two (for G09v1.97) SIE mass distributions whose centre is allowed to vary within 0.5" from the optical centre of the foreground galaxies. The parameter encoding for the strength of the deflector, or in other words the depth of the lensing potential, is the velocity dispersion σ_v, which is related to the Einstein radius by $R_{\rm Ein} = 4\pi\,(\sigma_v/c)^2$, in radians. The axis ratio q and orientation of the major axis in the plane of the sky are also left free.

The emitted light is assumed to be well captured by an elliptical exponential light profile, since the data do not have enough signal-to-noise to constrain a more flexible Sérsic profile. Bussmann et al. (2013) found that most of their de-lensed sources are well fitted with Sérsic indices consistent with unity, i.e. with exponential profiles. Unlike these authors, we use `sl_fit` a lens inversion code that is mostly tailored to fit optical/NIR data. We could not fit visibilities in the uv-plane with this code, as this feature is not

implemented yet but tried to account for synthesised beam and noise correlation in the CLEANed images, as described in (Gavazzi et al., 2011). A MCMC method, implementing the standard Metropolis-Hastings algorithm, was deployed to explore the parameter space and build samples of the parameters posterior probability distribution function.

Since continuum images generally are of substantially higher signal-to-noise, we used the integrated continuum dust emission to constrain the mass distribution and dust emission at the same time. Then, the best fit model is used to send back line emission in narrow frequency channels into the source plane and recover intrinsic magnification-corrected gas properties. We found this approach to capture most of the information content in the data. Deeper and higher resolution data would require a joint fit to continuum and line emission, and eventually to allow the large flexibility offered by a pixelated source as for the long baseline ALMA data of SDP81 (e.g. Dye et al., 2015).

We list the results of our lensing modelling using the dust continuum images in Tables 5.4 and 5.5. Positions for G09v1.97 are expressed in arc seconds relative to the reference position $\alpha = 08:30:51.166$ and $\delta = +01:32:24.20$. For NCv1.143, positions are expressed relative to the reference position $\alpha = 12:56:32.544$ and $\delta = +23:36:27.35$. Position angles of the major axis of ellipses is defined in degrees East of North. For line emissions, we report source parameters for the channel closest to the frequency centre of the line whereas magnification is integrated over the entire line.

5.4.1.1 G09v1.97

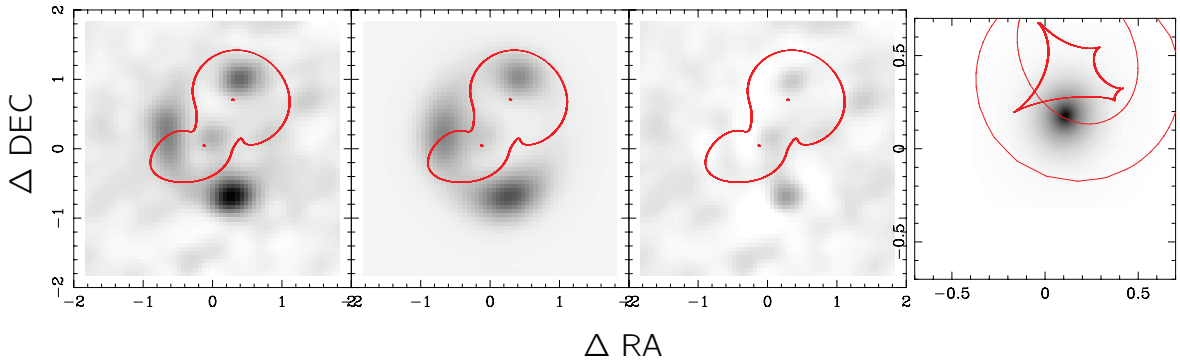

Fig. 5.12 Best-fit lens model of the dust continuum emission in G09v1.97. *From left to right*: 1) Observed image of the 2 mm continuum (see also Fig. 5.8). 2) Image reconstructed with the lens model parameters of Table 5.4. 3) Residuals from the difference between observed and model images. For 1) to 3), two red points indicates the best fitted positions of the two deflectors. The red line shows the critical curve. 4) Reconstructed dust continuum emission in the source plane. The red lines show the caustics.

The existence of a secondary lensing galaxy close to the northwest position of the primary one makes the lensing configuration an uncommon case. Using the lens model described above, we have constrained the mass model of the lensing deflectors of G09v1.97 at redshift $z = 0.626$ and $z = 1.002$ (as identified in Bussmann et al. 2013) from the 2 mm continuum image, with the parameters reported in Table 5.4. As shown in Fig. 5.12, this model provides a very good fit to the observed image of the 2 mm continuum and it has allowed us to reconstruct the image of the dust continuum emission in the source plane with a good accuracy. As reported in Table 5.4, it provides values for the average magnification factor of the 2 mm dust

continuum, $\mu_{2\,\mathrm{mm}} = 7.2 \pm 0.5$, and the radius of its extension, $R_{\mathrm{eff}} = (1.25 \pm 0.15)$ kpc, in general agreement with the values of Bussmann et al. (2013), $\mu_{880} = 6.9 \pm 0.6$ and $R_{\mathrm{eff}} = (0.85 \pm 0.07)$ kpc.

Table 5.4 Lens modelling results for G09v1.97

Parameters of SIE mass components				
x_{def} arcsec	y_{def} arcsec	q_{def}	$\mathrm{PA}_{\mathrm{def}}$ deg	R_{Ein} arcsec
-0.127 ± 0.266	0.045 ± 0.211	0.47 ± 0.18	-67 ± 35	0.441 ± 0.161
0.289 ± 0.292	0.706 ± 0.228	0.97 ± 0.21	4 ± 51	0.660 ± 0.164

Parameters of reconstructed source						
	x_{src} arcsec	y_{src} arcsec	q_{src}	$\mathrm{PA}_{\mathrm{src}}$ deg	R_{eff} arcsec	μ
continuum	0.110 ± 0.266	0.179 ± 0.211	0.87 ± 0.15	75 ± 25	0.17 ± 0.02	7.2 ± 0.5
CO(6–5)	0.089 ± 0.025	0.221 ± 0.025	0.73 ± 0.10	89 ± 48	0.189 ± 0.040	7.8 ± 1.0
$H_2O(2_{11}–2_{02})$	0.094 ± 0.018	0.235 ± 0.027	0.71 ± 0.10	77 ± 41	0.183 ± 0.040	6.9 ± 1.0

The ALMA high-quality datacubes of the $H_2O(2_{11}–2_{02})$ and CO(6–5) line of G09v1.97 allow us to perform the lens modelling as mentioned above for the images of the line emission at several velocity values. This enables us to not only study the intrinsic emission of the H_2O and CO lines, but also analyse the velocity structure of both lines in the source plane. The related discussion will be given in Section 5.5. Nevertheless, by comparing the intrinsic size of the $H_2O(2_{11}–2_{02})$ and the CO(6–5) line emission with that of the dust continuum, we find that the latter is smaller by a factor of 0.9 ± 0.2. This difference is much less significant than those found in NCv1.143 as we shall see in the following subsections. Nevertheless, a smaller size of the dust emission is consistent with other observation results of lensed SMGs (e.g. Fu et al., 2012; Spilker et al., 2015)

5.4.1.2 NCv1.143

Table 5.5 Lens modelling results for NCv1.143

SIE mass component				
x_{def} arcsec	y_{def} arcsec	q_{def}	$\mathrm{PA}_{\mathrm{def}}$ deg (East of North)	R_{Ein} arcsec
[0]	[0]	0.65 ± 0.03	-62 ± 2	0.69 ± 0.01

reconstructed source						
	x_{src} arcsec	y_{src} arcsec	q_{src}	$\mathrm{PA}_{\mathrm{src}}$ deg	R_{eff} arcsec	μ
continuum	$+0.000 \pm 0.004$	-0.093 ± 0.008	0.76 ± 0.07	-37 ± 16	0.113 ± 0.017	12.2 ± 1.2
CO(10–9)	-0.029 ± 0.016	-0.125 ± 0.016	0.40 ± 0.19	-38 ± 17	0.111 ± 0.032	10.1 ± 1.3
$H_2O(2_{11}–2_{02})$	$+0.006 \pm 0.026$	-0.123 ± 0.040	0.63 ± 0.17	25 ± 30	0.23 ± 0.10	8.3 ± 1.8
$H_2O(3_{21}–3_{12})$	$+0.102 \pm 0.019$	-0.106 ± 0.016	0.69 ± 0.13	-17 ± 60	0.158 ± 0.030	9.4 ± 1.0
H_2O^+	-0.20 ± 0.12	-0.06 ± 0.09	0.54 ± 0.18	43 ± 60	0.38 ± 0.20	5.0 ± 2.0

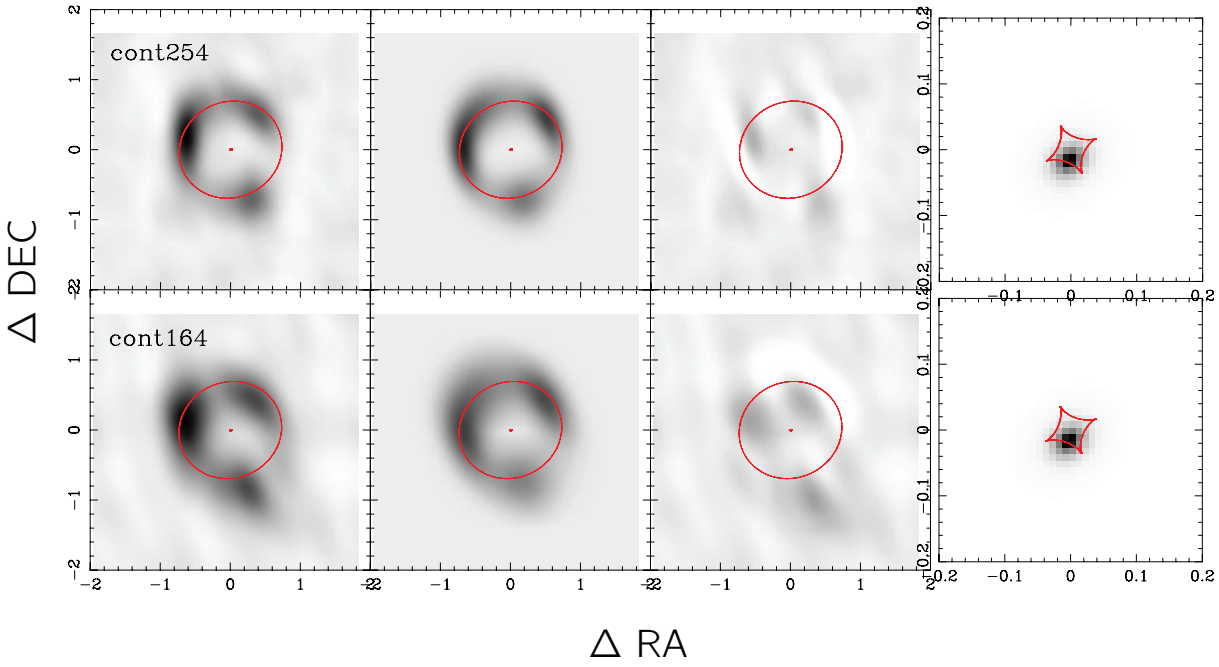

Fig. 5.13 Lens model of the 254 GHz (top row) and 164 GHz (bottom row) dust continuum emission in NCv1.143. *From left to right*: 1) Observed image of the 2 mm continuum. 2) Model images with the model parameters of Table 5.5. 3) Residuals from the difference between observed and model images. 4) Reconstructed image of the dust continuum emission in the source plane. The critical curves and caustics are shown in red lines in the first three column and the fourth columns, respectively. The position of the deflector are indicated by red points.

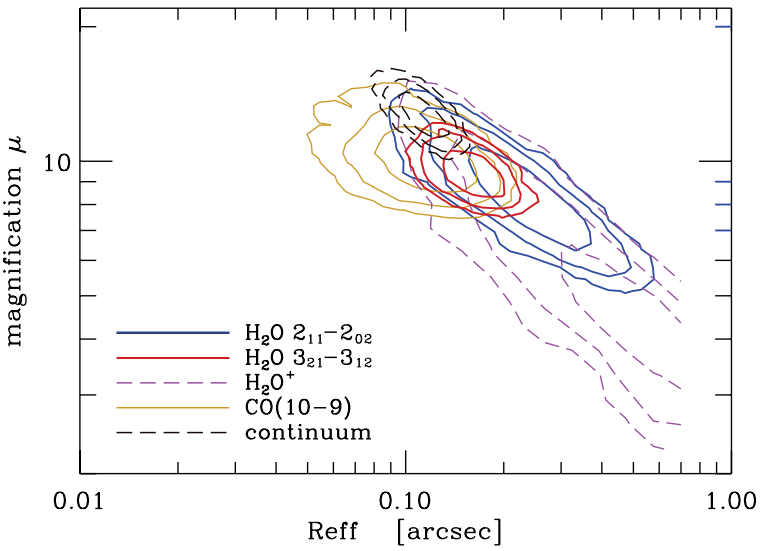

Fig. 5.14 Posterior possibility distributions of the $R_{\rm eff}$ and μ from the MCMC sampling. The contours are from 1 σ to 3 σ from inside out. Solid blue line, solid red line, dashed purple line, solid yellow line and the dashed black line indicate the results of $H_2O(2_{11}–2_{02})$, $H_2O(3_{21}–3_{12})$, H_2O^+, CO(10–9) and the dust continuum, respectively.

Using similar methods for G09v1.97, we have built lens models of the dust continuum images for NCv1.143. We have constrained the mass model of its lensing deflector at redshift z = 0.255 (Bussmann et al., 2013) from the 1.2 mm and 2 mm continuum images, with the parameters reported in Table 5.5. The two continuum images were simultaneous fitted with the assumption that their morphologies are identical in both channels. As shown in Fig. 5.5, this model provides a very good fit to the observed images of the 2 mm and 1.2 mm continuum and it has allowed us to reconstruct the image of the dust continuum emission in the source plane with a good accuracy. As reported in Table 5.5, it provides values for the average magnification factor of the dust continuum, $\mu_{2\,\rm mm}$ = 12.2±1.2, and the radius of its extension, $R_{\rm eff}$ = (0.8±0.1) kpc, in good agreement with, but with

a better accuracy than Bussmann et al. 2013's value of μ_{880} = 11.3±1.7. However, we find the size of the source is about twice larger than (0.4±0.1) kpc found in Bussmann et al. (2013). This will reduce the surface star formation rate they found for NCv1.143 from 2080 $M_\odot$ yr^{-1} kpc^{-2} down to ~ 1000 $M_\odot$ yr^{-1} kpc^{-2}. Such a difference could arise from a different estimation of the source position, namely that the source plane image in our lens model is a bit further from the caustic curve comparing to Bussmann et al. 2013's results.

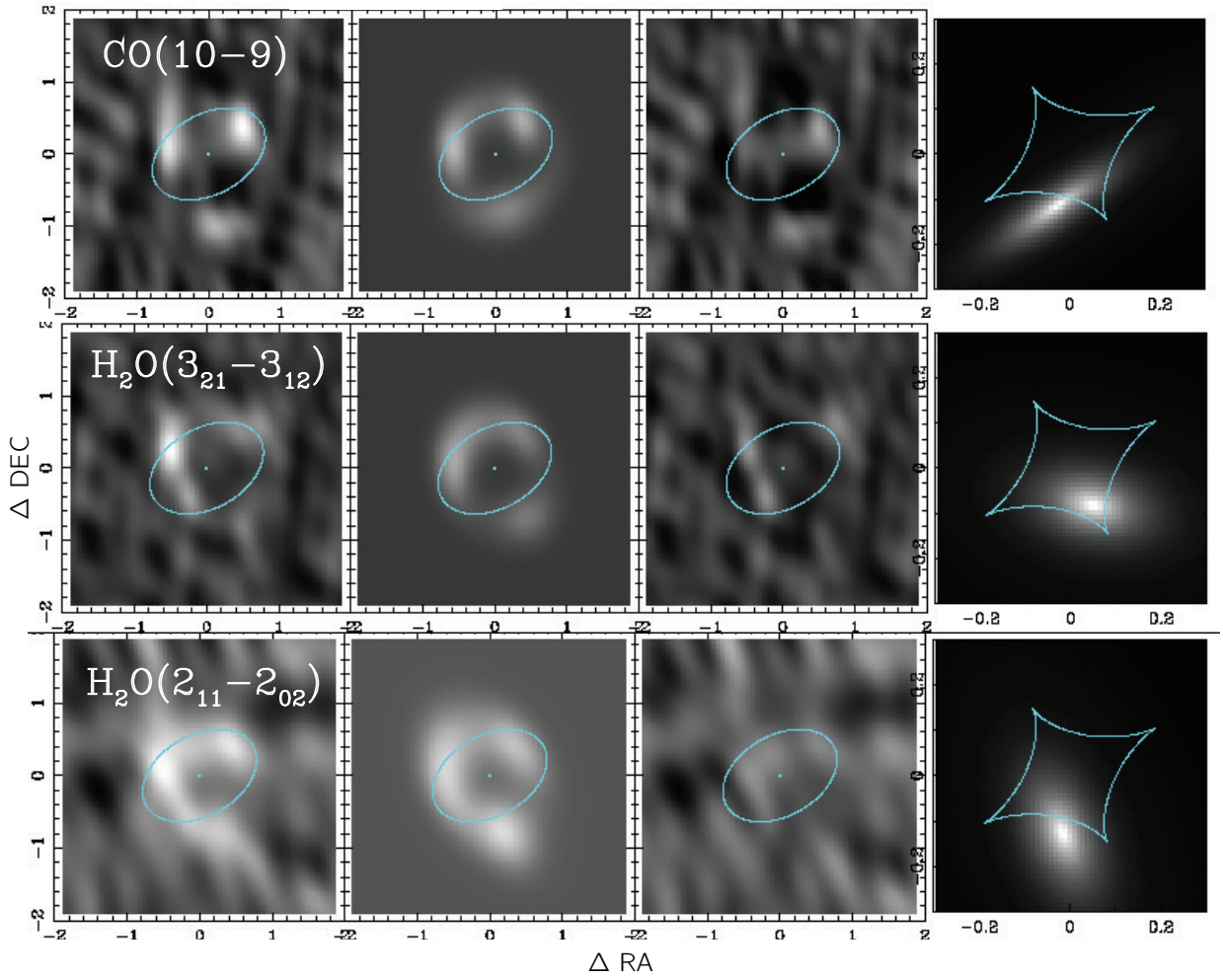

Fig. 5.15 *From top to bottom, each row*: Lens model of the CO(10–9), $H_2O(3_{21}–3_{12})$ and $H_2O(2_{11}–2_{02})$ lines in NCv1.143. *From left to right*: 1) Observed CLEANed images of the emission line. 2) Model images with the model parameters of Table 5.5. 3) Residuals from the difference between observed and model images. 4) Reconstructed images of the emission line in the source plane. The critical curves and caustics are shown in cyan lines in the first three columns and the fourth column, respectively. The position of the deflector is indicated by the cyan points. One should note that the position of the background source in the source plane is not well constrained. Thus, the differences seen in the positions of the three lines are not significant considering the uncertainties.

With the robust SIE models derived from dust continuum, we are able to apply such a mass distribution profile to the lens models of the H_2O and CO lines in NCv1.143. This could help reducing the uncertainties considering the limited S/N levels of the line emission images, so that the only variables are the ones that describe the Sérsic profiles for the line emissions. The best-fit results are shown in Fig. 5.15. From the figures, we see that the models can generally well recover the fluxes in the CLEANed images. The position

angle of the Sérsic profiles are not well constrained, though this will not much influence our conclusions in this work. Fig. 5.14 shows the posterior distributions of the fitted effective radius ($r_{\rm eff}$) versus the average magnification factor over the entire source. These results are summarised in Table 5.5. It is clearly shown in Fig. 5.14 that the size of dust emission and that of the CO(10–9) line emission are the most compact ones, which is about 0.111", corresponding to a physical scale of 0.8 kpc. The size of $H_2O(3_{21}–3_{12})$ is a bit larger but still close to that of the CO(10–9) line. The fitted $r_{\rm eff}$ is ~ 1 kpc. For the lowerly-excited $H_2O(2_{11}–2_{02})$ line, the size is ~ 2 kpc, being somewhat larger comparing to the dust emission and that of the CO(10–9) and $H_2O(3_{21}–3_{12})$ line. As mentioned in Chapter 3, especially Section 3.3.5, in NCv1.143, the excitation of the $H_2O(3_{21}–3_{12})$ line is dominated by far-IR pumping, while there exists a significant contribution from collisions to the more extended molecular gas component in which the $H_2O(2_{11}–2_{02})$ line is excited. Thus, the resulting differences in $r_{\rm eff}$ between CO(10–9)/$H_2O(3_{21}–3_{12})$/continuum and $H_2O(2_{11}–2_{02})$ is consistent with the far-IR pumping model. Nevertheless, from the excitation modelling of the observed $H_2O(2_{11}–2_{02})$, $H_2O(3_{21}–3_{12})$ and $H_2O(4_{22}–4_{13})$ lines (Section 3.3.5), the resulted sizes of both the cool and warm components are under-predicted by a small factor (Section 3.3.6).

5.5 Spatial and velocity structure of molecular lines in G09v1.97

The high-quality ALMA datacube of the line emission from G09v1.97 allows us to perform the lensing analysis for different velocity components, thus enabling us to reconstruct the velocity structures in the source plane. In the following sections, we will perform the analysis of the source properties for various velocity structures of the CO(6–5) and $H_2O(2_{11}–2_{02})$ lines. After binning the data cube into several velocity channels for the CO(6–5) and $H_2O(2_{11}–2_{02})$ lines, we use the SIE parameters derived from the lens model of the dust continuum (Table 5.4) to derive the source parameters for each velocity channel (including $x_{\rm src}$, $y_{\rm src}$, $q_{\rm src}$, $\rm PA_{src}$ and $R_{\rm eff}$). For the image of each velocity channel, we assume that the emission can be described by a single elliptical exponential light distribution and the deflector's mass profile of G09v1.97 is approximated by the two-SIE mass distribution (Section 5.4.1.1) derived from the dust-emission lens modelling. Then, we added the modelled (image plane) images weighted by their emission strength from each velocity channel together to compare with the observed velocity structure. The source plane velocity map can also be produced by adding the source plane image from each velocity channel. Although the smoothness of the reconstructed velocity fields in both the image and source plane depends a lot on the aforementioned assumptions, this is a good approximation given the current spatial resolution and sensitivity.

5.5.1 CO(6–5) line

Figure 5.16 displays the modelling of the velocity structure of the CO(6–5) line emission in G09v1.97. As mentioned in the previous sections, we have applied the SIE models of the deflector derived from the modelling of the dust continuum emission. Thus, we could build robust lens models for the CO(6–5) line emission of each channel representing different velocity components. In this figure, we compare the observed emission with its velocity structure to the model results. We find that our model produces images in the image plane that agree well with the observation. The reconstructed source in the source

plane shows a velocity structure similar to a rotating disk, whose major axis is in the north-south direction. The reconstructed spectrum also agrees well with the observed data as shown in the bottom right panel of Fig. 5.6. The red velocity component in the south is close to the caustic while the blue one is slightly further away. This makes the magnification of the emission from the red velocity component larger than that of the blue one. This could partially explain the asymmetrical line profile as shown in Fig. 5.6, since the blue velocity component is indeed less magnified comparing to the red one. However, the intrinsic spectrum shown by the green histogram in Fig. 5.16 also shows such a pronounced asymmetry. It is clear that both the asymmetry of the intrinsic velocity profile and differential lensing significantly contribute to the strong global asymmetry of the observed line profile. Since the data is in high S/N levels, we will further analyse the dynamical models for this line emission in Section 5.5.3.

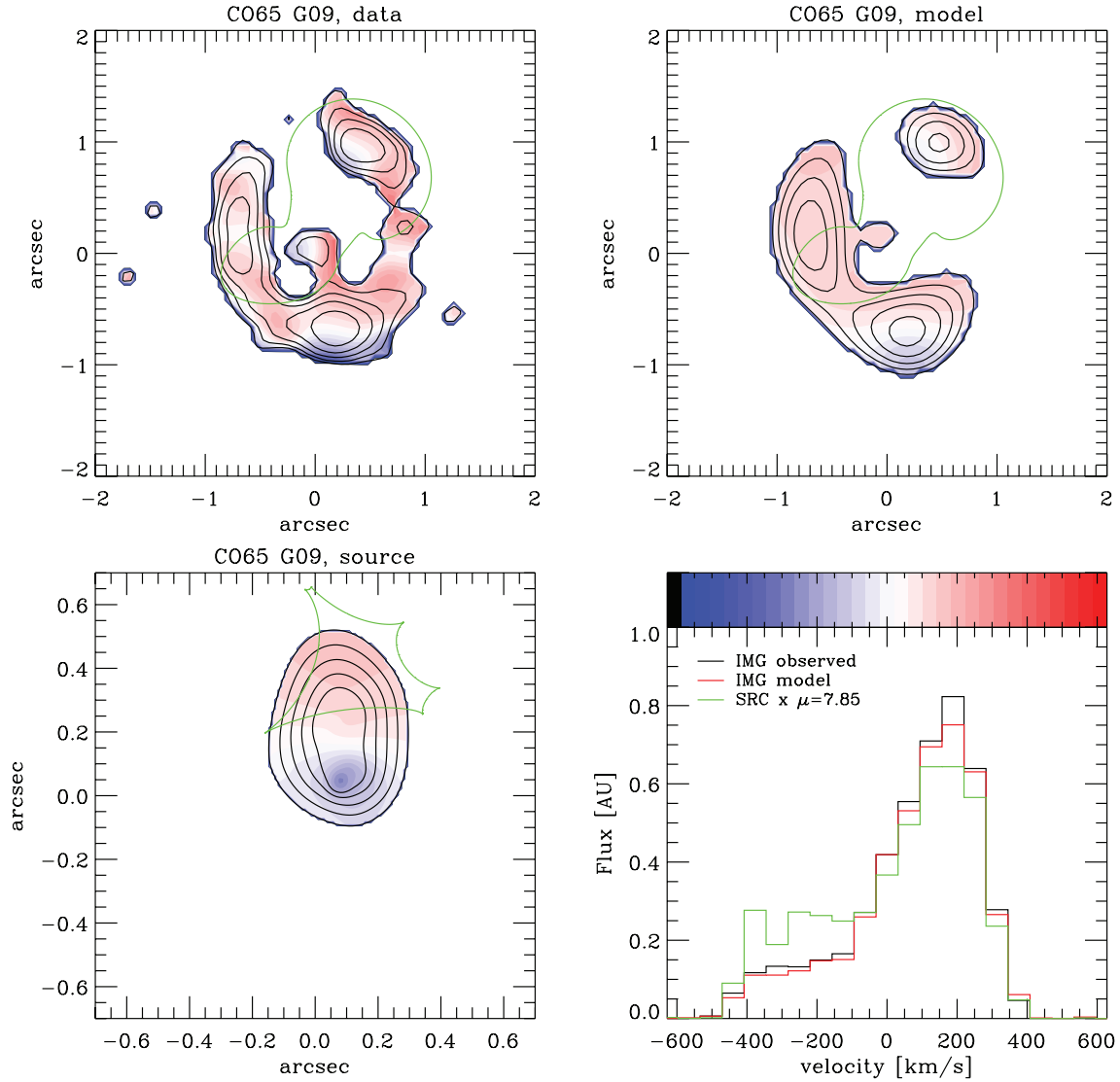

Fig. 5.16 Reconstructed CO(6-5) velocity map in G09v1.97 in several channels inside the line. *Top left*, colour-coded observed image. *Top right*, colour-coded model image (1" = 7.4 kpc). *Bottom left*, inferred colour-coded source plane emission spatial structure. *Bottom right*, rebinned line velocity profile: *black*, observed; *red*, modelled; *green*, in the source plane multiplied by a factor of 7.85 for comparison. "IMG" stands for image plane while "SRC" means source plane results.

5.5.2 H_2O line

Although the S/N level of the H_2O image is a bit lower than that of the CO(6–5), we were able to perform similar modelling as in Section 5.5.1. Fig. 5.17 displays the lens model of the $H_2O(2_{11}–2_{02})$ line in various velocity channels. The emission and the velocity structure of the H_2O line are very similar to those of the CO(6–5). However, there exists some small difference in the velocity structures between the CO(6–5) and $H_2O(2_{11}–2_{02})$ line, as mentioned in the spectral data comparison in Section 5.3.1.1, the $H_2O(2_{11}–2_{02})$ line is more red-shifted by 50 km s^{-1}. When comparing the emission extension, similar to the CO(6–5) line, the $H_2O(2_{11}–2_{02})$ molecular emission is found to be a bit more extended than the reconstructed continuum image of the dust emission (Fig. 5.8 and Table 5.4). When comparing the $H_2O(2_{11}–2_{02})$ image with that of the CO(6–5) the H_2O and CO emission appear to be similar.

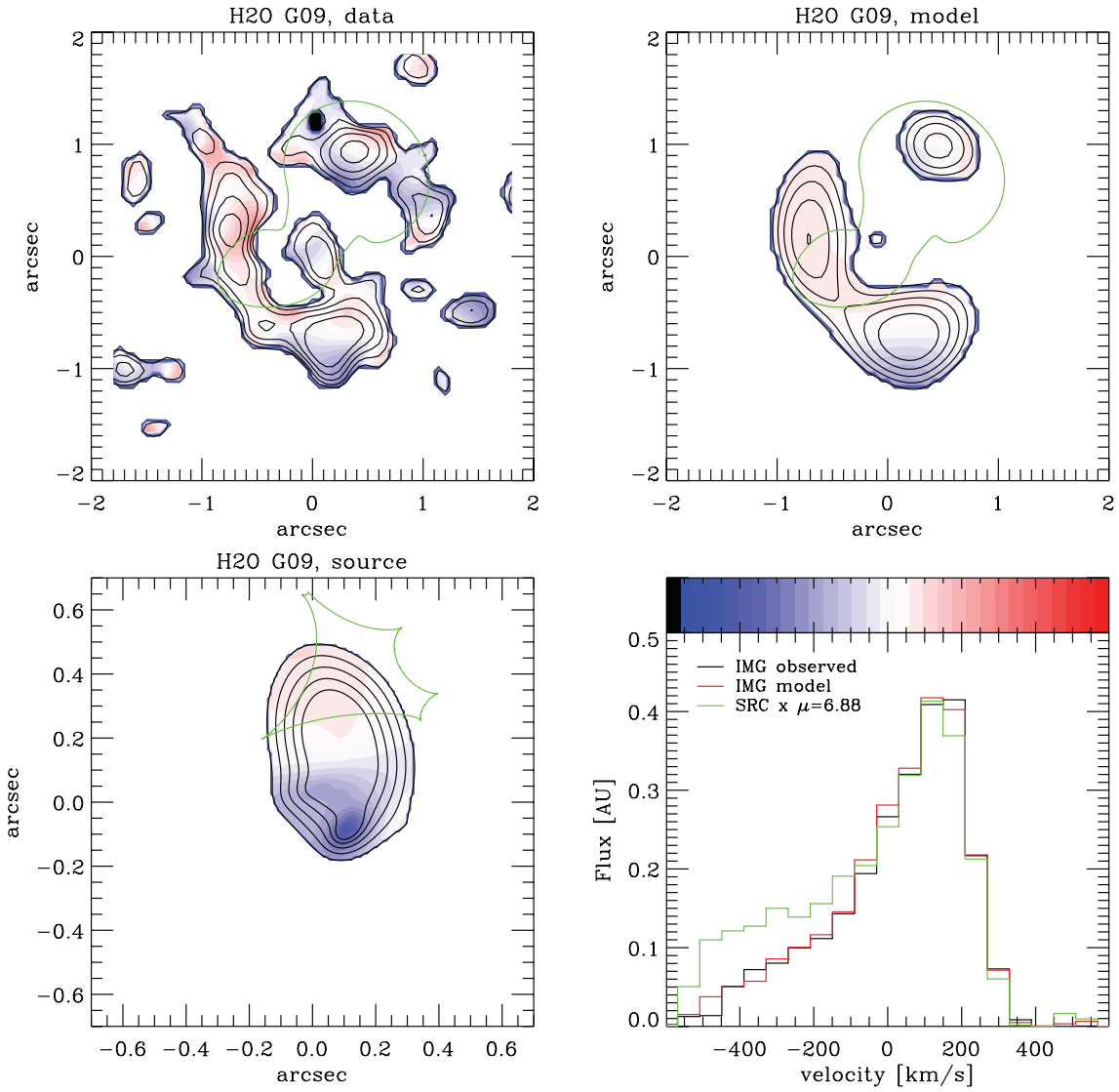

Fig. 5.17 Reconstructed $H_2O(2_{11}–2_{02})$ velocity map in G09v1.97 in different channels around the line. *Top left*, colour-coded observed image. *Top right*, colour-coded model image (1" = 7.4 kpc). *Bottom left*, inferred colour-coded source plane emission spatial structure. *Bottom right*, rebinned line velocity profile: *black*, observed; *red*, modelled; *green*, in the source plane multiplied by a factor of 6.88 for comparison. "IMG" stands for image plane while "SRC" means source plane results.

In the same way as for the CO line, it is seen that our model for the reconstructed H_2O profile shown in the bottom right panel of Fig. 5.17 reproduces a good part of the observed line asymmetry. It is confirmed that both the asymmetry of the intrinsic velocity profile and differential lensing significantly contribute to the strong global asymmetry of the observed $H_2O(2_{11}–2_{02})$ line profile.

5.5.3 Kinematical structure of G09v1.97

For the CO(6–5) line, the data allow us to perform an analysis of the gas dynamics using the lensing-model-reconstructed datacubes of the line emission. We thus, perform a kinematical modelling of the data using the same methods as in Gnerucci et al. (2011) (see also e.g. De Breuck et al., 2014; Paraficz et al., 2017).

The maps of the velocity structure of CO(6–5) as shown in the bottom right panel of Fig. 5.16 show typical signatures of a rotating disk. Such a gaseous disk regime is predicted by numerical models of SMGs, in which these populations of galaxies are dominated by secular evolution of massive gaseous disks (e.g. Hayward et al., 2012, 2011). Several observations also discovered disk-like SMGs (e.g. Hodge et al., 2012, 2016). However, some other observational results point out the nature of SMGs showing that they are dominated by major merger triggered bursts (e.g. Ikarashi et al., 2015; Tacconi et al., 2008) similar to local ULIRGs such as Arp 220. This regime of the nature of SMG is also supported by models of low-mass merging starbursts (Baugh et al., 2005).

We thus adopted a circularly rotating thin disk model for G09v1.97. We assume that the disk motion as traced by the CO(6–5) line is totally determined by the gravitational potential of the disk and neglect all the hydrodynamical influences. We also assume that the gravitational potential of the thin disk can be described by an exponential disk (Binney & Tremaine, 1987), so that the radial profiles of the surface mass density can be written as

$$\Sigma(R) = \Sigma_0 e^{-R/R_d}, \tag{5.1}$$

in which Σ_0 is the disk surface density, while $\Sigma(R)$ is the disk surface density at a radius of R, R_d is the disk radius. Following the calculation of Freeman (1970), the radial velocity distribution can thus be written as

$$V_c^2(R) = 4\pi G\Sigma_0 R_d y^2 [I_0(y)K_0(y) - I_1(y)K_1(y)], \tag{5.2}$$

in which $y = R/2R_d$, G is the gravitational constant, I_n and K_n are the Bessel functions of the first and second kind. Thus, the mass within the radius R can be calculated as

$$M(R) = 2\pi\Sigma_0 R_d^2 [1 - e^{-R/R_d}(1 + \frac{R}{R_d})]. \tag{5.3}$$

In order to fit the kinematic model to our data, we extract the velocity of the CO(6–5) line from the datacube in the source plane along the major axis as shown by the dashed line in Fig. 5.18. We then performed a χ^2 fitting to the data points of the line velocities along different radius. The best-fit results using the χ^2 gives a disk size r_e (or R_{eff}, the effective radius) of (0.6 ± 0.2) kpc, consistent with the size derived from lens modelling within $1\,\sigma$ uncertainty. In this analysis, we only fit the rotation curve along the major axis, thus it is impossible for us to disentangle the inclination angle from the modelling. Recall that the dynamical mass (the totally mass within r_e) can be expressed as

$$M_{dyn} \sin^2(i) = r_e V_c / G, \tag{5.4}$$

thus the fitted results give a projected dynamical mass $M_{\rm dyn}\sin^2(i) = (2.3\pm1.0)\times10^{10}\,M_\odot$. As suggested in Wang et al. (2013), the inclination angle can be inferred from the minor to major axis ratio $q_{\rm src}$ as $i = \cos^{-1}(q_{\rm src})$. The resulted inclination angle $i = 45\pm8°$. Thus, the dynamical mass of the source is likely to be $M_{\rm dyn} = (4.6\pm2.4)\times10^{10}\,M_\odot$, with a significant uncertainty. By taking the total molecular gas mass $M_{\rm gas} = (1.0\pm0.5)\times10^{10}\,M_\odot$ (see Yang et al, submitted in Chapter 4), we could derive a molecular gas mass fraction of $M_{\rm gas}/M_{\rm dyn}\sim25\%$, which is close to the values of other SMGs (e.g. Aravena et al. 2016b and the references within) and empirical model predictions (Béthermin et al., 2015).

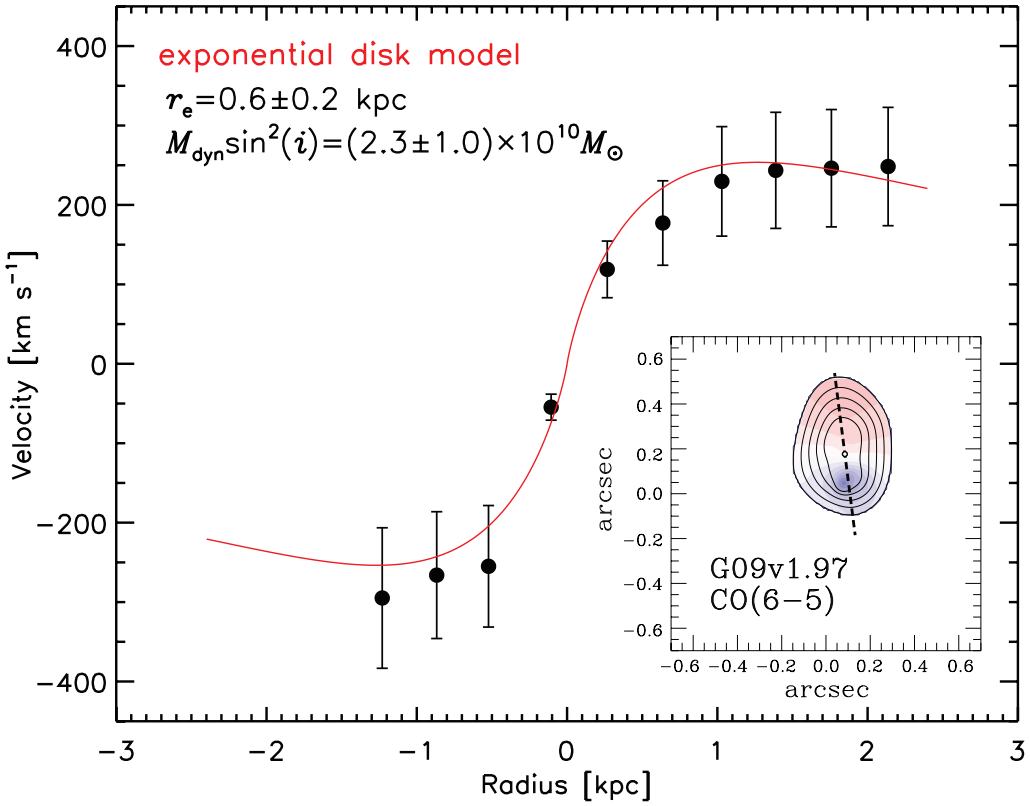

Fig. 5.18 Black data points show the measured velocity of the CO(6–5) line in G09v1.97 extracted along the major axis as indicated by the dashed line in the inset which displays the colour-coded velocity field of the source in the source plane. The fitted rotation curve based on an exponential disk model is shown by the solid red line. The best fitted parameters are indicated by the legends.

For gaseous disks, the Toomre Q parameter (Toomre, 1964) can be expressed as $Q(R) = \sigma(R)\kappa(R)/\pi G\Sigma(R)$, in which $\sigma(R)$ is the velocity dispersion at R, $\kappa(R)$ is the epicyclic frequency equal to aV_c/R (normally $a=\sqrt{3}$) (Wang & Silk, 1994). If the value of Q is smaller than 1, the disk will be unstable. At the radius $R = 0.6$ kpc, we find a Toomre Q value of $\lesssim0.5$, indicating that the disk is unstable. A slightly smaller value of Toomre Q has been found in SDP81, $Q = 0.30\pm0.10$ Swinbank et al. (2015), while in local ULIRGs, this Q value is a bit larger, $Q\sim1$ (Downes & Solomon, 1998).

5.6 Molecular gas properties as traced by CO, H_2O, H_2O^+ and $H_2^{18}O$ lines

In G09v1.97, the molecular gas emission is more smoothly distributed comparing with that of the dust continuum. The size and velocity structures are practically very similar for CO(6–5) and para-$H_2O(2_{11}$–$2_{02})$,

although a small shift in velocity was found in the spectral data. A difference can also be spotted in the line flux ratios between CO(6–5) and $H_2O(2_{11}–2_{02})$ for the blue and red velocity components, which are 1.6 ± 0.2 and 2.9 ± 0.4, respectively. Explanations such as the presence of a blue, warm, dense outflow, might be not excluded. The molecular gas traced by these two lines should correspond to the dense warm gas component found in modelling the excitation of CO in Chapter 4 with temperature $\gtrsim 150$ K and density $n_{H_2} \gtrsim 10^3 cm^{-1}$ (see Tables 6 and 7 of Section 4.2 for the LVG modelling results of the CO SLED in this source). Such high temperature and density should allow collisions to efficiently excite the relatively low $2_{11}–2_{02}$ energy level of H_2O in the extended warm component with also some contribution from far-IR pumping excitation.

Similar to the discovery we found in Yang et al. (2016) for NCv1.143, G09v1.97 and G15v2.779 (see also Chapter 3), using the new observations from ALMA, we derive that the ratio between the I_{H_2O} (transition $2_{11}–2_{02}$) and $I_{H_2O^+}$ (742.1 GHz line) is 3.6 ± 1.6 for the blue velocity component and 3.4 ± 1.5 for the red one, which agrees well with our previous findings. The line ratios are almost identical for the two velocity components, indicating very similar spatial distributions, thus kinematic structures, for H_2O and H_2O^+. Thus, in this case, any differential lensing between H_2O and H_2O^+ can be be negligible, the ratio between the observed flux can be treated as their intrinsic ratio. With this ratio, Meijerink et al. 2011's model suggests a high cosmic-ray ionization rate of 10^{-14}–10^{-13} s^{-1}. Such high cosmic-ray ionization rates drive the ambient ionization degree of the ISM to 10^{-3}–10^{-2}, rather than the canonical 10^{-4}. These cosmic rays are likely coming from intense massive star forming activities. They dominate the gas phase oxygen ion-neutral route of the oxygen chemistry (e.g. Meijerink et al., 2011; van der Tak et al., 2016).

Besides H_2O^+ lines, we also detected an emission line about 745.3 GHz, which can be explained by the emission from $H_2^{18}O(2_{11}–2_{02})$ ($E_{up} \sim 200$ K) with rest-frame frequency of 745.320 GHz. This important isotope molecule $H_2^{18}O$ (^{18}O is produced by He burning by massive stars, e.g. see Maeder 1983) has also been detected in emission in local ULIRGs as reported by our local *Herschel* archive survey (Yang et al., 2013) and also in the compact obscured nucleus in Zw 049.057 (Falstad et al., 2015). Several absorption lines of this molecule at shorter wavelength have also been detected by *Herschel*/PACS in local ULIRGs (González-Alfonso et al., 2012), thus pointing out that its excitation is much alike H_2O. The flux ratio between $H_2O(2_{11}–2_{02})$ and $H_2^{18}O(2_{11}–2_{02})$ is ~ 15. However, with only one line of $H_2^{18}O$ detected, it is very difficult to derive the abundance ratio of $^{18}O/^{16}O$, because of the very large optical thickness of the H_2O line. Note that this ratio could further help us to constrain the stellar IMF, since ^{18}O is a secondary nuclide as mentioned above.

After combining our new high-resolution NOEMA observation of NCv1.143 with our previous compact configuration data, we are able to improve the spectra quality comparing to that in Yang et al. (2016) and Chapter 3. With the combined data, we now confirm our detection of $H_2^{18}O(2_{11}–2_{02})$ at a level of $\sim 5\sigma$. Consistent with the results in Yang et al. (2016), the flux ratio of H_2O/H_2O^+ is about 3. This ratio is very similar to those found in G09v1.97, indicating similar physical conditions of the molecular gas ionization. The ratio between the flux of $H_2O/H_2^{18}O$ is about 12, also being similar to that of G09v1.97.

5.7 Summary and conclusions

We have observed two prominent strongly lensed z = 3.6 SMGs of our sample at high angular-resolution (~ 0.35") with ALMA or NOEMA in millimeter bands allowing the observation of several submm lines of H_2O and H_2O^+, one line of CO and of $H_2^{18}O$. By developing an elaborate lensing modelling of these two sources, we have thus met our main goal of comparing the spatial distribution of the submillimeter

emission of CO, H_2O and the dust continuum. The high sensitivity of ALMA observations of G09v1.97 has allowed us to reconstruct high quality images in the plane of this source for the 2 mm dust continuum and the strong lines CO(6–5) and $H_2O(2_{11}–2_{02})$. It is thus shown that 1). the spatial distribution and the line profiles of CO(6–5) and $H_2O(2_{11}–2_{02})$ are similar, showing a typical kinematical structure of a rotating thin disk, and 2). the emission of both lines is a bit more extended (~ 0.19", ~ 1.40 kpc) than the dust continuum at 430 μm in the rest frame (~ 0.17", ~ 1.25 kpc) (see Table 5.4). Such a difference seems compatible with the properties of the warm dense component of the molecular gas found in modelling the CO excitation (Chapter 4), which should be able to collisionally excite both lines, especially $H_2O(2_{11}–2_{02})$, without needing infrared excitation. The situation is less clear for the comparison of the emission extensions in NCv1.143 because of the poorer accuracy of NOEMA data. However, from the lens models (see Table 5.5), the extension of $H_2O(2_{11}–2_{02})$ (0.23", ~ 1.7 kpc) seems significantly larger than that of the $H_2O(3_{21}–3_{12})$ line (0.16", ~ 1.2 kpc) and the 2 mm continuum (0.11", ~ 0.8 kpc). In addition it seems that the position of the high-excitation $H_2O(3_{21}–3_{12})$ line might be significantly shifted from that of the continuum and other lines. The explanation of such an effect, if confirmed, does not seem clear.

The high quality of ALMA images of G09v1.97 (but not that of NOEMA images of NCv1.143) has also allowed us to address the issue of differential lensing raised in discussing CO line ratios and profiles in Chapter 4. Our model succeeds in capturing a part of the observed line asymmetry. However, it is clear that both the asymmetry of the intrinsic velocity profile and differential lensing significantly contribute to the strong global asymmetry of the observed line profile.

The reconstructed images of G09v1.97 at different velocities might suggest a rotating thin disk with a radius of 0.6 kpc. However, the very strong asymmetry of the CO and H_2O lines makes uncertain such an interpretation. It makes difficult, anyway, an accurate determination of the rotation curve, and hence of the dynamical mass and of the Toomre Q parameter.

As a byproduct of these new high-quality observations of both sources, the detection of weaker molecular lines included in the observed frequency range is much improved. H_2O^+ lines are detected with an excellent S/N ratio on their overall intensity and even a good one for their line profile which proves similar to the CO(6–5) and $H_2O(2_{11}–2_{02})$ asymmetric profiles. The series of H_2O^+ lines offer unique information about the cosmic-ray ionization rate of the ISM and also the oxygen chemistry in the gas phase of the ISM. The detection of $H_2^{18}O$ is fully confirmed from ALMA observation of G09v1.97, and it is consolidated from NOEMA data about NCv1.143. A complete set of high-quality ALMA observations of other transitions of $H_2^{18}O$ and H_2O and an elaborate modelling of radiative transfer of H_2O lines, might help us to constrain the abundance ratio of $^{18}O/^{16}O$, and thus the IMF of the high-redshift SMGs, offering us important opportunities to reveal the nature of these fascinating galaxies at high-z.

Chapter 6

Summary and outlook

6.1 Summary

The discovery of a population of submillimetre bright galaxies (SMGs) highly obscured by dust at high-redshift (high-z) has revolutionised our understanding of galaxy formation and evolution. Such a new population of galaxies is contributing a significant fraction of the energy generated by all galaxies over the history of the Universe (e.g. Blain et al., 2002). With the extreme physical conditions of their star-forming environments, star formation rate approaching the Eddington's limit of radiation pressure stability, SMGs greatly enrich our knowledge of star formation in extreme physical conditions. Their spectral energy distributions (SEDs) are dominated by the dust continuum emission at far-infrared in the rest-frame, which allows them to be studied with good sensitivity for a redshift from 1 to 6, in the millimetre/submillimetre domain with the help of negative K-correction. From a galaxy-evolution/formation-modelling point of view, SMGs are considered as progenitors of the most massive galaxies seen in the Universe today (e.g. Casey et al., 2014). Nevertheless, some theoretical models of galaxies evolution have been questioned by the very high SMG number counts discovered at high-z. Recent large extragalactic surveys, such as *Herschel*-Astrophysical Terahertz Large Area Survey (*H*-ATLAS, Eales et al., 2010), the *Herschel* Multi-tiered Extragalactic Survey (*Her*MES, Oliver et al., 2012), South Pole Telescope survey (Vieira et al., 2013) have discovered hundreds of thousands of them, opening up new opportunities to conduct statistically based studies of high-z SMGs, and their clustering connecting to the large-scale structure of the Universe.

The large sample size makes it possible to find a very rare, around one in a thousand, type of distant SMGs, which are strongly gravitationally lensed by massive objects at an intermediate distance. The massive objects are usually massive elliptical galaxies with a redshift between about 0.2 and 1.2. The strong lensing effect not only amplifies the source in brightness by a typical factor up to $\sim$20, but also increases the spatial resolution by an average value of around 2–5. Such a substantial increase in both sensitivity and effective angular resolution forms an enormous asset for studying SMGs at high-z, especially on observations of their ISM content and investigating their star formation conditions. Nevertheless, the complexity of the gravitational lensing requires construction of elaborate models for the best-effort reconstruction of the source plane images, namely the intrinsic emission information of the SMGs.

We thus conducted a series of works based on a lensed SMG sample selected from the *H*-ATLAS catalogue. This sample allows us to study the ISM conditions of high-z SMGs, and understand their extreme star formation conditions. The sample was initially selected with the aim of detecting submillimetre H_2O emission lines. For the submillimetre H_2O lines, our previous studies showed that they could be the

brightest molecular emitter after CO lines from local ULIRGs to high-z SMGs (e.g. Omont et al., 2013; Yang et al., 2013). The H_2O lines constitute a powerful diagnosis of the physical conditions of the ISM in local ULIRGs, linking the properties of the dust far-infrared radiation field with those of the molecular gas (e.g. González-Alfonso et al., 2014). Following our studies conducted in the local Universe, we have observed a large sample of high-z lensed SMGs for their H_2O lines, using the compact configuration mode of the NOEMA/IRAM interferometer. Besides, we have also observed multiple transitions of the CO molecule and [CI] from the sample at the IRAM 30m single-dish telescope. The CO and [CI] lines are standard gas tracers which served as a complementary diagnosis for our study. Other molecular lines such as H_2O^+ have also been detected, tracing the key oxygen chemistry processes, indicating the ionisation state of the ISM and the intensity of cosmic rays. In order to resolve the source and acquire the spatial distributions of emission from various gas tracers and cold dust, we have also observed two of our SMGs using ALMA and NOEMA in high angular resolution configuration. The images provide key information about the resolved gas structure, kinematics, and the robust lensing models for accurately recovering the intrinsic properties of the sources.

We selected a sample of 17 highly lensed high-z SMGs with strong fluxes at submillimetre band from half the $\sim 600\,\mathrm{deg}^2$ *Herschel*-ATLAS survey, ten in its equatorial ("SDP" and "GAMA") and seven in north-galactic-pole ("NGP") fields. With NOEMA, we have detected at least one of the H_2O lines (redshifted into the millimetre windows) in each of the SMGs. We found that the H_2O lines, similar to those found in local ULIRGs, are the brightest submillimetre lines after those of CO. A strong linear correlation between the H_2O line luminosity and that of the total infrared has been found for the high-z SMGs, with $L_{H_2O} \sim {L_{IR}}^{1.2}$. This indicates the important role of far-infrared pumping in exciting the H_2O lines. To further perform the diagnostic using the H_2O lines, we applied an infrared pumping model of H_2O excitation. Modelling reveals that the far-infrared radiation fields have warm dust temperature $T_{warm} \sim 45$–$75\,\mathrm{K}$, H_2O column density per unit velocity interval $N_{H_2O}/\Delta V \gtrsim 0.3 \times 10^{15}\,\mathrm{cm^{-2}\,km^{-1}\,s}$ and $100\,\mu\mathrm{m}$ continuum opacity $\tau_{100} > 1$ (i.e. optically thick), indicating that H_2O is likely to trace highly obscured warm dense gas, residing in an intense far-infrared radiation field generated by extremely active star formation. Several H_2O^+ lines were also detected in three of the SMGs within the NOEMA bands targeting the H_2O lines. The line luminosities between H_2O and H_2O^+ are tightly correlated, which extends from local ULIRGs to high-z SMGs. The corresponding high flux ratio of $H_2O^+/H_2O \sim 0.3$ suggests that very intense cosmic-rays produced by strong star-forming activities are dominating the gas-phase oxygen chemistry, which is the main route of H_2O and H_2O^+ formation. Furthermore, through observing the $H_2O(4_{22}$–$4_{13})$ lines in two of our SMGs, we were able to build more detailed H_2O excitation models using three H_2O lines together with the dust continuum SED. The modelling results can well reproduce the observed H_2O line fluxes and the dust SED. It shows a clear evidence that, for the ISM of high-z SMGs, there are at least two excitation components, one extended cold component with dust temperature T_d around 35 K, and one less extended warm component with $T_d \sim 75\,\mathrm{K}$.

For the standard gas tracer, CO, we have observed its multiple transitions mostly from $J_{up} = 3$ to $J_{up} = 8$ in thirteen of the SMGs in the sample, plus two weaker SMGs. With the EMIR multi-band millimetre spectrometer mounted on the IRAM 30m telescope, we have thus established the spectral line energy distribution of the CO lines of our sample. The CO SLEDs, peaking around $J_{up} \sim 5$–7, are found to be similar to those of the local starburst-dominated ultra-luminous infrared galaxies and other high-z SMGs. After correcting for gravitational lensing effect, we derived the global properties of the bulk of molecular gas in the SMGs using the large velocity gradient approximation, such as the molecular gas density n_{H_2} and the kinetic temperature T_k. The gas thermal pressure P_{th} ranging from $\sim 10^5$ to $10^6\,\mathrm{K\,cm^{-3}}$ is found to be correlated with star formation efficiency. This suggests that P_{th} can play an

important role in regulating star formation in galactic scale. Further decomposing the CO SLEDs into two excitation components, we find a low-excitation component with $n_{\rm H_2} \sim 10^{2.8}$–$10^{4.6}\,{\rm cm^{-3}}$ and $T_{\rm k} \sim 20$–$30\,{\rm K}$, which is less correlated with star formation, and a high-excitation one ($n_{\rm H_2} \sim 10^{2.7}$–$10^{4.2}\,{\rm cm^{-3}}$, $T_{\rm k} \sim 60$–$400\,{\rm K}$) which is tightly related to the on-going star-forming activity. Additionally, tight linear correlations between the FIR and CO line luminosities have been confirmed for the $J_{\rm up} \geq 5$ CO lines of these SMGs, implying that these CO lines are good tracers of star formation. The [CI](2–1) lines follow the tight linear correlation between the luminosities of the [CI](2–1) and the CO(1–0) line found in local starbursts. This indicates that [CI] lines could also serve as good total molecular gas mass tracers for high-z SMGs. The total mass of the molecular gas reservoir, $(1\text{–}30) \times 10^{10}\,M_\odot$, derived based on the CO(3–2) fluxes and $\alpha_{\rm CO(1-0)} = 0.8 M_\odot\,({\rm K\,km\,s^{-1}\,pc^2})^{-1}$, suggests a typical molecular gas depletion time $t_{\rm dep} \sim 20$–$100\,{\rm Myr}$ and a gas to dust mass ratio $\delta_{\rm GDR} \sim 30$–100 with $\sim 20\%$–60% uncertainty for the SMGs. The ratio between CO line luminosity and the dust mass $L'_{\rm CO}/M_{\rm dust}$ appears to be slowly increasing with redshift for high-z SMGs, which need to be further confirmed by a much complete SMG sample at various redshifts. Finally, through comparing the linewidth of CO and H_2O lines, we find that they agree well in almost all our SMGs, confirming that the emitting regions of the CO and H_2O lines are co-spatially located, namely they both trace the warm dense molecular gas that is tightly connected with starbursting activities.

The physical properties of the ISM are complicated and highly dynamical. A galaxy usually contains a variety of regions with very different conditions. Such a complexity and variety would require high-angular-resolution observations of extragalactic objects. In order to understand the spatially resolved properties of molecular emissions, their geometric structure and dynamic properties, it is crucial to obtain their images with high angular resolutions. Therefore, we observed the H_2O, CO and dust continuum emission from two of our SMGs with extended configurations of ALMA and NOEMA interferometers. By developing elaborate lens models of these sources, the imaging data allowed us to reconstruct the intrinsic properties of the emission with a better sensitivity and spatial resolution. We have thus shown that the emission region of the cold dust which releases a considerable amount of energy from the star-forming activities has a smaller size comparing to that of the mid-J CO and $J = 2$ H_2O line. However, the dust emission is found to have a similar size comparing to that of the high-J CO and $H_2O(3_{21}$–$3_{12})$ line. Nevertheless, the emission sizes of CO and H_2O are found similar. Modelling the dynamics of the SMG using the high-quality CO data, we have shown that the source can be well modelled by a gaseous thin rotating disk, from which we have been able to derive the projected dynamical mass and its effective radius. The dynamical mass is found to be $\sim 4.6\times10^{10}\,M_\odot$, and the corresponding gas fraction is about 25%, which agrees with previous measurements of SMGs. The high S/N spectral data also allowed us to confirm the detection of the rare isotopologue, $H_2^{18}O$ in these two sources, that might help us to constrain the abundance ratio of $^{18}O/^{16}O$, and thus the IMF of the high-z SMGs, offering us important opportunities to reveal the nature of these fascinating galaxies at high-z.

6.2 Ongoing and future work: Observing the dense molecular gas tracers in the high-z lensed SMGs

Given the fact that HCN/HNC/HCO^+ have large dipole moments, they are very good dense gas tracers ($n_{\rm crit} \gtrsim 10^4\,{\rm cm^{-3}}$). A tight linear correlation between total IR and HCN luminosity holds from dense cores of GMCs in our Milky Way (Wu et al., 2005) to local ULIRGs (Gao & Solomon, 2004), and this correlation is even thought to be valid for all the dense gas tracers with $n_{\rm crit} \gtrsim 10^4\,{\rm cm^{-3}}$ (Zhang et al., 2014a) indicating that HCN directly traces the star-forming gas throughout the history of our universe. However, the meagre

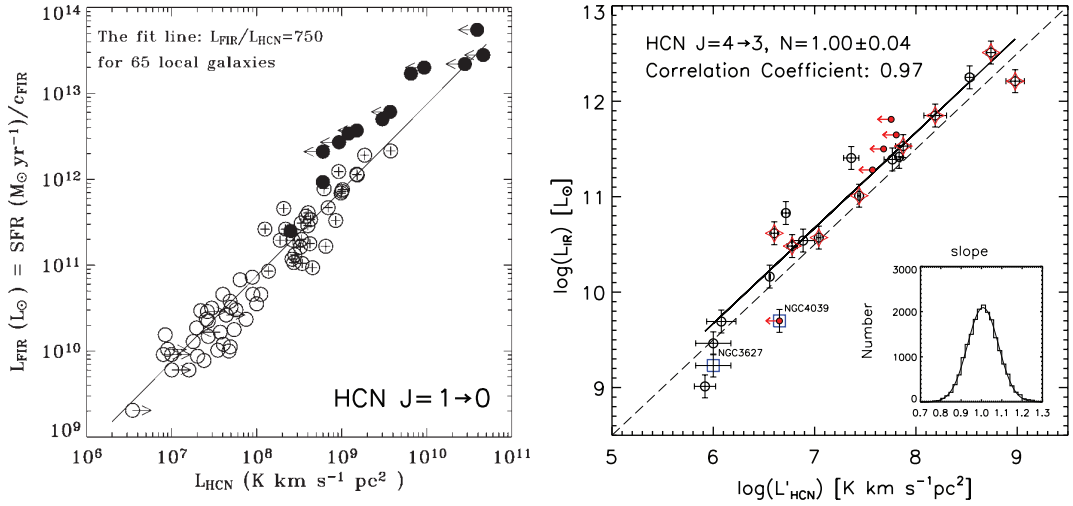

Fig. 6.1 Linear correlation between HCN line luminosity and star formation rate for the transition HCN(1–0) and HCN(4–3), as reported by Gao & Solomon (2004) (reproduced from figures of Gao & Solomon 2004 in Gao et al. 2007) and Zhang et al. (2014a), respectively.

HCN/HNC/HCO$^+$ detections at high-z are almost exclusively in lensed AGNs/QSOs so far (Carilli & Walter 2013, however, see Oteo et al. (2017); Spilker et al. (2014)). Their huge amount of IR output could have a substantial fraction unrelated to star formation. Besides, slightly higher $L_{\rm IR}/L'_{\rm HCN}$ ratios are found both in local and high-z ULIRGs (Gao et al., 2007; Gao & Solomon, 2004; García-Burillo et al., 2012). Nevertheless, it is difficult to evaluate the accurate contribution from AGN to $L_{\rm IR}$. Thus, it would be very important to explore the dense molecular gas physical condition through proper radiative modelling, to help us to fully understand the star formation process in those high-z ULIRGs, especially star formation dominated sources around the peak of the cosmic star formation density, i.e. the epoch of galaxy assembly. Recently, the successful detections of multi-J H_2O emissions in almost all the local ULIRGs (Yang et al., 2013), and also in 20 high-z lensed ULIRGs (Chapter 3, see also Omont et al. 2011, 2013; Yang et al. 2016) offer a lot of information about the central warm dense gas in those systems. Submm H_2O lines are found tightly correlated with total infrared luminosities, and IR-pumping is suggested to play an important role in exciting the $J = 3, 4$ H_2O lines ($E_u/k \sim 300$–450 K) in local ULIRGs (González-Alfonso et al., 2014). Besides, similar correlation between $L_{\rm HCN}$ and $L_{\rm IR}$ has been found by García-Burillo et al. 2012, suggesting that the millimeter HCN emission and submm H_2O probably arise from same regions, with similar physical properties (GA14). Through LVG modelling the HCN/HNC/HCO$^+$ lines together with multi-J CO lines, Riechers et al. (2010) found a strong IR-radiation field efficiently pumping the high-lying dense molecular gas tracers in the strongly lensed QSO, APM 08279+5255. Accordingly, by combining multi-J submm H_2O and CO lines with our mm detections of HCN/HNC/HCO$^+$ transitions (see Fig. 6.2 and Table 6.1), we will be able to constrain the physical and chemical properties of the molecular gas and the radiation field that powers the gas excitation in unprecedented detail.

To investigate the dense molecular gas content, we therefore conducted several observations: 1). NOEMA compact-array observations of HCN/HNC/HCO$^+$ (5–4) lines in NCv1.143 ($\sim$ 4 hours on source with compact D-configuration) and G09v1.97 ($\sim$ 1.5 hours one source with compact D-configuration); 2). JVLA compact-array observations of HCN/HCO$^+$(1–0) lines of NCv1.143. We have detected the targeted lines in NCv1.143 at a S/N level of $\sim$ 6 for HCN (5–4) and higher than a level of 3 detection for HNC (5–4) and HCO$^+$ (5–4) and ^{13}CO (4–3), while the detections in G09v1.97 are tentative (Fig. 6.2).

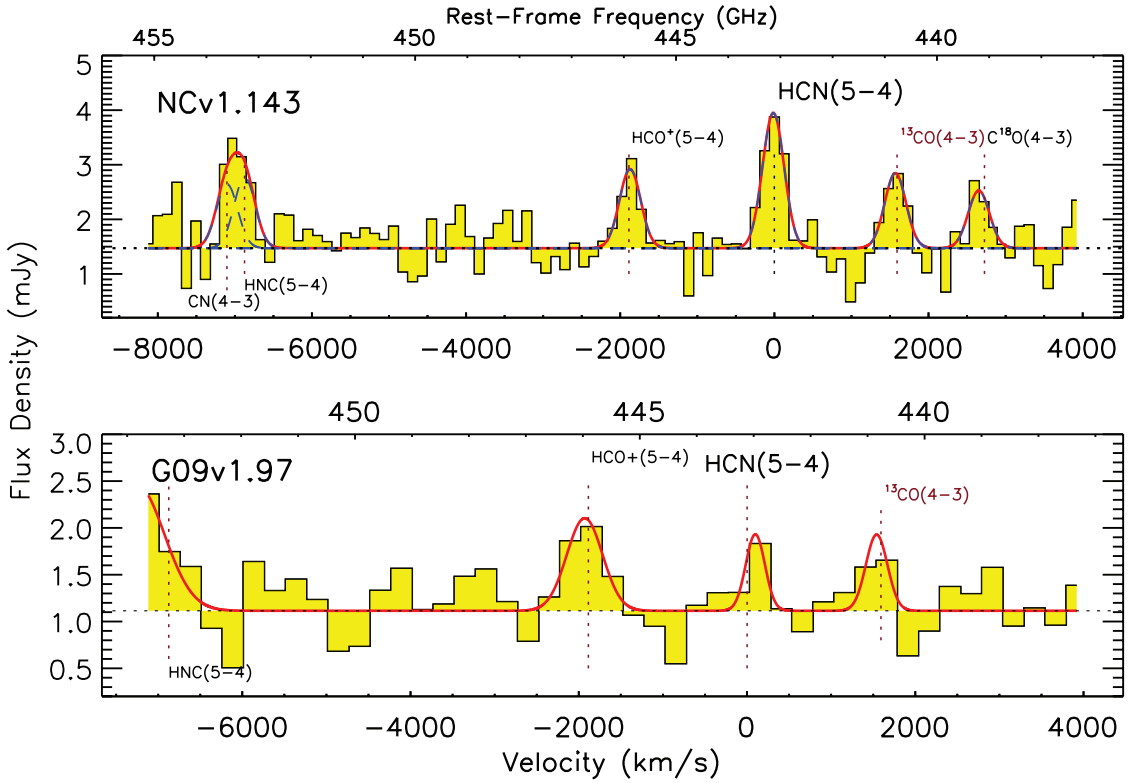

Fig. 6.2 The NOEMA spectra data of HCN/HNC/HCO$^+$(5–4), CN(4–3), ^{13}CO(4–3) and C^{18}O(4–3) in NCv1.143 and G09v1.97.

Table 6.1 Observed properties dense gas tracers in NCv1.143 and G09v1.97.

Line	$\nu_{\rm line}$ GHz	$I_{\rm line}$ Jy km s^{-1}	$\Delta V_{\rm line}$ km s^{-1}
NCv1.143, $z = 3.565$			
HCN(5–4)	97.068	0.87±0.15	328±62
HCO$^+$(5–4)	97.679	0.50±0.11	325^a
HNC(5–4)^b	99.292	0.45±0.15	325^a
CN(4–3)^b	99.366	0.41±0.14	325^a
^{13}CO (4–3)	96.553	0.47±0.12	325^a
C^{18}O (4–3)	96.553	0.36±0.12	325^a
G09v1.97, $z = 3.634$			
HCN (5–4)	95.623	0.23±0.13	268^c
HCO$^+$(5–4)	96.224	0.53±0.17	500^c
^{13}CO (4–3)	95.115	0.26±0.10	301^c

Note: The line frequency corresponds to the central frequency of each line given z = 3.565. $^{(a)}$: In order to reach better constrains on the flux using Gaussian fit, we assume the linewidth of all the molecular lines are the same and fix the linewidth to 325km s^{-1} while perform the fitting. $^{(b)}$: The line HNC(5–4) and CN(4–3) are blended. Nevertheless, we were able to fit the line with two Gaussian profiles by fixing the linewidth, and setting the central line position and peak flux free. $^{(c)}$: the parameters are not well constrained.

The observations of the dense gas tracers will enable us to have a detailed understanding of the physical conditions and chemical properties of various gas components by combining our previous multi-J H_2O and CO data in extreme star-forming environments. Using the HCN/HNC/HCO^+ (5–4) detected by NOEMA combining the HCN(1–0) detections from JVLA, we will be able to analysis the excitation states of the dense molecular gas, by using a non-LTE LVG modelling. Also, the HCN, HNC and HCO^+ abundances (wrt CO) will be compared with the predictions of physicochemical models, such as the `Meudon-PDR` model and `ASTROCHEM` (see examples, e.g. Ceccarelli et al., 2014). Ultimately, this should permit us to estimate the average FUV field as well as the average cosmic rays ionization rate. Both quantities, in turn, provide us with the star formation rate at those very early times, as the FUV field is due to O, B stars and and cosmic rays are produced by supernovae. Additionally, we have robust lens models to recovery the real emission properties from the gravitational magnification with the help of the lensing expert in our team, and the differential lensing issue for G09v1.97 was evaluated in Chapter 5. Besides the HCN/HNC/HCO^+(5–4) lines, we have also tentatively detected ^{13}CO(4–3) and C^{18}O(4–3). Combining our detections of the $H_2^{18}O$ lines, we could have a better estimation of the IMF of the high-z SMGs.

6.2.1 Prospective with ALMA and NOEMA for understanding the nature of high-z SMGs

Since the discovery of the first SMGs in the late 1990s, this field of research has passed through its major milestones, thanks to the fast development of the detectors working at submillimetre bands, ground-based sub/millimetre interferometers and also the space telescopes working at far-infrared. The launch of *Herschel* space observatory has greatly improved our knowledge of the ISM in the Milky Way and local Universe through observation of the dust emission and the main (mostly) molecular/atomic gas tracers, which were difficult to be observed from the ground. Using the local studies as templates/analogies, similar methods are extended to the high-z Universe, especially the SMGs, that are enhanced in the sub/millimetre band thanks to the negative K-correction. The operation of the most powerful sub/millimetre interferometer, ALMA, also has an unprecedented influence on the study of high-z SMGs. In parallel, the future complete NOEMA will offer the best resolution and sensitivity in the northern sky.

With the advantage of those far-infrared/sub/millimetre instruments, mostly ALMA and NOEMA, the study of the SMGs could much progress from (but not limited to) the following prospectives: 1) Study the high-z SMGs, especially the lensed ones, with long baseline observations of ALMA/NOEMA (down below ~ 100 pc), into the scale of massive clumps of molecular gas, and providing a fresh view of the detailed physics and chemistry in the early Universe. 2) Statistical analysis of the SMG population based on a large unbiased sample, thanks to the unprecedented sensitivity and good uv-coverage of ALMA. Snapshot observations with ALMA could offer an efficient method to study the dust/gas emission in a large number of SMGs, even for those unlensed ones (if unresolved). Such studies could help us to better understand the role of the SMGs in the cosmic star formation history. 3) Extending astrochemistry at high-z which is now possible by the combined power of ALMA and gravitational magnification. Thanks to gravitational lensing, the high-z SMGs can now be observed at a sensitivity through which we are able to approach the strong line confusion 'noise' limit so that molecular line surveys similar to those which have been conducted in the Orion region and local ULIRGs can now be conducted in high-z SMGs. We could thus have a rich information about the chemical abundances and processes in those systems. The fast development of such instruments brings us into the "golden age" of SMG studies. Nevertheless, we are still far from having a full picture of the physical processes taking place in those fascinating galaxies and their formation/evolution.

References

Alaghband-Zadeh, S., Chapman, S. C., Swinbank, A. M., et al. 2013, MNRAS, 435, 1493
ALMA Partnership, Vlahakis, C., Hunter, T. R., Hodge, J. A., et al. 2015, ApJ, 808, L4
Ao, Y., Weiß, A., Downes, D., et al. 2008, A&A, 491, 747
Aravena, M., Decarli, R., Walter, F., et al. 2016a, ApJ, 833, 68
Aravena, M., Spilker, J. S., Bethermin, M., et al. 2016b, MNRAS, 457, 4406
Banerji, M., Chapman, S. C., Smail, I., et al. 2011, MNRAS, 418, 1071
Barger, A. J., Cowie, L. L., Chen, C.-C., et al. 2014, ApJ, 784, 9
Barger, A. J., Cowie, L. L., Sanders, D. B., et al. 1998, Nature, 394, 248
Bartelmann, M. & Schneider, P. 2001, Phys. Rep., 340, 291
Barvainis, R., Tacconi, L., Antonucci, R., Alloin, D., & Coleman, P. 1994, Nature, 371, 586
Baugh, C. M., Lacey, C. G., Frenk, C. S., et al. 2005, MNRAS, 356, 1191
Becker, R. H., White, R. L., & Helfand, D. J. 1995, ApJ, 450, 559
Béthermin, M., Daddi, E., Magdis, G., et al. 2015, A&A, 573, A113
Bigiel, F., Leroy, A., Walter, F., et al. 2008, AJ, 136, 2846
Binney, J. & Tremaine, S. 1987, Galactic dynamics
Bisbas, T. G., Papadopoulos, P. P., & Viti, S. 2015, ApJ, 803, 37
Blain, A. W., Smail, I., Ivison, R. J., Kneib, J.-P., & Frayer, D. T. 2002, Phys. Rep., 369, 111
Bolatto, A. D., Wolfire, M., & Leroy, A. K. 2013, ARA&A, 51, 207
Bothwell, M. S., Aguirre, J. E., Aravena, M., et al. 2017, MNRAS, 466, 2825
Bothwell, M. S., Aguirre, J. E., Chapman, S. C., et al. 2013a, ApJ, 779, 67
Bothwell, M. S., Smail, I., Chapman, S. C., et al. 2013b, MNRAS, 429, 3047 (Bo13)
Bournaud, F., Daddi, E., Weiß, A., et al. 2015, A&A, 575, A56
Bradford, C. M., Aguirre, J. E., Aikin, R., et al. 2009, ApJ, 705, 112
Bradford, C. M., Bolatto, A. D., Maloney, P. R., et al. 2011, ApJ, 741, L37
Broadhurst, T. & Lehar, J. 1995, ApJ, 450, L41
Bussmann, R. S., Pérez-Fournon, I., Amber, S., et al. 2013, ApJ, 779, 25 (B13)
Carilli, C. L. & Walter, F. 2013, ARA&A, 51, 105
Casey, C. M., Narayanan, D., & Cooray, A. 2014, Phys. Rep., 541, 45
Ceccarelli, C., Baluteau, J.-P., Walmsley, M., et al. 2002, A&A, 383, 603
Ceccarelli, C., Dominik, C., López-Sepulcre, A., et al. 2014, ApJ, 790, L1
Chapman, S. C., Blain, A. W., Smail, I., & Ivison, R. J. 2005, ApJ, 622, 772
Cheung, A. C., Rank, D. M., Townes, C. H., Thornton, D. D., & Welch, W. J. 1969, Nature, 221, 626
Combes, F., Rex, M., Rawle, T. D., et al. 2012, A&A, 538, L4
Condon, J. J. & Ransom, S. M. 2016, Essential Radio Astronomy
Conley, A., Cooray, A., Vieira, J. D., et al. 2011, ApJ, 732, L35
Cooray, A., Calanog, J., Wardlow, J. L., et al. 2014, ApJ, 790, 40
Cox, P., Krips, M., Neri, R., et al. 2011, ApJ, 740, 63
Daddi, E., Dannerbauer, H., Liu, D., et al. 2015, A&A, 577, A46

Daddi, E., Dickinson, M., Chary, R., et al. 2005, ApJ, 631, L13
Daniel, F., Dubernet, M.-L., & Grosjean, A. 2011, A&A, 536, A76
Danielson, A. L. R., Swinbank, A. M., Smail, I., et al. 2011, MNRAS, 410, 1687
De Breuck, C., Williams, R. J., Swinbank, M., et al. 2014, A&A, 565, A59
Donovan Meyer, J., Koda, J., Momose, R., et al. 2013, ApJ, 772, 107
Downes, D., Neri, R., Wiklind, T., Wilner, D. J., & Shaver, P. A. 1999, ApJ, 513, L1
Downes, D., Radford, J. E., Greve, A., et al. 1992, ApJ, 398, L25
Downes, D. & Solomon, P. M. 1998, ApJ, 507, 615
Downes, D., Solomon, P. M., & Radford, S. J. E. 1993, ApJ, 414, L13
Draine, B. T. 1985, ApJS, 57, 587
Draine, B. T. 2011, Physics of the Interstellar and Intergalactic Medium (Princeton University Press)
Dubernet, M.-L., Daniel, F., Grosjean, A., & Lin, C. Y. 2009, A&A, 497, 911
Dunlop, J. S., McLure, R. J., Biggs, A. D., et al. 2017, MNRAS, 466, 861
Dye, S., Furlanetto, C., Dunne, L., et al. 2017, ArXiv e-prints [arXiv[arXiv]1705.05413]
Dye, S., Furlanetto, C., Swinbank, A. M., et al. 2015, MNRAS, 452, 2258
Eales, S., Dunne, L., Clements, D., et al. 2010, PASP, 122, 499
Einstein, A. 1936, Science, 84, 506
Elitzur, M., ed. 1992, Astrophysics and Space Science Library, Vol. 170, Astronomical masers
Falstad, N., González-Alfonso, E., Aalto, S., et al. 2015, A&A, 580, A52
Frayer, D. T., Ivison, R. J., Scoville, N. Z., et al. 1999, ApJ, 514, L13
Frayer, D. T., Ivison, R. J., Scoville, N. Z., et al. 1998, ApJ, 506, L7
Freeman, K. C. 1970, ApJ, 160, 811
Fu, H., Jullo, E., Cooray, A., et al. 2012, ApJ, 753, 134
Gao, Y., Carilli, C. L., Solomon, P. M., & Vanden Bout, P. A. 2007, ApJ, 660, L93
Gao, Y. & Solomon, P. M. 2004, ApJ, 606, 271
García-Burillo, S., Usero, A., Alonso-Herrero, A., et al. 2012, A&A, 539, A8
Gavazzi, R., Cooray, A., Conley, A., et al. 2011, ApJ, 738, 125
Genzel, R., Tacconi, L. J., Combes, F., et al. 2012, ApJ, 746, 69
Gérin, M., de Luca, M., Black, J., et al. 2010, A&A, 518, L110
Gnerucci, A., Marconi, A., Cresci, G., et al. 2011, A&A, 528, A88
Goldreich, P. & Kwan, J. 1974, ApJ, 189, 441
González-Alfonso, E. & Cernicharo, J. 1999, ApJ, 525, 845
Gonzalez-Alfonso, E., Cernicharo, J., Bachiller, R., & Fuente, A. 1995, A&A, 293
González-Alfonso, E., Fischer, J., Aalto, S., & Falstad, N. 2014, A&A, 567, A91 (G14)
González-Alfonso, E., Fischer, J., Bruderer, S., et al. 2013, A&A, 550, A25
González-Alfonso, E., Fischer, J., Graciá-Carpio, J., et al. 2012, A&A, 541, A4
González-Alfonso, E., Fischer, J., Isaak, K., et al. 2010, A&A, 518, L43
Griffin, M. J., Abergel, A., Abreu, A., et al. 2010, A&A, 518, L3
Harris, A. I., Baker, A. J., Frayer, D. T., et al. 2012, ApJ, 752, 152
Harwit, M., Neufeld, D. A., Melnick, G. J., & Kaufman, M. J. 1998, ApJ, 497, L105
Hatsukade, B., Tamura, Y., Iono, D., et al. 2015, PASJ, 67, 93
Hayward, C. C., Jonsson, P., Kereš, D., et al. 2012, MNRAS, 424, 951
Hayward, C. C., Kereš, D., Jonsson, P., et al. 2011, ApJ, 743, 159
Hezaveh, Y. D., Dalal, N., Marrone, D. P., et al. 2016, ApJ, 823, 37
Hjalmarson, Å., Frisk, U., Olberg, M., et al. 2003, A&A, 402, L39
Hodge, J. A., Carilli, C. L., Walter, F., et al. 2012, ApJ, 760, 11
Hodge, J. A., Swinbank, A. M., Simpson, J. M., et al. 2016, ApJ, 833, 103
Holland, W. S., Robson, E. I., Gear, W. K., et al. 1999, MNRAS, 303, 659

Hughes, D. H., Serjeant, S., Dunlop, J., et al. 1998, Nature, 394, 241
Ikarashi, S., Ivison, R. J., Caputi, K. I., et al. 2015, ApJ, 810, 133
Inoue, K. T., Minezaki, T., Matsushita, S., & Chiba, M. 2016, MNRAS, 457, 2936
Ivison, R. J., Papadopoulos, P. P., Smail, I., et al. 2011, MNRAS, 412, 1913
Ivison, R. J., Smail, I., Le Borgne, J.-F., et al. 1998, MNRAS, 298, 583
Ivison, R. J., Smail, I., Papadopoulos, P. P., et al. 2010, MNRAS, 404, 198
Kamenetzky, J., Glenn, J., Rangwala, N., et al. 2012, ApJ, 753, 70
Karim, A., Swinbank, A. M., Hodge, J. A., et al. 2013, MNRAS, 432, 2
Keeton, C. R. 2001, ArXiv Astrophysics e-prints [arXivastro-ph/0102340]
Kennicutt, Jr., R. C. 1998, ApJ, 498, 541
Kessler, M. F., Steinz, J. A., Anderegg, M. E., et al. 1996, A&A, 315, L27
Kormann, R., Schneider, P., & Bartelmann, M. 1994, A&A, 284, 285
Le Floc'h, E., Papovich, C., Dole, H., et al. 2005, ApJ, 632, 169
Leroy, A. K., Bolatto, A., Gordon, K., et al. 2011, ApJ, 737, 12
Leroy, A. K., Walter, F., Brinks, E., et al. 2008, AJ, 136, 2782
Lewis, G. F., Chapman, S. C., Ibata, R. A., Irwin, M. J., & Totten, E. J. 1998, ApJ, 505, L1
Lilly, S. J., Le Fevre, O., Hammer, F., & Crampton, D. 1996, ApJ, 460, L1
Lis, D. C., Neufeld, D. A., Phillips, T. G., Gerin, M., & Neri, R. 2011, ApJ, 738, L6
Liu, D., Gao, Y., Isaak, K., et al. 2015, ApJ, 810, L14
Lo, K. Y. 2005, ARA&A, 43, 625
Lonsdale, C. J., Farrah, D., & Smith, H. E. 2006, Ultraluminous Infrared Galaxies, ed. J. W. Mason (Springer), 285
Lu, N., Zhao, Y., Díaz-Santos, T., et al. 2017, ApJS, 230, 1
Lupu, R. E., Scott, K. S., Aguirre, J. E., et al. 2012, ApJ, 757, 135
Madau, P. & Dickinson, M. 2014, ARA&A, 52, 415
Madau, P., Ferguson, H. C., Dickinson, M. E., et al. 1996, MNRAS, 283, 1388
Maeder, A. 1983, A&A, 120, 113
Magdis, G. E., Daddi, E., Elbaz, D., et al. 2011, ApJ, 740, L15
Magnelli, B., Lutz, D., Santini, P., et al. 2012, A&A, 539, A155
Magnelli, B., Popesso, P., Berta, S., et al. 2013, A&A, 553, A132
Markwardt, C. B. 2009, in Astronomical Society of the Pacific Conference Series, Vol. 411, Astronomical Data Analysis Software and Systems XVIII, ed. D. A. Bohlender, D. Durand, & P. Dowler, 251
Marshall, P., Blandford, R., & Sako, M. 2005, New A Rev., 49, 387
Meijerink, R., Kristensen, L. E., Weiß, A., et al. 2013, ApJ, 762, L16
Meijerink, R. & Spaans, M. 2005, A&A, 436, 397
Meijerink, R., Spaans, M., Loenen, A. F., & van der Werf, P. P. 2011, A&A, 525, A119
Melnick, G. J. & Bergin, E. A. 2005, Advances in Space Research, 36, 1027
Melnick, G. J., Stauffer, J. R., Ashby, M. L. N., et al. 2000, ApJ, 539, L77
Menten, K. M., Melnick, G. J., & Phillips, T. G. 1990a, in BAAS, Vol. 22, Bulletin of the American Astronomical Society, 740
Menten, K. M., Melnick, G. J., Phillips, T. G., & Neufeld, D. A. 1990b, ApJ, 363, L27
Meylan, G., Jetzer, P., North, P., et al., eds. 2006, Gravitational Lensing: Strong, Weak and Micro
Michałowski, M. J., Dunlop, J. S., Koprowski, M. P., et al. 2017, MNRAS, 469, 492
Moustakas, L. A., Marshall, P., Newman, J. A., et al. 2007, ApJ, 660, L31
Murphy, E. J., Chary, R.-R., Dickinson, M., et al. 2011, ApJ, 732, 126
Narayanan, D. & Krumholz, M. R. 2014, MNRAS, 442, 1411
Narayanan, D., Krumholz, M. R., Ostriker, E. C., & Hernquist, L. 2012, MNRAS, 421, 3127
Nayyeri, H., Keele, M., Cooray, A., et al. 2016, ApJ, 823, 17
Negrello, M., Amber, S., Amvrosiadis, A., et al. 2017, MNRAS, 465, 3558

Negrello, M., Hopwood, R., De Zotti, G., et al. 2010, Science, 330, 800
Negrello, M., Perrotta, F., González-Nuevo, J., et al. 2007, MNRAS, 377, 1557
Neufeld, D. A., Goicoechea, J. R., Sonnentrucker, P., et al. 2010, A&A, 521, L10
Oliver, S. J., Bock, J., Altieri, B., et al. 2012, MNRAS, 424, 1614
Omont, A. 2007, Reports on Progress in Physics, 70, 1099
Omont, A., Neri, R., Cox, P., et al. 2011, A&A, 530, L3
Omont, A., Yang, C., Cox, P., et al. 2013, A&A, 551, A115 (O13)
Oteo, I., Zhang, Z., Yang, C., et al. 2017, ArXiv e-prints [arXiv[arXiv]1701.05901]
Oteo, I., Zwaan, M. A., Ivison, R. J., Smail, I., & Biggs, A. D. 2016, ApJ, 822, 36
Papadopoulos, P. P. & Greve, T. R. 2004, ApJ, 615, L29
Paraficz, D., Rybak, M., McKean, J. P., et al. 2017, ArXiv e-prints [arXiv[arXiv]1705.09931]
Phillips, T. G., Kwan, J., & Huggins, P. J. 1980, in IAU Symposium, Vol. 87, Interstellar Molecules, ed. B. H. Andrew, 21–24
Pilbratt, G. L., Riedinger, J. R., Passvogel, T., et al. 2010, A&A, 518, L1
Planck Collaboration, Ade, P. A. R., Aghanim, N., et al. 2014, A&A, 571, A1
Poglitsch, A., Waelkens, C., Geis, N., et al. 2010, A&A, 518, L2
Preibisch, T., Ossenkopf, V., Yorke, H. W., & Henning, T. 1993, A&A, 279, 577
Rangwala, N., Maloney, P. R., Glenn, J., et al. 2011, ApJ, 743, 94
Rawle, T. D., Egami, E., Bussmann, R. S., et al. 2014, ApJ, 783, 59
Reid, M. J. & Moran, J. M. 1981, ARA&A, 19, 231
Riechers, D. A., Bradford, C. M., Clements, D. L., et al. 2013, Nature, 496, 329
Riechers, D. A., Walter, F., Carilli, C. L., & Lewis, G. F. 2009, ApJ, 690, 463
Riechers, D. A., Weiß, A., Walter, F., & Wagg, J. 2010, ApJ, 725, 1032
Rosenberg, M. J. F., van der Werf, P. P., Aalto, S., et al. 2015, ApJ, 801, 72
Rowan-Robinson, M., Broadhurst, T., Oliver, S. J., et al. 1991, Nature, 351, 719
Rybak, M., McKean, J. P., Vegetti, S., Andreani, P., & White, S. D. M. 2015a, MNRAS, 451, L40
Rybak, M., Vegetti, S., McKean, J. P., Andreani, P., & White, S. D. M. 2015b, MNRAS, 453, L26
Schmidt, M. 1959, ApJ, 129, 243
Schöier, F. L., van der Tak, F. F. S., van Dishoeck, E. F., & Black, J. H. 2005, A&A, 432, 369
Schruba, A., Leroy, A. K., Walter, F., et al. 2011, AJ, 142, 37
Scoville, N. Z. & Solomon, P. M. 1974, ApJ, 187, L67
Sersic, J. L. 1968, Atlas de galaxias australes
Shapley, A. E. 2011, ARA&A, 49, 525
Simpson, J. M., Swinbank, A. M., Smail, I., et al. 2014, ApJ, 788, 125
Smail, I., Ivison, R. J., & Blain, A. W. 1997, ApJ, 490, L5
Smail, I., Ivison, R. J., Blain, A. W., & Kneib, J.-P. 1998, ApJ, 507, L21
Smolčić, V., Aravena, M., Navarrete, F., et al. 2012, A&A, 548, A4
Sobolev, V. V. 1960, Moving envelopes of stars
Solomon, P., Vanden Bout, P., Carilli, C., & Guelin, M. 2003, Nature, 426, 636
Solomon, P. M., Downes, D., & Radford, S. J. E. 1992, ApJ, 387, L55
Solomon, P. M., Rivolo, A. R., Barrett, J., & Yahil, A. 1987, ApJ, 319, 730
Solomon, P. M. & Vanden Bout, P. A. 2005, ARA&A, 43, 677
Spilker, J. S., Aravena, M., Marrone, D. P., et al. 2015, ApJ, 811, 124
Spilker, J. S., Marrone, D. P., Aguirre, J. E., et al. 2014, ApJ, 785, 149
Spilker, J. S., Marrone, D. P., Aravena, M., et al. 2016, ApJ, 826, 112
Spinoglio, L., Pereira-Santaella, M., Busquet, G., et al. 2012, ApJ, 758, 108
Swinbank, A. M., Dye, S., Nightingale, J. W., et al. 2015, ApJ, 806, L17
Swinbank, A. M., Simpson, J. M., Smail, I., et al. 2014, MNRAS, 438, 1267

Swinbank, A. M., Smail, I., Longmore, S., et al. 2010, Nature, 464, 733
Tacconi, L. J., Genzel, R., Neri, R., et al. 2010, Nature, 463, 781
Tacconi, L. J., Genzel, R., Smail, I., et al. 2008, ApJ, 680, 246
Tacconi, L. J., Neri, R., Genzel, R., et al. 2013, ApJ, 768, 74
Tamura, Y., Oguri, M., Iono, D., et al. 2015, PASJ, 67, 72
Tielens, A. G. G. M. 2005, The Physics and Chemistry of the Interstellar Medium (Cambridge University Press)
Tielens, A. G. G. M. 2013, Reviews of Modern Physics, 85, 1021
Toomre, A. 1964, ApJ, 139, 1217
Treu, T. 2010, ARA&A, 48, 87
Umetsu, K. 2010, ArXiv e-prints [arXiv[arXiv]1002.3952]
Valiante, E., Smith, M. W. L., Eales, S., et al. 2016, MNRAS, 462, 3146
van der Tak, F. F. S., Black, J. H., Schöier, F. L., Jansen, D. J., & van Dishoeck, E. F. 2007, A&A, 468, 627
van der Tak, F. F. S., Weiß, A., Liu, L., & Güsten, R. 2016, A&A, 593, A43
van der Werf, P. P., Berciano Alba, A., Spaans, M., et al. 2011, ApJ, 741, L38
van der Werf, P. P., Isaak, K. G., Meijerink, R., et al. 2010, A&A, 518, L42
van Dishoeck, E. F., Herbst, E., & Neufeld, D. A. 2013, Chemical Reviews, 113, 9043
Vieira, J. D., Crawford, T. M., Switzer, E. R., et al. 2010, ApJ, 719, 763
Vieira, J. D., Marrone, D. P., Chapman, S. C., et al. 2013, Nature, 495, 344
Wang, B. & Silk, J. 1994, ApJ, 427, 759
Wang, R., Wagg, J., Carilli, C. L., et al. 2013, ApJ, 773, 44
Wardlow, J. L., Cooray, A., De Bernardis, F., et al. 2013, ApJ, 762, 59
Weiß, A., De Breuck, C., Marrone, D. P., et al. 2013, ApJ, 767, 88
Weiß, A., Downes, D., Neri, R., et al. 2007, A&A, 467, 955
Weiß, A., Henkel, C., Downes, D., & Walter, F. 2003, A&A, 409, L41
Williams, D. A. & Viti, S. 2013, Observational Molecular Astronomy (Cambridge University Press)
Williams, D. A. & Viti, S. 2014, Observational Molecular Astronomy
Wilson, C. D. 1995, ApJ, 448, L97
Wong, K. C., Ishida, T., Tamura, Y., et al. 2017, ArXiv e-prints [arXiv[arXiv]1707.00702]
Wong, K. C., Suyu, S. H., & Matsushita, S. 2015, ApJ, 811, 115
Wu, J., Evans, II, N. J., Gao, Y., et al. 2005, ApJ, 635, L173
Yang, B., Stancil, P. C., Balakrishnan, N., & Forrey, R. C. 2010, ApJ, 718, 1062
Yang, C., Gao, Y., Omont, A., et al. 2013, ApJ, 771, L24 (Y13)
Yang, C., Omont, A., Beelen, A., et al. 2016, A&A, 595, A80
Zhang, Z.-Y., Gao, Y., Henkel, C., et al. 2014a, ApJ, 784, L31
Zhang, Z.-Y., Henkel, C., Gao, Y., et al. 2014b, A&A, 568, A122
Zhang, Z.-Y., Papadopoulos, P. P., Ivison, R. J., et al. 2016, Royal Society Open Science, 3, 160025

List of figures

List of tables

université PARIS-SACLAY
ÉCOLE DOCTORALE
Astronomie et Astrophysique d'Île-de-France

Titre : Conditions physiques du milieu interstellaire dans les galaxies à fort rayonnement submillimétrique à haut redshift

Mots clés : galaxie, infrarouge, haut redshift, gaz moléculaire, lentille gravitationnelle

Résumé : La découverte d'une population de galaxies submillimétrique (SMG) obscurcies par la poussière à grand décalage spectral, à l'aide de caméras submm, a révolutionné notre connaissance de l'évolution des galaxies et de la formation stellaire dans les conditions physiques extrêmes. Elles sont les flambées de formation stellaire les plus intenses dans l'Univers, approchant la limite d'Eddington et sont considérées comme les progéniteurs des galaxies actuelles les plus massives. Les modèles théoriques d'évolution de galaxies ont été remis en question par la découverte d'un grand nombre de SMGs à grand décalage spectral. Quelques-unes sont fortement lentillées gravitationnellement par une galaxie. Les grands relevés extragalactiques récemment effectués en ont découvert plusieurs centaines, ouvrant de nouvelles opportunités pour observer le milieu interstellaire dans ces objets exceptionnels.

Nous avons donc sélectionné un échantillon de SMG fortement lentillées à l'aide des densités de flux submm du relevé *Herschel*-ATLAS. À l'aide des télescopes de l'IRAM, nous avons construit un échantillon de 16 SMG détectées par la raie de l'eau. Nous avons trouvé une corrélation linéaire forte entre les luminosité d'H_2O et infrarouge totale. Cela indique le rôle important du pompage IR lointain dans l'excitation des raies de l'eau. En utilisant un modèle de pompage IR lointain, nous avons obtenu les propriétés physiques du gaz et de la poussière. Nous avons montré que l'eau trace un gaz chaud et dense qui peut être étroitement lié à la formation des étoiles. Plusieurs raies d'H_2O^+ ont également été détectées dans trois SMG, montrant une corrélation étroite entre les luminosités des raies de H_2O/H_2O^+ des ULIRG locales aux SMG. Le rapport de flux H_2O^+/H_2O suggère que les rayons cosmiques provenant des activités fortes de formation stellaire sont probablement à l'origine de la chimie de l'oxygène.

Nous avons observé de multiples transitions de CO dans chacune de nos SMG. Nous avons mis en évidence un effet significatif de lentillage différentiel qui peut entraîner une sous-estimation de la largeur de raie d'un facteur ~2. A l'aide d'une modélisation de type LVG et en utilisant une approche bayésienne, nous avons estimé la densité et la température du gaz, ainsi que sa densité de colonne. Nous avons ensuite mis en évidence une corrélation entre la pression thermique du gaz et l'efficacité de la formation stellaire. Nous avons également étudié les propriétés globales du gaz moléculaire et sa relation avec la formation d'étoiles ainsi que le rapport masse de gaz sur poussière et le temps d'épuisement du gaz. La détections de raies de carbone atomique dans ces SMG a étendu la corrélation linéaire locale entre luminosité des raies de CO/CI. Enfin, nous avons comparé les largeurs de raie de CO/H_2O et constaté qu'elles étaient en bon accord. Cela suggère que les régions émettrices sont co-spatiales.

Afin de comprendre les propriétés des émissions moléculaires dans ces sources, et plus généralement, leur structure et leur propriétés dynamiques, il est crucial d'acquérir des images à haute résolution angulaire. Nous avons donc observé deux sources avec ALMA/NOEMA en configuration étendue. Ces données nous permettent de reconstituer la morphologie intrinsèque de la source. Les émissions de poussière froide ont une plus petite taille en comparaison avec le gaz CO/H_2O, tandis que les deux derniers sont de taille similaire. En ajustant le modèle dynamique aux données CO, nous avons montré que ces galaxies peuvent être modélisées avec un disque en rotation, duquel nous avons pu déduire leurs masses dynamiques projetées et leurs rayons effectifs.

Avec le futur NOEMA/ALMA, nous pourrons étendre ce genre d'observations à un plus grand nombre de SMG fortement amplifiées et même à des SMG non lentillées, afin d'étudier divers traceurs du gaz moléculaire et de comprendre les conditions physiques du milieu interstellaire et leur relation avec la formation des étoiles.

Université Paris-Saclay
Espace Technologique / Immeuble Discovery
Route de l'Orme aux Merisiers RD 128 / 91190 Saint-Aubin, France

université PARIS-SACLAY | ÉCOLE DOCTORALE Astronomie et Astrophysique d'île-de-France

Title: Physical conditions of the interstellar medium in high-redshift submillimetre bright galaxies

Keywords: galaxy, infrared, high redshift, molecular gas, gravitational lensing

Abstract: The discovery of a population of high-redshift dust-obscured submillimeter galaxies (SMGs) from ground-based submm cameras has revolutionised our understanding of galaxy evolution and star formation in extreme conditions. They are the strongest starbursts in the Universe approaching the Eddington limit and are believed to be the progenitors of the most massive galaxies today. However, theoretical models of galaxy evolution have even been challenged by a large number of detections of high-redshift SMGs. A very few among them are gravitationally lensed by an intervening galaxy. Recent wide-area extragalactic surveys have discovered hundreds of such strongly lensed SMGs, opening new exciting opportunities for observing the interstellar medium in these exceptional objects.

We have thus carefully selected a sample of strongly gravitational lensed SMGs based on the submillimeter flux limit from the *Herschel*-ATLAS sample. Using IRAM telescopes, we have built a rich H_2O-line-detected sample of 16 SMGs. We found a close-to-linear tight correlation between the H_2O line and total infrared luminosity. This indicates the importance of far-IR pumping to the excitation of the H_2O lines. Using a far-IR pumping model, we have derived the physical properties of the H_2O gas and the dust. We showed that H_2O lines trace a warm dense gas that may be closely related to the active star formation. Along with the H_2O lines, several H_2O^+ lines have also been detected in three of our SMGs. We also find a tight correlation between the luminosity of the lines of H_2O and H_2O^+ from local ULIRGs to high-redshift SMGs. The flux ratio between H_2O^+ and H_2O suggests that cosmic rays from strong star forming activities are possibly driving the related oxygen chemistry.

Another important common molecular gas tracer is the CO line. We have observed multiple transitions of the CO lines in each of our SMGs with IRAM 30m telescope. By analysing the CO line profile, we discovered a significant differential lensing effect that might cause underestimation of the linewidth by a factor of ~ 2. Using LVG modelling and fitting the multi-J CO fluxes via a Bayesian approach, we derived gas densities and temperature, and CO column density per unit velocity gradient. We then found a correlation between the gas thermal pressure and the star formation efficiency. We have also studied the global properties of the molecular gas and its relationship with star formation. We have derived the gas to dust mass ratio and the gas depletion time, they show no difference compared with other SMGs. With the detections of atomic carbon lines in our SMGs, we extended the local linear correlation between the CO and CI line luminosity. Finally, we compared the linewidths of the CO and H_2O emission line, which agree very well with each other. This suggests that the emitting regions of these two molecules are likely to be co-spatially located.

In order to understand the properties of molecular emission in high-redshift SMGs, and more generally, the structure and the dynamical properties of these galaxies, it is crucial to acquire high-resolution images. We thus observed two of our brightest sources with ALMA and NOEMA interferometers using their high spatial resolution configuration. These images have allowed us to reconstruct the intrinsic morphology of the sources. We compared the CO, H_2O and dust emission. The cold dust emission has a smaller size compared with the CO and H_2O gas, while the latter two are similar in size. By fitting the dynamical model to the CO data of the source, we have shown that the source can be modelled with a rotating disk. We derived the projected dynamical mass and the effective radius of those sources.

With the future NOEMA and ALMA, we will be able to extend such kind of observations to a larger sample lensed SMGs and even to unlensed SMGs, to study various gas tracers, and to understand the physical conditions of the ISM and their relation to the star formation.

Université Paris-Saclay
Espace Technologique / Immeuble Discovery
Route de l'Orme aux Merisiers RD 128 / 91190 Saint-Aubin, France